CFD Modeling and Simulation in Materials Processing 2018

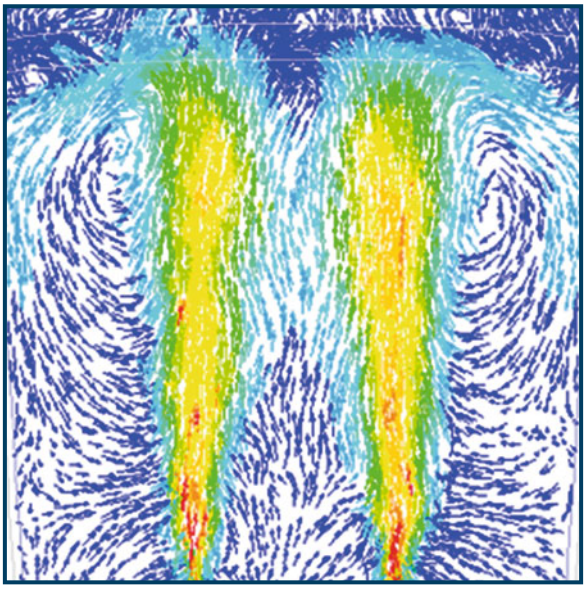

Edited by
Laurentiu Nastac, Koulis Pericleous,
Adrian S. Sabau, Lifeng Zhang,
and Brian G. Thomas

TMS

Springer

The Minerals, Metals & Materials Series

Laurentiu Nastac · Koulis Pericleous
Adrian S. Sabau · Lifeng Zhang
Brian G. Thomas
Editors

CFD Modeling and Simulation in Materials Processing 2018

TMS

Springer

Editors
Laurentiu Nastac
The University of Alabama
Tuscaloosa, AL
USA

Koulis Pericleous
University of Greenwich
London
UK

Adrian S. Sabau
Oak Ridge National Laboratory
Oak Ridge, TN
USA

Lifeng Zhang
University of Science and Technology Beijing
Beijing
China

Brian G. Thomas
Colorado School of Mines
Golden, CO
USA

ISSN 2367-1181 ISSN 2367-1696 (electronic)
The Minerals, Metals & Materials Series
ISBN 978-3-319-72058-6 ISBN 978-3-319-72059-3 (eBook)
https://doi.org/10.1007/978-3-319-72059-3

Library of Congress Control Number: 2017959908

Printed on acid-free paper

This Springer imprint is published by Springer Nature
The registered company is Springer International Publishing AG
The registered company address is: Gewerbestrasse 11, 6330 Cham, Switzerland

Preface

This book contains the proceedings of the symposium "CFD Modeling and Simulation in Materials Processing" held at the TMS 2018 Annual Meeting & Exhibition in Phoenix, Arizona, USA, March 11–15, 2018.

This symposium dealt with computational fluid dynamics (CFD) modeling and simulation of engineering processes. The papers published in this book were requested from researchers and engineers involved in the modeling of multiscale and multiphase phenomena in material processing systems.

The symposium focused on the CFD modeling and simulation of the following processes: Additive Manufacturing (Selective Laser Melting and Laser Powder Bed Fusion); Gas Atomization, Iron and Steelmaking (Continuous Casting, Blown Converter, Reheating Furnace, and Ladle Metallurgical Furnace); Submerged Arc Furnaces; Electrokinetic Deposition; Core Injection Molding; Evaporation of Metals; Friction Stir Welding; Ingot Casting; High Pressure Die Casting; and Casting and Solidification with Electromagnetic Field Interaction.

The symposium also covered applications of CFD to engineering processes and demonstrated how CFD can help scientists and engineers to better understand the fundamentals of engineering processes.

On behalf of all symposium organizers
and participants,
Laurentiu Nastac

Contents

Part III Processing: I

Part IV Processing: II

Part V Processing: III

About the Editors

Laurentiu Nastac is an Associate Professor of Metallurgical and Materials Engineering at The University of Alabama, Metallurgical and Materials Engineering Department, Tuscaloosa, Alabama, and a Key FEF Professor and the Director of the Solidification and Ultrasonic Laboratory and of the UA-COE foundry. More details on his teaching and research interests can be found on his website: http://lnastac.people.ua.edu/.

Dr. Nastac received the Diploma Engineering degree in Metallurgy and Materials Science from the University "Politehnica" of Bucharest, Romania in 1985 and the M.S. and Ph.D. degrees in Metallurgical and Materials Engineering from The University of Alabama, Tuscaloosa in 1993 and 1995, respectively. He has held various engineering, research, and academic positions in Romania and the United States. At Caterpillar he conducted research in the area of macro transport and solidification-kinetics modeling and developed specialized casting simulation software. At Concurrent Technologies Corporation (CTC) he conducted research primarily in the area of advanced metalcasting and solidification processes with emphasis on the modeling and simulation of casting phenomena. In 1999, in recognition of his work on solidification of Ti-based alloys and superalloy remelt ingots, he received the prestigious "Bunshah Best Paper Award" from the American Vacuum Society, Vacuum Metallurgy Division. More recently, he received the NMC (Navy Metalworking Center) achievement award and 2 CTC awards.

Dr. Nastac has developed 8 software tools, made 188 presentations, and co-authored 3 patents, 104 peer-review conference articles, 72 journal articles, 69 scientific and technical reports, and 18 books; one of the books is a monograph titled *Modeling and Simulation of Microstructure Evolution in Solidifying Alloys* published by Springer in 2004. He is a Key Reader for *Metallurgical and Materials Transactions*, a member of the Editorial Board of the *International Journal of Cast Metals Research*, and a member of the TMS Solidification and Process Technology and Modeling Committees. He served in scientific committees and as an organizer for international conferences and also as a guest editor for journals dedicated to CFD modeling and simulation in the materials processing area and for casting and solidification processes.

Koulis Pericleous holds the Chair of Computational Fluid Dynamics at the University of Greenwich, London, and is Director of the Centre for Numerical Modelling and Process Analysis. Details of his current research interests and other academic activities can be found at http://staffweb.cms.gre.ac.uk/~pk01.

Dr. Pericleous received his bachelor's degree in Aeronautics at Queen Mary College, University of London, in 1974 followed by a Ph.D. in Unsteady Aerodynamics. He learned the intricacies of CFD in CHAM LTD under Professor Brian Spalding, as part of the development team for the first commercial CFD code PHOENICS. For the next decade, he held various positions in CHAM, rising to Head of Consultancy Services in 1987. Under his direction, his team worked on a wide range of industrial problems, many in the metals processing sector. A notable example was the development through CFD of the novel HiSmelt process in Australia, for the production of iron directly from ore. He re-joined Academia at the University of Greenwich in 1989, becoming a full Professor in 1994. In his 28 years at Greenwich, he led several U.K. government and European funded projects in the area of advanced materials. Examples include the cold crucible melting and casting of TiAl turbine blades, the gas atomization of NiAl Raney powders, the production of lightweight metal-matrix nanocomposites using electromagnetic interaction, the ultrasonic processing of flowing volumes of aluminum, and modeling

levitated melts in the ISS MSL facility. In this period, Dr. Pericleous and his team developed a number of CFD tools for industry, including the multi-physics code PHYSICA, the microstructure evolution code TESA and the aluminum electrolysis code MHD-Valdis. He is the author of more than 300 publications and has supervised 35 Ph.D. students. He is a grant reviewer for several U.K. and European national bodies and on the editorial board of archival journals.

Adrian S. Sabau received his Diploma de Inginer in Mechanical Engineering/Materials Processing from the University of Craiova, Romania in 1992 and a Ph.D. degree in Mechanical Engineering from Southern Methodist University in 1996. In 1999, Dr. Sabau joined Oak Ridge National Laboratory as a Research Staff Member of the Materials Science and Technology, where he has been a Senior Research Staff Member since 2008. Dr. Sabau is the recipient of two R&D 100 awards in process sciences. He seeks to advance materials processing, metal casting, photonic processing, and materials for energy applications through the development of solution algorithms, computational and experimental methodologies for the property measurement, process analysis, and materials behavior in response to conditions experienced in service. Dr. Sabau has published more than 60 journal articles and 80 conference papers, and he has 2 patents and 6 patent applications.

Lifeng Zhang is a professor and the dean of the School of Metallurgical and Ecological Engineering at University of Science and Technology Beijing, and a Distinguished Professor of Yangtze River Scholars of China. Dr. Zhang received his Ph.D. degree from the University of Science and Technology Beijing in 1998 and has extensive teaching and research work at different universities—University of Science and Technology Beijing, Missouri University of Science and Technology, Norwegian University of Science and Technology, University of Illinois at Urbana-Champaign, Technical University of Clausthal, and Tohoku University. Dr. Zhang has compound backgrounds in primary production, refining, casting, and

recycling of metals, recycling of electronic wastes and solar grade silicon, and process modeling for metallurgical processes. He has published over 300 papers and given over 180 presentations at meetings and conferences. He is Key Reader of *Metallurgical and Materials Transactions A* and *Metallurgical and Materials Transactions B*, Advisory Board member of *ISIJ International*, Member of Editorial Board of *Steel Research International*, *Ironmaking and Steelmaking*, *Metallurgical Research and Technology* (*Revue de Métallurgie*), *Advances in Manufacturing*, and Member of Board of Review of Iron and Steel Technology (*AIST Transactions*). Dr. Zhang is a member of TMS, AIST, and ISIJ. He has received several best paper awards from TMS and AIST, and has been a reviewer for more than 80 journals.

Brian G. Thomas is a Professor of Mechanical Engineering at the Colorado School of Mines, and Director of the Continuous Casting Center. His research efforts focus on computational modeling of continuous casting of steel and related processes. He received his Bachelors of Metallurgical Engineering from McGill University, (Montreal, Canada) in 1979 and Ph.D. in Metallurgical Engineering in 1985 from the University of British Columbia, Canada. He has worked in the Research Departments of Algoma Steel, Sault Ste. Marie, Canada and BHP in Melbourne, Australia. Dr. Thomas has coauthored more than 400 papers, and been recognized with several awards: Presidential Young Investigator Award from NSF, Outstanding Young Manufacturing Engineer Award from SME, Xerox Award from UIUC, Distinguished Scientist and Application to Practice Awards from TMS, Baosteel Honorary Professor, HPC Innovation Award, Fellow of ASM International, Distinguished Member and Fellow of AIST, and 14 best paper awards (from AFS, AIME, ISS, AIST, TMS, CIM, and ASM International). He has given over 200 presentations worldwide and co-instructed many short courses to industry, including the annual Brimacombe Continuous Casting Course.

Part I
Casting and Solidification: I

Numerical Simulation on Solidification Structure of $30Cr_2Ni_4MoV$ Steel Under Different Temperature Gradient Using Procast Software

Zheng Chen and Jieyu Zhang

Abstract The $30Cr_2Ni_4MoV$ steel is used to fabricate rotors for the nuclear industry. It required a high grade of the grain size. For the regular grain growth during solidification process under different thermal conditions, a study was performed to simulate the grain structure in different zones in heavy ingot. Based on the café module in procast software, a numerical simulation was conducted. The simulation results show that if the parameters a2 and a3 are set to 8.9×10^{-6} and 4.5×10^{-6}, respectively, then the simulation results are fit to the experimental results. The numerical simulations provides data on the grain morphology and the ratio of the columnar and equaixed areas. The numerical results are useful as the grain structure in heavy ingots can be revealed.

Keywords $30Cr_2Ni_4MoV$ steel · Heavy ingot · Procast software
Grain structure

The quality of a heavy steel ingot is determined by the raw materials used to forge the ingot and the solidification process [1]. Due to its good balance of strength, toughness, and wear resistance, $30Cr_2Ni_4MoV$ ultra-super-critical rotor steel (American grade: 3.5 Ni-Cr-Mo-V) is widely used to produce turbine rotors and disks for ultra-super-critical (USC) generation units [2]. Among factors affecting the properties of heavy steel ingots, the coarse grain structure and shrinkage porosity are the most significant because these two factors are strongly connected to the formation of macro-segregation and inclusions. The final properties of the ingot are

Foundation Item: Item Sponsored by Foundation for University Key Teacher abroad visiting program of Anhui Province Education Ministry (gxfxZD2016248) and Natural Science Foundation of Anhui Province Colleges (KJ2016A702)

Z. Chen (✉) · J. Zhang
Shanghai University, Shanghai, China
e-mail: chren1981@shu.edu.cn

Z. Chen
Tongling University, Tongling, China

L. Nastac et al. (eds.), *CFD Modeling and Simulation in Materials Processing 2018*, The Minerals, Metals & Materials Series,
https://doi.org/10.1007/978-3-319-72059-3_1

related to the grain size of the material. Many of defects are difficult to eliminate during forging or heat treatment. Hence, the grains should be refined and homogenized during solidification with the use of casting modeling software. However, it is difficult to establish a nucleation and growth model to predict grain structure.

Many experiments have been performed to study he behavior of $30Cr_2Ni_4MoV$ rotor steels [3–6], and several studies have attempted to understand the mechanism of CET (columnar to equiaxed transition) during the solidification process. However, the grain growth process is complex due to the large solidification times required for large ingots. Furthermore, the large latent heat causes the cooling rate to be very slow, which has a significant effect on grain growth.

Several methods have been proposed to study the solidification process in heavy ingots. Combeau et al. [7] accounted for the motion of dendritic and globular grains and performed computations using a fixed solid phase. Subsequently, they analyzed the solidification and macro-segregation formation due to grain motion and flow in the inter-dendritic liquid. Wu et al. [8–10] studied the influence of nucleation and melt convection on grain microstructure using a modified volume-averaged equiaxed solidification model. Li et al. [11] analyzed the fully dissected and etched longitudinal sections of heavy ingots with different sizes and proposed that the flotation of oxide-based inclusions drives segregation. Shen et al. [12] predicted the carbon distributions and variations in both the tundish and the mold of a 292 t steel ingot. Gäumann et al. [13] developed the nucleation model ahead of the advancing interface in directional solidification.

Although the abovementioned methods have significantly enhanced our understanding of grain growth during the solidification processes of heavy ingots, one problem remains. While the classical macro-segregation theories have been developed based on the observation grain microstructure in bisected heavy ingots [14], individual heavy ingots differ, even when produced under the same manufacturing conditions. Therefore, variations in quality are inevitable, affecting the cost and time for production. Gu et al. [15] numerically simulated the melt convection and macrosegregation in casting of a large steel ingot. During the alloy solidification of heavy ingot, Pardeshi et al. [16] presented the modeling of convection and macrosegregation through appropriate consideration of multiphase and multiscale phenomena.

Numerical models have been proposed to model the nucleation and growth of dendritic grains from the liquid phase. Wu et al. [17] presented a volume-averaging multiphase solidification model that account for mixed columnar-equiaxed solidification and their influence on macrostructure and macrosegregation. The algorithms used in these models were validated for simple thermal situations by comparing the predicted grain shapes with those obtained from analytical models. Rappaz [18] summarized the basic concepts of macroscopic and microscopic phenomena which occur during any solidification process, such as mould filling, fluid flow, macrosegregation and thermal stresses. However, for heavy ingots, the large model size restricts the modeling of grain growth. Moreover, the meshes used to simulate the thermal and flow fields in the numerical models were too large to simulate the growth of small grains. Until now, small computer capacity has prevented the simultaneous simulation of thermal and flow fields and grain growth for large ingots.

A numerical model for the flow and thermal field during solidification process can be used to predict the temperature distribution and cooling curves [19]. Zhai et al. studied the predicted porosity during heavy ingot solidification and solidification structure under different cooling rate conditions, measured the second dendritic arm spacing (SDAS) to fit the relationship between SDAS and cooling rate.

In this study, the cast structures for different cooling rates were simulated using different temperature conditions and using CAFÉ module in software Procast. The simulation model of the casting process considered the effect of temperature field, the undercooling and anisotropy with solute diffusion controlled model. Several simulation parameters were varied to attain an acceptable comparison with experimental results.

Experimental

The chemical composition of the ingot is listed in Table 1.

The thermal gradient during ingot solidification was considered. First, the thermal and flow fields during the heavy ingot solidification process were numerically simulated using the Procast software package to predict the cooling curve along the centerline of the heavy ingot. The size of the 22 ton heavy ingot was that considered in [20]. The following assumptions were made in the model: (1) the free surface rises steadily as the top pouring liquid is evenly distributed to simulate the smooth filling process; (2) the solute effect is ignored; and (3) the convection is driven only by thermal buoyancy. The filling time was considered to be negligible, and the initial temperatures of the ingot and mold were set at 1550 and 800 °C, respectively. The thermal simulation zone was limited to an ingot height of 1100 mm. The cooling considerations were obtained at several locations-from the center to the surface of the ingot. The temperature curves corresponding to every 150 mm from the center to the outer surface of the heavy ingot were plotted in Fig. 1a. It's shown that the temperature difference between line-0 and line-150 is smaller than that between line-300 and line-450 in the Fig. 1a. The thermal gradients corresponding to these cooling curves of every 150 mm distance are shown in Fig. 1b.

To obtain experimental data on thermal gradients, a 20 kg steel ingot was melted under vacuum. The dimension of these ingots were 100 × 150 × 180 mm. These ingots represented the cases for cooling rate of 8–10 °C/min. From ingot "a" to the ingot "d" in the Fig. 2, ingots represent the slow cooling condition in the 22-ton

Table 1 The element content of low pressure rotor $30Cr_2Ni_4MoV$ steel

Element	C	Si	Mn	S	P	Cr	Ni	Mo	V
Content (weight %)	0.28	0.38	0.25	0.017	0.019	1.63	3.34	0.49	0.094

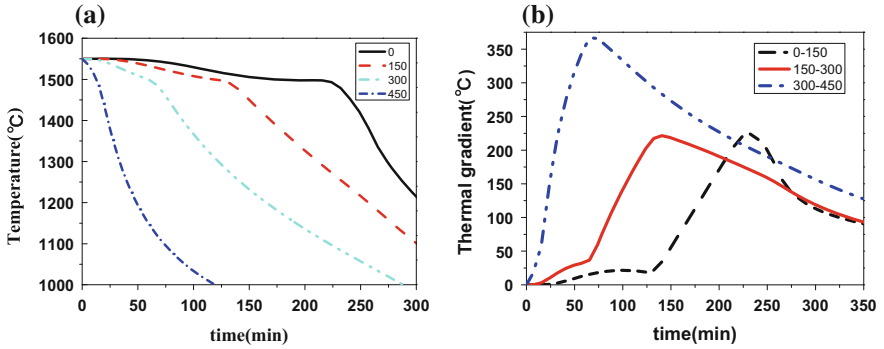

Fig. 1 Temperature and thermal gradients as a function of time. **a** Temperature at 4 locations the numbers in the legend indicate distances from the center to the ingot surface and **b** thermal gradients for 150 mm domain distances from the center

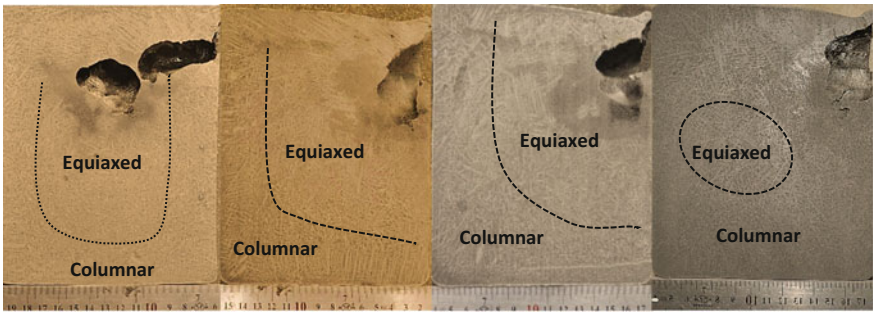

(a) $1^{\#}$ (b) $2^{\#}$ (c) $3^{\#}$ (d) $4^{\#}$

Fig. 2 The experimental results for different cooling conditions showing the equaixed zone

heavy ingot. After solidification, the ingot was cut along the axle plane and machined by milling. The milled surface was then prepared for metallurgical analysis using several grinding and polishing steps. The surface was etched by dilute nitric acid to reveal the microstructure of the ingot. Figure 2 shows the experimental results, whose sectioned surface and the magnified centerline shrinkage porosity as well as the macro-examination of the etched ingot.

Numerical Simulation Results

For the simulation of the controlled experiments, several parameters were used in the Procast software 2011. The number of cells and nodes in the mold mesh was 149,752 and 31,458, respectively. The heat transfer coefficient between the ingot

Table 2 The growth parameters used in microstructure simulations

Parameter	$n_{s,\max}$	$\Delta T_{s,\max}$	$\Delta T_{s,\sigma}$	$n_{v,\max}$	$\Delta T_{v,\max}$	$\Delta T_{v,\sigma}$
Value	5×10^7	0.5	0.1	7×10^8	2.5	1

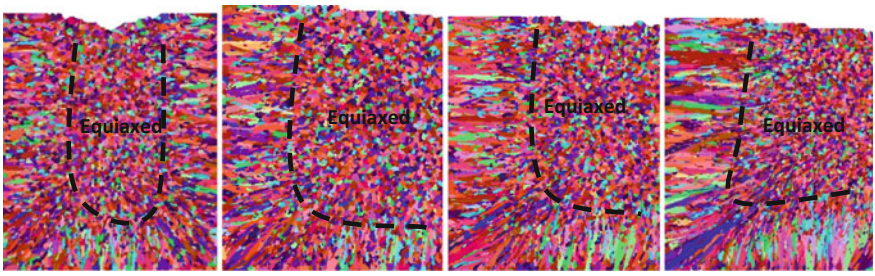

(a) $1^{\#}$ (b) $2^{\#}$ (c) $3^{\#}$ (d) $4^{\#}$

Fig. 3 The microstructure simulation results in different thermal conditions

and mold was 200 W/(m^2·K). At the bottom surface, the heat transfer coefficient between the ingot and mold bottom was 500 W/(m^2·K). The initial temperature of the liquid steel was considered to be 1550 °C.

The Gibbs-Thompson coefficient Γ was taken to be 3×10^{-7} m·K and the other parameters used in the numerical simulation process are shown in the Table 2.

When the temperature field simulation completed, the café module in the Procast software was used to calculate the grain growth. For the microstructure simulation, KGT model was used the two parameters a2 = 8.9×10^{-6} and a3 = 4.5×10^{-6}. In the Fig. 3, different colors represent different crystallographic orientations, and the dotted line is differentiates the equiaxial crystal region. It is shown that the prediction of equaixed grain zone is in good agreement with the experimental result shown in Fig. 2.

Conclusions

This study aimed to simulate the solidification structure under different thermal gradient conditions and compared the model simulation results with the experimental results. By simulating the grain structure under different thermal gradient conditions, it is found that the appropriate set of a2 and a3 parameters in the solidification model are a2 = 8.9×10^{-6} and a3 = 4.5×10^{-6}.

References

1. Wang JQ, Fu PX, Liu HW, Li DZ, Li YY (2012) Shrinkage porosity criteria and optimized design of a 100-ton $30Cr_2Ni_4MoV$ forging ingot. Mater Des 35:446–456
2. Chen F, Cui ZS, Chen SJ (2011) Recrystallization of $30Cr_2Ni_4MoV$ ultra-super-critical rotor steel during hot deformation. Part I: dynamic recrystallization. Mater Sci Eng A 15: 5073–5080
3. Wang YP, Han CJ, Wang C, Li SK (2011) A modified Johnson–Cook model for $30Cr_2Ni_4MoV$ rotor steel over a wide range of temperature and strain rate. J Mater Sci 9:2922–2927
4. Chen F, Cui ZS, Chen SJ (2012) Recrystallization of $30Cr_2Ni_4MoV$ ultra-super-critical rotor steel during hot deformation. Part III: metadynamic recrystallization. Mater Sci Eng A 540:46–54
5. Cui ZS, Li CD, Chen F, Sui DS (2013) Modeling and simulation of austenite grain evolution for heavy forging steel $30Cr_2Ni_4Mo$ V undergoing hot deformation. Paper presented at the 11th International Conference on Numerical Methods in Industrial Forming Processes 2013, pp 166–174
6. Wang YB, Chu WY, Qiao LJ (2000) Stress Corrosion Cracking and Blue Brittleness of Rotor Steels in High Temperature Aqueous Solutions. J Mater Sci Technol 6:631–633
7. Combeau H, Založnik M, Hans S, Richy E (2009) Prediction of macrosegregation in steel ingots: influence of the motion and the morphology of equiaxed grains. Metall Mater Trans B 40:289–304
8. Wu M, Ludwig A (2009) Modeling equiaxed solidification with melt convection and grain sedimentation—II. Model verification. Acta Mater 57:5632–5644
9. Zaloznik M, Combeau H (2012) The influence of the morphology evolution of free-floating equiaxed grains on the macrosegregation in a 3.3-ton steel ingot. Paper presented at the 141th TMS Annual Meeting, Orlando, Florida, 11–15 March 2012, 452–460
10. Wu M, Ludwig A (2009) Modeling equiaxed solidification with melt convection and grain sedimentation—I: model description. Acta Mater 57:5621–5631
11. Li DZ, Chen XQ, Fu PX, Ma XP, Liu HW, Chen Y, Cao YF, Luan YK, Li YY (2014) Evidence of Stranski–Krastanov growth at the initial stage of atmospheric water condensation. Nature Communication 5:1–8
12. Li W (2014) Modeling of species transport and macrosegregation in heavy steel ingots. Metall Mater Trans B 45:464–471
13. Gäumann M, Trivedi R, Kurz W (1997) Nucleation ahead of the advancing interface in directional solidification. Mater Sci Eng A 226–228:763–769
14. Lesoult G (2005) Macrosegregation in steel strands and ingots: characterisation, formation and consequences. Mater Sci Eng A 413–414:19–29
15. Gu JP, Beckermann C (1999) Simulation of convection and macrosegregation in a large steel ingot. Metall Mater Trans A 30:1357–1366
16. Pardeshi R, Dutta P, Singh AK (2009) Modeling of convection and macrosegregation through appropriate consideration of multiphase/multiscale phenomena during alloy solidification. Ind Eng Chem Res 48:8789–8804
17. Wu M, Fjeld A, Ludwig A (2010) Modelling mixed columnar-equiaxed solidification with melt convection and grain sedimentation–Part I: model description. Comput Mater Sci 50:32–42
18. Rappaz M (1989) Modelling of microstructure formation in solidification processes. Int Mater Rev 34:93–24
19. Zhao J, Zhang J, Zhai Q (2014) Numerical simulation of flow and heat transfer during ingot solidification process. Shanghai Metal 1:55–58
20. Li W, Shi W (2011) Numerical simulation of macrosegregation during steel ingot solidification using continuum model. J Shanghai JiaoTong Univ (Science) 2:145–148

Influence of Coil Configuration on Flow Characteristics in Electromagnetic Solidification Systems

Gregory M. Poole and Laurentiu Nastac

Abstract This paper examines the role of new coil configurations on the stirring of an aluminum alloy in electromagnetic solidification processes. The model presented describing the fluid flow phenomena is based on a dual-zone description of the solidifying region, with coherency occurring at very low solid fraction, and accounts for damping of turbulence due to phase change within the control volume. Calculations were performed for Al 3104 alloy placed within a six-turn coil of various turn configurations. In comparison to previous work, it was found that the turn configurations do not have as strong of an effect as that of coil translation along the long axis of the casting. The implications with regards to solidification behavior will be discussed.

Keywords Solidification · Electromagnetic stirring · Coil design
Turbulence

Introduction

Electromagnetic (EM) stirring technologies have found extensive use in solidification processing as a means to produce fine-grained structure castings and promote the early occurrence of the columnar-to-equiaxed transition [1, 2]. The flow serves as a means to homogenize the temperature field within the melt [3], which encourages uniform growth kinetics, and to rapidly dissipate the superheat, promoting nucleation [4]. The nucleation potential is further increased due to the flow increasing fragmentation of the secondary dendrite arms [3, 5, 6]. This makes clear

G. M. Poole (✉)
Department of Mechanical Engineering, University of South Alabama, Mobile, AL, USA
e-mail: gpoole@southalabama.edu

L. Nastac
Department of Metallurgical and Materials Engineering, University of Alabama, Tuscaloosa, AL, USA

L. Nastac et al. (eds.), *CFD Modeling and Simulation in Materials Processing 2018*, The Minerals, Metals & Materials Series,
https://doi.org/10.1007/978-3-319-72059-3_2

the necessity of understanding the flow characteristics, and by corollary the EM field as well, in order to control the grain structure of cast alloys. The flow behavior in EM solidification systems is generally controlled by both: (1) The type of magnetic field applied (e.g., stationary [4, 7, 8], traveling [5, 9], or rotating magnetic fields [10]); and (2) The coil configuration and positioning [11–14].

During past decades, extensive work by investigators such as El-Kaddah [9, 15], Evans [16, 17], and Szekely [18], have fostered a reasonably good understanding of the key flow phenomena within EM stirred melts. Their models for single-phase flow involve the solution of the Maxwell equations for the electromagnetic field and the Navier-Stokes equations for the velocity field, with supplementary relations to describe the turbulent characteristics. However, implementation of this approach is complicated by the presence of two-phase flow in solidification systems.

Recently, the authors and El-Kaddah [19–21] have proposed a new dual-zone solidification model for EM-stirred flows. This model includes solution of the EM field using the coil geometry and operating conditions as fundamental inputs, and also accounts for the damping of the flow in the two-phase region due to interactions between the turbulent eddies and growing solid phase. This model was used to investigate influence of coil position [20] and the influence of adjacent conducting media [21], both of which were shown to greatly modify the flow field and temperature gradients within the melt. In this paper, we shall continue this investigation by examining two new coil geometries on the flow patterns and intensities within the melt.

Model Formulation

The mutual inductance technique was used to solve for the EM field characteristics. A detailed description may be found in Ref. [22]. In essence, the melt and surrounding conducting domains are divided into elementary circuits, with each assumed to possess constant current density. The current density in each loop may be described in terms of the contributions of all the other circuits by

$$\oint \mathbf{J}.d\mathbf{l}_i = -j\omega\sigma\left[\sum_{m=1}^{metal} M_{i,m}(\mathbf{J}\cdot\mathbf{S})_m + \sum_{c=1}^{shields} M_{i,c}(\mathbf{J}\cdot\mathbf{S})_c + \sum_{k=1}^{coil} M_{i,k}I_k\right] \quad (1)$$

where

$$M_{i,k} = \frac{\mu_0}{4\pi}\oint\oint \frac{d\mathbf{l}_k \cdot d\mathbf{l}_i}{r'} \quad (2)$$

is the mutual inductance. This leads to a linear system of equations; after a solution is obtained via Choleski factorization, the magnetic field, **B**, Joule heating, S_{em}, and Lorentz force, $\mathbf{F}_{em}$, may be respectively obtained by:

$$\mathbf{B} = -\frac{\nabla \times \mathbf{J}}{j\omega\sigma} \tag{3}$$

$$S_{em} = \frac{1}{2}\mathrm{Re}\left(\frac{\mathbf{J}\cdot\mathbf{J}^*}{\sigma}\right) \tag{4}$$

$$\mathbf{F}_{em} = \frac{1}{2}\mathrm{Re}(\mathbf{J}^* \times \mathbf{B}) \tag{5}$$

Heat Transfer

Assuming a linear variation of solid fraction with respect to temperature in the mushy region, the heat conservation equation including phase change is given by

$$\rho C^*\left(\frac{\partial T}{\partial t} + \mathbf{u}\cdot\nabla T\right) = \nabla\cdot(k^*\nabla T) + S_{em} \tag{6}$$

where

$$C^* = \begin{cases} c_{p,l} & T \geq T_L \\ c_{p,s} + \frac{L}{T_L - T_S} & T_S < T < T_L \\ c_{p,s} & T \leq T_L \end{cases} \tag{7}$$

is the effective specific heat, and

$$k^* = \begin{cases} k_l + \frac{\mu_t c_{p,l}}{\mathrm{P}_T} & T \geq T_L \\ (1 - f_S)k_l + f_S k_s & T_S \leq T < T_L \\ k_s & T \leq T_S \end{cases} \tag{8}$$

is the effective thermal conductivity, which includes turbulent effects, and ρ is the density.

Fluid Flow

The flow in the bulk liquid and mushy region is governed by the incompressible Navier-Stokes and continuity equations, given respectively as:

$$\nabla\cdot\mathbf{u} = 0 \tag{9}$$

$$\rho\frac{\partial \mathbf{u}}{\partial t}+\rho\mathbf{u}\cdot\nabla\mathbf{u}=-\nabla P+\nabla\cdot\left(\mu\left(\nabla\mathbf{u}+\nabla\mathbf{u}^{T}\right)\right)+\lambda(\mathbf{F}_{em}+\mathbf{F}_{d})-\frac{\mu^{*}}{K}(\mathbf{u}-\mathbf{u}_{s}) \tag{10}$$

where λ is a switch parameter to distinguish between the suspended and fixed particle regions, and $\mathbf{F}_d$ is the damping force due to turbulent interactions with the crystallites in the suspended particle region, given by

$$\mathbf{F}_{d}=\frac{2\left(1-f_{L}^{2}\right)\sqrt{c_{d}}\rho k}{D_{g}\left(1-\left(\frac{6(1-f_{L})}{\pi\beta}\right)^{1/3}\right)}\,\hat{\mathbf{e}}_{j} \tag{11}$$

where D_g is the final grain size, k is the turbulent kinetic energy given by the low-Re model of Jones and Launder [23]. The viscosity, μ, is given as the sum of the laminar and turbulent components, with the laminar viscosity in the suspended particle region being determined from the expression by Thomas [24] for the rheological properties of suspensions.

Results and Discussion

Calculations were performed for the unidirectional solidification of 3104 Aluminum alloy in a bottom chill mold. The alloy properties are those given in Ref. [25]. The boundary conditions at the periphery of the casting were insulating ones with the exception of the bottom chill, whose heat transfer coefficient was held constant at 300 W/m^2·K. Stirring was accomplished using a coil current of 200 A rms and frequency of 500 Hz. Both the height and diameter of the casting were 80 mm, and the various coil configurations are shown in Fig. 1a–d. These configurations include: A coil in which all the turns are aligned vertically (straight coil), analogous to those found in previous works (Fig. 1a) [19–21]; Shifting of the bottom two turns to form a second row behind the remaining four turns (Fig. 1b); and for Fig. 1c, d stacking the turns in right and equilateral triangles, respectively. In each case, the innermost coils, each with a diameter of 8 mm, were placed at a distance of 65 mm from the centerline, and the top turns were aligned with the free surface of the casting. The crystallites were assumed to be approximately spherical (β = 0.954), corresponding to a coherency solid fraction of 0.5, and have a characteristic grain size of 200 microns. The pour temperature was 675 °C.

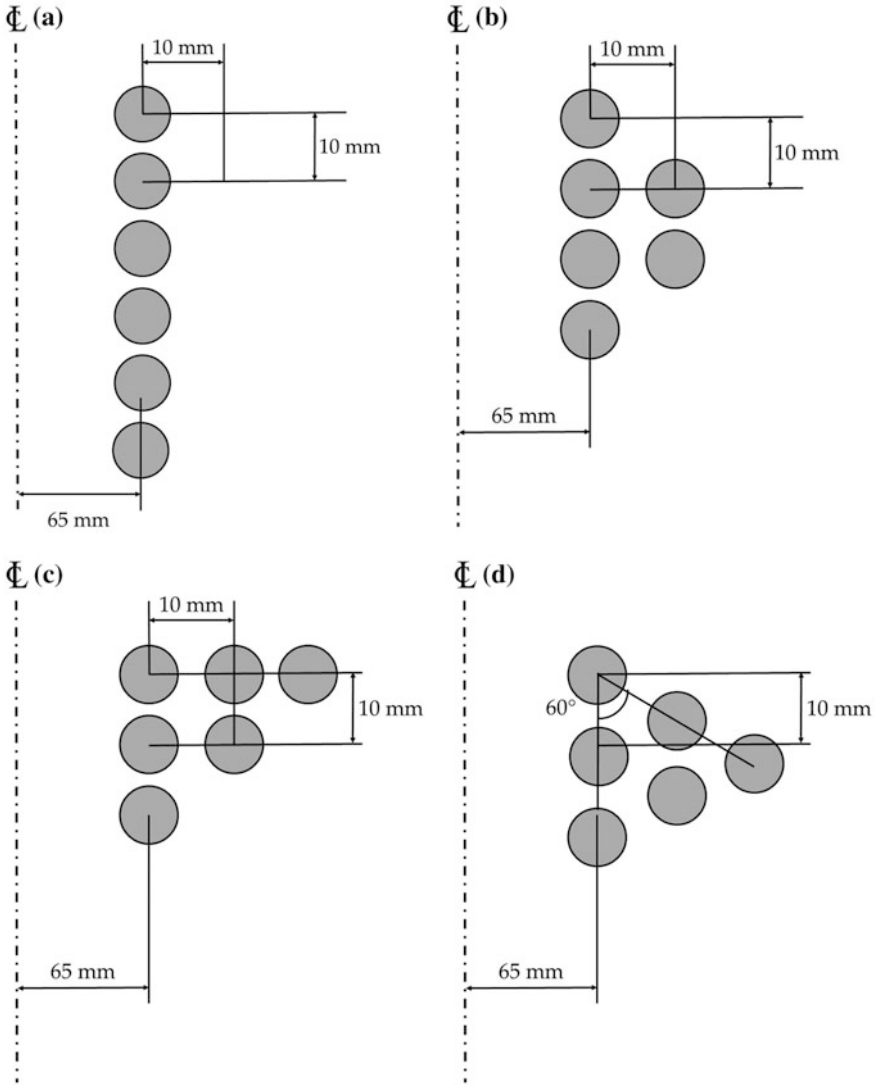

Fig. 1 Coil configurations considered in this study: **a** Straight coil; **b** 4 + 2 coil; **c** 45° stacked coil; **d** 60° stacked coil

Figure 2a–d show the initial computed velocity profiles for each case corresponding to each respective coil configuration shown in Fig. 1. As seen in these figures, the characteristic velocity for all cases was on the order of 150 mm/s. This is expected given the identical operating conditions of the coil. However, it is

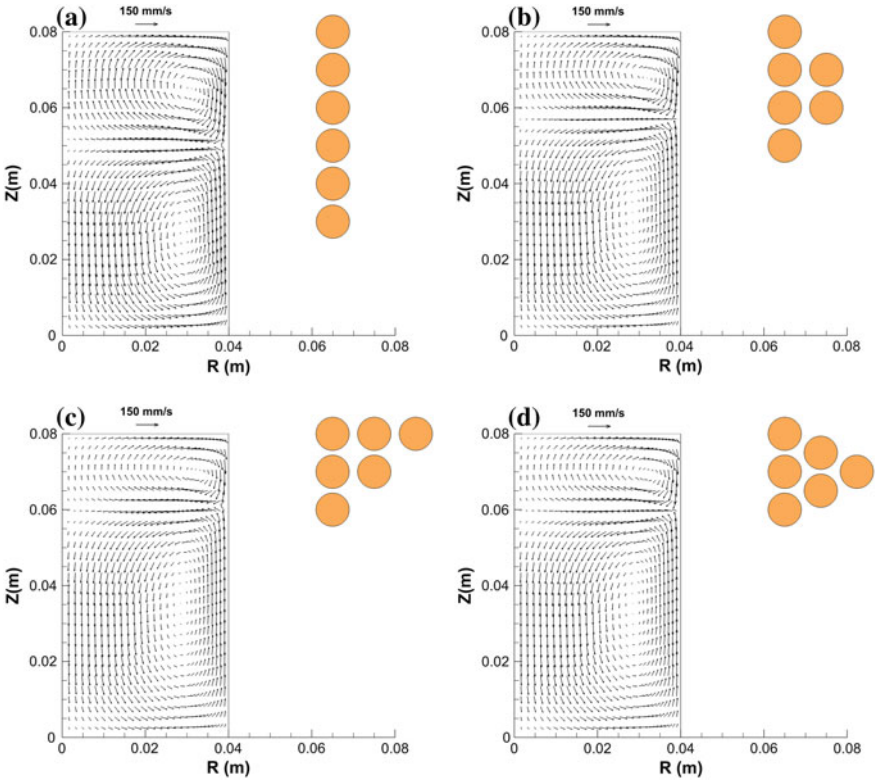

Fig. 2 Initial computed flow profiles corresponding to the coil configurations shown in Fig. 1

observed that the sizes of the upper and lower flow loops are modified as more of the turns are shifted upwards. From an earlier work by the authors [26], it was shown that the flow reverses when the rotational component of the Lorentz force, which drives the flow, changes sign. This is demonstrated in the corresponding plots of curl ($\mathbf{F}_{em}$) in Fig. 3. It is important to note that the shifts of zero contour of the curl observed in the stacked coil configurations are marginal compared to that of the 4 + 2 coil. This is attributed to the magnitude of the forces being inversely proportional to $|\mathbf{r} - \mathbf{r}'|^2$. It can be concluded that manipulation of the flow pattern is not effectively accomplished through the rearrangement of the coil, but by comparison to the literature it is clear that such alteration of the flow is best accomplished through translation of the coil along the z axis [20].

While the flow pattern is largely invariant with respect to the coil configurations shown, it was found that the flow intensity is more greatly affected by the coil

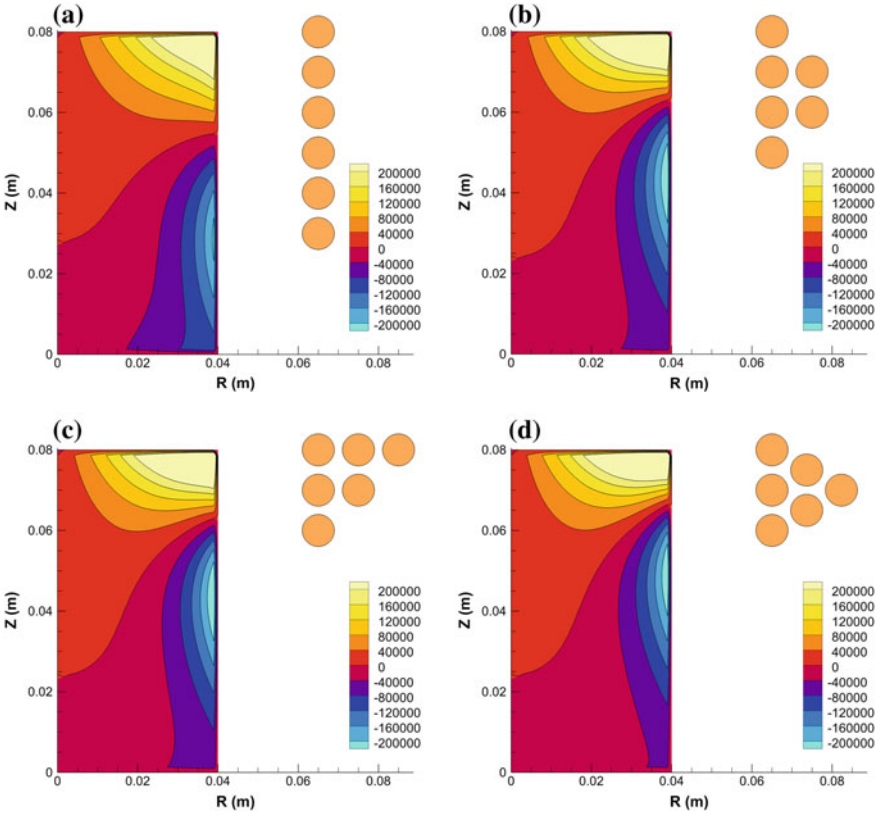

Fig. 3 Rotational component of the Lorentz Force (N/m^4) for each coil configuration

configuration. For the straight coil (Fig. 2a), the maximum velocity near the outer radius approaches 180 mm/s; however, this velocity drops to 160 mm/s for the 4 + 2 configuration and decreases even further to ~70 mm/s for the stacked configurations. As a result, the heat generated via electrical energy dissipation is not advected as effectively throughout the casting, which would slow down the rate of solidification as seen in Fig. 4. Furthermore, it is seen that solidification is more rapid with the 45° stacked configuration (Fig. 4c) than that of the 60° case. This is explained by the 2nd and 3rd coil rows coupling less with the casting, which in turn leads to decreased Joule heating. Further investigation of solidification behavior with the inverted 45° coil configuration (i.e., shifting the 2nd and 3rd rows down instead of up) is warranted, as it would be expected that the solidification time would be larger than either cases C or D.

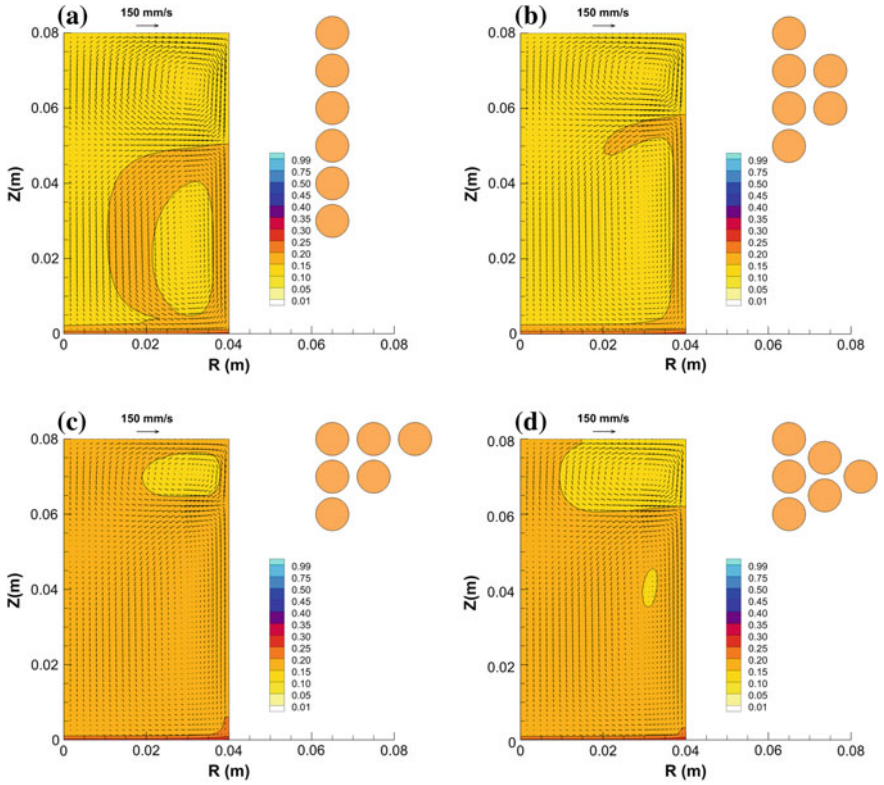

Fig. 4 Solid fraction profiles within the casting after 200 s for each coil configuration

Conclusions

This effect of coil configuration on the solidification behavior was investigated via simulation. The model used a dual-zone formulation for the solid fraction and incorporating the effect of turbulent damping by the crystallites. Computed results showed that the changes in coil configuration did not significantly influence the flow pattern, particularly for the stacked coil configurations. On the other hand, the coil configuration did have an effect on the flow intensity, which in turn affected the solidification rate within the casting. This confirms that coil configuration, along with coil position and operating conditions, must be considered when designing an EM solidification system.

References

1. Chalmers B (1963) The structure of ingots. J Aust Inst Metals 8(3):255–263
2. Dantzig JA, Rappaz M (2009) Solidification (Engineering Sciences: Materials). EPFL Press, Lausanne
3. Willers B et al (2005) The columnar-to-equiaxed transition in Pb–Sn alloys affected by electromagnetically driven convection. Mater Sci Eng A 402(1):55–65
4. Vives C, Perry C (1986) Effects of electromagnetic stirring during the controlled solidification of tin. Int J Heat Mass Transf 29(1):21–33
5. Griffiths WD, McCartney DG (1996) The effect of electromagnetic stirring during solidification on the structure of Al-Si alloys. Mater Sci Eng A 216(1–2):47–60
6. Campanella T et al (2004) Grain refinement induced by electromagnetic stirring: a dendrite fragmentation criterion. Metall Mater Trans A 35(10):3201–3210
7. Campanella T et al (2003) Influence of permeability on the grain refinement induced by forced convection in copper-base alloys. Scripta Mater 49(10):1029–1034
8. El-Kaddah N, Szekely J (1983) The turbulent recirculating flow field in a coreless induction furnace, a comparison of theoretical predictions with measurements. J Fluid Mech 133:37–46
9. El-Kaddah N, Szekely J, Carlsson G (1984) Fluid flow and mass transfer in an inductively stirred four-ton melt of molten steel: a comparison of measurements and predictions. Metall Mater Trans B 15(4):633–640
10. Travnikov V et al (2012) Radial solidification of Al-Si alloys in the presence of a rotating magnetic field. In: IOP conference series: materials science and engineering, vol 33, p 012048
11. McKelliget JW, El-Kaddah N (1988) The effect of coil design on materials synthesis in an inductively coupled plasma torch. J Appl Phys 64(6):2948–2954
12. Bojarevics V, Pericleous K, Cross M (2000) Modeling the dynamics of magnetic semilevitation melting. Metall Mater Trans B 31(1):179–189
13. Bojarevics V, Roy AA, Pericleous K (2010) Magnetic levitation of large liquid volume. Magnetohydrodynamics 46(4):317–329
14. Stelian C et al (2005) Bridgman growth of concentrated GaInSb alloys with improved compositional uniformity under alternating magnetic fields. J Crys Grow 275(1):1571–1578
15. Meyer J, Szekely J, El-Kaddah N (1987) Calculation of the electromagnetic force field for induction stirring in continuous casting. Trans Iron Steel Inst Japan 27(1):25–33
16. Tarapore ED, Evans JW (1976) Fluid velocities in induction melting furnaces: Part I. Theory and laboratory experiments. Metall Mater Trans B 7(3):343–351
17. Tarapore ED, Evans JW, Langfeldt J (1977) Fluid velocities in induction melting furnaces: Part II. Large scale measurements and predictions. Metall Trans B 8(1):179–184
18. Nakanishi K, Fujii T, Szekely J (1975) Possible relationship between energy dissipation and agitation in steel-processing operations. Ironmaking Steelmaking, 2(3), 193–197
19. Poole G, El-Kaddah N (2013) An improved model for the flow in an electromagnetically stirred melt during solidification. Metall Mater Trans B 44(6):1531–1540
20. Poole G, El-Kaddah N (2014) Effect of coil design on the temperature and velocity fields during solidification in electromagnetic stirring processes. ISIJ Intl 54(2):321–327
21. Poole G, Nastac L (2014) Flow and temperature field evolution during solidification of an electromagnetically stirred melt: influence of magnetic shields. Paper presented at MS&T 2014, Pittsburgh, Pennsylvania, 12–16 October 2014
22. El-Kaddah N, Szekely J (1983) The electromagnetic force field, fluid flow field, and temperature profiles in levitated metal droplets. Metall Mater Trans B 14(3):401–410
23. Jones WP, Launder B (1972) The prediction of laminarization with a two-equation model of turbulence. Int J Heat Mass Transfer 15(2):301–314
24. Thomas DG (1965) Transport characteristics of suspension: VIII. A note on the viscosity of Newtonian suspensions of uniform spherical particles. J Colloid Sci 20(3):267–277

25. Prasso DC, Evans JW, Wilson IJ (1994) Mathematical modeling of heat transfer and solidification and comparison with measurements on a pilot caster at Reynolds Metals Company. In: Light Metals 1994. TMS, Warrendale, pp 817–877
26. Poole G, Nastac L (2015) On the influences of adjacent conducting media and coil frequency on the electromagnetic field and flow characteristics in solidifying melts. J Manuf Sci Prod 15(1):13–22

Effect of Hook Formation During Initial Solidification on Distribution of Subsurface Inclusions in Ultralow Carbon Steel Slabs

Pengcheng Xiao, Jingyi Zhou, Liguang Zhu, Caijun Zhang and Yi Liu

Abstract Entrapment of macro-inclusions under the shell surface would lead to the surface quality of final steel products, which is closely related to the formation of oscillation mark hooks during the initial shell solidification. In this study, the distribution of inclusions at different depths beneath the shell surface was analyzed by auto-SEM. Water simulations and particle image velocimetry (PIV) measurements were conducted to reveal the mechanism of inclusions captured by hooks. The results shown that the inclusions were maximizing at 1 mm depth from the slab surface. Three kinds of inclusion movements in hook region were found: being captured by the meniscus; being captured below the meniscus; and some of captured inclusions returned to liquid steel. Most of the inclusions were captured near the meniscus which might lead to the highest inclusion amount near the surface of slab. Additionally, the number of inclusions captured by hooks would be reduced with increasing the casting speed.

Keywords IF steel · Surface layer inclusions · Hooks

Introduction

The ultralow carbon (ULC) steel are widely used for skin panels in automotive sheet applications, and their deep drawing properties and surface quality requirements are very strict [1, 2]. Non-metallic inclusions are known to be primarily responsible for the sliver defects in cold rolled steel sheets. In order to guarantee the quality of ULC steel sheets, many enterprises carry out the flame cleaning and

P. Xiao · J. Zhou · L. Zhu (✉) · C. Zhang · Y. Liu
High Quality Steel Continuous Casting Engineering Technology Research Center, College of Metallurgy and Energy, North China University of Science and Technology, Tangshan 063009, Hebei, China
e-mail: zhulg@ncst.edu.cn

L. Nastac et al. (eds.), *CFD Modeling and Simulation in Materials Processing 2018*, The Minerals, Metals & Materials Series,
https://doi.org/10.1007/978-3-319-72059-3_3

grinding treatment for continuous casting (CC) slab, which leads to higher cost and lower efficiency of IF products. Entrapment of macro-inclusions under the shell surface, which is closely related to the formation of oscillation mark hooks during initial shell solidification, would have a negative influence on the surface quality of final steel products. Subsurface hook formation during initial solidification in the CC mold was studied intensively by Thomas et al. [3, 4] and hold the view that hooks degrades the quality of steel slabs owing to the associated entrapment of argon bubbles and non-metallic inclusions. In addition, Kumar et al. [5] determined the overall distribution of entrapped macro inclusions across the slab thickness and found that the inclusions was maximum at the surface and went on decreasing up to 12 mm slab depth. Wang et al. [6] tested subsurface inclusions in deep-drawing steel slabs and also found that subsurface macro-inclusions are closely related to the hook structure. However, there is not enough research on the process of inclusion captured by hooks. Therefore, it is necessary to study the effect mechanism of hooks on distribution of subsurface inclusions in ultralow carbon steel slabs.

In this study, the distribution of inclusions at different depths beneath the CC slab surface was analyzed by auto-SEM. To reveal the mechanism of inclusions captured by hooks, water simulations model were designed. Particle image velocimetry (PIV) measurements were conducted as well.

Methodology

Inclusion Statistics

Three slab sections at different casting length were cut by flame. The sizes of slab sections are 300 × 1180 × 200 mm (length × width × thickness). The slab sections were cast in the basically same parameters, whose temperature in the tundish is 1555 °C and casting speed is 1.4 m/min. Sixteen samples were cut at different depths beneath the wide face and narrow face of the slab separately at 1 mm step thickness with accuracy of step ±0.1 mm. Every sample was examined with an automatic scanning electron microscope (auto-SEM) to detect inclusions larger than 15 μm. The scanning area of every sample is 25 × 25 mm. The location of sampling and detection is shown in Fig. 1. The chemical compositions of the slabs are shown in Table 1.

Water Simulations and PIV Measurements

A 2:1 water model of tundish and mold was made of plexiglass, whose mold sizes are 100 × 690 × 10,000 mm (thickness × width × hight), as is shown in Fig. 2. The analog hooks is installed in the range 0–100 mm below the meniscus. Floating

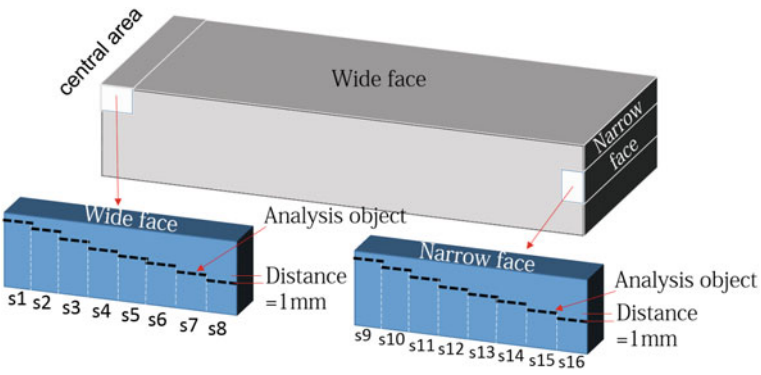

Fig. 1 Schematic diagram for sampling in the slab

Table 1 Chemical composition of the ULC steel slabs

C	Mn	S	P	Si	Als	Ti
$\leq$ 0.003	0.15–0.18	<0.10	<0.10	<0.10	0.025–0.035	0.050–0.070

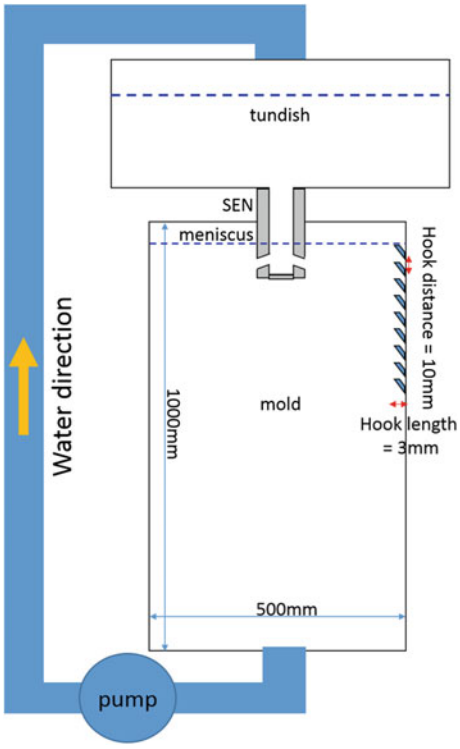

Fig. 2 Schematics of 2:1 beam blank model of a mold

beads (SiO_2-Al_2O_3, 50–100 μm) were added into the water of the tundish and stirred continuously to simulate the inclusions moving in the molten steel. The high-speed camera is placed directly ahead of the model to record the trajectory of the beads. The principle of the PIV measurements system can be found in Ref. [7]. In this study, the laser is placed on the right side of the model to analyze the variation characteristics of the flow field in the mold.

Results and Discussion

Inclusion Content in Different Surface Layers

By means of auto-SEM, the inclusions can be mainly divided into two categories, one is the Al_2O_3 class inclusion (including Al_2O_3 and Al_2O_3-TiO_x) (Fig. 3a shows), the other is slag class which containing K, Na, etc. (Fig. 3b shows).

The distribution of inclusions at depths of 1–8 mm beneath the wide face is shown in Fig. 4. It can be seen that the contents of both the Al_2O_3 class and slag

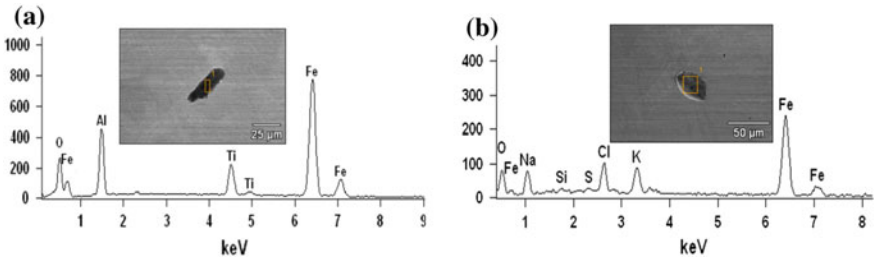

Fig. 3 Morphology and energy spectrum of typical inclusions. **a** Al_2O_3-TiO_x type inclusion, **b** mold flux type inclusions

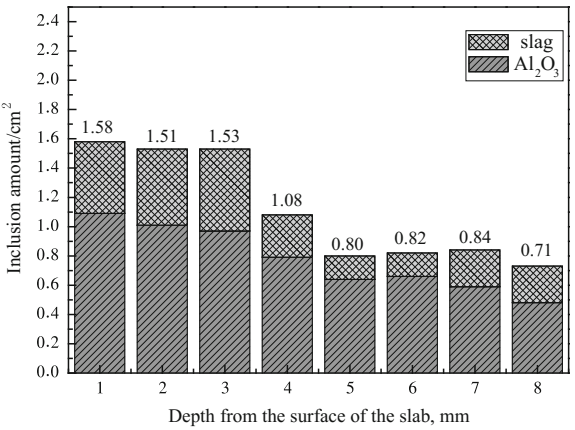

Fig. 4 Distribution characteristics of inclusions in wide surface

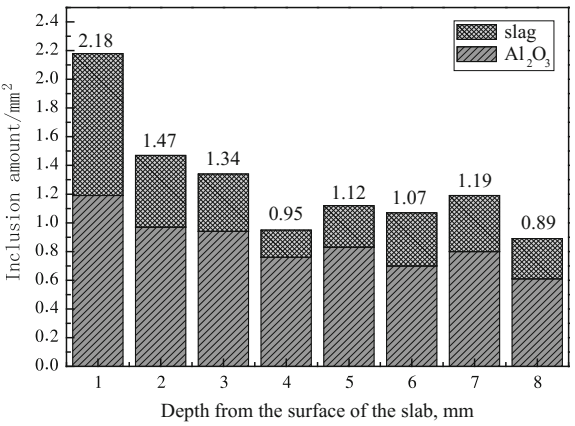

Fig. 5 Distribution characteristics of inclusions in narrow surface

class inclusions at the 1–3 mm are higher than that of 4–8 mm depth. It means that more inclusions are trapped in the solidified 1–3 mm of the shell. This is consistent with the study results of Kumar [5] and Bao et al. [8]. The distribution of inclusions at depths of 1–8 mm beneath the narrow face is shown in Fig. 5. The figure shows that the content of inclusions 1 mm below the slab surface is higher than that of other depths. This is related to the flow field of molten steel in the mold. The content of inclusion in subcutaneous 2–3 mm is higher than 4–8 mm, which is close to the distribution of inclusions at the center of wide surface. Figures 4 and 5 show that Al_2O_3 inclusions in the surface layer of IF steel slab are obviously higher than that of slag inclusions. When the depth is more than 4 mm, the proportion of slag inclusion decreases.

Inclusion Movements in Hook Region

A group of 60 s consecutive photographs with a speed of 1000 pictures per second were taken while the casting speed was 1.4 m/min. Three kinds of inclusion movements in hook region were found: captured by the meniscus, captured below the meniscus, and some of captured inclusions return to liquid steel. The typical process of inclusions captured by the meniscus is shown in Fig. 6, whose content is more than other two kinds. This phenomenon can explain the result that the content of inclusions 1 mm below the slab surface is higher than that of other depths. Obviously, the initial shell near the meniscus is very thin and finally locate in the outermost layer of the slab. Some of inclusions are trapped in the molten steel several centimeters below the meniscus, as is shown in Fig. 7. It can be concluded that these inclusions will eventually appear in a few millimeters of depth below the slab surface. During the simulated casting, several inclusions were found return to the liquid steel after being captured by hooks, as shown in Fig. 8. The possible reason is that the turbulent flow of liquid steel has an influence on the residence state of inclusions in hook.

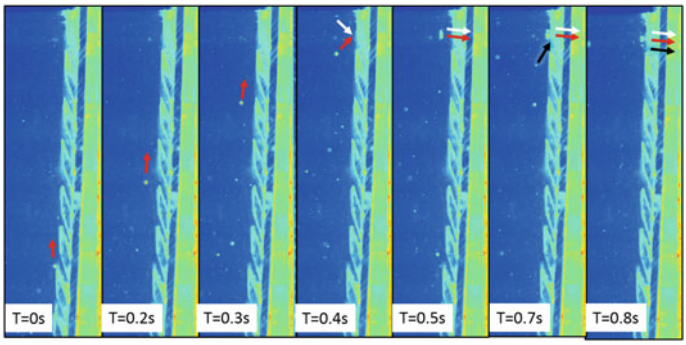

Fig. 6 The inclusions captured by hooks in the meniscus

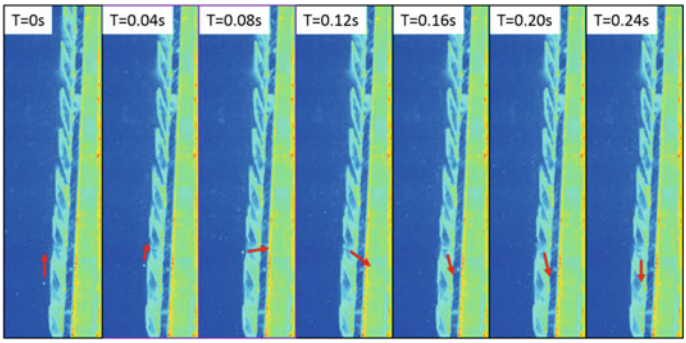

Fig. 7 The inclusions captured by hooks below the meniscus

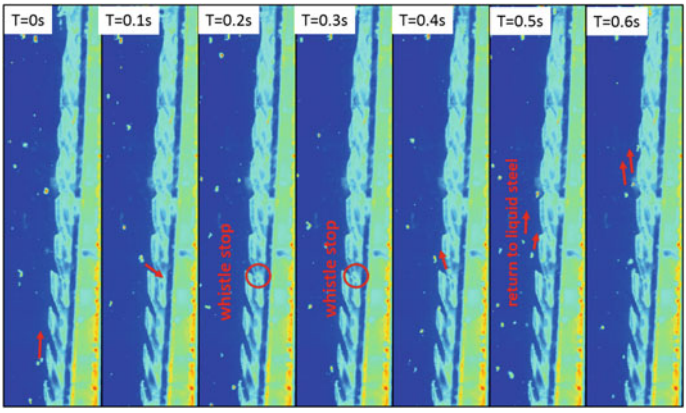

Fig. 8 Some of captured inclusions return to liquid steel

Characteristics of Molten Steel Flow in Hook Region

In order to reveal the movement mechanism of inclusions in the hook region and the reasons for the inclusion distribution in the surface of continuous casting slab, PIV measurements were taken at the casting speed of 1.0, 1.2, 1.4, 1.6 m/min.

By PIV measurements, it was found that there are periodic faint flows move toward the direction of slab shell in the region near the meniscus, as is shown in Fig. 9. These flows can be considered to be the source of the motion of the inclusions near the meniscus move toward the hook (as shown in Fig. 6). There are powerful liquid steel flows towards the shell 150–250 mm below the meniscus. These flows maybe have less influence on inclusion captured by the hooks. The reason is that the temperature of the liquid steel is high and it's kinetic energy is very powerful, so the hooks may be eroded and the captured inclusions may be return to the liquid steel. So there are fewer inclusions in the inner layers of the slab. The above analysis further explains the reason why more inclusions appear on the near surface of the slab. Furthermore, it can be concluded that improving electromagnetic braking, especially reducing the flow velocity of molten steel near the meniscus, is helpful to alleviate the agglomeration of inclusions on the surface of the shell.

The flow velocity distribution in the mold under different casting speeds is shown in Fig. 10. As seen from the picture, the flow field in the mold is not symmetrical in real time. As the casting speed increases, the flow of liquid steel in the mold is accelerated, resulting in increased erosion of the hooks, and inclusions are not easily caught in the hook region. In addition, the increasing casting speed will take more high temperature steel and melt the newly generated hooks, which would reduce the probability of inclusion being captured.

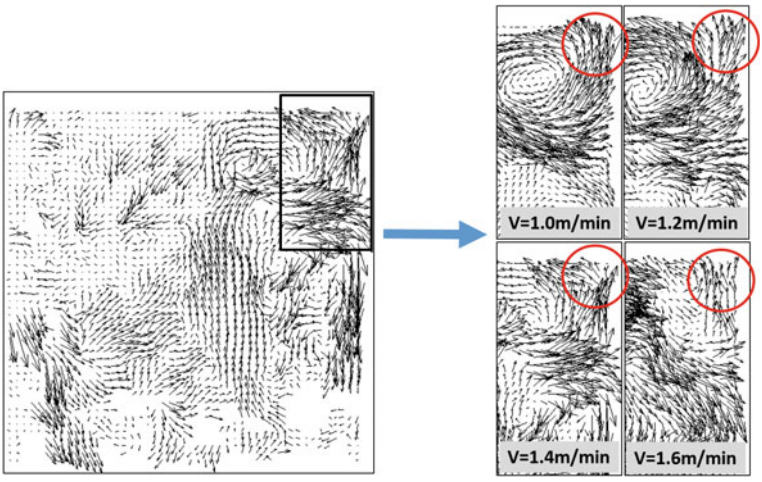

Fig. 9 The typical flow direction near the meniscus

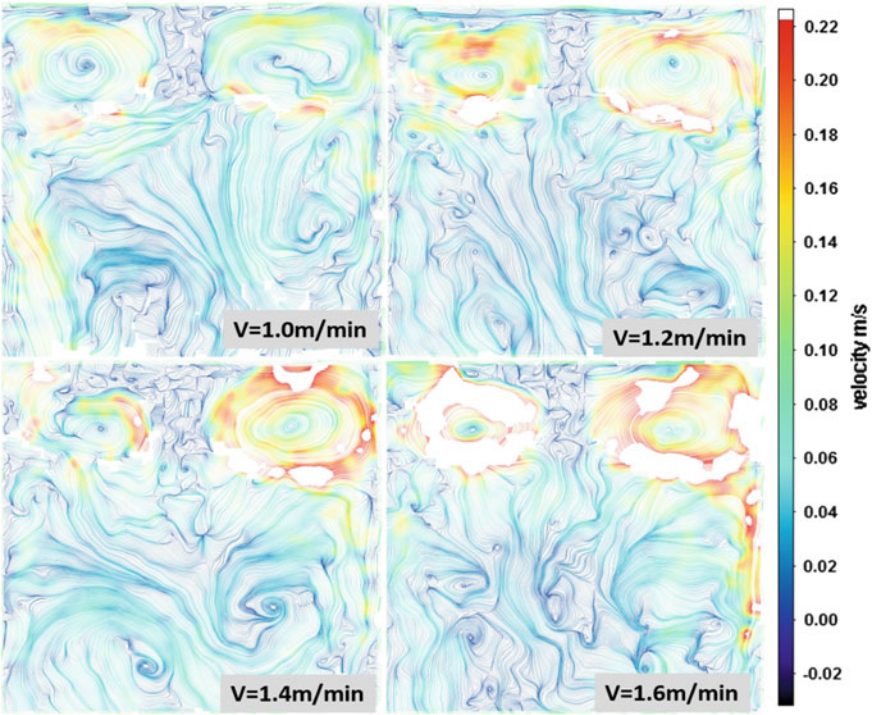

Fig. 10 The flow velocity distribution in the mold under different casting speeds

Conclusions

The distribution of inclusions at different depths beneath the shell surface was analyzed by auto-SEM. Water simulations and particle image velocimetry (PIV) measurements were conducted to reveal the mechanism of inclusions captured by hooks. The results show that:

1. The inclusions are maximizing at 1 mm depths from the slab surface.
2. Three kinds of inclusion movements near hooks were found, 1. Captured by the meniscus, 2. Captured below the meniscus and 3. Some of captured inclusions return to liquid steel.
3. Most of the inclusions were captured near the meniscus which may lead to the highest inclusions amount near the surface of slab. Additionally, the number of inclusions captured by hooks will reduce with increasing the casting speed.

References

1. Basu S, Choudhary SK, Girase NU (2004) Nozzle clogging behaviour of Ti-bearing Al-killed ultra low carbon steel. ISIJ Int 44(10):1653–1660
2. Wang M, Bao Y, Zhao L et al (2015) Distribution and detriment of bubbles in continuous casting interstitial free steel slab. ISIJ Int 55(4):799–804
3. Lee GG et al (2009) Prediction and control of subsurface hooks in continuous cast ultra-low-carbon steel slabs. Ironmaking Steelmaking 36.1:39–49
4. Braun TB, Elliott JF, Flemings MC (1979) The clustering of alumina inclusions. Metall Mater Trans B 10(2):171–184
5. Kumar A, Choudhary SK, Ajmani SK (2012) Distribution of macroinclusions across slab thickness. ISIJ Int 52.12:2305–2307
6. Yu H et al (2015) Characteristics of subsurface inclusions in deep-drawing steel slabs at high casting speed. Metall Res Techno 112.6:608
7. Peixoto JJM, Gabriel WV, Ribeiro LQ, da Silva CA, da Silva IA, Seshadri V (2016) Computational and physical simulation of fluid flow inside a beam blank continuous casting mold. J Mater Process Techno 233:89–99
8. Wang M, Bao YP, Cui H et al (2011) Surface cleanliness evaluation in Ti stabilized ultralow carbon (Ti-IF) steel. Ironmaking Steelmaking 38(5):386–390

Part II
Casting and Solidification: II

Numerical Investigation on the Effect of Steel Strip Feeding on Solidification in Continuous Casting

Ran Niu, Baokuan Li, Zhongqiu Liu and Xianglong Li

Abstract Steel strip feeding into continuous casting mold is an innovative technology improving the thick slab quality through decreasing the melt superheat and increasing the proportion of equiaxed dendrites. To investigate the embedded complex melting and solidification processes, a mathematical model has been developed to model all the essential physical behaviors of the fluid flow, heat transfer, melting and solidification during steel strip feeding into the mold. The enthalpy method is adopted to describe both the melting of steel strip and the solidification of slab. Based on the numerical findings, three periods are divided during the whole melting process of the moving strip. The effect of strip feeding on the fluid flow, temperature distribution and shell solidification in continuous casting mold are investigated. The turbulent flow in the mold is enhanced due to the fast moving of strip and the fluid nearby is cooled down which redistributes the melt superheat inside slab.

Keywords Melting · Strip feeding · Continuous casting · Heat transfer

Introduction

Recently developments of continuous casting (CC) technology have resulted in a great increase of production capacity of cast bloom. Eliminating or significantly reducing the defects is of great importance to achieve satisfactory products [1]. A creative method that adding vibrating consumable strip to mold has been put forward by the Azovstal' Metallurgical Combine in Ukraine, to alleviate segregation and central porosity detects of CC slab [2, 3]. The concept of the process can be illustrated in a schematic diagram as shown in Fig. 1.

As depicted, a thin consumable steel strip is fed into the liquid metal in the mold by a strip feeding apparatus. The strip feeding apparatus is mainly consists of a few

R. Niu · B. Li (✉) · Z. Liu · X. Li
School of Metallurgy, Northeastern University, Shenyang 110819, Liaoning, China
e-mail: libk@smm.neu.edu.cn

L. Nastac et al. (eds.), *CFD Modeling and Simulation in Materials Processing 2018*, The Minerals, Metals & Materials Series,
https://doi.org/10.1007/978-3-319-72059-3_4

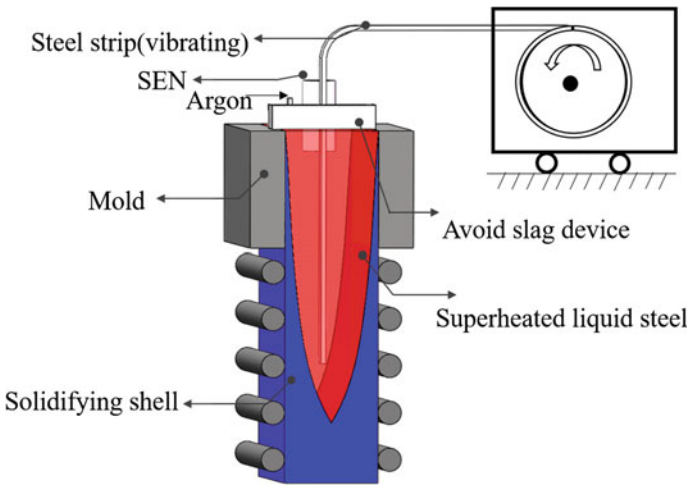

Fig. 1 Schematic diagram of the strip feeding process

main units for strip storage, strip sending and strip straightening. Chemical composition of the strip must be chosen to match with the composition of the slab. The strip is fed at the speed much faster than the casting speed to vicinity of the SEN for removing the superheat directly from the central part of the slab. At the same time, for preventing the entrapment of mold flux, an argon protection is equipped around the strip at the top surface. Benefit from the melting of strip, the superheat at the central of a slab could be decreased. The nucleation formation could be therefore promoted; widening the equiaxed zone and narrowing the columnar dendritic zone. Furthermore, the strip also accelerates the slab solidification rate; increasing the casting speed and the corresponding continuous caster capacity. The above advantages may make the strip feeding technology becoming an economical alternative to improve the quality of slab in compared to other expensive and complex technologies [3].

The present work undertakes to investigate the characteristics of steel strip melting in a liquid steel flowing continuous casting mold. A coupled model including fluid flow, heat transfer and phase change is developed to describe the strip melting and the strand shell solidifying, simultaneously. The strip melting evolution, melting rate and its effect on the distribution of turbulence and temperature in mold are studied

Mathematical Model

In order to investigate the phase change of the moving strip inside the continuous casting mold, a three-dimensional numerical model which incorporates all the essential physical phenomena such as fluid flow, heat transfer, solidification and

melting has been proposed and developed. To simplify the calculation, in the present study, the strip feeding technology is applied to a round bloom. The cast bloom is considered as perfectly vertical and the solid steel strip is assumed to be fed vertically throughout the whole melting process. As a straight nozzle is adopted, the jet flow has little influence on the movement of the strip, so only the movement along the feeding direction is taken into considered. The strip with the same properties as the melt, the convective effect of solutes is neglected.

General Equations of the Model

The continuity and momentum equations under turbulent conditions are:

$$\frac{\partial(\rho u_i)}{\partial x_i} = 0 \tag{1}$$

$$\rho \frac{\partial u_i u_j}{\partial x_j} = \frac{\partial}{\partial x_j}\left[\mu_{eff}\left(\frac{\partial u_i}{\partial x_j} + \frac{\partial u_j}{\partial x_i}\right)\right] - \frac{\partial P}{\partial x_i} + \rho g_i + F_B + S_p \tag{2}$$

where μ_{eff}, the effective viscosity coefficient, is the sum of the laminar (μ_l) and turbulent (μ_t) viscosity.

To calculate turbulence viscosity and phase change phenomena simultaneously in the continuous casting process, the low-Reynolds number k-ε eddy viscosity model is applied. The turbulent viscosity formulation as a function of turbulent kinetic energy, k, and dissipation rate of turbulent kinetic energy,ε, is defined as:

$$\mu_t = \rho \cdot C_\mu \cdot \frac{k^2}{\varepsilon} \tag{3}$$

where C_μ is a function of the mean strain and rotation of the fluid, and it prevents unrealizable values for the large mean strain rate. The model coefficients used in this study is based on the empirical constants, C_μ = 0.09 [4].

A sink term S_p is presented in the momentum equation to account for the resistance force induced by columnar dendrites and is described with the Darcy's Law:

$$S_p = \frac{\left(1-\beta^2\right)}{\left(\beta^3+\varepsilon\right)} A_{mush}\left(u_i - u_{s,i}\right) \tag{4}$$

where ($u_i - u_{s,i}$) is the relative motion between fluid phase and solid phase, $u_{s,i}$ is the average solid phase velocity in direction *i;* In slab shell pulling zone, $u_{s,i} = v_c$; In strip feeding zone, $u_{s,i} = v_a$. v_c and v_a are casting-speed and feeding strip speed, respectively. ε is a small number (0.001) to avoid dividing by zero; A_{mush} is the mushy zone constant to describe the attenuation level of velocity.

For the source term in Eq. (2), F_B is the thermal buoyancy due to the non-isothermal flow field induced by strip melting and slab cooling boundary conditions. The thermal buoyancy effect in momentum equations is assumed with the Boussinesq approximation, the gravity source term-natural convection is defined as follows:

$$F_B = \frac{\rho \beta_T \left(H - H_{ref}\right)}{c_l} g_i \tag{5}$$

where c_l is the liquid steel specific heat, H_{ref} is the enthalpy of the reference temperature.

The general equation for melting, solidification and heat transfer is:

$$\frac{\partial(\rho H)}{\partial t} + \frac{\partial\left(\rho u_j H\right)}{\partial x_j} = \frac{\partial}{\partial x_j}\left[\left(\lambda_{eff} + C_p \frac{\mu_t}{\sigma_t}\right)\frac{\partial H}{\partial x_j}\right] \tag{6}$$

where H is the enthalpy and λ_{eff} is the thermal conductivity coefficient [5]. σ_t is the turbulent Prandtl number, and equals to 1.0.

The temperature-dependent conductivity is given as follows [6]:

$$\lambda_{eff}(T) = \begin{cases} \lambda_s = 13.86 + 1.113T \times 10^{-2} & T < T_s \\ \lambda_s + \frac{\lambda_l - \lambda_s}{T_l - T_s}(T - T_s) & T_s \le T \le T_l \\ \lambda_l = 39 & T > T_l \end{cases} \tag{7}$$

The enthalpy H over a temperature range is described by the following equations:

$$H(T) = \begin{cases} c_s T & T < T_s \\ c_s T + \frac{L(T - T_s)}{(T_l - T_s)} & T_s \le T \le T_l \\ c_s T + L + c(T_l - T_s) & T > T_l \end{cases} \tag{8}$$

Boundary Conditions

The heat transfer and solidification problem of the 500 mm bloom is complicated by the varying cooling boundary conditions along the casting direction. The detailed boundary conditions of heat transfer at the bloom surface are summarized as follows:

(1) The heat loss along the casting direction firstly occurs in cooper mold cooled by water, the flux of heat transferred is given as [7]:

$$q = \frac{\rho c_w W(T_{in} - T_{out})}{S} \tag{9}$$

where W is cooling water flux, $m^3\ h^{-1}$, T_{in} and T_{out} are the cooling water temperature in and out of mold, S is the contact area between melt and mold, m^2.

(2) Following the cooper mold is the secondary cooling zone where cooling water sprayed on the freezing shell surface directly by nozzle, surface heat transfer coefficient is:

$$h_{spray} = A \times Q_w^c \times \left(1 - b \times T_{spray}\right) \tag{10}$$

where Q_w^c is water flux in the spray zones. According to the Nozaki's empirical correlation, $A = 0.3025$ and $b = 0.0075$, which has been used successfully by other modellers [8].

(3) Below the secondary cooling section is the radiation zone, where the heat is removed by the radiation and convection to the surrounding air. In radiation zone, the heat extraction due to radiation can be evaluated as [9]:

$$h_{rad} = \sigma \times \varepsilon\left(T_{surf} + T_{amb}\right)\left(T_{surf}^2 + T_{amb}^2\right) \tag{11}$$

Computational Procedure

To ensure the accuracy and efficiency of the coupled model, the computational domain of the continuous casting system is reasonably divided according to the characteristic of macroscopic transport during casting process. It is observed that the melt in a small distance below the meniscus shows a turbulent flow pattern. And then the plug flow is formed when the fluid velocity equals to casting speed. So the whole computational domain is divided into two main regions: turbulent flow region and laminar flow region. To transmit the datum like velocity, temperature and liquid fraction between the two regions, the coordinate interpolation algorithm is adopted. A schematic diagram of the computational domain, cooling boundary conditions and the meshes of the two regions are illustrated in Fig. 2. A velocity-inlet boundary condition was imposed at the top SEN. The melt inlet velocity and the strip inlet was specified according to the casting and feeding speed respectively. Initially, the solid phase strip was assumed to be at ambient temperature of 20 °C and the liquid steel is specified at a superheat temperature of 10, 30 and 50 K respectively. All the governing equations were discretized by the finite volume method (FVM). The SIMPLE algorithm was adopted to resolve the velocity-pressure coupling in the momentum equation. Moreover, the upwind differencing scheme was used to approximate the convective and diffusive terms giving second order accuracy in space and time. Throughout the simulation, the liquid fraction was updated based on the temperature from the previous time step by solving the discretized equations associated with the appropriate boundary conditions. For melting, the volume temperature at the previous time-step should be

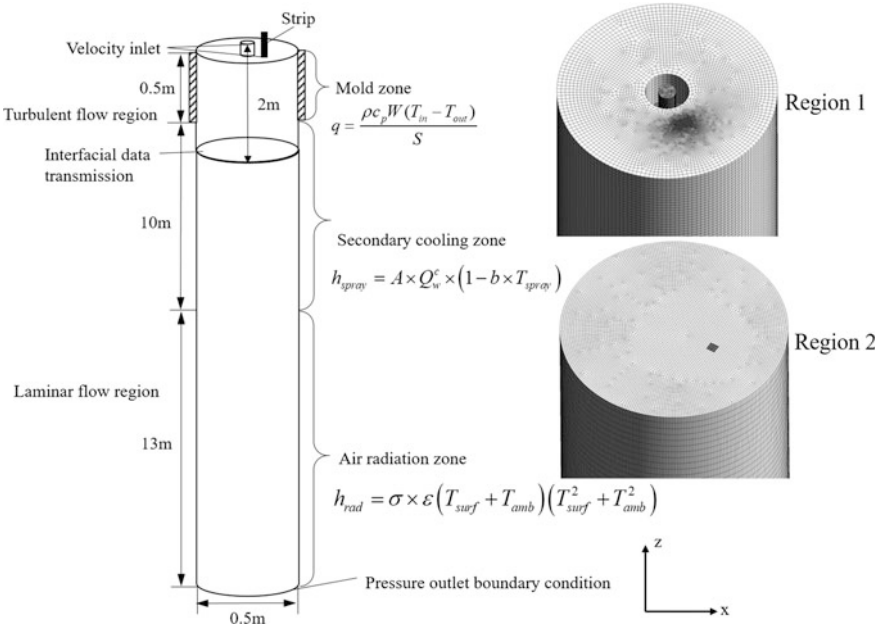

Fig. 2 Schematic diagram of the computational domain, cooling boundary conditions and the meshed computational region division

lower than at the 'actual' time step, and vice versa for solidifying. This concept was therefore used to provide the solver with the required information to determine whether the steel in a specific volume is melting or solidifying. A fixed time step scale of 0.001 s was adopted for the entire simulation. The adopted thermophysical parameters for the steel and operating parameters are summarized in Table 1. The simulation was terminated until a pseudo-steady state has reached implying that the strip melting speed is roughly the same with the strip feeding speed and the strip tip is located in a fixed position with insignificant fluctuation.

Table 1 Thermophysical parameters for the steel and operating parameters in casting

Parameters	Value	Parameters	Value
Viscosity of the liquid steel (kg/m s)	6.2×10^{-3}	Casting speed (m/min)	0.35
Latent heat (KJ/kg)	272	Mold water inlet temperature (K)	298
Density (kg/m^3)	7020	Mold water outlet temperature (K)	306
Liquidus temperature (K)	1790	Mold cooling water flow rate (L/min)	4600
Solidus temperature (K)	1749	Secondary cooling water flow rate (L/min)	27

Results and Discussion

Validation

For melting, the accuracy of the mathematical model has been verified through comparison with experimental results performed in Baosteel [10]. Liquid steel is accommodated in a crucible which can be heated through the induction furnace. The strip is fed into the melt held by a strip holder controlled by a lifting device, as depicted in Fig. 3a. Here, the strip used was 3 mm thick. By lifting the strip out and measuring the thickness of strip at a 2 mm distance away from the tip at a fixed time interval, the total strip thickness evolution has been recorded. The comparison of the predicted and measured strip thickness versus immersion time is demonstrated in Fig. 3b. Reasonable agreement of the whole melting time as well as the maximum thickness of the strip was obtained indicating the reliability of the model.

Evolution of Strip Melting

Strip Thickness Evolution

According to the validation results, the process of melting with solidifying consists of three stages. During the first stage, a short period of sheath is formed in the immersed part of strip. The thickness of the sheath first increases and then reaches a maximum. After that, the sheath begins to melt until disappears. After melting of the sheath, melting of the strip starts. The third stage ends with complete melting of the strip, total melting time is t_m. A typical melting curve is presented in Fig. 4a to better understand mechanism of melting of strip in liquid metal. The complicated

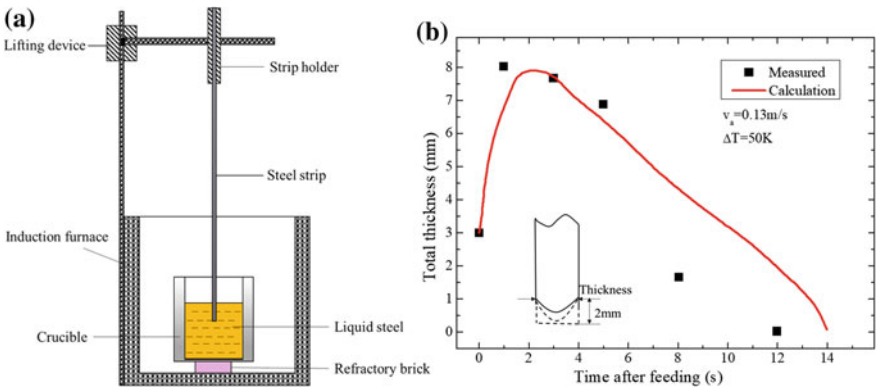

Fig. 3 **a** Schematic diagram of experiment **b** Comparison between experimental results and predicted results

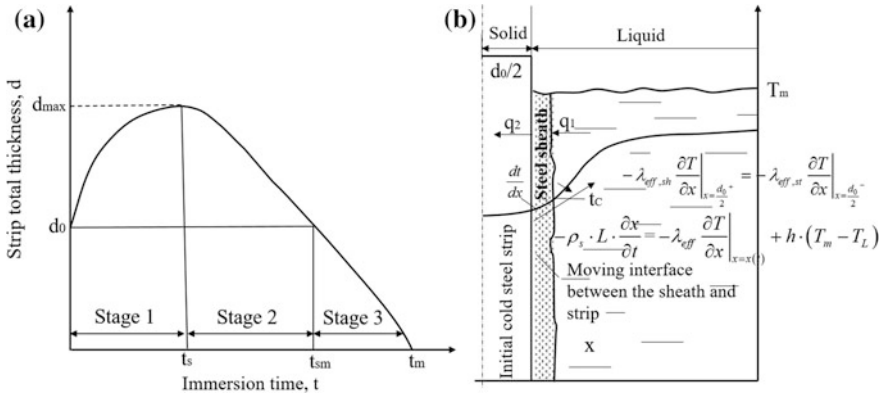

Fig. 4 **a** Melting curve of the strip versus time **b** The complicated heat transfer between the strip and liquid melt

heat transfer between the strip and the molten steel is depicted in Fig. 4b. At the first moment after immersion of the strip, due to high thermal conductivity of the strip, the magnitude of heat flux drawn by the strip is larger than the magnitude associated with the convective heat flux. During this period, the intensity of metal cooling by the strip is gradually reduced. The thickness of the sheath continues to increase, but the rate of this increase gradually drops. By the ts, the strip temperature rises to such an extent that the intensity of liquid metal cooling becomes not high enough for the process of solidification of the sheath to continue. Then the further growth of the sheath thickness ceases. The melting of this solid sheath begins when the rate of heat transfer from the melt by convection becomes greater than the rate of heat conduction through the sheath. The end of the period II denotes the time at which the encasing steel sheath has entirely melted back to expose the original strip. The moving strip in the slab melt to vanish to avoid "the un-melted frozen in shell" before reaching the end of liquid core.

Strip Travels Distance

The distance travelled is the distance travelled by the strip before a dynamic steady state is got between the continuously poured in hot melt, cooling boundary conditions and the strip melting. The effect of strip feeding speed, strip initial thickness and liquid steel superheat on the distance travelled by the strip has been shown in Fig. 5. It has been observed that although the melting time decreases with the increase in strip feeding speed, whether the strip will travel deeper or not is dictated by whether the decrease in melting time is significantly higher or not. With the relatively low feeding speed, the distance travelled increases with strip feeding speed. With the increase of the strip thickness, the total heat requirement for melting of the strip increases as there is more strip mass to be melted and the strip travels

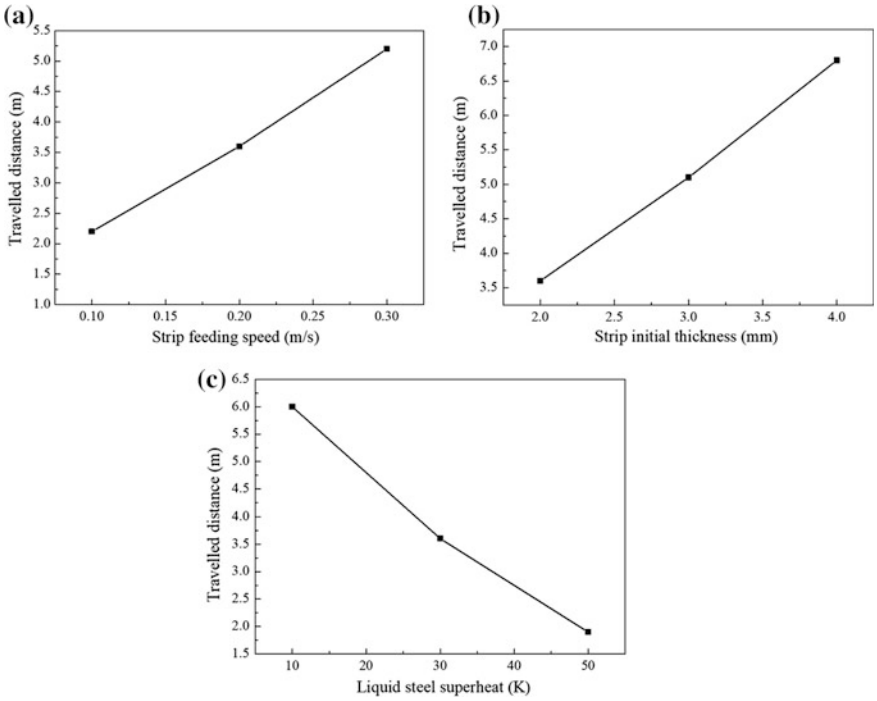

Fig. 5 The travelled distances of the strip under different feeding scenarios **a** Different strip feeding speeds **b** Different strip thicknesses **c** Different liquid steel superheat

longer. As the superheat is increased, the maximum thickness of the sheath decreases due to the increased amount of heat supplied from the melt to the strip. Additionally, the total melting time decreases and the travelled distance is decreased.

Effect of Strip Feeding on Fluid Flow

Figure 6 shows the three dimensional streamline distribution in mold with a strip feeding in, the strip morphology is also presented. The effect of the continuously moving strip on flow field can be clearly identified. It is seen that the molten steel, supplied by normal straight nozzle, passes straight down with a high speed and then tends upward approaching to the solidification shell. As the strip moves at a speed much faster than the flowing fluid (i.e., 0.2 m/s), the molten steel around it flows downward carried by the strip. Thus, the turbulent flow in the mold is enhanced. Meanwhile, with the cold strip melting, the nearby downward fluid is therefore cooled down. Outside the undercooled zone, the fluid is lighter and the buoyancy force is upward. This combination of the downward and upward fluids results in the enhancement of the recirculation of the fluid flow.

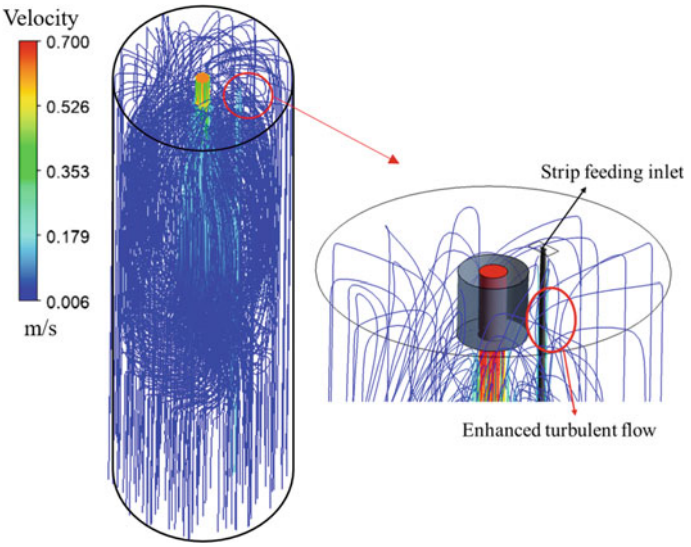

Fig. 6 The streamline distribution in a round bloom mold with a strip feeding in

Effect of Strip Feeding on Liquid Steel Superheat

Accompany with the phase change, the temperature of the melt around the strip is decreased. Figure 7 shows the temperature distribution around the strip during the three stages when a steady state is reached. It can also be observed that with the increment of the distance the strip travels, the strip temperature increases. Besides,

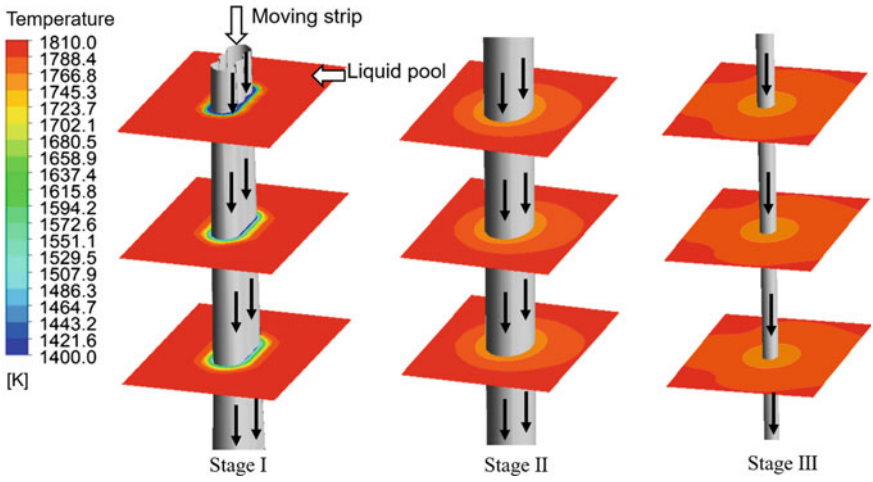

Fig. 7 Temerature distribution around the strip during the three stages

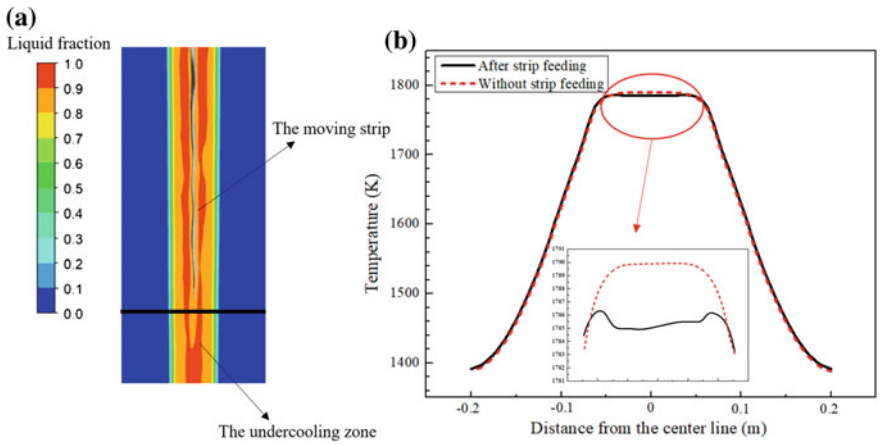

Fig. 8 Temperature decrease action by the end of liquid core

with the decreasing superheat of the liquid pool, the cooling effect is enhanced. On the other hand, it is seen that during the sheath formation stage I, the range of cooling zone is limited. As the melting goes on, the cooling zone range is further extended.

During the steady state, the strip tip is by the end of the slab liquid core, the strip and shell morphlogy are depicted in Fig. 8, and the temperature distribution along the black line is ploted. It is seen that after strip feeding, the temperature in the central zone is decreased by up to 5 K. And the range width of the action is around 0.1 m. Here, a strip with 3 mm thickness is adopted. The overcooled zone forms another center of solidification which is conductive to the development of equaixed dendrites.

Conclusions

1. Steel strip suffers three periods when fed into the mold, including the steel sheath formation stage, steel sheath melting stage and steel strip melting stage.
2. The turbulent flow is enhanced by the forced convection induced by the fast moving strip. And due to the cooling effect of the strip, the combination of the downward and upward fluids enhances the recirculation of the fluid flow.
3. The melt superheat in the vicinity of the strip is decreased by up to 5 K at melting end. And a 0.1 m overcooled zone is developed around the moving strip to form another center of solidification.

Acknowledgements This work was financially supported by the National Natural Science Foundation of China (No: 51574068) and the Fundamental Research Funds for the Central Universities (No. N162504009).

References

1. Luo S et al (2014) Characteristics of solidification structure of wide-thick slab of steel Q345. In: 5th International Symposium on High-Temperature Metallurgical Processing. TMS, Warrendale
2. Isaev OB (2005) Effectiveness of using large cooling elements to alleviate axial segregation in continuous-cast ingots. Metallurgist 49(7):324–331
3. Golenkov MA (2014) Improvement of internal quality of continuously cast slabs by introducing consumable vibrating macrocoolers in a mold. Russ Metall 12:961–965
4. Sun H, Zhang J (2014) Study on the macrosegregation behavior for the bloom continuous casting: model development and validation. Metall Mater Trans B 45(3):1133–1149
5. Hu H, Argyropoulos SA (1996) Mathematical modelling of solidification and melting: a review. Modell Simul Mater Sci Eng 4(4):371–396
6. Li C, Thomas BG (2004) Thermomechanical finite-element model of shell behavior in continuous casting of steel. Metall Mater Trans B 35(6):1151–1172
7. Alizadeh M, Jenabali JA, Abouali O (2008) A new semi-analytical model for prediction of the strand surface temperature in the continuous casting of steel in the mold region. Isij Int 48 (2):161–169
8. Hardin RA, Liu K, Beckermann C, Atul K (2003) A transient simulation and dynamic spray cooling control model for continuous steel casting. Metall Mater Trans B 34(3):297–306
9. Melissari B, Argyropoulos SA (2005) Development of a heat transfer dimensionless correlation for spheres immersed in a wide range of Prandtl number fluids. Int J Heat Mass Trans 48(21):4333–4341
10. Li YT, Zhang L, Zhang HW (2011) Melting process of steel strip and microstructure of ingot with steel-strip fed in molten steel. J Iron Steel Res 23(11):54–58

Numerical Modeling and Experimental Verification of Macrosegregation and CET Predictions in Large Steel Roll Ingots

L. Nastac, K. Redkin, C. Hrizo, Sean M. Loney and K. Marsden

Abstract A multi-component Computational Fluid Dynamics (CFD) model developed to study macrosegregation phenomena in 65-tons 2.5 m diameter round-sided steel ingots has been verified through advanced microstructural characterization, chemical analysis and non-destructive testing. Radial and central bars machined out from the full-scale as-cast ingot were compared against the model predictions in terms of columnar-to-equiaxed transition (CET), channel segregation as well as centerline segregation within the central zone of the ingot, which are inherent in the production of industrial scale alloy ingots. The CFD model solves for volume fraction of phases, time-dependent temperature distribution, mass and species transfer to predict segregation patterns in the solidifying ingot. It addresses the influence of various process parameters and mold design aspects on solidification behavior, such as: mold system, pouring rate, superheat, hence, resulted cooling rates, thermal gradients and chemical composition variations. The numerical and experimental results were compared and discussed.

Keywords Roll casting · Steel alloy solidification · Macrosegregation Columnar-to-Equiaxed-Transition · Computational fluid dynamics (CFD) modeling and simulation

Introduction

Injecting a dilute steel alloy via a submerged entry nozzle (SEN) into the liquid center of an up-hill teemed net-shaped ingot has been employed on an industrial scale to mitigated undesirable consequences of solute enrichment. Applying an

L. Nastac (✉)
Department of Metallurgical and Materials Engineering, The University of Alabama, Tuscaloosa, AL 35487, USA
e-mail: lnastac@eng.ua.edu

K. Redkin · C. Hrizo · S. M. Loney · K. Marsden
Whemco, Inc., Pittsburgh, PA, USA

L. Nastac et al. (eds.), *CFD Modeling and Simulation in Materials Processing 2018*, The Minerals, Metals & Materials Series,
https://doi.org/10.1007/978-3-319-72059-3_5

alternative non-SEN (Direct Ladle Pouring) DLP technology to control solidification behavior within the main body section of the net-shaped ingot achieves similar improvement without producing undesirable turbulence. Both the centerline segregation problems and mid-radius channel segregates can be minimized by using these technologies.

A multi-phase, multi-component computational fluid dynamics (CFD) code was used for studying the macrosegregation and columnar-to-equiaxed (CET) formation for a 65-tonne 1.6 m diameter steel roll ingot using the DLP technology. It addresses the influence of various process parameters and mold design aspects such as: mold system, pouring rate and superheat, on the resulted cooling rates, thermal gradients and chemical composition variations. The CFD code solves for the temperature, flow and solute balance in multi-component alloy systems [1].

The ingot segregation model was customized for commercially produced cast steel cast steel back-up roll ingots [2–6]. The CFD multi-phase modeling development effort includes up-hill teeming of the base alloy, SEN or DLP top pouring of the dilute alloy, species transfer during filling, and multi-component segregation during solidification. Customization also includes the development and implementation of initial and boundary conditions, mesh, thermophysical and solidification/segregation properties of the base and diluted steel alloys. A comparison between experimental data and simulation results is provided as well.

Model Description

A comprehensive analysis tool capable to model macro-segregation during ingot casting and solidification of multi-component alloys was developed and implemented into a CFD code. The viscous standard k-ε with standard wall functions, species transport and modified Scheil-based solidification models were used. The Scheil micro-segregation equation was corrected to account for diffusion in the solid phase (e.g., back-diffusion) in a multi-component system based on the microstructure characteristics of the alloy under consideration and the cooling conditions [7–10]. Thus, a framework for studying macro-segregation in various casting processes was developed by solving in a fully coupled mode for the temperature, flow and solute balance in the system. Special flux boundary conditions as a function of time (including the evolution of the air gap at the metal/mold interface) were developed by using experimental temperature data for a 65-tonne 1.6 m diameter steel roll. All thermo-physical properties (including density) and solidification parameters of the steel alloys used in the simulations are functions of temperature.

The CFD model was validated using literature numerical results [11–13]. More literature validation and calibration of the multi-component segregation model was performed using the analytical solution and the experiments in [1–7].

Simulation Conditions

The geometry of the roll is presented in Fig. 1. The process and material parameters for the processed rolls are as follows:

- 10-in (254 mm) wall thickness of the steel body chills (thermally insulated):
- Steel alloy composition of the studied roll (TP is the pouring temperature):
- Up-hill teemed alloy [TP = 2767 F (1793 K)]:
  C = 0.47 wt%, Cr = 4.0 wt%, Mo = 0.7 wt%.
- DLP dilute alloy [TP = 2903 F (1868 K)]:
  C = 0.33 wt%, Cr = 4.0 wt%, Mo = 0.17 wt%.
- 38 min bottom pouring time, 26 min solidification, then 1.5 min top pouring time.
- Cast iron body chills: initial temperature of these chills in the simulated roll is shown in Fig. 1. In the experimental DLP roll, which was cast after the simulation presented in this study was performed, the average temperature of the body chills were: 300 F (422 K), 485 F (525 K), 620 F (600 K), and 730 F (661 K).

Results and Discussion

Figure 2 illustrates the simulation results in terms of liquid fraction, temperature, the liquidus temperature variation (TL) for the DLP roll toward the end of solidification (time = 28 h). Figure 3 presents the predicted C, Cr, and Mo profiles for the DLP roll toward the end of solidification.

Figures 4 and 5 show a comparison of the segregation profiles of predicted and experimental C, Cr and Mo for the DLP case. The simulation results compare favorably with the experimental measurements. The predicted overall dilution and

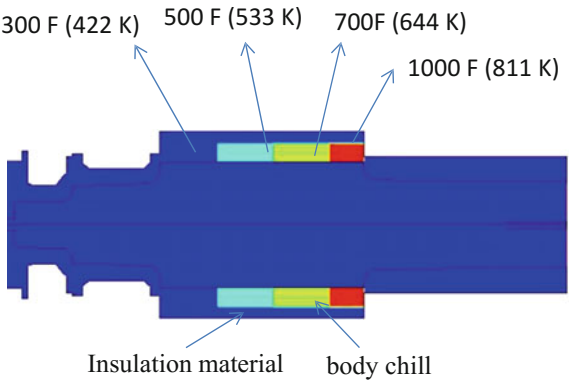

Fig. 1 DLP geometry and the initial temperatures of the steel body-chills

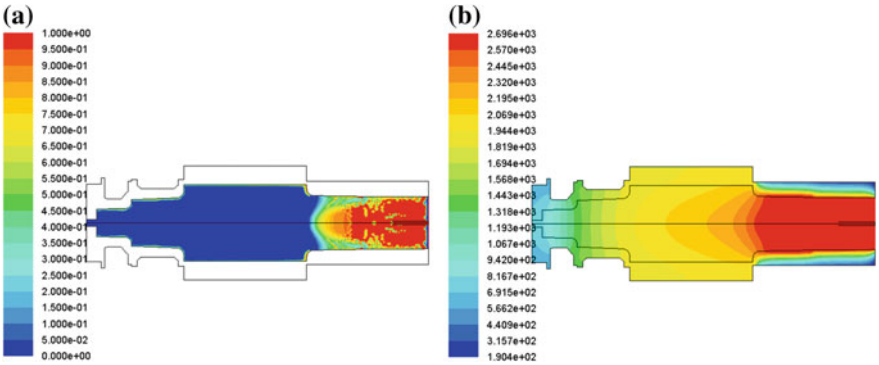

Fig. 2 Liquid fraction (**a**) and temperature (in deg. F) (**b**) distributions at the end of solidification (time = 28 h) in the DLP roll

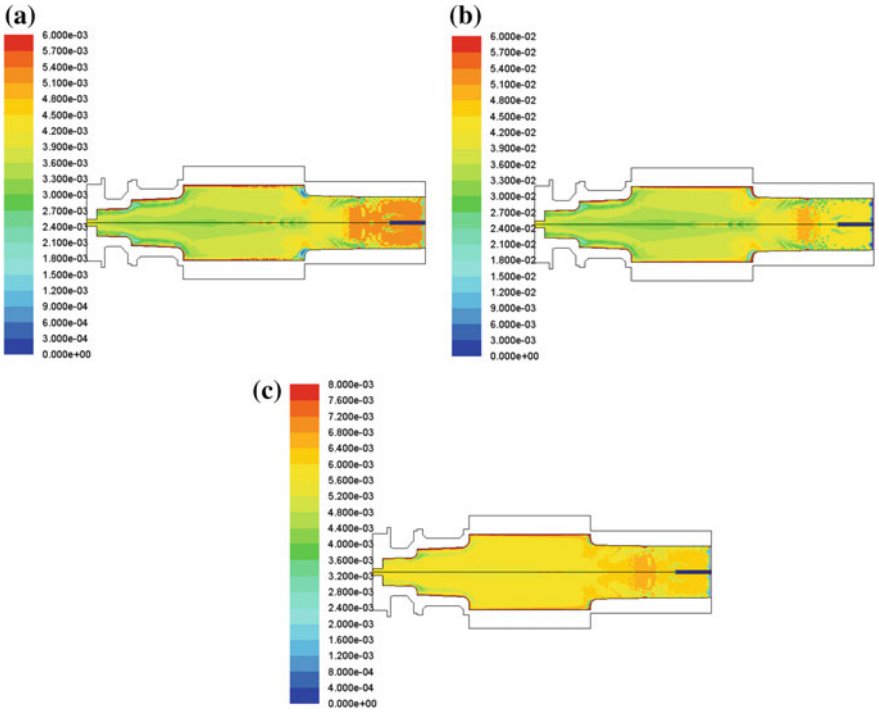

Fig. 3 Distributions of **a** C, **b** Cr, and **c** Mo mass fractions at the end of solidification (time = 28 h) in the DLP roll

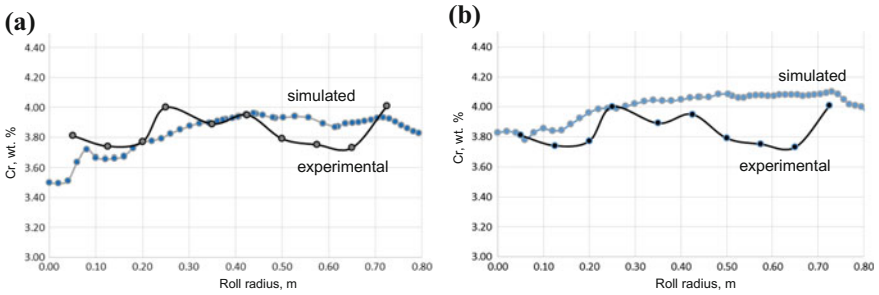

Fig. 4 Comparison of experimental and predicted Cr (in wt%) near the bottom (**a**) and near the top (**b**) of the DLP main body roll

mixing process predicted by simulation compares reasonably well with the experimental measurements except for the top of the roll (Fig. 5). One of the reason is that the temperature of the top body chill (700 F) in the experiment differs from the simulated chill (1000 F). Also, the top pouring process was done with a lip pouring ladle in the experimental roll and with a steel bottom pouring ladle with a 150 mm nozzle in the simulation. Therefore, it is possible that lesser penetration of the dilute alloy that was obtained in the experimental roll was because of these 2 factors. Also, the fusion zone (the distinct area between the shell and core zones) is indeterminate in the DLP process (Fig. 5).

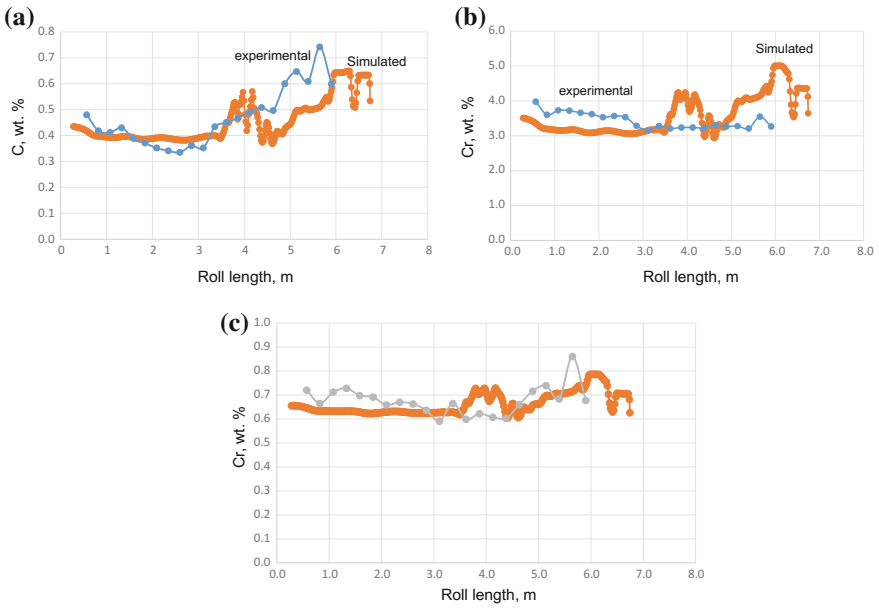

Fig. 5 Comparison of experimental and predicted C, Cr, and Mo (in wt%) centerline segregation along the DLP roll length

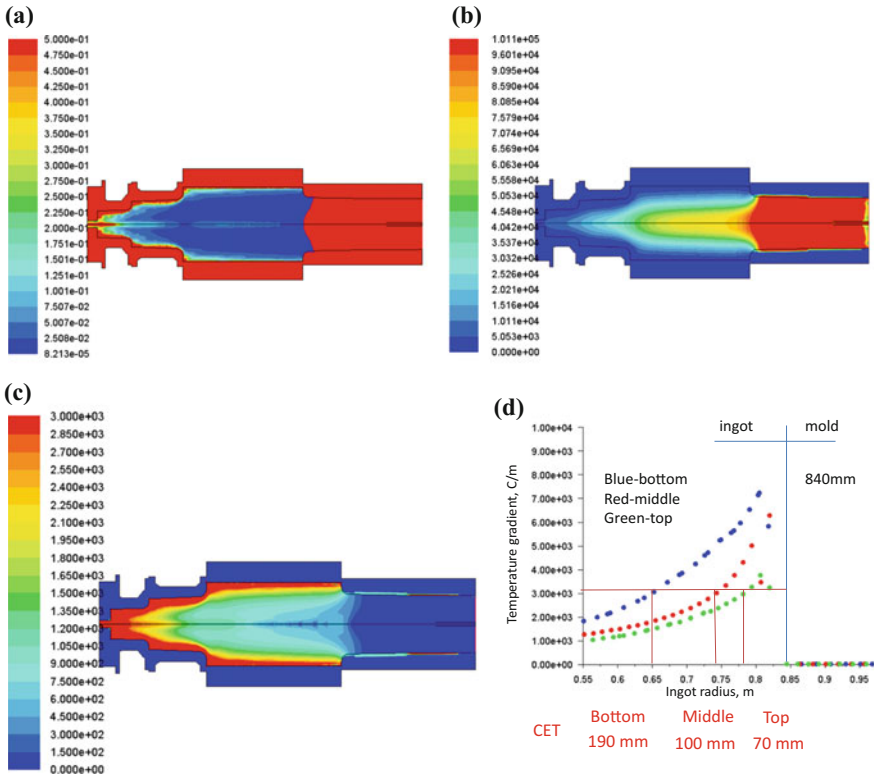

Fig. 6 Distributions of **a** cooling rates (K/s), **b** local solidification times (s), and **c** and **d** temperature gradients (K/m) and (at time = 28 h) in the DLP roll

Figure 6 shows the predicted cooling rates, temperature gradients and local solidification times toward the end of solidification of the DLP roll. The temperature gradients (G, in K/m) (Fig. 6c, d) are computed at the liquidus temperature (*TL*). Columnar-to-equiaxed transition (CET) can be estimated by a critical temperature gradient (G_{cr}) below which equiaxed grains may start to nucleate and grow. Typically, G_{cr} is alloy chemistry dependent and process independent and its value can be estimated via unidirectional solidification experiments. Grain refinement will affect the formation of CET. Normal values of G_{cr} for unrefined dendritic alloys range from 1000 to 5000 K/m. The predicted CET using a G_{cr} = 3000 K/m is also shown in Fig. 6c, d.

Figures 7, 8 and 9 illustrate solidification structure characteristics revealed by ultrasonic inspection of the back-up roll produced from the DLP ingot. The CET measurement profile in Fig. 9 matches reasonably the predicted CET in Fig. 6c, d.

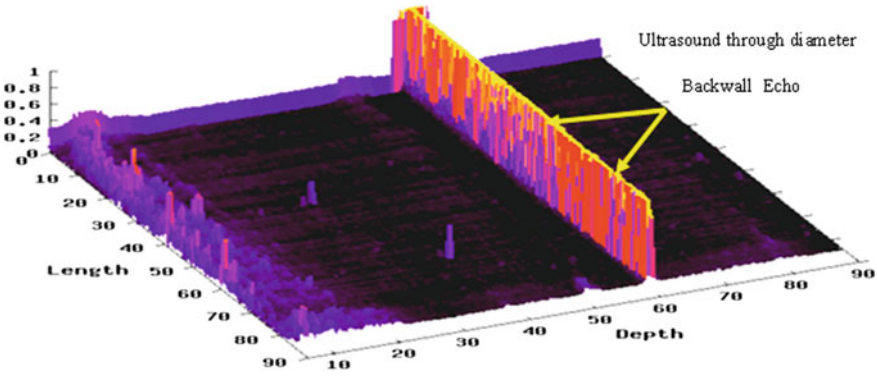

Fig. 7 Conventional ultrasonic inspection through the cross section of the roll

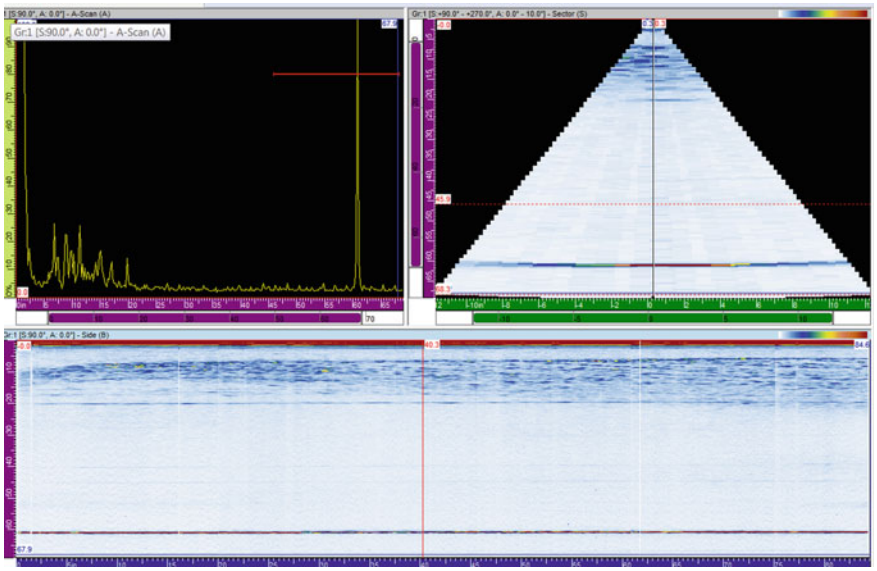

Fig. 8 Phased Array ultrasonic inspection examines the center ingot structure

Figure 10 presents the microstructures at a common radial location near the CET zone on samples removed from the bottom, mid-height and top of the main body section of the net-shaped DLP roll ingot. The microstructures in these samples are equiaxed dendritic with secondary dendrite arm spacing (SDAS) values in the range of 0.5–1.0 mm. By using the local solidification times from Fig. 6b for the location of these samples and the SDAS equation from Ref. [14], a similar range of SDAS values can be predicted based on the current simulation.

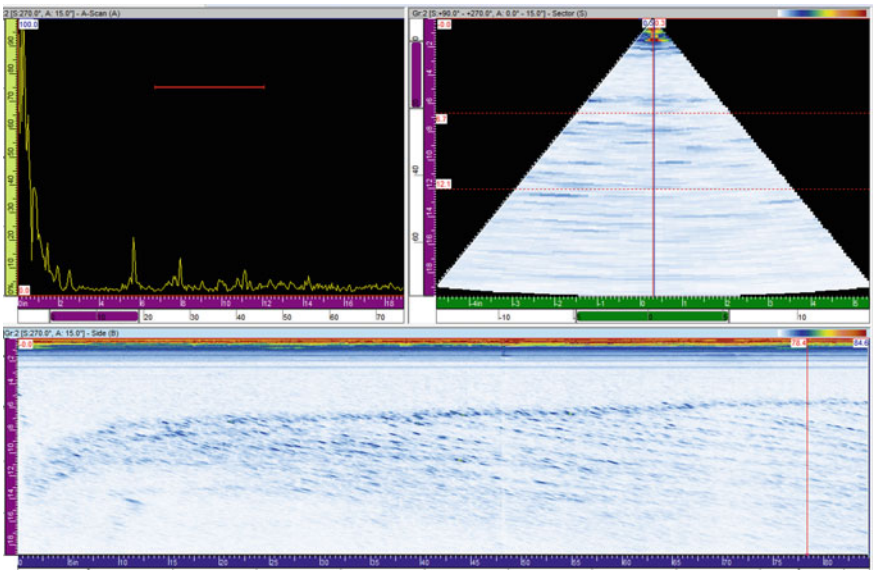

Fig. 9 Phased array ultrasonic inspection of the outer 500 mm zone examines features related to the CET and the channel segregate pattern

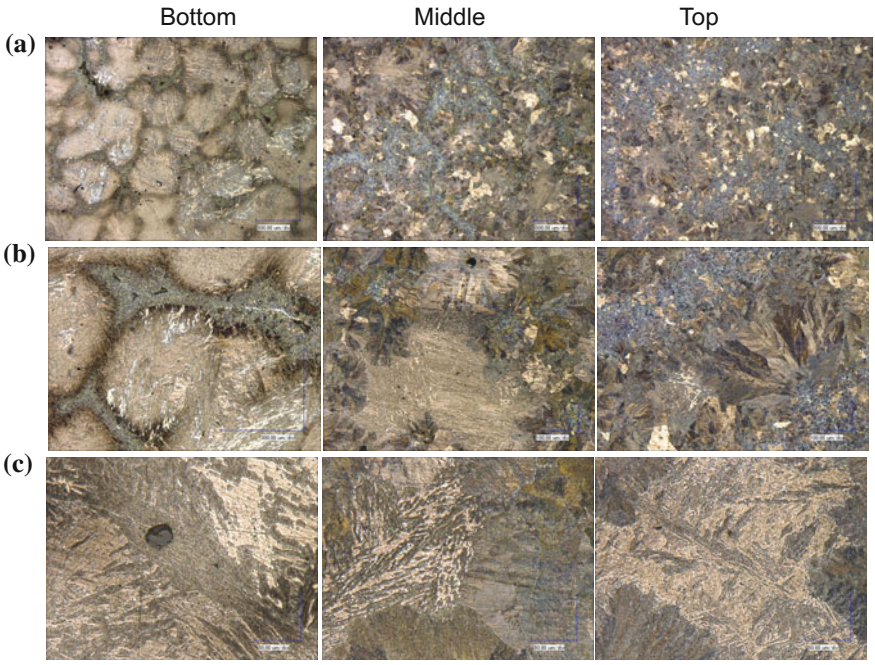

Fig. 10 DLP roll microstructures at ×100 (**a**), at ×300 (**b**) and at ×1000 (**c**)

Conclusions

A numerical modelling approach for predicting macro-segregation in casting was developed and implemented into a CFD code. A validation was performed using experimental measurements for a 65-tonne 1.6 m diameter steel roll that was cast using the DLP technique. The CET predictions match reasonably well the phase array ultrasonic measurements. It was determined that the overall dilution/mixing behavior is comparable for the DLP predictions and experiments except for the top of the roll. Also, the predicted segregation profiles for C, Cr, and Mo compare favorably with the experimental radial and centerline measurements.

References

1. L. Nastac, CFD Modeling of Macro-Segregation during Solidification of Superalloy Castings, The 2nd International Symposium on Cutting Edge of Computer Simulation of Solidification and Casting (CSSC2010), Sapporo, Japan, 2010, *ISIJ*, Vol. 50, No. 12, pp. 1829–1834, 2010.
2. L. Nastac, Computational Fluid Dynamics Modeling of Macro-Segregation and Shrinkage in Large Diameter Steel Roll Castings, *Met Trans B*, 42B, 1231–1243, 2011.
3. Nastac L, Marsden K (2012) Proceedings of ICRF2102, Aachen, Germany, EUROGRESS, 3–7 June 2012, pp 1–10
4. Nastac L, Marsden K (2012) Ninth international conference on CFD in the minerals and process industries CSIRO, Melbourne, Australia, 10–12 Dec 2012, pp 1–6
5. L .Nastac, Numerical Modeling of Macro-Segregation and Shrinkage in Large Diameter Steel Roll Castings: A Mold Study, *International Journal of Cast Metals Research*, Vol. 26, No. 6, pp. 374–82, 2013 (http://doi.org/10.1179/1743133613Y.0000000076).
6. Nastac L, Marsden K (2014) Proceedings of ICRF2014, Milan, 7–9 May 2014, pp 1–7
7. Nastac L (2004) Modeling and simulation of microstructure evolution in solidifying alloys. Springer, New York. ISBN 978-1-4020-7831-6
8. L. Nastac and D. M. Stefanescu, A Model for Solute Redistribution during Solidification of Plate, Columnar or Equiaxed Grains, *Metallurgical Transactions*, Vol. 24A, pp. 2107–2118, 1993.
9. T. Clyne, W. Kurz, Solute redistribution during solidification with rapid solid state diffusion, *Met. Trans A*, 1981, vol. 12A, pp. 965–971.
10. S. Ganguly, S. Chakraborty, A Generalized Formulation of Latent Heat Functions in Enthalpy-Based Mathematical Models for Multicomponent Alloy Solidification Systems, *Met. Trans B*, 2006, vol. 37B, pp. 143–145.
11. P. J. Prescott, F. P. Incropera, Convective transport phenomena and macrosegregation during solidification of a binary metal alloy: I-Numerical predictions, *J. of Heat Transfer*, 1994, vol. 116, pp. 735–749.
12. C. Beckermann, R. Viskanta, Double-diffusive convection during dendritic solidification of a binary mixture, *Physicochemical Hydrodynamics*, 1998, vol. 10, pp. 195–213.
13. M. Rappaz, V. Voller, Modeling of micro-macrosegregation in solidification processes, *Met. Trans A*, 1990, vol. 21A, pp. 749–753.
14. M. El-Bealy and B. G. Thomas, Prediction of Dendrite Arm Spacing for Low Alloy Steel Casting Processes. *Met. Trans B*, 1996, vol. 27B, pp. 689–693.

Numerical Simulation of Electromagnetic and Heat Transfer Phenomena in Inductively Heated Risers

Michael R. Cox and Gregory M. Poole

Abstract Electromagnetic induction heating of open risers presents an energy efficient means to maintain the alloy in its molten state for mass feeding whilst allowing riser size reduction and substantial material savings. This paper presents preliminary simulation results of solidification phenomena in an inductively heated top riser. The electromagnetic field was calculated using a hybrid control volume/integral method to solve the magnetic diffusion equation with accompanying boundary conditions, and used temperature dependent electrical conductivity. The heat transfer equation was solved using the control volume method. Computed results show that it is possible to prevent premature solidification of the riser even though traditional design criteria are violated. The significance of these findings pertaining to sand and ingot casting systems will be discussed.

Keywords Casting · Induction · Solidification · Riser

Introduction

The metal casting industry is one of the most energy-intensive manufacturing sectors due to the melting operations required, which consume approximately 55% of the energy required for plant operation [1, 2]. This makes reducing the scrap production rate a particular priority, of which risers constitute a sizable portion. While it would be ideal to have a riser which contains only the mass required to ensure a sound casting, geometrical constraints must be taken into consideration such that the riser solidifies after the casting. If it solidifies beforehand, the liquid remaining in the riser can no longer feed into the casting, leading to the shrinkage defects [3]. Furthermore, the use of feeding necks and gates must also be considered, as their solidification equally serve to choke the flow.

M. R. Cox · G. M. Poole (✉)
Department of Mechanical Engineering, University of South Alabama, Mobile, AL, USA
e-mail: gpoole@southalabama.edu

L. Nastac et al. (eds.), *CFD Modeling and Simulation in Materials Processing 2018*, The Minerals, Metals & Materials Series,
https://doi.org/10.1007/978-3-319-72059-3_6

The first, and still most commonly used, rule in geometrical reasoning methods in riser design is that of Chvorinov [4], who established that the volume to surface ratio, or modulus, of the riser and neck must be greater than that of the casting. Ciobanu and colleagues [5] found that the ratio of the solidification times of the casting, neck, and riser, and by corollary the moduli, must be approximately 1:1.2:1.45, respectively, to ensure sound castings in complex geometries.

However, such geometrical design rules for risers assume no net heat input from the surroundings to the riser. Such input allows a riser to defy criteria like Chvorinov's rule, yet still allow for sound castings, as the additional heat input to the riser "buys time" for the casting to solidify prior to the riser. To this end, the use of exothermic sleeves has garnered extensive use in the steel industry [6–10]. Used as an insert in direct contact with the riser, these sleeves contain a thermite fuel which undergoes a highly exothermic reaction upon reaching its ignition temperature. The result is a very large release of heat into the riser via diffusion through the sleeve material. Extensive modeling has been done on the effectiveness of exothermic sleeves on riser design, examples of which may be found in Refs. [6, 7, 10]. There are several drawbacks, however. First, each exothermic sleeve is single-use, and therefore must be replaced for each casting run. Second, the products of the exothermic reaction have been shown to contaminate the molten metal during solidification, either via mass or boundary layer diffusion, leading to defects such as the fish-eye variety [9].

Electromagnetic induction heating provides an efficient alternative to the exothermic sleeve, and has found use over the past half century in preheating of aluminum and steel slabs prior to rolling, as well as hardening of steels [11]. In this method, an alternating current is passed through a suitable induction coil, inducing eddy currents within the workpiece. Due to the internal resistance of the alloy, these currents are subsequently dissipated as heat (aka Joule heating). Application of this technology to risers has recently garnered interest among both academia [12] and industry alike [13–15]. Preliminary measurements and simulations of EM field quantities have been performed by Xu et al. [12] for steel in a simplified geometry, but examined only the riser component comparing their results. Although it was a good first step, two things must be noted. First, the work did not give any specifics as to the rate of Joule heating within the riser, the ultimate goal of this design. Lastly and most important, however, the authors did not consider the coupling of the electromagnetic field with the casting itself. Numerical simulations by one of the authors have shown that the presence of adjacent conducting media has a distorting effect on the both the force field and Joule heating within the alloy [16, 17].

This paper presents preliminary results for the solidification behavior of a concentric, cylindrical casting with induction heating. The solution domain includes both the riser and casting, and the influence of coil operating conditions such as current and frequency were examined.

Model Formulation

Figure 1 shows a sketch of a generalized, inductively-heated casting and riser assembly. As seen in this figure, the system is comprised of an insulating refractory mold surrounded by an induction coil. The mathematical description of EM heating during solidification must include, at a minimum, the heat conduction equation with phase change in conjunction with subsidiary relationships to describe the Joule heating within the system, which includes both the alloy and the mold.

Electromagnetic Field

In this work, the EM field was formulated using the magnetic vector potential, **A**. Doing so takes advantage of the axisymmetric nature of the casting system, thereby reducing the two-dimensional nature of the magnetic field to one of only the azimuthal direction. Thus the magnetic diffusion equation becomes

$$\nabla^2 A_\theta = j\mu\sigma\omega A_\theta \tag{1}$$

where j, μ, and ω are the square root of −1, permeability of free space, and the angular frequency of the inductor, respectively. The electrical conductivity, σ, for each material was assumed to vary logarithmically as

$$\sigma = C_1 + C_2 \ln(T) \tag{2}$$

where C_1 and C_2 are fitting constants. In this paper, the hybrid technique given by Meyer et al. [18] was used. In this method, Eq. (1) is solved within the solution domain, and the boundary conditions are resolved using the vector potential form of the Biot–Savart law:

$$A_\theta = \frac{\mu_0}{4\pi}\left[\int_V \frac{\mathbf{J}(\mathbf{r}')}{|\mathbf{r}-\mathbf{r}'|} d^3 r' + \sum_{k=1}^{N_{coil}} I_k \oint \frac{dl_k}{|\mathbf{r}-\mathbf{r}'|}\right] \tag{3}$$

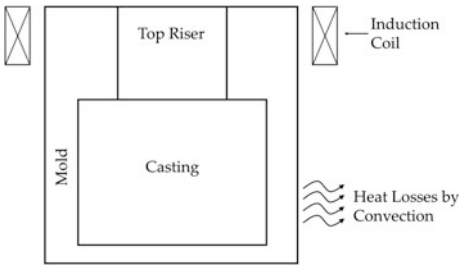

Fig. 1 General sketch of an inductively heated top riser

where **J** and I_k are the induced current density and applied current of the kth coil turn. The induced current and Joule heating may be related by

$$J_\theta = -j\omega\sigma A_\theta \tag{4}$$

$$\dot{q}_{em} = \frac{\mathbf{J}\cdot\mathbf{J}^*}{2\sigma} \tag{5}$$

where the * superscript denotes the complex conjugate of the vector.

Heat Transfer

Using the methodology of Szekely and Themelis [19], and assuming a linear variation of solid fraction with respect to temperature in the mushy region, the heat conservation equation including phase change is given by

$$\rho C^* \frac{\partial T}{\partial t} = \nabla\cdot(k\nabla T) + \dot{q}_{em} \tag{6}$$

where

$$C^* = \begin{cases} c_{p,l} & T \geq T_L \\ c_{p,s} + \frac{L}{T_L - T_S} & T_S < T < T_L \\ c_{p,s} & T \leq T_L \end{cases} \tag{7}$$

is the effective specific heat, k is the thermal conductivity, and T_L and T_S are the liquidus and solidus temperatures, respectively.

Both the magnetic diffusion and heat equations were solved using the control volume technique as outlined in Pun and Spalding [20].

Results and Discussion

In this section, we shall present computed results for solidification of commercially pure aluminum in a casting whose riser is surrounded by an induction coil. The induction coil employed in this study consists of six turns arranged in a triangular, close packed configuration and situated at the top of the riser. Calculations were carried out for no heating, followed by a baseline coil current and frequency of 800 A rms and 500 Hz, respectively. The coil current and frequency were then varied, but in a manner that yielded the same rate of heat input. Based on assumptions made for natural convection heat transfer for vertical tubes, the heat transfer

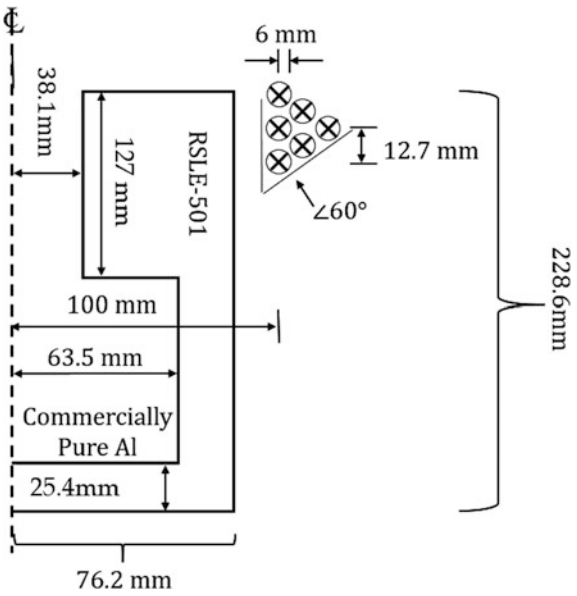

Fig. 2 Dimensions of the system and materials used in this study

coefficient along the periphery of the mold was assumed to be 60 W/m^{2}K. The dimensions of the system are given in Fig. 2 and the thermophysical properties are given in Table 1.

To establish a baseline, it was necessary to compute the solidification behavior of the system without heating. Figure 3 shows the spatial variation of solid fraction at the time of riser solidification (959 s). For clarity, outlines of the riser, casting, and mold regions have been added. As expected, the solidification time of the riser is shorter than that of the casting, consistent with traditional riser design criteria [3–5]. As seen in the figure, there is a substantial quantity of liquid remaining, also called a "hot spot," directly below the riser at the centerline, where solid fraction is as low as 0.36 at z = 0.08 m, while the riser is completely solidified. Thus it is expected there would be severe shrinkage porosity present, leading to rejection of the casting.

Induction heating was shown to appreciably change the solidification characteristics within the casting. As seen in Fig. 4, the induced eddy currents within the riser significantly slowed the rate of solidification within the riser long enough for the casting to solidify, as indicated by the shift in the hot spot from the top of the casting to the bottom of the riser. Intuitively, the solidification time of the casting increased to 1070 s due to the additional heat input from electrical energy dissipation. However, it should be noted that this is only a marginal improvement, as there would likely be insufficient metallostatic pressure to feed the final solidifying region of the casting.

It is generally known that the spatial distribution and intensity of the induced eddy current, and thus Joule heating, are directly influenced by the applied coil current and frequency. However, to ensure the same power input as the case shown in Fig. 4, an increase in coil current, which increases Joule heating by its square,

Table 1 Thermophysical properties and initial conditions

Aluminum	
k (solid) (W/m K)	$228.1 - 0.1157\ T + 6.175 \times 10^{-5}\ T^2$ [21]
k (liquid) (W/m K)	93 [22]
ρ (solid) (kg/m^3)	2700 [22]
ρ (liquid) (kg/m^3)	2390 [22]
C_p (solid) (J/kg K)	$897 + 0.5809\ T - 1.234 \times 10^{-4}\ T^2$ [21]
C_p (solid) (J/kg K)	1170 [22]
σ (solid)	4.41×10^7–5.29×10^6 T Mho/m
σ (liquid)	4.0×10^6 Mho/m
T_L	662 °C
T_S	658 °C
Zircar RSLE-501 (Mold)	
k	$0.515–2.15 \times 10^{-4}$ T W/m K
ρ	2100 kg/m^3
C_p	780 J/kg K
σ (solid)	1.33×10^{-8} Mho/m
Initial temperatures	
Aluminum	700 °C
Mold	100 °C

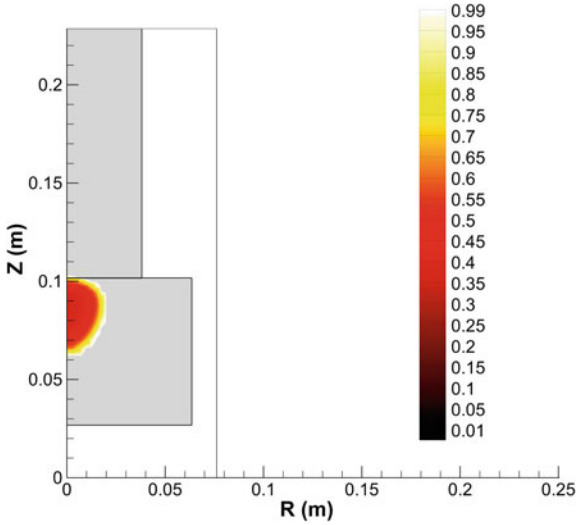

Fig. 3 f_S profile at the time of riser solidification for no heating (959 s)

was countered by a concomitant decrease in coil frequency, which has a square root correlation according to prior work by El-Kaddah [23] and one of the authors [24]. Figure 5 shows the solid fraction profiles at the time of casting solidification for

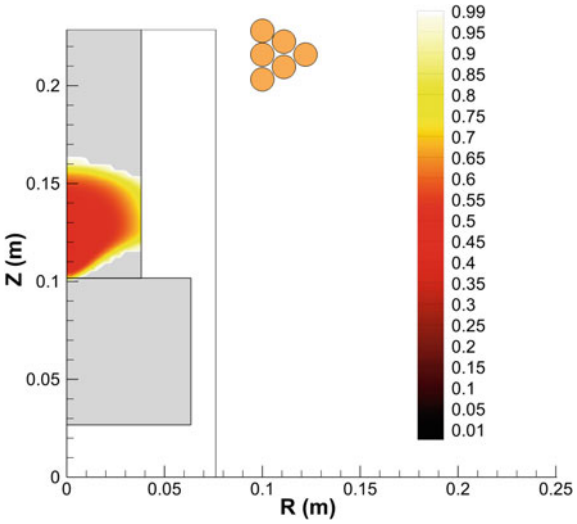

Fig. 4 f_S profile at time of casting solidification (I = 800 A; f = 500 Hz)

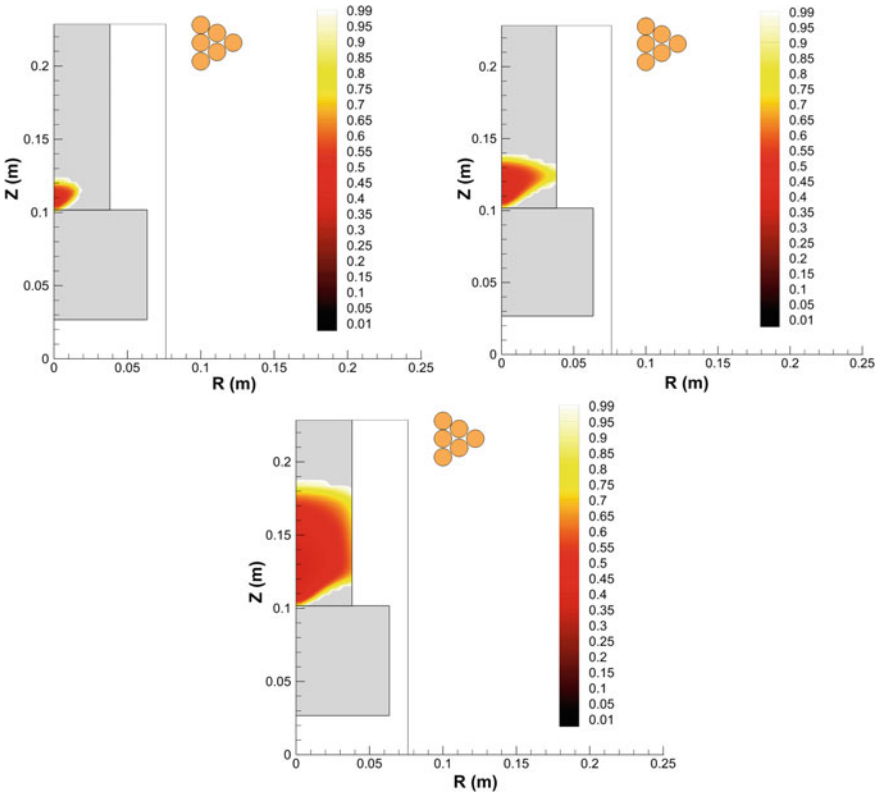

Fig. 5 Hot spot maps at time of casting solidification for three coil/frequency combinations: (top left) 400 A, 2 kHz; (top right) 565 A, 1 kHz; (bottom) 1130 A, 250 Hz

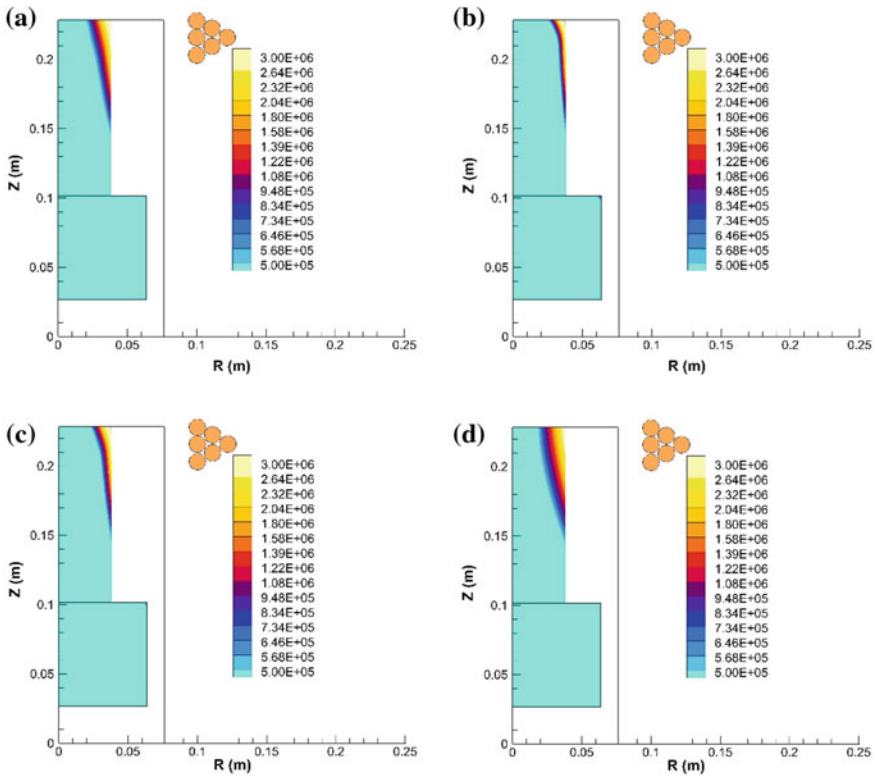

Fig. 6 Spatial distribution of Joule heating (in W/m^3) for various coil/frequency combinations: **a** 800 A, 500 Hz; **b** 400 A, 2 kHz; **c** 565 A, 1 kHz; **d** 1130 A, 250 Hz

three different current/frequency combinations. It should be noted that the solidification times were within 0.1% of the solidification time for the 800 A, 500 Hz combination, indicating that the heat generation rates within the riser are essentially equal. It is clearly seen that the hot spot size within the riser markedly increases as the coil frequency is decreased. This is due to the increase in the skin depth δ, which is given by

$$\delta = \sqrt{\frac{2}{\mu_0 \omega \sigma}} \tag{8}$$

Contours of Joule heating over the riser and casting are shown in Fig. 6. It can therefore be concluded from these results that the frequency chosen should be one such that the penetration depth of the current, and thus heating, goes very deep within the riser. However, further investigation is needed to quantify the effect of stirring forces [11].

Conclusions

A model has been presented to describe the electromagnetic field and heat transfer phenomena in an inductively heated top riser. Calculations showed that the application of induction heating can prolong the solidification time sufficiently enough to prevent the formation of shrinkage porosity, even though the riser is in violation of commonly-used design rules. It was also found that the use of lower frequencies is desirable to avoid only heating at the riser/mold interface, so long as the coil current is simultaneously increased. Future work includes the expansion of the model to determine the effects of fluid flow within the riser and casting during solidification, incorporation of porosity prediction criteria, and to determine what effects use of this technology would have on solute segregation.

References

1. Naranjo RD et al (2005) Advanced melting technologies: energy saving concepts and opportunities for the metal casting industry. BCS, Incorporated. https://energy.gov/sites/prod/files/2013/11/f4/advancedmeltingtechnologies.pdf. Accessed 7 June 2017
2. Worrell E et al (2011) Energy efficiency improvements and cost saving opportunities for the US Iron and Steel Industry: an ENERGY STAR guide for energy and plant managers. Lawrence National Laboratories, Berkeley. LBNL-4779E
3. Flinn RA (1963) Fundamentals of metal casting. Addison-Wesley, Boston
4. Chvorinov N (1940) Theory of solidification of castings. Giesserei 27:177–225
5. Ciobanu I et al (2014) Riser analysis using casting solidification techniques during solidification. Int J Metalcast 8:63–75
6. Midea AC (1999) Accurate thermal data for exothermic/insulating feeding systems. Foundry Manage Technol 50–57
7. Ignaszak Z, Popielarski P (2006) Problems of heat source modeling in iso-exothermic materials used as riser sleeves in foundry. Mater Sci Forum 514–516:1438–1442
8. Kossy S, Boddey RF (1952) Exothermically reacting sleeve for risers. US Patent 2,591,105
9. Aufderheide RC et al (2002) Eliminating fish eye defects in ductile castings. AFS Trans 02-047
10. Hardin RA, Williams TJ, Beckermann C (2013) Riser sleeve properties for steel castings and the effect of sleeve type on casting yield. In: Proceedings of the 67th SFSA technical and operating conference, Paper No 5.2
11. Zinn S, Semiatin SL (1988) Elements of induction heating. ASM International, Materials Park
12. Xu CJ et al (2016) Magnetic field distribution in the electromagnetic feeding riser of rectangle steel ingot. Metallurgia 55:593–596
13. Tonseth S (2014) Making greener ship propellers. ScienceNordic. http://sciencenordic.com/making-greener-ship-propellers. Accessed 11 Oct 2016
14. Induction Casting Riser. Dai-ichi High Frequency Co, Ltd. http://www.dhf.co.jp/eng/products/induction/induction.html. Accessed 11 Oct 2016
15. Takahashi S, Nakagawa Y, Hosoda Y (1984) Method for heating a riser of molten refractory material. US. Patent 4,460,524. 17 July 1984
16. Poole G, Nastac L (2014) Flow and temperature field evolution during solidification of an electromagnetically stirred melt: influence of magnetic shields. Paper presented at MS&T 2014, Pittsburgh, Pennsylvania, 12–16 Oct 2014

17. Poole G, Nastac L (2015) On the influences of adjacent conducting media and coil frequency on the electromagnetic field and flow characteristics in solidifying melts. J Manufact Sci Prod 15:15–21
18. Meyer JL, El-Kaddah N, Szekely J (1987) A new method for computing electromagnetic force fields in induction furnaces. IEEE Trans Mag 23(2):1806–1810
19. Szekely J, Themelis NJ (1971) Finite difference technique—variable heat contact. In: Rate phenomena in process metallurgy. Wiley, New York, pp 329–341
20. Pun WM Spalding DB (1977) A general computer program for two-dimensional elliptic flows. Imperial College of Science and Technology, London
21. Goldsmith A, Waterman TE, Hirschhorn HJ (1961) Handbook of thermophysical properties of solid materials: volume I—elements. Pergamon Press, New York
22. Stefanescu DM (2009) Science and engineering of casting solidification, 2nd edn. Springer, New York
23. El-Kaddah N (1992) The magnetic suspension melting process—a containerless melting technique for quality castings. In: Magnetohydrodynamics in process metallurgy. The Minerals, Metals & Materials Society, Warrendale, pp 283–289
24. Poole G, Larrazábal CA, Monroe CA (2015) Electromagnetic field characteristics in an inductively-heated molten metal on demand system. Paper presented at the 2015 NADCE Die Casting Congress, Indianapolis, Indiana, 5–7 Oct 2015

Part III
Processing: I

A Multiphase CFD Model for the Prediction of Particulate Accumulation in a Laser Powder Bed Fusion Process

A. M. Philo, D. Butcher, Stuart Sillars, C. J. Sutcliffe, J. Sienz, S. G. R. Brown and N. P. Lavery

Abstract Laser Powder Bed Fusion (L-PBF) is a powder based subcategory of metal additive manufacturing. In L-PBF systems an inert gas flow is used to avoid oxidation of the metal alloy powder and components but is also used to remove unwanted by-products produced from the vaporisation of material. By-products produced during in L-PBF can cause attenuation of the laser and re-deposition of unwanted by-products over the processing area which can affect the mechanical properties of as built components. The two main by-products produced in L-PBF are spatter caused from melt pool instabilities and recoil pressure from the metal vapour plume, and particulate condensates. A multiphase computational fluid dynamics model developed in ANSYS Fluent simulates the argon gas flow in a Renishaw AM250 machine validated using hotwire anemometry testing. This model is then coupled with a spatter expulsion discrete phase model supported by high speed imaging analysis and a tertiary phase model for a representative expulsion of particulate condensates is developed.

Keywords Laser powder bed fusion · Additive manufacturing
Shielding gas flow · CFD

A. M. Philo (✉) · D. Butcher · S. Sillars · J. Sienz · S. G. R. Brown · N. P. Lavery
College of Engineering, Swansea University, Bay Campus Crymlyn Burrows, Swansea SA1 8EN, UK
e-mail: adam.philo@swansea.ac.uk

C. J. Sutcliffe
School of Engineering, University of Liverpool, Brownlow Hill, Liverpool L69 3GH, UK

A. M. Philo · D. Butcher · C. J. Sutcliffe
Additive Manufacturing Products Division, Renishaw plc, Brooms Road, Stone Business Park, Stone, Staffordshire ST15 0SH, UK

L. Nastac et al. (eds.), *CFD Modeling and Simulation in Materials Processing 2018*, The Minerals, Metals & Materials Series,
https://doi.org/10.1007/978-3-319-72059-3_7

Introduction

Additive manufacturing is a rapidly developing process which is attracting end users in a variety of different sectors, such as medical, automotive and aerospace. Within metal additive manufacturing there are two main subcategories. Wire fed and powder based metal additive manufacturing systems. Within the powder based subcategory there is blown powder systems and also powder bed based systems. Laser Powder Bed Fusion (L-PBF) is a powder bed system and in the present work a Renishaw AM250 laser powder bed fusion machine is used. In a L-PBF process a virtual component is constructed using computer aided design (CAD) package and then sliced into small layers (typically 20 μm–1 mm) defined as the layer thickness. The scanning strategy (pre-defined depending on the application) and the previously generated sliced CAD model are uploaded to the processing machine. The base plate is heated, usually to about 170 °C depending on the machine, and then an initial powder layer, equivalent to one layer thickness is dosed over the base plate. The laser selectively scans the powder bed creating very small molten pools of the material, then when the material temperature drops it solidifies. Once a layer is complete the build platform is dropped one layer thickness and a new powder layer is re-coated over the previous layer and the next scanning path commences. This continues until the entire component is complete. Once the process is completed un-melted powder can be sieved and then used for subsequent builds.

The by-products produced in L-PBF are produced from the melting and vaporisation of the metal powder. Due to the large differences in thermal conductivity of the metal powder and the substrate material the heat in the molten melt pool is not easily transmitted to the surrounding material. This poor transmission can cause the temperature of the exposed powder particles to exceed that of the melting and vaporisation temperature of the metal alloy. The two primary by-products produced during the L-PBF process are a metal vapour plume and spatter. A summary of the potential by-products in L-PBF are shown in Fig. 1 taken from high speed imaging of the process.

By-Products and Shielding Gas Flow

When the molten pool reaches the vaporisation temperature, a phase transformation occurs where a metal gas is produced; the rapidly moving evaporated materials expand and generate a recoil pressure on the melt pool. Low levels of recoil pressure can cause the melt pool to be flattened, whilst high recoil pressure causes the removal of molten material by melt expulsion in the form of a metallic jet. This metallic jet then condensates into a metal vapour welding plume containing nano-particulates. This welding plume can disturb the laser causing it to re-focus and can also cause attenuation of the laser. Both of which can lead to inefficient

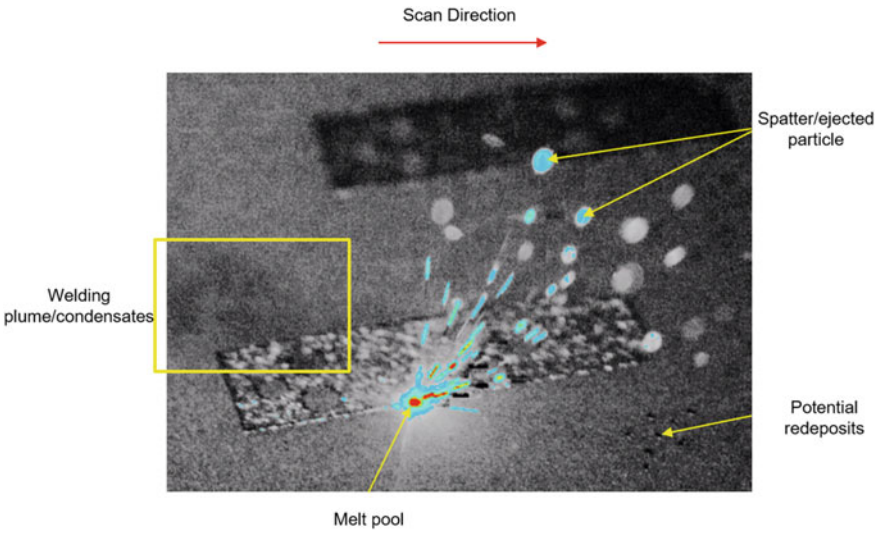

Fig. 1 Outline of potential by-products in the laser powder bed fusion process via high speed imaging analysis

melting of the powder or poor fusion of the laser track which can lead to detrimental effects on the mechanical properties.

The vapour recoil pressure can also cause expulsion liquid metal out of the melt pool. This ejected material is known as spatter. Spatter can also be formed from melt pool instabilities due to Marangoni effects. The inherent problem with spatter is that it can become redeposited into the powder bed making the layer thickness larger, which can lead to incomplete fusion in the build. This can cause porosity which can negatively affect the mechanical properties of the finished component. The expelled liquid metal may also have a high affinity to oxygen which if consolidated into the build material can make the part more brittle and reduce the tensile properties [1].

To minimise the disturbance of the process by-products the shielding gas flow system is utilised to remove the by-products from within the build chamber. The flow characteristics of the gas flow will directly govern where material by-products are transported. Ideally all of the by-products will be transported directly out through the outlet. However, this is not always the case, and a large proportion of the by-products can be left within the build chamber with a proportion being redeposited onto the processing area.

There has however been limited published literature on the effects of the shielding gas flow system to the L-PBF process. The shielding gas flow, usually argon, nitrogen or helium is used in the L-PBF processes mainly to provide an inert atmosphere reducing reactive gas pick-up by the liquid metal largely against oxidisation and nitration [2]. Its secondary function is for the removal of by-products.

The extent to which the importance and relevance of the removal of by-products from the process zone is becoming more apparent.

Ferrar et al. [3] demonstrated that the flow of argon in the gas flow system has a significant effect on the porosity and strength of as built parts and concluded that a uniform flow distribution is essential for component homogeneity across a build platform and for optimal build quality. Anwar and Pham [4] test the effect of scan direction, part location and gas flow velocity on the ultimate tensile strength of Selective Laser Melting (SLM) parts they found that the mean ultimate tensile strength of as built tensile bars increased from approximately 275–315 Mpa when they increased the flow rate from 30 to 60 of the gas flow system. This translated to an approximate local gas velocity of 1.43–2.87 m/s respectively. Ladewig et al. [5] studied the effect of the gas flow system on the width of single welds in the L-PBF process using an EOS Eosint M280 machine. They discovered that if the local flow velocity is too low then the probability of re-deposition of by-products is much higher as well as attenuation of the laser by the welding plume. They concluded that both of these effects can lead to balling which causes incomplete fusion within the material.

Some modelling in the area of the shielding gas flow has also been utilised. Masmoudi et al. [6] created a multiphase CFD model to understand the laser-material-atmosphere interaction to understand the effect of process parameters and protective gas pressure on the spatial thermal distribution in the process where they showed that a decrease of pressure gave rise to a strong expansion of the metal vapour in the interaction region of their model which could imply a larger attenuation of the laser. In addition, in other areas of AM technologies Ding et al. [7] showed that a local shielding device in wire + arc additive layer manufacturing caused three orders of magnitude improvement of contamination levels of oxygen below 2000 ppm and showed that mechanical properties (hardness) were not affected as long as the level was below 4000 ppm.

The production and analysis of spatter produced in welding processes has been more extensively analysed where primary research has investigated its fundamental production and also its effects on the mechanical properties of as built components.

Liu et al. [1] presented the effect of spatter on the mechanical properties of AISI 316L stainless steel. They performed single line experiments using a high speed camera to analyse spatter behaviour where they found that the amount of energy inputted to the system affects the size, scattering state and jetting height of the recorded spatter. They then performed tensile testing of spatter contaminated powder against uncontaminated powder and found that the spatter contaminated powder yielded significantly poorer tensile properties in comparison to the uncontaminated powder. Simonelli et al. [2] designed an experiment to understand the production of spatter on the processing of 316L stainless steel, Al-Si10-Mg and Ti-6Al-4V. The found that in the steel and aluminium based alloys that the surface of spatter particles were enriched with oxides in the most volatile alloying elements but there was no oxidation in the bulk of the microstructure. They noted that the surface oxides could reach up to several microns in thickness. In addition, regardless of the material being processed the spatter had spherical morphology and is much larger than the original pre-processed powder.

In the work presented a model of the shielding gas flow of a Renishaw AM250 laser powder bed fusion machine has been created and validated against Hot Wire Anemometry (HWA) velocity readings. The aim was to then create representative models of the two primary by-products. The first is a spatter expulsion model which was created using a Discrete Phase Model (DPM) approach supported by high speed experimental analysis which was coupled to the shielding gas flow model. The second is a representative metal vapour plume model which has been developed but not coupled to other models on the macroscale and is still in development.

Experimental Gas Flow Testing

To categorise the gas flow for an L-PBF process a hot wire anemometer (Airflow TA 465 Series, UK) was used to measure the gas flow velocity in a Renishaw AM250 laser powder bed fusion machine. A Perspex screen with a series of holes, shown in Fig. 2 was mounted to the front of the machine and velocity readings were taken using the HWA probe. During a reading the remainder of the holes were closed as to not to disturb the flow and to avoid leakage. To categorise the flow field two planes of readings were taken. One directly above the processing area and one plane normal to the inlets of the gas flow system. A series of measurements with 6 holes along the width at 50 mm intervals and 11 readings per insertion depth at 25 mm intervals were taken. Each readings was recorded for 20 s with the manufacturer's accuracy of ±3% or ±0.015 m/s error; whichever is greater. A 2 min break between consecutive readings was observed to allow the flow to settle.

These measurements resulted in 66 readings per plane. During an actual build using the Renishaw AM250 the chamber first pulls a vacuum and then fills the chamber with argon. In the experiments performed air was used instead of argon.

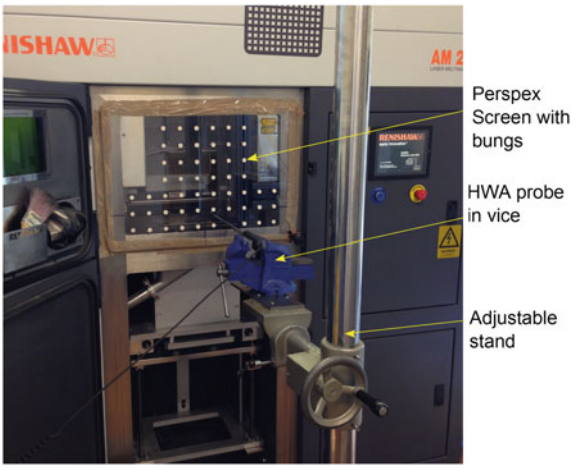

Fig. 2 Hot wire anemometer testing set up

Air was used instead of argon for health and safety concerns as there was a possibility of leakage. In addition, it allowed for the experimental gas to remain constant and to avoid a mixture of fluids. As argon and air have similar densities 1.622 and 1.225 kg/ m^3, respectively, this difference would have minimal effect on the fluid flow properties; namely turbulence regimes and compressibility.

Shielding Gas Flow Model

To reproduce the fluid flow profile in the AM250 machine the commercial CFD software package ANSYS Fluent was used. The model developed was steady, three dimensional, incompressible and turbulent. To categorise the fluid flow regime based on the Reynolds number the diameter of a single jet, 0.012 m was defined as the characteristic length scale. Using an estimated velocity of 5 m/s, the density of air and dynamic viscosity, 1.225 kg m^{-3} and 1.789×10^{-5} kg m^{-1} s^{-1} respectively the Reynolds number was calculated to be in the order of 4000 placing the flow in the transitional fully turbulent regime. A range of two-equation turbulence models were analysed and a comparison of localised velocity values to the HWA results was used as a guide for the most accurate turbulence model. It was found that a $\kappa - \epsilon$ realizable turbulence model with Menter-Lechner wall functions gave the most accurate results. This model is most accurate for flows in the far field zones, which is applicable for this flow scenario.

Boundary Conditions and Mesh

The geometry of the fluid flow volume along with the mesh of the volume is shown in Fig. 3. A mass flow inlet boundary conditions was defined as a mass flow rate at the beginning of the inlet rail. The volumetric flow rate of the closed looped gas flow system was set at 15 m^3/hr in the experiments. The mass flow rate, $\dot{m}$, was then calculated from this value giving a mass flow rate of 0.0051 kg/s for air. In addition, the outlet was defined as an outflow boundary condition. The mesh was created using a cut cell Cartesian assembly meshing method in ANSYS. This allowed for a nearly purely hexahedral mesh which is preferable for CFD simulations.

Meshes varying from 300,000 to 7,000,000 were tested to find grid independence for the solution. Grid independence was found using a mesh of approximately 2,500,000 elements.

In addition, to couple the momentum and pressure equations a SIMPLE (Semi-Implicit Method for Pressure Linked Equations) algorithm was used. A solution was considered converged when continuity and momentum reach 1×10^{-4}. For later models which include the energy equation a solution was considered converged when this reached 1×10^{-6}.

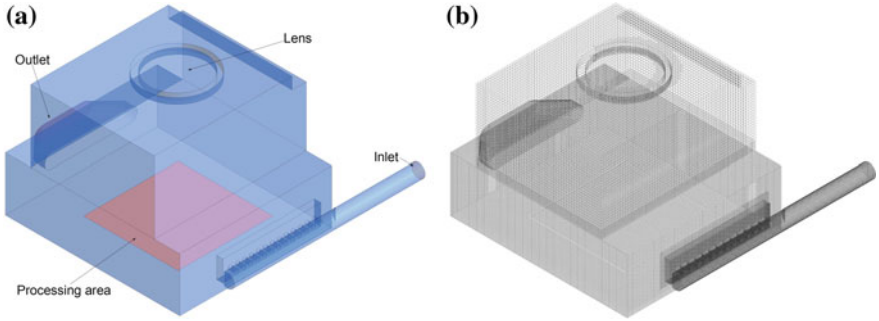

Fig. 3 **a** Fluid volume identifying boundary conditions. **b** 3D shell mesh used for simulations

Validation of Simulation Against Experimental Results

Experimental results were used to guide the development of the argon phase model. Figure 4 shows the final computational model used for simulations against the experimental values for each recorded velocity plane.

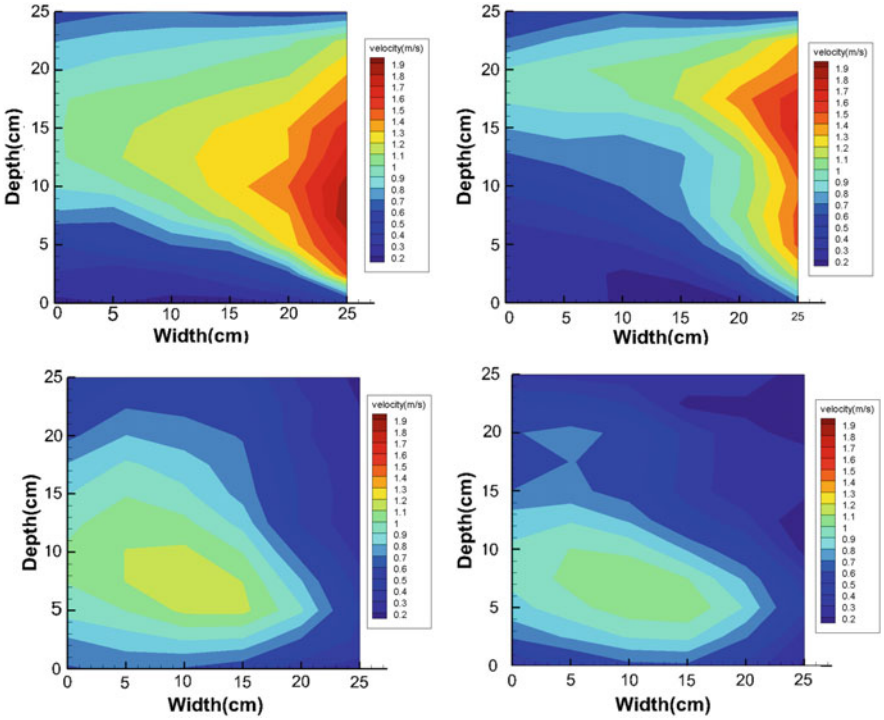

Fig. 4 Experimental (HWA) against simulated (CFD) results; top-left HWA centre plane, top-right CFD centre plane, bottom-left HWA base plane and bottom-right CFD base plane

It can be observed that the velocity distributions produced via a CFD model are comparable with the HWA experimental readings. The simulations accurately capture the general trend of the flow. However, some discrepancies between simulated and experimental results can be observed. This is most likely due to the hopper not being modelled in simulations but was present during experimental readings and the fact that a 3D transitional regime fluid flow is being modelled which includes rapid flow expansions. This model is to be developed for practical engineering purposes and in this sense the differences are seen negligible with respect to their effects on the overall flow field prediction.

Spatter Expulsion Model

To model the accumulation of spatter build up in the AM250 machine a discrete phase model (DPM) was developed to represent spatter expulsion. This model is based on analysing the spatter experimentally instead of solving the complex fluid flow at the scale of the melt pool. These experimental analyses provide the required inputs for the DPM spatter expulsion model which is coupled with the argon phase fluid flow model to determine particulate accumulation. Within the DPM model particle size distributions, velocity values and magnitudes and compositions were imported from the experiments.

A FASTCAM SA4 500K-M1 high speed imaging camera was used to capture the expulsion of spatter for single lines experiments of 316L Stainless Steel. The Photron FASTCAM software was used to optimise the images produced so that moving particles could be highly distinguished for particle analysis. The ImageJ mosaic particle tracking software [8] was used to capture the particle locations and trajectories. From this analysis an in-house matlab script was used to analyse the output files produced from ImageJ to give an approximate velocity distribution for the tracked particles. An outline of the particle tracking is shown in Fig. 5.

In the L-PBF process the powder is sieved before being recirculated back into the system. The oversized particles which remained were analysed using a Malvern Mastersizer where sizes ranged from 60 to 120 μm. In addition, the oversized particles did exhibit a slightly higher oxygen content in comparison to standard 316L SS powder. However, for modelling purposes this was considered negligible. Therefore, in the simulations presented the standard properties of 316L SS were used.

The spatter size, composition and initial particle velocities and magnitudes were then incorporated into a user defined function (UDF) in ANSYS fluent to create a representative spatter expulsion model. 11 lines with 25 mm intervals were set over the processing area to represent the majority of the processing area.

The DPM model used in ANSYS is based on an Euler-Lagrange approach for fluid dynamics. The fluid phase; the argon phase, is treated as a continuum whilst the dispersed phase; the spatter expulsion, is calculated by tracking the particles through the flow field. In the model presented particle-particle interactions are

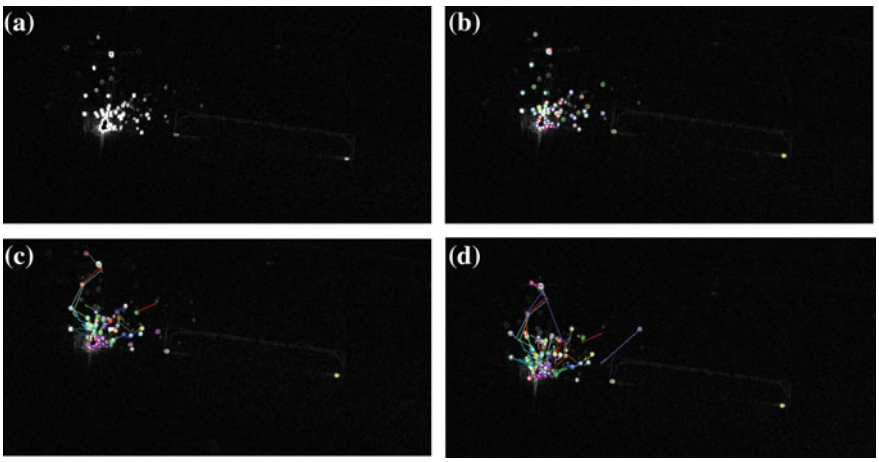

Fig. 5 Particle identification and recorded trajectories analysis of high speed imaging data. **a** Enhanced image. **b** Particle identification. **c** Particle tracking. **d** Extended particle tracking

ignored as this was not observed in experiments. The particles are spherical and non-reacting and there is no biased given to particle velocities based on speed and direction of the laser and is also not dependent on welding mode of the melt pool. In addition, there is two-way coupling between the continuum and dispersed phase, which is required for analysis of particle accumulation on boundaries.

Metal Vapour Plume Model

It is known that when the molten melt pool reaches the vaporisation temperature of the material a phase transformation will occur and mass from the melt pool will be transferred into a metal gas. The modelling approach to predict condensation of particulates within the build chamber was to introduce a separate metal gas phase which has been defined by a mass flow rate. Currently the model is only for one release location due to computational expense. This model will be extended for a mass flow rate along the same 11 release locations as the spatter expulsion model so that a more representative accumulation of the metal vapour condensates can be observed. In the Renishaw AM250 machine a modulated laser is used to melt metal powder. Therefore, the 11 release locations will be a function of laser radius, point distance and exposure time. This model once extended will be able to predict the accumulation of the metal vapour plume condensates within the entire build chamber.

Analysis and Discussion

The shielding gas flow argon phase and spatter expulsion model have been coupled to determine the accumulation of spatter within the build chamber of a Renishaw AM250 machine shown in Fig. 6. An example of the developed metal vapour plume model is also shown in the same figure.

It can be observed that the spatter is generally transported and deposited towards to back end of the machine near the outlet port and towards the outlet end of the processing bed. This is reinforced by powder size distributions of samples taken before and after the build in 3 different locations. Sample 1 was taken underneath the hopper before a build indicating the unprocessed powder. Sample 2 was taken next to the outlet port on the left side of the processing area after a build and sample 3 was taken at the front of the processing area after a build. There is a clear increase in the oversized particles in D10, D50 and D90 fractions in sample 2 shown in Table 1.

The modelling demonstrates the deposition of spatter particulates over the processing area which is highly undesirable. In addition, a recirculation zone can be observed from the flow analysis. This recirculation zone could trap particulates within the machine and be deposited in unwanted areas. Unfortunately this cannot be quantified in an effective manner. The problem is when by-products agglomerate

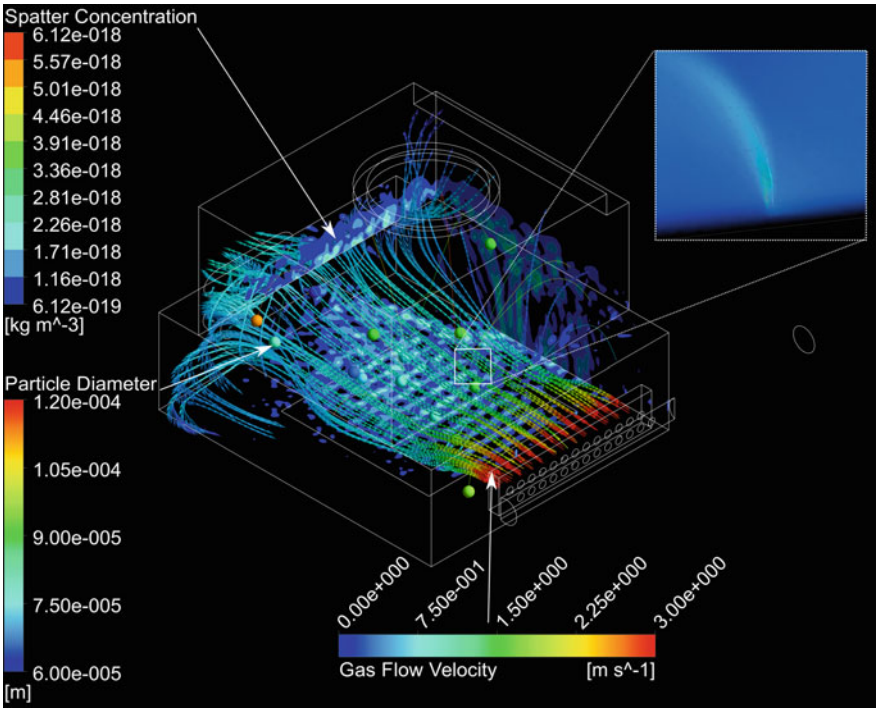

Fig. 6 Outline of shielding gas flow and spatter model with outline of local metal gas plume

Table 1 Powder size distributions of 3 samples taken at different locations

Sample 1			Sample 2			Sample 3		
Under hopper before build			Under outlet after build			At front of plate after build		
D10	D50	D90	D10	D50	D90	D10	D50	D90
18.4 μm	29.0 μm	46.8 μm	30.6 μm	65.7 μm	129.1 μm	18.7 μm	29.5 μm	47.4 μm

on the lens within the chamber which can have similar effects as localised laser attenuation but on a larger scale as the particulates continue to accumulate. Also the flow leaving the inlet is not uniform which is contributing to the inhomogeneous localised gas flow over the processing area again which is undesirable. This model can be used to highlight important performance indicators in the L-PBF process: processing area flow uniformity, localised gas flow velocity and by-products accumulation on walls.

Conclusions

In this work a multiphase computational fluid dynamics model of the shielding gas flow in a laser powder bed fusion process including its by-products has been developed. The shielding gas flow phase and the spatter expulsion model are solved in the Eulerian-Lagrange formulation. The metal vapour phase and the shielding gas flow model are solved in an Eulerian-Eulerian formulation but due to computational limitations are not yet coupled on the scale of the build chamber. The shielding gas flow model is the most important model as its forces will dictate the transport of particulate phases. This model has been validated using experimental results taken using HWA where results are in good agreement and capture the important aspects of the flow field. Both the spatter and metal vapour condensates need to be controlled as they can be detrimental to the final mechanical properties of an L-PBF component. In the model presented it allows for analysis of important flow properties of the shielding gas flow, namely localised velocity and flow uniformity. It also allows for a characterisation of spatter accumulation within all boundaries in the machine and also the visualisation of recirculation zones which are not favourable in the L-PBF process. The future of this work aims to extend the metal vapour model for more representative release locations and then use these models as a design tool to develop and test future design iterations of L-PBF machines with the aim of removing and or controlling the produced by-products.

Acknowledgements The authors would like to thank the Additive Manufacturing Products Division at Renishaw Plc., and the Engineering Doctoral Training schemes MATTER (ESPRC funded) and Materials and Manufacturing Academy M2A (European Social Fund). In addition, the authors would like to acknowledge the Centre for Materials Advanced Characterisation (MACH1) for the use of state-of-the-art equipment funded by the Welsh Government and the Advanced Sustainable Manufacturing Technologies (ASTUTE 2020) funded by the Welsh European Funding Office.

References

1. Liu Y, Yang Y, Mai S, Wang D, Song C (2015) Investigation into spatter behavior during selective laser melting of AISI 316L stainless steel powder. Mater Des 87:797–806
2. Simonelli M, Tuck C, Aboulkhair NT, Maskery I, Ashcroft I, Wildman RD, Hague R (2015) A study on the laser spatter and the oxidation reactions during selective laser melting of 316L stainless steel, Al-Si10-Mg, and Ti-6Al-4V. Metall Mater Trans A 46(9):3842–3851
3. Ferrar B, Mullen L, Jones E, Stamp R, Sutcliffe CJ (2012) Gas flow effects on selective laser melting (SLM) manufacturing performance. J Mater Process Technol 212(2):355–364
4. Bin Anwar A, Pham QC (2017) Selective laser melting of AlSi10 Mg: effects of scan direction, part placement and inert gas flow velocity on tensile strength. J Mater Process Technol 240:388–396
5. Ladewig A, Schlick G, Fisser M, Schulze V, Glatzel U (2016) Influence of the shielding gas flow on the removal of process by-products in the selective laser melting process. Addit Manufact 10:1–9
6. Masmoudi A, Bolot R, Coddet C (2015) Investigation of the laser–powder–atmosphere interaction zone during the selective laser melting process. J Mater Process Technol 225: 122–132
7. Ding J, Colegrove P, Martina F, Williams S, Wiktorowicz R, Palt MR (2015) Development of a laminar flow local shielding device for wire+arc additive manufacture. J Mater Process Technol 226:99–105
8. Sbalzarini IF, Koumoutsakos P (2005) Feature point tracking and trajectory analysis for video imaging in cell biology. J Struct Biol 151(2):182–195

CFD Modelling of High Pressure Gas Atomization of Liquid Metals

Andrew M. Mullis, Aadhithya Priyadharshini Ashok Kumar and Duncan J. Borman

Abstract High pressure gas atomization (HPGA) is a technique for the manufacture of fine spherical metal powders. Supersonic gas jets are used to disrupt a stream of liquid metal into droplets which then solidify in flight. We construct a CFD model for gas flow within a gas atomizer which is compared against high-speed video footage of a research scale atomizer. Good agreement between simulation and experiment is found for the presence of Prandtl-Meyer waves on the surface of the spray cone. The simulation also reproduces the location of the recirculation zone below the melt delivery nozzle. Simulation results indicate a radially outward flow from the bore of the melt nozzle to the circumferential edge which would facilitate pre-filming.

Keywords High pressure gas atomization · Supersonic flow · Metal powders

Introduction

Close coupled gas atomization (CCGA) is the technique of choice for the production of fine metal powders. The maturing market for additive layer manufacturing (ALM) means that demand for such powders is increasing year-on-year, with BCC estimating that the global market for metal powder shipments will increase from £5.5 bn in 2015 to over £9 bn by 2020. One of the principal advantages of CCGA powders for ALM applications is that, due to their very high degree of sphericity, they display excellent flowability. Obtaining an in-depth understanding of this conceptually simple, but in practice complex, production technique is therefore essential if the increasingly stringent needs of the ALM sector are to be met.

A. M. Mullis (✉) · A. P. Ashok Kumar
School of Chemical and Process Engineering, University of Leeds, Leeds LS2 9JT, UK
e-mail: A.M.Mullis@leeds.ac.uk

D. J. Borman
School of Civil Engineering, University of Leeds, Leeds LS2 9JT, UK

L. Nastac et al. (eds.), *CFD Modeling and Simulation in Materials Processing 2018*, The Minerals, Metals & Materials Series,
https://doi.org/10.1007/978-3-319-72059-3_8

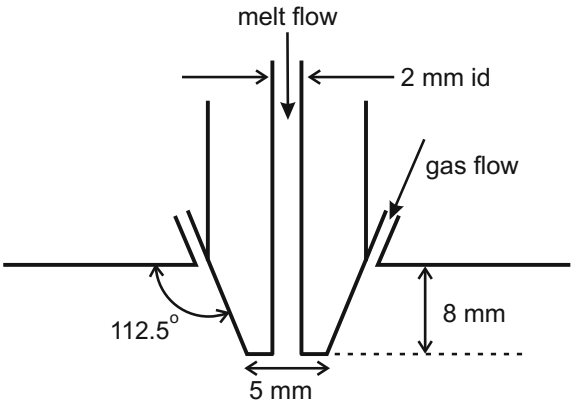

Fig. 1 Schematic diagram of the close-coupled gas atomization configuration used in this study

Figure 1 gives an overview of the CCGA process. Liquid metal is fed down the central bore of a ceramic nozzle, whereupon impinging supersonic gas jets disrupt the stream of molten metal into a spray of fine droplets. These subsequently solidify in flight to yield the powder product. A key aspect of this production route is the process of pre-filming. Upon emerging from the bore of the nozzle, recirculation of the high pressure gas forces the melt to spread out, wetting the nozzle tip. Atomization then occurs at the circumferential edge of the nozzle via the liquid film breakup mode, rather than by the breakup of the liquid column. Droplet size during liquid film breakup is related to the film thickness. Consequently, a much smaller particle size is obtained during primary atomization when compared to liquid column breakup, as would be encountered during free-fall atomization.

The role of pre-filming in atomization has been studied extensively with regard to fuel sprays, particularly in gas turbine engines (see e.g. [1, 2]). However, such studies are much less well developed with regard to the atomisation of liquid metals. Anderson and co-workers have observed that during pre-filming the nozzle tip is not uniformly wet with melt. Rather, there is partial irregular wetting, prompting them to propose a slotted melt delivery nozzle to increase the uniformity of wetting [3]. Using 20 ns pulsed laser illumination, [4] identified that wetting was by means of fine filaments. Fourier analysis techniques have shown that these wetting filaments have a very regular precessional motion [5], the frequency of which depends upon the nozzle design and the physical properties of the melt. Recently, pressure swirl nozzles have been proposed by [6] as a means of improving pre-filming during CCGA.

The purpose of this paper is to use CFD modelling in the region near the atomization nozzle to help to elucidate the pre-filming process. Such techniques have previously been used investigating phenomena such as the formation of Mach disks and oblique shocks [7], aspiration pressure [8, 9] and wake-closure [10–12]. We also present the results of experimental work based on high-speed filming of the gas atomization process, which serve as a validation of the computational models.

Computational Methods

Solutions to the equations for mass, energy and momentum conservation were obtained using a finite volume approach within the CFD package ANSYS Fluent 17. The SST k-ω turbulence model has been used here, although as shown by [13] the results are relatively insensitive to the choice of turbulence model used. The governing equations were solved for the r-z components of a cylindrical system which is independent of φ. A number of authors [7, 10, 11] have previously shown this to be a reasonable approximation for the simulation of gas flow in CCGA. The SIMPLE algorithm was applied with an implicit 2nd order upwind scheme to solve the governing equations.

The computational domain is shown in Fig. 2, with flow being from left to right. High pressure gas is fed into the atomizer via an annular slit. The left hand end of the melt nozzle is a constant pressure boundary condition allowing flow to be drawn down the bore of the nozzle by the aspiration pressure generated by the supersonic gas jets. However, to simplify the calculation, this is considered to be the same fluid as the high pressure gas. Consequently, once the low pressure fluid entering the domain via the melt nozzle merges with the high pressure fluid entering via the gas die the two become indistinguishable. No attempt is made to track the fluid entering via the melt nozzle after the two merge.

The outlet of the domain was taken as a constant pressure condition at atmospheric pressure, allowing the gas to exit the domain. The outer boundaries for the chamber, melt delivery nozzle and the gas die were all considered as a walls with a no-slip velocity boundary condition. For the upper boundary two models were considered, a wall with no-slip condition and an atmospheric pressure outlet. Simulations were undertaken for both types of boundary condition. It was found that, provided the upper boundary was sufficiently far from the gas outflow, the model was insensitive to this choice. A wall boundary was adopted here as this improved convergence speed. All boundaries were maintained at 300 K.

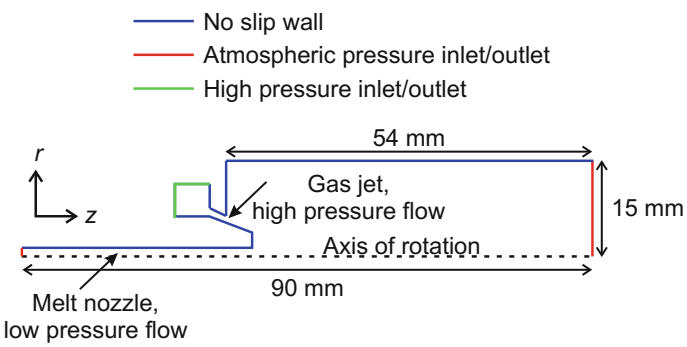

Fig. 2 Computational domain used in the CFD simulations of gas atomization

The mesh used in this study contained 23,000 elements, this having been found to be a suitable number to ensure complete mesh independence of the solution. Transient solutions were performed for inlet gas pressures between 1.0 and 3.0 MPa. The flow pattern in all cases rapidly obtained steady-state after the decay of the initial transient.

Experimental Methods

Atomization experiments were conducted on a research scale atomizer using 6 kg batches of 17–4 PH grade stainless steel. The nozzle configuration was as shown schematically in Fig. 1, with an atomizing gas pressure of 2.5 MPa. The melt was superheated by 200 K, giving a melt temperature prior to ejection of $\sim$1900 K. Consequently, the atomization spray cone was sufficiently bright for filming to take place in radiant light only. External lighting was not required.

Filming was performed using a Photron high speed camera operating at 16,000 frames per second. This was fitted with high magnification optics which gave an equivalent resolution of 82.5 μm per pixel. Each pixel had an 8-bit grey level depth.

Individual frames show a range of complex and chaotic behaviors which make comparison with steady-state simulation difficult. For this reason the following procedure is adopted. We label the grey level intensity in each frame as I_{ij}^{n}, where i, j label the pixel rows and columns respectively and n labels the frame number. We then construct the following two quantities.

$$\bar{I}_{ij} = \frac{1}{N}\sum_{n=1}^{N} I_{ij}^{n} \tag{1}$$

$$\dot{I}_{ij} = \frac{1}{2N}\sum_{n=1}^{N} \left| I_{ij}^{n+1} - I_{ij}^{n-1} \right| \tag{2}$$

The interpretation of Eq. (1) is straightforward, $\bar{I}_{ij}$ is the time averaged grey level intensity and as such gives a measure of the mean quantity of material at location i, j. With regard to Eq. (2), $\frac{1}{2}\left[I_{ij}^{n+1} - I_{ij}^{n-1}\right]$ is a measure of the rate of change in the intensity at location i, j for frame n. The absolute value of this rate of change is then averaged over N frames to give $\dot{I}_{ij}$. On the assumption that we were viewing a relatively disperse suspension of hard spheres under uniform lighting conditions, I would change only as a consequence of the motion of particles. Consequently $\dot{I}_{ij}$ would represent a map of the scaled particle velocities. Unfortunately, when viewing an atomization spray cone this is not the case. Typically we are viewing

features that are actually agglomerates[1] of particles. Consequently, not only do they move between frames but they do not preserve their shape. They are also cooling as they move so the illumination is changing. Moreover, because we are looking through a dense plume features often move in front of each other, merge or split apart. However, as both the dispersion of these particle agglomerates and their cooling rate will be strong functions of velocity, we contend that $\dot{I}_{ij}$ still gives information regarding the relative velocity within the spray cone.

Results

Figure 3 shows a typical result from the CFD simulations, while Fig. 4a, b show the maps for $\bar{I}_{ij}$ and $\dot{I}_{ij}$ obtained from the high speed video for $N = 1000$. Various features visible in the computational simulations are mirrored in the experimental results, indicating that the simulation captures many of the salient points of the atomization process. In particular, we note that the outer envelope of the time-averaged intensity, effectively the average shape of the spray cone, clearly shows the Prandtl-Meyer wave evident in the gas only simulation. We also note, with reference to Fig. 4b, the recirculation zone immediately below the nozzle tip which, on average, displays very low velocity. Again this is clearly also present in the simulations. By comparing Fig. 4a, b it can also be seen that the stagnation zone contains the highest density of material, as gauged by optical intensity. This is because there is a constant feed of material from the melt delivery nozzle but the material is not easily able to escape the stagnation zone. Of course, being single phase, this is not captured by the simulation. However, it is also clear from Fig. 4b that once material escapes the stagnation zone it rapidly streams away from the nozzle, again in good agreement with the simulation results.

Figure 5 shows detail from the near tip region of the melt delivery nozzle, allowing some conclusions to be drawn regarding the likely occurrence of pre-filming. The light blue colour, corresponding to a linear velocity around 50 m s^{-1}, clearly indicates a flow of material down the central bore of the melt delivery nozzle. Immediately below the bore the dark blue colour indicates a region of stagnant gas, indicating that material emerging from the bore would be unlikely to experience liquid column flow. Instead, the stream from the central bore of the nozzle is directed towards its circumferential edge where it connects with the high velocity gas stream. However, this is not quite the flow that would result in true

[1]We use the term agglomerate here to denote a group of particles co-located in space. We do not imply any form of bonding between the individual particles, as would for instance be the case in an aqueous suspension.

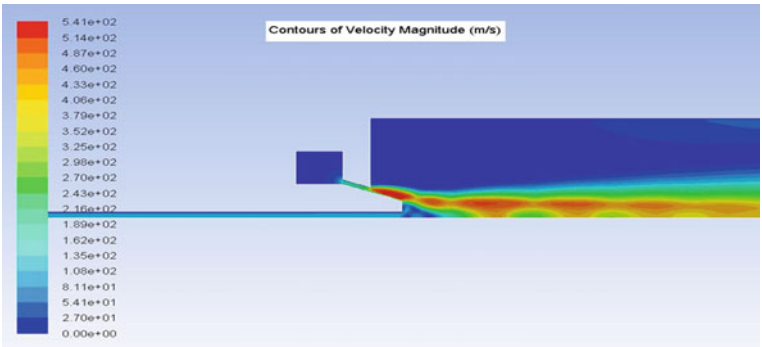

Fig. 3 CFD simulation of gas flow during close-coupled gas atomization. Colour bar gives gas velocity in units of m s^{-1}

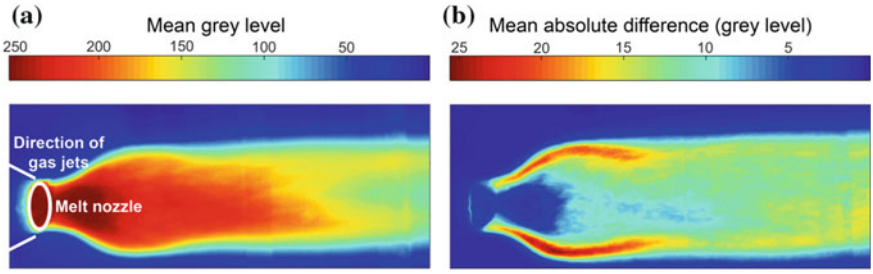

Fig. 4 **a** Mean grey level and **b** mean absolute rate of change in grey level between frames, as determined from high speed video footage of gas atomization. Annotation on part (**a**) shows the position of the flat tip of the melt delivery nozzle, all of which is wet with melt, and the direction of the incoming gas jets

pre-filming, as the flow is not connected to the surface of the nozzle tip. It is not clear at the moment whether this is an artefact of the model or whether the surface tension of the second fluid is an essential ingredient in true pre-filming.

With regard to the experimental data, we note in Fig. 4b the lobes at the margins of the spray cone where $\dot{I}_{ij}$ is high. These appear to originate close to the circumferential edge of the nozzle. As such they may be indicative of the flow of material as it is stripped off the nozzle following pre-filming. These two high velocity lobes coincide with regions of relatively low average material density in Fig. 4a. Coupled with the high density of material in the recirculation zone this is likely to indicate that pre-filming is not complete and that some material is fed directly from the central bore of the nozzle into the recirculation zone.

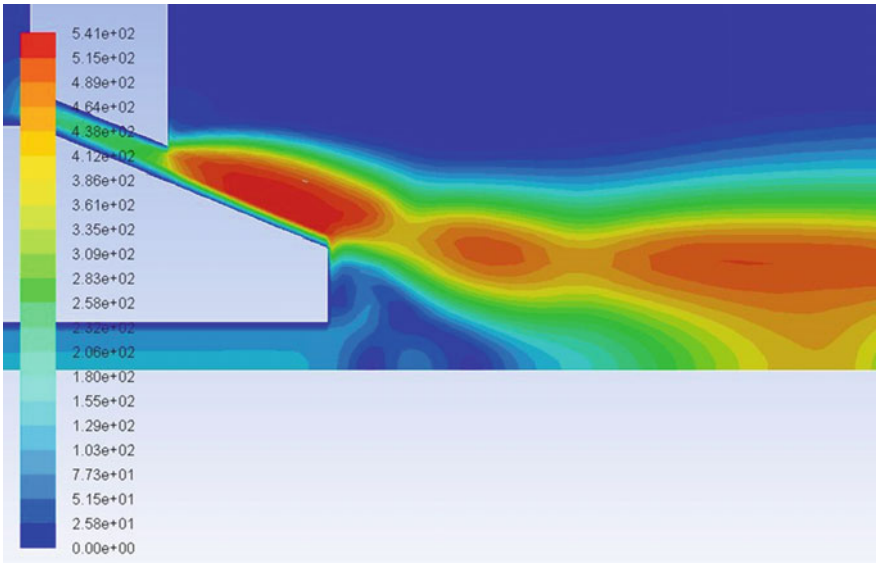

Fig. 5 Detailed view of the CFD simulation in the vicinity of the melt delivery nozzle. Note flow contours that indicating that flow from the nozzle bore will be directed towards the circumferential edge of the nozzle, suggesting the likelihood of pre-filming. Colour bar gives gas velocity in units of m s^{-1}

Summary and Conclusions

A CFD model of gas flow within a close-coupled gas atomizer has been constructed and compared against experimental data obtained from high-speed filming of the atomizer. Good agreement is found between the simulations and the time-averaged experimental data with regard to features such as Prandtl-Meyer waves and the recirculation zone. The simulation displays near nozzle flow patterns that appear to be indicative of pre-filming behaviour. High velocity lobes are observed in the experimental data that appear to coincide with regions of relatively low particle density in the spray cone. Together with a high density of material in the recirculation zone this appears to suggest only partial pre-filming may be occurring experimentally.

Acknowledgements This research was supported under MAPP: EPSRC Future Manufacturing Hub in Manufacture using Advanced Powder Processes (EP/P006566/1).

References

1. Strasser W, Battaglia F (2016) The effects of retraction on primary atomization in a pulsating injector. Proc ASME Int Mech Eng Congr 7A:V07AT09A043
2. Gepperth S, Guildenbecher D, Koch R, Bauer HJ (2010) Pre-filming primary atomization: experiments and modelling. In: 23rd annual conference on liquid atomization and spray systems, Brno, Czech Republic, September 2010
3. Anderson IE, Terpstra RL, Rau S (2001) Progress toward understanding of gas atomisation processing physics. In: Bauckhage K, Uhlenwinkel V (eds) Spray forming, kolloquium band 5, books on demand GmbH, Norderstedt, 2001, pp 1–16. ISBN 3-88722-508-2
4. Mullis AM, McCarthy IN, Cochrane RF (2011) High speed imaging of the flow during close-coupled gas atomisation: effect of melt delivery nozzle geometry. J Mater Process Technol 211:1471–1477
5. Mullis AM, Adkins NE, Aslam Z, McCarthy IN, Cochrane RF (2008) High frame rate analysis of the spray cone geometry during close-coupled gas atomization. Int J Powder Metall 44:55–64
6. Anderson IE, Achelis L (2017) Two fluid atomization fundamentals in deposition. In: Henein H, Uhlenwinkel V, Fritsching U (eds) Metal sprays and spray deposition. Springer, Cham, pp 49–88. ISBN 978-3-319-52687-4
7. Mi J, Figliola RS, Anderson IE (1996) A numerical simulation of gas flow field effects on high pressure gas atomization due to operating pressure variation. Mater Sci Eng A 208: 20–29
8. Mi J, Figliola RS, Anderson IE (1997) A numerical investigation of gas flow effect on high pressure gas atomization due to melt tip geometry variation. Metall Mater Trans B 28: 935–941
9. Xinming Z, Xu J, Zhu X, Zhang S (2009) Effect of atomization gas pressure variation on the gas flow field in the supersonic gas atomization. Sci China Ser 52:3046–3053
10. Ting J, Anderson IE (2004) Computational fluid dynamics investigation of wake closure phenomena. Mater Sci Eng A 379:264–276
11. Tong M, Browne DJ (2009) Modelling compressible gas flow near the nozzle of a gas atomiser using a new unified model. Comput Fluids 38:1183–1190
12. Motaman S, Mullis AM, Cochrane RF, Borman DJ (2015) Numerical and experimental investigation of the effect of melt delivery nozzle design on the open- to closed-wake transition in closed-coupled gas atomization. Metall Mater Trans B 46:1990–2004
13. Motaman S, Mullis AM, Cochrane RF, McCarthy IN, Borman DJ (2013) Numerical and experimental modelling of back stream flow during close-coupled gas atomization. Comput Fluids 88:1–10

Computational Analysis of Thermo-Fluid Dynamics with Metallic Powder in SLM

Subin Shrestha and Kevin Chou

Abstract Selective Laser Melting (SLM) is a powder bed additive manufacturing (AM) process. The metallic powder particles are subject to melting-solidifying along each line scanning which consequently results in intense thermo-capillary convection within the melt pool. Therefore, in order to accurately capture the fluid dynamics, discrete powder particles should be properly modelled. In this study, a 3D thermo-fluid model using the volume of fluid approach with powder particles incorporated was developed using ANSYS/FLUENT. A sequential powder adding algorithm was utilized to generate randomly dispersed particles of a given size distribution in a powder bed. As a result of continuous melting and solidification, the temperature distribution, the molten metal flow, and the free-surface formation can be numerically analyzed. The influence of sequential addition of powder particles to the transport phenomena can be studied and the mechanisms of different pore formation investigated. When the powder particles are melted, the formed melt pool would solidify to form the single track and its density depends on the process parameters. The high speed, 1600 mm/s, of laser would result in less dense tracks with numerous pores would further aggravate with increasing layers.

Keywords Powder distribution · Selective laser melting · Thermo-fluid model

Introduction

Additive manufacturing (AM) is a process in which parts are built in a layer by layer fashion. Selective Laser Melting (SLM) is one of the most applied powder bed AM process in which parts are fabricated by selectively melting powder:

S. Shrestha · K. Chou (✉)
Additive Manufacturing Research Center, University of Louisville, Louisville, KY 40292, USA
e-mail: kevin.chou@louisville.edu

S. Shrestha
e-mail: subin.shrestha@louisville.edu

L. Nastac et al. (eds.), *CFD Modeling and Simulation in Materials Processing 2018*, The Minerals, Metals & Materials Series,
https://doi.org/10.1007/978-3-319-72059-3_9

the moving laser strikes the powder layer and immediately melts the powder. The powder then solidifies in the wake of beam due to various forms of heat transfer and forms a solidified track with certain width and height.

As there is continuous flow of energy through heat transfer and mass through melt flow, we may say that the inherent characteristics associated during the melting of powder in SLM process is temperature distribution and the melt pool size. Therefore these characteristics should be known before completely understanding other underlying properties as most other features depend on their occurrence. Moreover, the end parts of SLM process is highly dependent on the process parameters selected and it is always desired to optimize the process parameters. To achieve this, numerous experimental studies have been performed [1, 2]. The SLM process occurs line by line in each layer and therefore the property of final part strongly depend on the property of each scan track [3]. Childs et al. [4] pointed out that resultant single track may have different forms: continuous track with crescent or elliptical section, discontinuous which may be irregularly broken or balled or only partially melted. These forms depend on the process parameter selected. The balling phenomenon occurs due to the lower wetting ability and is dominant when for lower laser power and higher scanning speed [5, 6]. These single scan track experiments help narrow down the process parameter window that would result in dense part and good surface finish.

Experimental study shows the end results, that is track geometry and surface profile from various combinations of process parameters. But it is desired to know the inherent fluid flow that leads to such phenomena. Therefore, thermo-fluid modeling should be used to study the underlying physics during the melting process. However, the SLM process being powder based, it is important to model the powder particle itself in order to accurately capture the fluid flow and heat transfer. In this regard, there has been a progressive advance towards mesoscopic modelling of SLM process. Khairallah and Anderson [7] demonstrated the ability of predicting the single track formation with the mesoscopic model. The model applied constant surface tension which was good enough to predict the free surface formation. In addition, Lee and Zhang [8] developed a 3D thermo-fluid model using commercial Flow-3D software and back and forth scanning was used to predict the melt flow behavior and formation of tracks. The simulation result obtained after two-track scanning was compared with experiment and the model was able to predict the melt overlap and the depth. Similar modeling approach has also been applied to predict the effect of powder layer thickness on the single track formation [9]. Khairallah et al. [10] improved their model including complex physical phenomenon and elaborated the mechanisms of pore formation, spatter and denudation zones.

The surface is formed by the accumulation of single tracks. Mesoscopic model, being able to predict the single track formation may also be able to predict the overall surface formed after SLM process. Moreover, the average roughness of the build surface may also be possible. The raster scanning applied to mesoscopic model may accurately predict the build surface formation and surface roughness of SLM parts. In the past, there have been some studies on build surface formation in AM processes through continuum model. Dai and Gu [11] developed a 3D continuum model to predict the surface formation during SLM process. Similar model

has also been developed for Powder Bed Electron Beam Additive Manufacturing (PB-EBAM) process [12].

In this study, a 3D powder scale VOF model was developed to predict the single track formation during SLM process. A moving-volumetric Gaussian heat source is applied to randomly distributed powder over solid substrate. The applied heat source immediately melts the powder and the solidified track is formed at the wake of beam. The thermo-fluid dynamics is studied to understand the formation of single track in SLM process. Moreover, a two layer simulation is performed to predict the formation of interlayer pores.

Numerical Modeling Approach

Powder Scale Model

A 3D model with domain size 1600 µm × 500 µm × 150 µm is developed as shown in Fig. 1 to perform single layer single track simulation. The powder particles are defined by using sequential powder addition algorithm [13]. With this algorithm, random powder distribution can be obtained which would statistically represent the actual powder bed condition. For this study, the powder size distribution from 20 to 40 µm has been considered. The powder particles are defined over the 90 µm solid Inconel 625 as depicted in Fig. 1 which shows the volume fraction of the Inconel 625 defined over the domain. The blue zone is the argon gas where there is no volume fraction of In625, and therefore the phase-2 volume fraction in this region is 0. The red zone represents both solid base and powder as this is a two phase simulation. And the free surface of the powder lies between volume fraction of 0 and 1. The solid base is designed such that it is bigger than the melt pool depth such that the boundary does not interfere with the melt flow. The scan length of 1.2 mm is used for all single track simulation.

The hexahedral mesh is defined over the domain. In order to make the simulation time reasonable, mesh size of 5 µm was used. The powder particles generated by sequential addition algorithm was read through FLUENT user defined function (UDF).

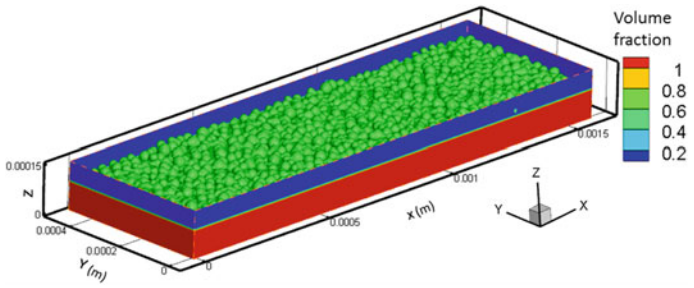

Fig. 1 3D computational domain used for single track simulation

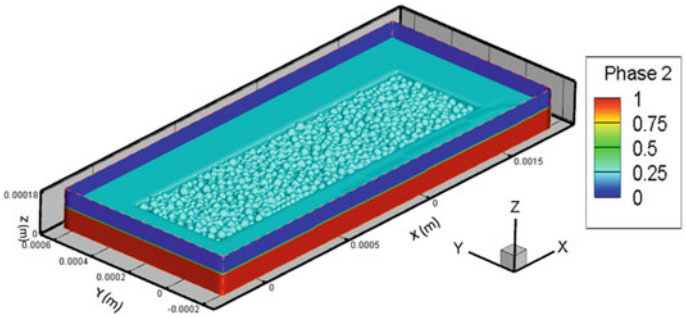

Fig. 2 3D computational domain used for two-layer simulation

For the two layer simulation, the free surface from first layer scanning is obtained and powder particles are spread over the free surface from first layer. Since, the adiabatic boundary condition is defined for all walls in the domain; there would be residual heat during the dwell time for multi-layer simulation. Therefore, the model size was increased to reduce the effect of residual temperature on the second layer simulation. The two-layer model configuration is shown in Fig. 2.

The basic governing equations associated with the Thermo-fluid model have been presented [12]. Adiabatic boundary condition has been defined over all the faces in domain. In this study, VOF model is used to track the free surface. In this model, two phases have been used-argon and Inconel 625. A free surface of the powder which interacts with the argon has the volume fraction between 0 and 1. UDF is used to identify the free surface mesh to appropriately apply the volumetric heat source.

Application of Volumetric Heat Source

The powder being a spherical surface, the free surface should be properly identified in order to apply the volumetric heat source. In addition, the surface is continuously deforming during the melting process. Therefore, the topmost cell with non-zero phase-2 volume fraction which is the actual free surface has to be tracked after iteration which is achieved through UDF. The free surface cell information is stored and utilized to define the magnitude of heat source for other cells.

Material Properties

The physical properties such as thermal conductivity, specific heat, density are the function of temperature. Therefore, the temperature dependent material properties

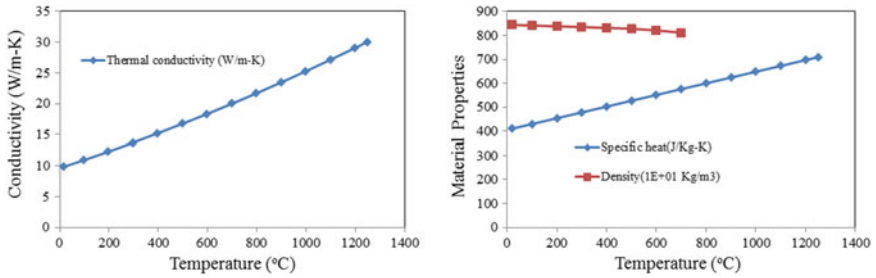

Fig. 3 Temperature dependent material properties of Inconel 625 [14]

Table 1 Properties of Inconel 625

Parameters	Values
Solidus temperature, T_S (°C)	1290
Liquidus temperature, T_L (°C)	1350 15]
Latent heat of fusion, L_f (kJ/Kg)	227
Beam diameter, d (μm)	100
Hatch spacing (μm)	100
Power (W)	195
Viscosity (kg/m s)	0.006
Emissivity, ε	0.5 [16]
Stefan-Boltzmann constant, σ	5.67×10^{-8}

summarized in Fig. 3 are used to define solid and powder Inconel 625. As the properties are almost linear with the temperature, they are defined as piece-wise linear in Fluent. Besides these, surface tension is also the function of temperature. Additional material properties of Inconel 625 have been summarized in Table 1. Generally the surface tension of metal can be defined by the Eq. 1.

$$\gamma = \gamma_m + \frac{d\gamma}{dT}\Delta T \tag{1}$$

where γ is the surface tension, γ_m is the surface tension at the melting point, $\frac{d\gamma}{dT}$ is the surface tension gradient and ΔT is the temperature difference. In this study, only constant surface tension has been considered. Moreover, the surface tension for Inconel 625 has been approximated with that of Inconel 718 [8].

Results and Discussion

Single Layer-Single Track Simulation

As the defined heat source is applied over the powder layer, it immediately melts the powder particles. The melted powder fills the void between powder particles

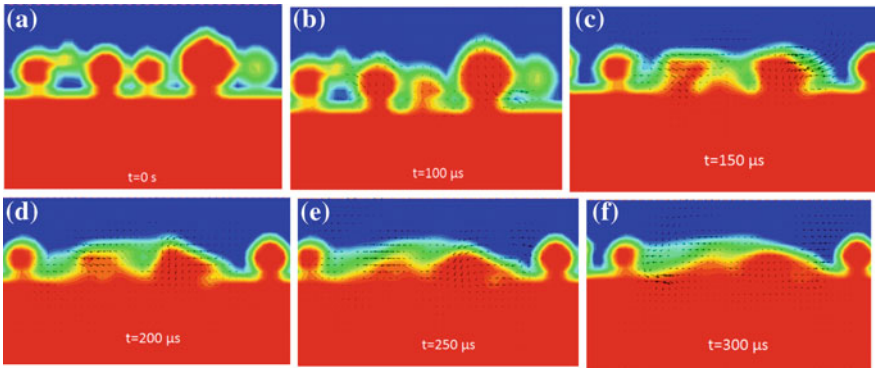

Fig. 4 Melt pool dynamics and formation of track profile at the beginning of single scan

due to the continuous flow of liquid Inconel 625 and the melt pool becomes dense. Figure 4 shows the dynamics of melt pool in transverse plane at the beginning of the scanning with scanning speed of 400 mm/s and power of 195 W, when constant surface tension of material is used. At the initial condition (Fig. 4a), when the heat source is not applied, the powder particles remain solid. As the laser beam is defined, the temperature of the powder increases and the powder starts to melt. The powder particles at the center of the laser beam melts first. Moreover, the smaller powder particles would melt before larger powder particles. As seen from Fig. 4b, the powder particle at the center starts to melt which is then followed by melting of surrounding powder particles. As the melt pool is formed, the flow fills the argon gap between the powders and finally dense melt is formed. This mechanism continues throughout the single scan. When the energy density is very high, the smaller powder particles may face to rapid increment in temperature which may exceed the boiling point of the material. This would result in evaporation and result in formation of depression. In this paper, the evaporation and recoil pressure have not been included and the fluid flow has been simplified.

The temperature distribution and melt formation for scanning speed of 400 mm/s during a single scan track simulation is depicted in Fig. 5. Figure 5a shows the temperature distribution while the laser is still scanning the powder layer. At this point, the maximum temperature is 2900 °C. The scanning continues and after reaching its end point the heat source is no more defined and only heat loss occurs from that point on. The result after scanning and cooling for some time is shown in Fig. 5b. We may observe that all the melted areas have been solidified as the temperature is below melting point and the single track has formed permanently.

The longitudinal and transverse cross section of the solidified surface has been presented in Fig. 6. These figures with phase volume fraction show that the melting of the powder particles would form a dense single track. Therefore, process simulation with single track would help to identify the process window which would result in dense single tracks. In addition, it is observed that there is a shallow area at the end of the scan track. This may be due to the insufficient flow of melt pool at the

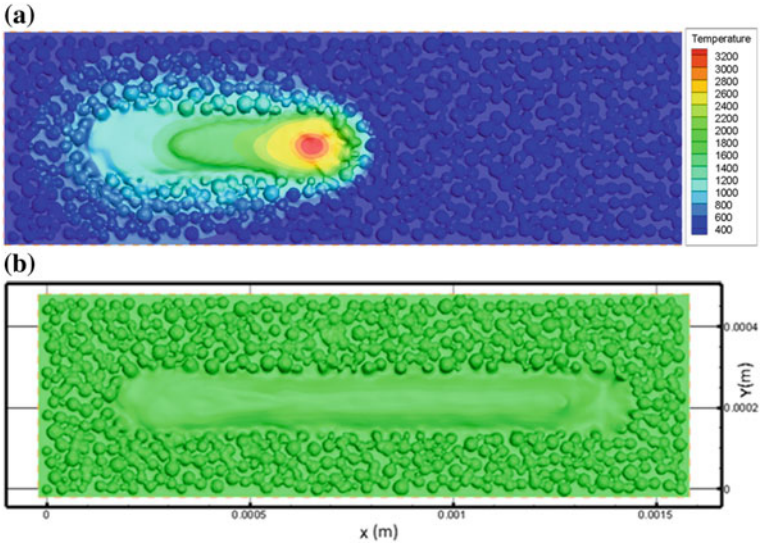

Fig. 5 **a** Temperature distribution (in K) during powder melting and **b** after melting (v = 400 mm/s)

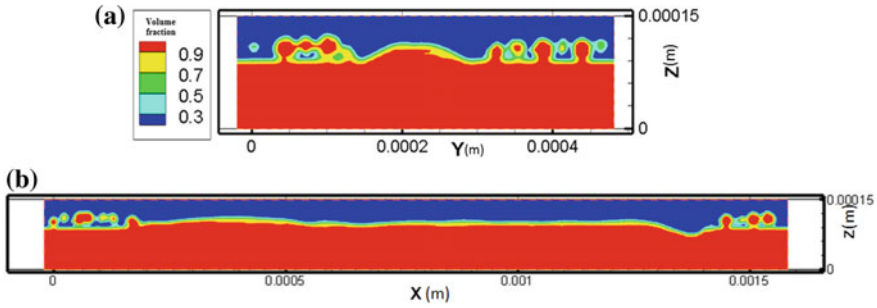

Fig. 6 Transverse and longitudinal cross section of solidified single track (v = 400 mm/s)

end of the scan track. When the laser is turned off, the melt immediately solidifies leaving a shallow region at the end of the scan track. Moreover, if the energy density is too high and shallow depression is formed, this may lead to formation of pores at the end of the scan track.

Two Layer-Single Track Simulations

A single layer single track simulation can be applied to study the effect of different process parameters towards the formation of single track morphology and possible

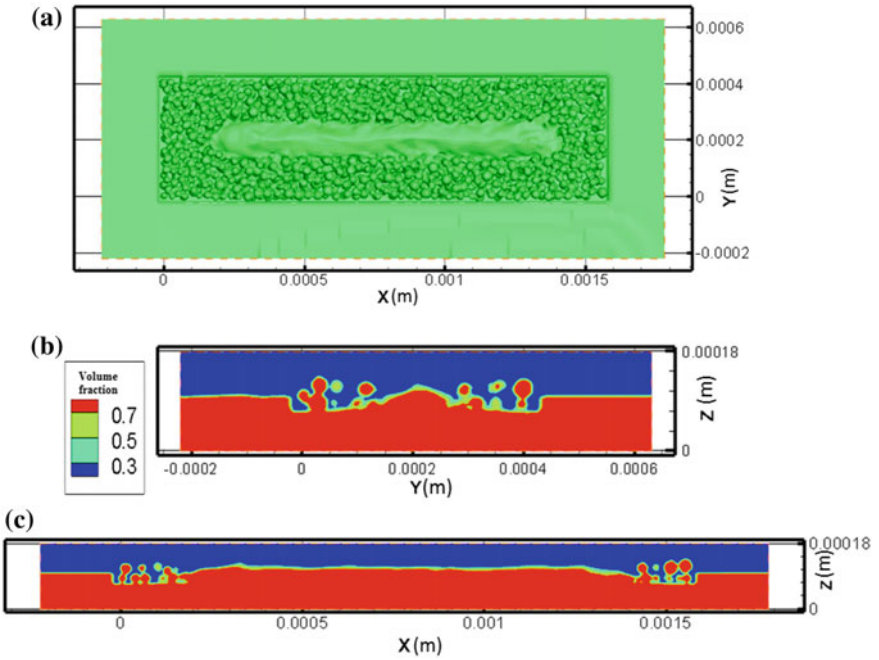

Fig. 7 **a** Solidified single track after second layer scanning, **b** transverse and **c** longitudinal cross section of solidified two layer-single track (v = 800 mm/s)

pores in the surface. However, the SLM process being a layer by layer process, it is necessary to predict the bonding between the layers as well. The solidified track from previous layer would affect the powder particle distribution. Therefore, a two layer simulation is carried out, this time will lower energy density compared to single layer case. At first, 800 mm/s scanning speed is used with 195 W power. The solidified surface and its transverse and longitudinal cross sections have been summarized in Fig. 7. These set of parameters resulted in solid and dense single track as well. It is observed that the track is shallow at the end of the scan track as well, however the morphology of the scan track is different compared to 400 mm/s speed case.

Now, the speed was even doubled to 1600 mm/s to make an extreme case which would probably result in partial melting. With this speed, the maximum temperature was very low, below 1700 °C and therefore there was insufficient melting. As seen from Fig. 8a, the pores are formed in the build surface due to partial melting of powder particles. If the scanning is continued to another layer, then the porosity would get worse. The build surface formation during second layer scanning and the temperature distribution is shown in Fig. 8b.

The low energy density would result in formation of pores in the build surface. The two layer simulation result is presented in Fig. 9. Transverse and longitudinal cross section of volume fraction shows variation in density within the solidified

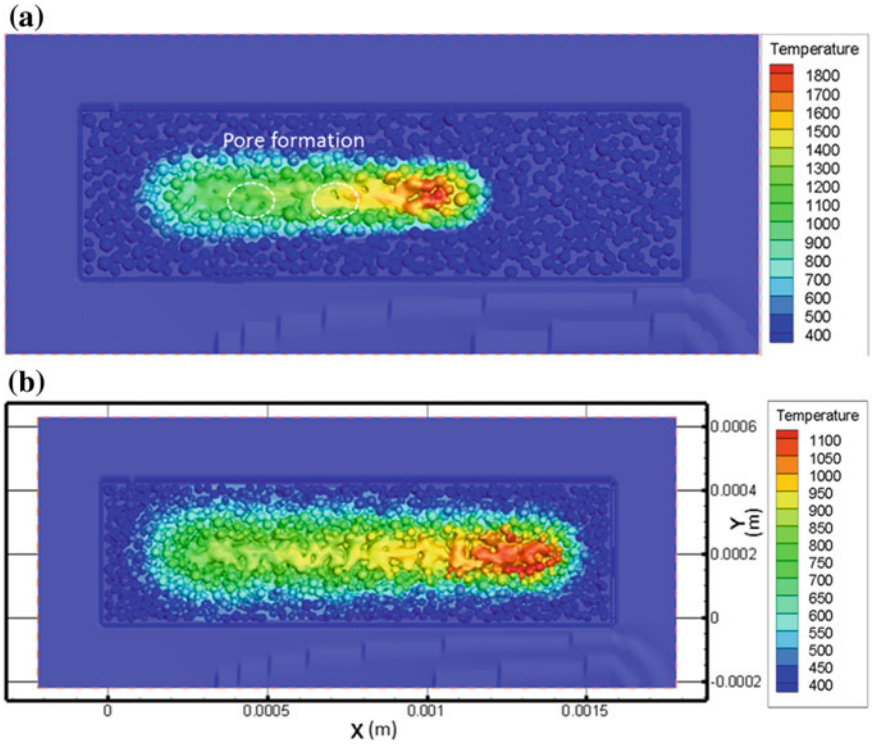

Fig. 8 Temperature distribution during **a** first layer scanning and **b** second layer scanning (v = 1600 mm/s)

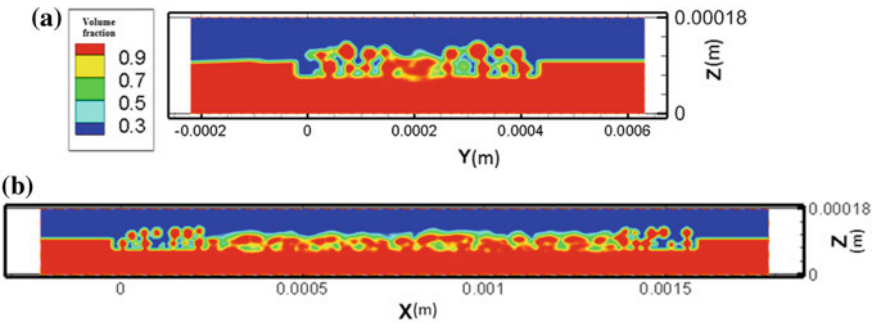

Fig. 9 Transverse and longitudinal cross section of solidified two layer-single track (v = 1600 mm/s)

track. Due to incomplete melting as in previous two cases, there pores are formed, both intra-layer and interlayer. With these set of parameters, the build may fail due to inappropriate bonding between the layers with such case, and if the build is successful, the part would have very low density and high porosity.

Conclusions

In this study, two powder scale models, single layer single track and two layers single track, have been developed to study the fluid dynamics in the melt pool and formation of single track. Different scanning speeds were used to study the temperature distribution, fluid flow and eventually the formation of pores. Based on the simulation results, following conclusions can be made:

- With the appropriate energy density, the single scan tracks formed are dense. The scanning speed of 400 and 800 mm/s resulted in dense scan tracks without porosity.
- When the single track formed are dense, it may be the case that the subsequent layer tracks are also dense as observed from 800 mm/s case.
- The partial melting of powder particles would form both intra-layer pores and interlayer pores and therefore should be avoided during the part build.

Acknowledgements This research is partially supported by NIST (70NANB16H029) and NSF (1662662).

References

1. Kruth J-P, Froyen L, Van Vaerenbergh J, Mercelis P, Rombouts M, Lauwers B (2004) Selective laser melting of iron-based powder. J Mater Process Technol 149(1):616–622
2. Yadroitsev I, Bertrand P, Smurov I (2007) Parametric analysis of the selective laser melting process. Appl Surf Sci 253(19):8064–8069
3. Yadroitsev I, Gusarov A, Yadroitsava I, Smurov I (2010) Single track formation in selective laser melting of metal powders. J Mater Process Technol 210(12):1624–1631
4. Childs T, Hauser C, Badrossamay M (2004) Mapping and modelling single scan track formation in direct metal selective laser melting. CIRP Ann-Manuf Techn 53(1):191–194
5. Li R, Liu J, Shi Y, Wang L, Jiang W (2012) Balling behavior of stainless steel and nickel powder during selective laser melting process. Int J Adv Manuf Technol 59(9–12):1025–1035
6. Dilip J, Anam MA, Pal D, Stucker B (2016) A short study on the fabrication of single track deposits in SLM and characterization
7. Khairallah SA, Anderson A (2014) Mesoscopic simulation model of selective laser melting of stainless steel powder. J Mater Process Technol 214(11):2627–2636
8. Lee Y, Zhang W (2016) Modeling of heat transfer, fluid flow and solidification microstructure of nickel-base superalloy fabricated by laser powder bed fusion. Add Manuf 12:178–188
9. Panwisawas C, Qiu C, Anderson MJ, Sovani Y, Turner RP, Attallah MM, Brooks JW, Basoalto HC (2017) Mesoscale modelling of selective laser melting: thermal fluid dynamics and microstructural evolution. Comput Mater Sci 126:479–490
10. Khairallah SA, Anderson AT, Rubenchik A, King WE (2016) Laser powder-bed fusion additive manufacturing: physics of complex melt flow and formation mechanisms of pores, spatter, and denudation zones. Acta Mater 108:36–45
11. Dai D, Gu D (2015) Tailoring surface quality through mass and momentum transfer modeling using a volume of fluid method in selective laser melting of TiC/AlSi10Mg powder. Int J Machine Tools Manuf 88:95–107

12. Shrestha S, Chou K (2017) A build surface study of powder-bed electron beam additive manufacturing by 3D thermo-fluid simulation and white-light interferometry. Int J Machine Tools Manuf 121:37–49
13. Zhou J, Zhang Y, Chen J (2009) Numerical simulation of random packing of spherical particles for powder-based additive manufacturing. J Manuf Sci Eng 131(3):031004
14. Capriccioli A, Frosi P (2009) Multipurpose ANSYS FE procedure for welding processes simulation. Fusion Eng Des 84(2):546–553
15. Lemster K, Delporte M, Graule T, Kuebler J (2007) Activation of alumina foams for fabricating MMCs by pressureless infiltration. Ceram Int 33(7):1179–1185
16. Kobayashi M, Otsuki M, Sakate H, Sakuma F, Ono A (1999) System for measuring the spectral distribution of normal emissivity of metals with direct current heating. Int J thermophys 20(1):289–298

Evaporation and Diffusion of Mn in Inert Systems

Håkon Aleksander Hartvedt Olsen, Stefan Andersson and Gabriella Tranell

Abstract This research is aimed to improve our knowledge on the dust formation and clustering in the ferroalloy industry. Specifically, this paper focuses on the evaporation of manganese metal, and how different parameters influence the evaporation rate. Experiments were done with pure manganese metal heated to between 1400 and 1700 °C in a pure argon atmosphere, where the change in weight was measured to calculate the loss of manganese over time. A mathematical model was constructed to link theoretical values to the results from the experiments. The high control over the system parameters allowed for the validation, rejection or creation of values and theories used in the model.

Keywords Manganese · Evaporation · Diffusion · CFD

Introduction

Airborne particulate matters, originating from various sources in the metallurgical industry are not only a concern in terms of workers health, but the fumes from industrial plants also contribute to the so-called fugitive emissions which may be harmful to the local, urban communities as well as the environment at large.

The aerosols produced in most metallurgical processes may be harmful if inhaled and exposure to high levels of particles has been linked to cancer, pneumonia,

H. A. H. Olsen (✉) · G. Tranell
Department of Materials Science and Engineering, Norwegian University of Science and Technology, Alfred Getz vei 2, 7491 Trondheim, Norway
e-mail: hakon.a.h.olsen@ntnu.no

G. Tranell
e-mail: Gabriella.tranell@ntnu.no

S. Andersson
SINTEF Materials and Chemistry, P.O. Box 4760 Trondheim, 7465 Trondheim, Norway
e-mail: Stefan.Andersson@sintef.no

L. Nastac et al. (eds.), *CFD Modeling and Simulation in Materials Processing 2018*, The Minerals, Metals & Materials Series,
https://doi.org/10.1007/978-3-319-72059-3_10

chronic obstructive pulmonary disease (COPD) and other respiratory and cardiovascular syndromes [1–5]. Inhalation of certain manganese (Mn) compounds has also been linked to inflammation and neuropsychological disturbances [6–8].

Characteristic properties of the particles, especially particle size and chemical composition, may influence their impact on human health. It is now well known that ultrafine particles (nanoparticles, particles <100 nm) have a much greater surface area and different physic-chemical characteristics [9, 10] compared to their larger counterparts. They may therefore be more reactive, behave differently in the respiratory system, and give rise to increased biological responses [11].

As the chemical composition and morphology (particle shape) of particles originating from different ferroalloy industries and processes vary greatly, it is important to understand the mechanisms of which dusts are generated and how the characteristic properties of the particles depend on process parameters. With such knowledge, primary dust generation may be partially controlled.

An important and not yet thoroughly studied part of the dust formation from liquid manganese alloys such as ferromanganese (FeMn) and silicomanganese (SiMn) is the evaporation and gas-phase diffusion of manganese. In contrast to silicon, which has a very low vapor pressure and will mostly react with oxygen to form dust, manganese evaporates noticeably at temperatures close to the melting point. With silicomanganese, this leads to possible reactions between silicon oxides and manganese fumes, but can also cause a competition for oxygen close to the surface where if no oxygen reaches the surface, one might get no silicon in the dust at all [12]. Because of these reasons, the experimental study and subsequent modelling of evaporation rates of Mn is important.

Model Development

In the production process for ferroalloys such as ferromanganese and silicomanganese, the produced melt is in contact with air during several steps of the process. Most notably during tapping, refining and casting, the melt is exposed to air without a protective slag layer over an extended duration. During this time, there are two possible reactions for each metal in the alloy, Evaporation and oxidation, which may be summed as shown in Eqs. 1 and 2.

$$\mathrm{Me(l)} \Rightarrow \mathrm{Me(g)} \tag{1}$$

$$\mathrm{Me(l)} + \mathrm{xO_2(g)} \Rightarrow \mathrm{MeO_{2x}(s,\,l)} \tag{2}$$

Both reactions are thermodynamically driven towards equilibrium, and the distance from equilibrium is the driving force of the mass flux. This work purely studies reaction 1. for pure manganese, and the equilibrium partial pressure for this reaction is defined as shown in Eq. 3.

$$p_{eq} = \frac{1}{\exp\left(-\Delta G/_{R*T}\right)} \tag{3}$$

where R is the gas constant, T is the temperature in Kelvin, and ΔG is the change in Gibbs free energy. The Gibbs free energy for each side of the equation is calculated as shown in Eq. 4.

$$G = H - TS \tag{4}$$

where S is the entropy and H is the enthalpy of formation. The flux from evaporation at the surface can then be defined as shown in Eq. 5,

$$Flux_{evaporation} = \left(p_{eq} - p\right) * \sqrt{\frac{Mm}{N_A * 2 * \pi * k_B * T}} \tag{5}$$

Here, N_A is Avogadro's number, k_B is Boltzmann's constant, and Mm is the molar mass of Mn. For diffusion, the flux can be defined by Eq. 6,

$$Flux_{diffusion} = D * \frac{\left(n_{eq} - n_{bulk}\right)}{DiffZ} * \frac{Mm}{N_A} \tag{6}$$

where DiffZ is the diffusion layer thickness defined by Eq. 7 [13], D is the diffusion coefficient, and n is the molar concentration of Mn(g) for equilibrium and bulk gas respectively.

$$DiffZ = \frac{L * 4.52}{Re^{1/2} * Sc^{1/3}} \tag{7}$$

Reynold's number and Schmidt's number are defined by Eqs. 8 and 9 respectively. L is here defined as the radius of the crucible, v is the viscosity, v is the bulk flow velocity, D is the diffusion coefficient and ρ is the density of the gas.

$$Re = \frac{v * L * \rho}{v} \tag{8}$$

$$Sc = \frac{v}{D * \rho} \tag{9}$$

In order to model the evaporation and diffusion kinetically, diffusion coefficients for Mn and Ar gas as well as a Mn–Ar gas mixture were derived from Chapman-Enskog kinetic theory [14] based on Lennard-Jones parameters for Ar–Ar and a Morse potential used to describe the Mn–Mn and Mn–Ar interactions. The Ar–Ar parameters were taken from the literature [14] whereas the Mn–Ar and Mn–Mn interaction potentials were evaluated by high-level quantum chemical calculations. Coupled cluster with single and double excitations with a perturbative

treatment of triple excitations [CCSD(T)] [15] calculations were applied to Mn–Mn and Mn–Ar pair interactions at a range of separation distances (3–7 Å) using the CFOUR program package [16]. These results were subsequently fitted to Morse potentials, respectively, since the Lennard-Jones potential was found not to reproduce the calculated interaction energy curves well enough. Expressions and values of collision integrals for calculating diffusion coefficients for the two types of potential were taken from literature [14, 17].

The model for the evaporation was created in two parts: One that calculated the flux of vaporization using thermodynamic and kinetic data, and one that calculated the diffusion flux from flow conditions and kinetic theory. For each temperature and flow rate investigated experimentally (see Section "Experiments"), the gas velocity over the metal surface was calculated using a Comsol model. The model uses finite element analysis, assuming steady state and incompressible flow, and using laminar flow conditions as the calculated Reynold's number for the relevant area is less than 100. The mesh used is shown in Fig. 1, it can be noted that a finer mesh is used near the metal surface. For the surfaces, no slip is the assumed boundary condition, and for each element, a form of the Navier-Stokes equation and the continuity equation are solved. The exact equations solved are shown in Eqs. (10) and (11) [18].

$$\rho(\boldsymbol{u} \cdot \nabla)\boldsymbol{u} = \nabla\left[-\mathrm{p}\mathbf{I} + \mu\left(\nabla\mathbf{u} + (\nabla\mathbf{u})^{T}\right)\right] + \boldsymbol{F} \tag{10}$$

$$\rho\nabla \cdot (\mathbf{u}) = 0 \tag{11}$$

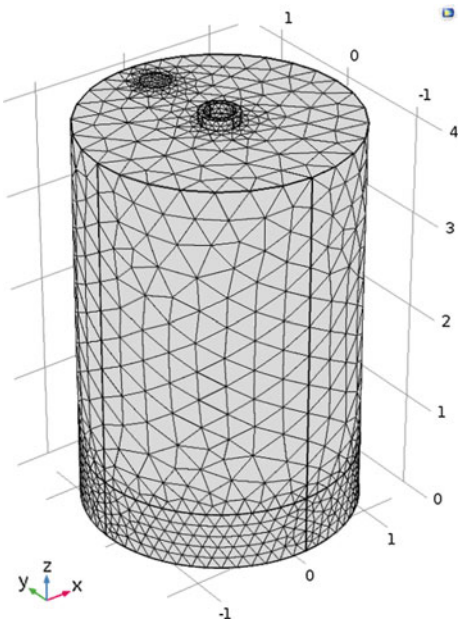

Fig. 1 The mesh used in the comsol model. It has a total of 36587 domain elements, 4286 boundary elements, and 395 edge elements

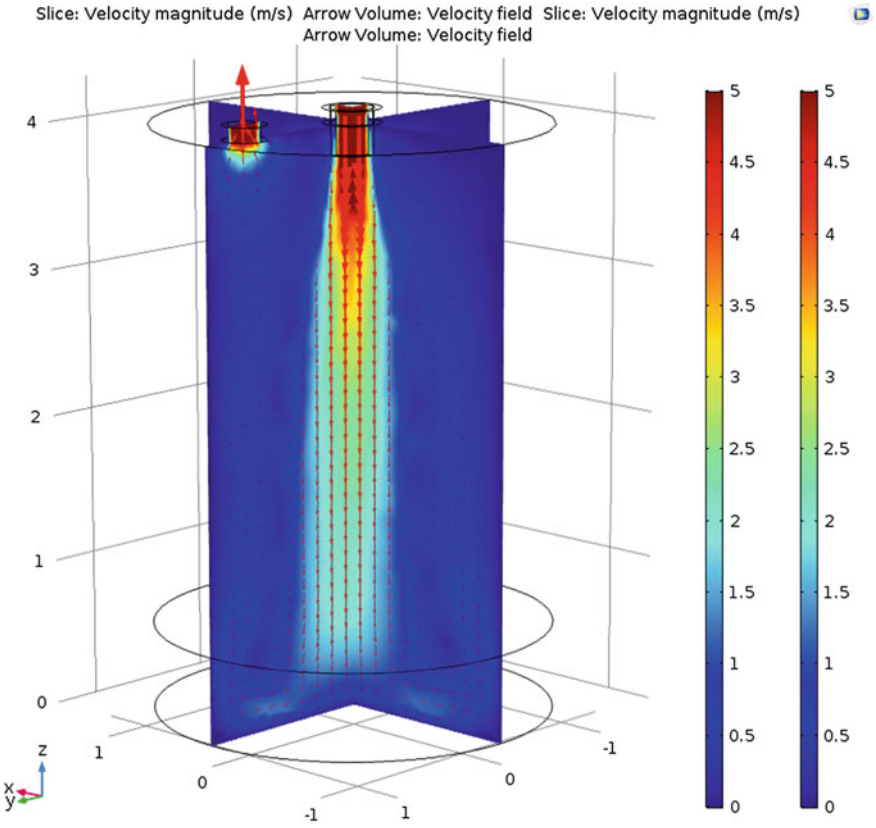

Fig. 2 Flow conditions inside crucible, model made using Comsol software. Conditions assumed: laminar flow, no slip boundaries, incompressible flow, steady state. This image was from an experiment with T = 1550 °C and 0.5 l/min flow rate

where **u** is the velocity field, ρ is the density, μ is the dynamic viscosity, p is the pressure, **F** is the external force, and **I** is the identity matrix. The flow pattern for one experiment is shown in Fig. 2, with Fig. 3 showing a more detailed image of the flow pattern close to the metal surface.

The thermodynamic data used in the model was taken from NIST-JANAF Thermochemical Tables [19], where values for gases below boiling temperature were extrapolated from the data given. The extrapolated data was found not to deviate much at 1400 °C. Other parameters used in the model are listed in Table 1.

These two parts are both dependent on the partial pressure of Mn(g) just above the surface of the metal. We know however, that under stable conditions, there is a constant flux of vapour from the surface to the bulk phase, which means the flux from metal to diffusion layer and through the layer to the bulk must be equal. Using the solver function in Excel, the partial pressure at which these two fluxes are equal can then be found, which gives the total flux through the system.

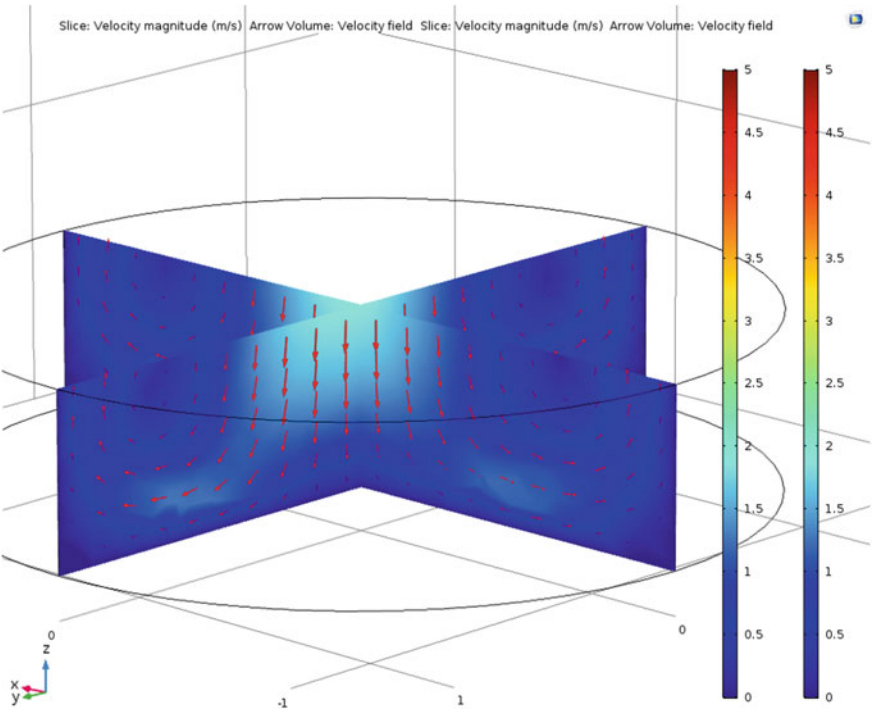

Fig. 3 Flow conditions near the metal surface, model made using Comsol software. Conditions assumed: laminar flow, no slip boundaries, incompressible flow, steady state. This image was from an experiment with T = 1550 °C and 0.5 l/min flow rate

Table 1 Parameters used in the model

Parameter	Value
L	0.0135 m
Mm_{Mn}	0.054938 kg/mol
v	$8.42 - 7.87 \times 10^{-5}$ Pa*s
D	$2.93 - 3.97 \times 10^{-4}$ m^2/s
ρ	0.246 − 0.290 kg/m^3

Experiments

The apparatus used for the experiments was a graphite tube furnace, the design which is sketched in Fig. 4. The inside of the furnace was kept in an 6 N argon atmosphere of around 1.3 bar to avoid oxidation. Inside the graphite tube, an alumina crucible with height 40 mm and diameter 27 mm was used as the container for the experiments. The crucible was fitted with a lid to further limit contamination from the surrounding atmosphere, and an alumina paste was used to seal the lid. An alumina tube with inner diameter of 3 mm was inserted into a hole in the center of

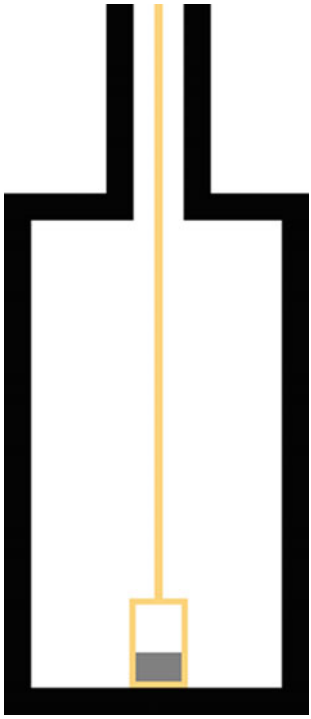

Fig. 4 Sketch of the experimental setup. An outer tube of graphite with an inner alumina crucible and tube connected to an argon source. The atmosphere inside the tube was purged with argon before and during the experiments, and argon was blown at different rates through the tube in each experiment

the lid, through which argon was blown into the crucible. Another hole in the lid with diameter 3 mm was the only outlet in the system. Figure 5 shows a crucible after a finished experiment, without the alumina tube.

The crucible was filled with 15 (±0.5) grams of 99.9% Mn chips. The chips had a slightly tarnished, oxidized surface before the experiments and as such, there was a small amount of oxide present in the experiments. However, as a first approach, this was assumed not to affect the evaporation rate. Each sample was pre-treated at 150 °C for 30 min to remove any humidity from the sample and the sealing paste, and the crucible set-up was weighted before and after pre-treatment as well as after the experiment. Longer pre-treatment time or higher temperatures were found not to produce any further weight loss in the sample.

The sample was inserted into the furnace, which was then vacuumed to between 80 and 200 mTorr before it was purged with argon and kept at around 1.3 bar. After purging, the chamber was heated to the desired temperature over 30 min and held at that temperature for further 60 min before being cooled. During the entire heating, holding and cooling period, argon was inserted through the alumina tube at a constant flowrate. The different temperatures and flowrates for each experiment are shown in Table 2.

Fig. 5 Alumina crucible after finished experiment. The middle hole was used for the alumina tube, while the smaller hole was used as the outlet for the gas and vapor

Table 2 Flow rates, temperatures, holding times, and Sample contents for the experiments

Exp #	Ar flow rate (l/min)	Temp (°C)	Holding time (min)	Sample content
10	0.0	1400	60	100% Mn
5	0.5	1400	60	100% Mn
7	1.0	1400	60	100% Mn
2	0.0	1550	60	100% Mn
12	0.25	1550	60	100% Mn
3	0.5	1550	60	100% Mn
6	0.5	1550	60	100% Mn
1	1.0	1550	60	100% Mn
4	1.0	1550	60	100% Mn
8	0.0	1700	60	100% Mn
11	0.5	1700	60	100% Mn
9	1.0	1700	60	100% Mn
13	1.0	1700	60	100% Mn

After cooling, the crucible weight was again measured and the mass loss calculated. As the only reaction happening was evaporation of Mn, the flux of Mn out of the system could be calculated for each experiment.

Table 3 Experimental results: Total mass loss and flux for each set of parameters

Exp #	Ar flow rate (l/min)	Temp (°C)	Loss (g)	Flux (g/m^2s)
10	0.0	1400	−0.11	−0.07
5	0.5	1400	0.40	0.25
7	1.0	1400	1.00	0.61
2	0.0	1550	0.07	0.04
12	0.25	1550	0.78	0.48
3	0.5	1550	1.66	1.02
6	0.5	1550	1.63	1.00
1	1.0	1550	3.67	2.25
4	1.0	1550	3.18	1.95
8	0.0	1700	0.29	0.18
11	0.5	1700	7.75	4.76
9	1.0	1700	11.24	6.90
13	1.0	1700	10.3	6.32

Results

The measured weight losses for each experiment are shown in Table 3 together with the calculated mass flux and the parameters. Figure 6 show the mass loss as a function of the flow rate with linear trend lines for each temperature.

Discussion

The crucible from experiment 10 (1400°, no Ar flow) has increased in weight by a very small amount. A potential reason for this might be a small amount of oxygen, supplied either from the ppm concentration in the Ar, the alumina crucible or from the tarnished starting Mn-chip surface reacting with the metal to form heavier oxides. The amount would not be very high however, and it is assumed that there has been practically no evaporation of manganese in this experiment.

The two experiments at 1700 °C and with 1 l/min flow rate were found to have very little metal left at the end of the experiment. This would likely cause a lower rate of evaporation during the later stages of the experiment as the surface area would be smaller. This would also explain why there is not the same linearity for the 1700 °C experiments as for the lower temperatures. Figure 7 shows the inside of crucible #13, where the metal content has been reduced to the point where it no longer covers the full area of the crucible.

The model does show the same tendency to taper off at higher flow rates, but not to the same degree as in the experiments.

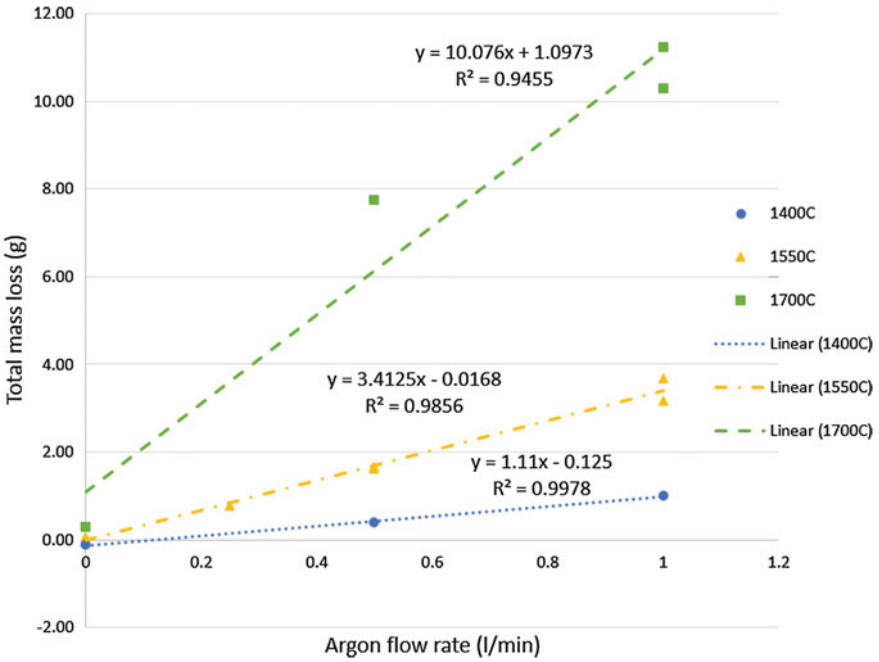

Fig. 6 Total mass loss in grams over the flow rate of argon in l/min. Linear trend lines are given for each temperature

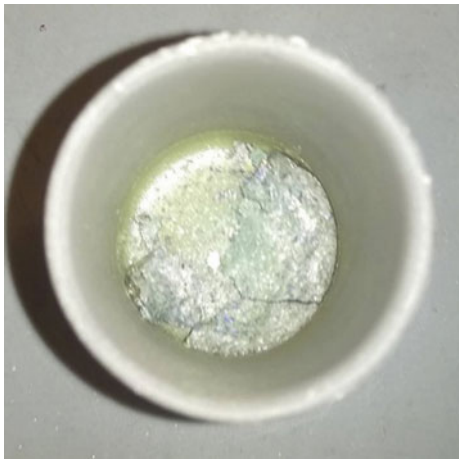

Fig. 7 Crucible from experiment #13, 1700 °C and 1 l/min flow rate. The surface area of the metal is clearly reduced due to excessive evaporation

Data from the experiments can be compared with the model, which was used to generate data points for the same parameters as the experiments. These values are shown in Table 4, and plotted in Fig. 8.

Table 4 Modelling results: total mass loss for a choice set of parameters

Ar flow rate (l/min)	Temp (°C)	Loss (g)
0.25	1400	0.06
0.5	1400	0.08
1.0	1400	0.12
0.25	1550	0.36
0.5	1550	0.50
1.0	1550	0.71
0.25	1700	1.55
0.5	1700	2.20
1.0	1700	3.11

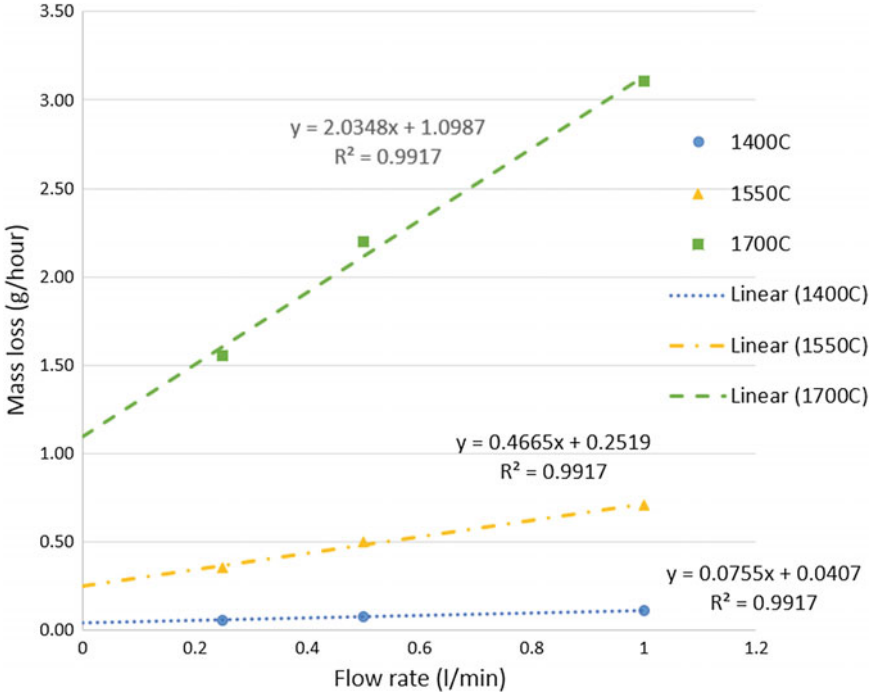

Fig. 8 Modelled mass loss in grams/hour over the flow rate in l/min from the model

The mass loss calculated with the model are around one fourth of the experimental values for all parameters. For comparison, Fig. 9 shows both data sets together.

The curves are similar, but the model has evaporation rates that are about a fourth of the experimental values. Figure 10 shows both data sets together, but with the values from the model multiplied by 4 to show the similarities in the curves.

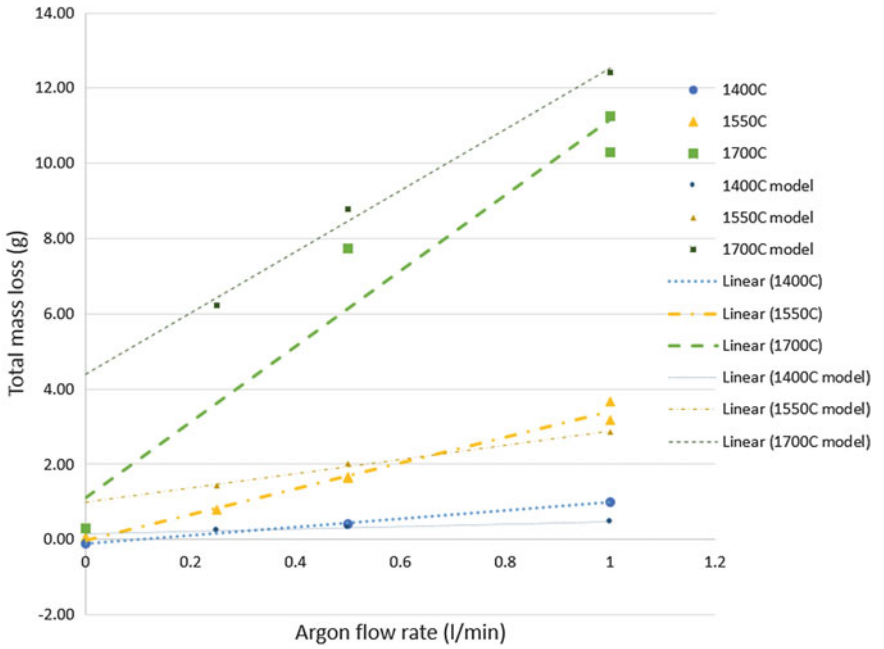

Fig. 9 Mass loss in grams over the flow rate in l/min. Experimental and modelled values. Values from model are multiplied by 4

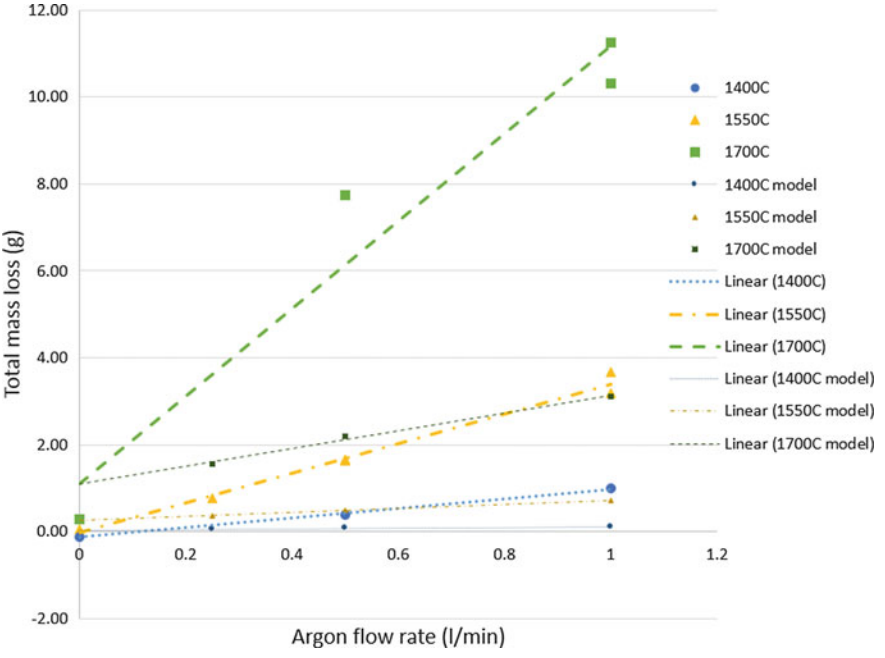

Fig. 10 Mass loss in grams over the flow rate in l/min. Experimental and modelled values

Conclusions

In order to better understand the kinetics of fume/dust formation in the Mn-ferroalloys production industries, experiments investigating the evaporation rate and diffusion of Mn in an argon atmosphere at different temperatures and flow conditions, have been carried out. The results were compared to values calculated using a mathematical model of the same system. There was a mismatch in the results between model and experiments on the scale of factor 4, but the trends shown were very similar. Possible uncertainties in the model include the diffusion coefficient, enthalpy and entropy at lower temperatures, approximation of Reynolds number, and the gas velocities from the Comsol model.

There are also uncertainties in the experimental work, which could have influenced the experimentally obtained results. The evaporation during heating and cooling might have been measurably large, as there is up to fifteen minutes of time where the temperature is above the melting point during heating and cooling. The flux would in that time probably lie between the values for our experiments. The thin layer of oxide might have slowed the evaporation process, and the temperature profile might be inaccurate as there is a delay between the outside of the tube where the furnace measures temperature, and the inside of the crucible.

The data from the experiments can be further used when modelling the dust formation in more complex systems where Mn evaporation is just a part of the whole. If improved, the model can also be expanded to take further reactions into account.

Further Work

This work is the beginning of a larger study, and there is much work still to be done. Following is a list of planned work in the continuation of the project:

- Perform experiments where the temperature is measured inside the crucible to find temperature delay.
- Perform experiment without holding time to measure mass loss during heating and cooling.
- Etch the Mn before the experiment to remove any oxides.
- Use a crucible that doesn't contain oxides.
- Perform experiments with 0.25 l/min flow rate for 1400 and 1700 °C.
- Review assumptions and uncertainties in the model, and then improve on it.
- Continue the experiments and model work with manganese and iron alloys, as well as including oxygen in the gas.

References

1. Johnsen et al (2008) Prediction of dropout from respiratory symptoms and airflow limitation in a longitudinal respiratory study, Int Arch Occup Environ Health 81:451–459
2. Johnsen HL (2009) PhD-thesis. University of Oslo, Fakultetsdivisjon Akershus universitetssykehus
3. Hobbesland et al (1997) Mortality from nonmalignant respiratory diseases among male workers in Norwegian ferroalloy plants, Scand J Work Environ Health 23(5):334–341
4. Søyseth et al (2011) Incidence of airflow limitation among employees in Norwegian smelters, Am J Ind Med 54(9):707–713
5. Gibbs et al (2014) Mortality and cancer incidence in aluminum smelter workers: a 5-year update. J Occup Environ Med 56(7):739–764
6. Bast-Pettersen et al (2004) Neuropsychological function in manganese alloy plant workers. Int Arch Occup Environ Health 77:277–287
7. Luccini et al (2009) From manganism to manganese-induced parkinsonism: a conceptual model based on the evolution of exposure. Neuromol Med 11:311–321
8. Racette et al (2012) Pathophysiology of manganese-associated neurotoxicity. Neurotoxicology 33(4):881–886
9. Monteiller et al (2007) The pro-inflammatory effects of low-toxicity low-solubility particles, nanoparticles and fine particles, on epithelial cells in vitro: the role of surface area. Occup Environ Med 64:609–615
10. Obersdörster (2001) Pulmonary effects of inhaled ultrafine particles. Int Arch Occup Environ Health 74:1–8
11. Schmid et al (2009) Dosimetry and toxicology of inhaled ultrafine particles. Biomarkers 14(1): 67–73
12. Ma Y, Kero I, Tranell G (2017) Fume formation from oxidation of liquid SiMn alloy. Oxidation of Metals:1–21
13. Bakken JA, Lobo S, Kolbeinsen L (2009) Compendium fluid flow and heat transfer advanced course, NTNU
14. Bird RB, Stewart WE, Lightfoot EN (2007) Transport phenomena. Wiley, New York
15. Stanton JF, Gauss J, Harding ME, Szalay PG, Auer AA, Bartlett RJ, Benedikt U, Berger C, Bernholdt DE, Bomble YJ et al (2015) CFOUR, coupled-cluster techniques for computational chemistry, 2015. For the current version, see http://www.cfour.de
16. Bartlett RJ, Musial M (2007) Coupled-cluster theory in quantum chemistry. Rev Mod Phys 79:291–352
17. Smith FJ, Munn RJ (1964) Automatic Calculation of the Transport Collision Integrals with Tables for the Morse Potential. J Chem Phys 41:3560–3568
18. Comsol Multiphysics http://www.comsol.com/comsol-multiphysics. Accessed 6 Sept 2017
19. Chase MW Jr (1998) NIST-JANAF thermochemical tables, 4th edn. J Phys Chem Ref Data Monograph 9 1–1951

Part IV
Processing: II

Recent Development and Applications of CFD Simulation for Friction Stir Welding

Gaoqiang Chen, Qingyu Shi and Shuai Zhang

Abstract Friction stir welding (FSW) has been successfully applied in fabricating many critical structures, e.g. rocket fuel tanks. Generally, CFD simulation is required to better understand the in-process material flow during FSW. In this paper, we discuss the concepts and the approaches that have been employed in the recent development and application of the CFD simulation for FSW. First, special considerations on friction, heat generation and transient tool motion have been adopted to capture the fully-coupled heat-and-mass-flow phenomenon during FSW. Second, temporal evolution of the material state during welding is analyzed by interpolation and integration along the flow paths, which is further used to predict the typical feature and defects in the welds. Third, the CFD-based predictions on the temperature and the material flow are validated by experimental measurements. Finally, the current concepts and approaches in the simulation of FSW could be applied in CFD-based studies on other similar thermal-mechanical processes.

Keywords Friction stir welding · Computational fluid dynamics
Numerical simulation · Material flow

Introduction

Friction stir welding (FSW) [1] is an advanced solid state welding process, which has been successfully applied in fabricating lots of important engineering structures, such as rocket fuel tanks and high speed train bodies. FSW relies on the complex high-temperature plastic flow of solid-state material around the rotating welding tool to achieve sound joints. The in-process thermal mechanical condition, e.g. temperature field and material flow field, in the vicinity of the welding tool is of critical importance in both fundamental understanding and engineering design of

G. Chen (✉) · Q. Shi · S. Zhang
Department of Mechanical Engineering, Tsinghua University, Beijing 100084, People's Republic of China
e-mail: cheng1@tsinghua.edu.cn

L. Nastac et al. (eds.), *CFD Modeling and Simulation in Materials Processing 2018*, The Minerals, Metals & Materials Series,
https://doi.org/10.1007/978-3-319-72059-3_11

the FSW process due to its critical role in governing many performance-related processes [2], such dynamic recrystallization [3] and heat generation [4, 5]. Despite its critical importance, the in-process thermal-mechanical condition around the welding tool, especially the material flow behavior, is still one of the yet-least understood phenomenon in FSW.

Owing to its solid-state welding nature, the flow behaviors of solid-state material in FSW is significantly different from that of molten material that occurs in casting and fusion welding. Due to the difficulties in direct experimental observation, computer simulation is required to better understand and control the in-process material flow during FSW. To this end, the computational fluid dynamics (CFD) simulation has been widely applied and playing a very important role in studying the material flow of FSW, as the complex underlying physical couplings between the interfacial friction, heat generation, severe plastic deformation and heat transfer are readily to be implemented owing to the high computational efficiency and the diversity of the boundary conditions. The application of three-dimensional CFD simulation can be traced back to the first decade of this century [6]. The formulation [7] which links the viscosity and the flow stress of the solid-state material is the fundamental to for application of CFD approach in simulating FSW. The calculation of heat and mass transfer during FSW is implemented by the conventional governing equations for the laminar flow [7–9], while specially designed source terms and boundary conditions are developed to capture the friction-induced fully coupled thermal-mechanical phenomena during the FSW process.

In this paper, the concepts and the approaches that have been employed in development and application of the recent CFD simulation of FSW are discussed.

General Governing Equations for Simulation of FSW

In order to analyze the thermal-mechanical condition in FSW, the general governing equations for the heat transfer and the material flow for incompressible fluid are generally used in the CFD simulation. The welding tool is assumed as a rigid body, which is not included in the computation domain of fluid. The workpiece is taken as a single-phase [8] or multi-phase [10] viscous fluid in the literatures. The general used conservation equations of mass and momentum are given as,

$$\frac{\partial \rho}{\partial t} + \nabla \cdot (\rho \vec{v}) = 0 \tag{1}$$

$$\frac{\partial \rho \vec{v}}{\partial t} + \nabla \cdot (\rho \vec{v}\vec{v}) = -p + \nabla \cdot \left(\mu\left(\nabla \vec{v} + \nabla \vec{v}^{T}\right)\right) \tag{2}$$

where ρ is fluid density, μ is fluid viscosity, p is pressure, $\vec{v}$ is fluid velocity and t is flow time. The energy conservation equation is given by,

$$\frac{\partial \rho H}{\partial t} + \nabla \cdot (\rho \vec{v} H) = \nabla \cdot (k \nabla T) + S_V \tag{3}$$

where H is enthalpy, T is temperature in K, k is thermal conductivity and S_V is a spatial source term.

Special Considerations in CFD Simulation of FSW

The CFD simulation approach has been successfully applied to study the flow of conventional fluid, such as air and water. In the field of material processing, it has been applied in the study of casting and the fusion welding process, where the flow of the molten metal is critical. But simulating the flow of solid-state metal during FSW is quite different. As such, special considerations are required to build a model for capturing the in-process thermal-mechanical behaviors during FSW. In this section, we are going to discuss these special considerations.

Interfacial friction. The interfacial friction between the welding tool and the workpiece is important due to its essential role in governing the heat generation and driving the plastic flow. In that both the welding tool and workpiece are in its solid state. For the solid state metal, the interfacial frictional state can be very complex due to the variation of interfacial conditions. For example, if the contact pressure between the tool and the workpiece is not adequate, there will not be enough frictional resistance so that the interfacial slipping can occur, which is a slipping state. Otherwise, in the case of ideal contact at the tool/workpiece interface, there will be enough frictional force to keep the workpiece flowing with the welding tool at the same velocity, which is a sticking state. Actually, the contact state and the interfacial motion state will change owing to the variation of pressure, temperature and deformation rate [11, 12]. In order to handle this potential sticking and slipping at the interface quantitatively, much work has been done on developing a friction boundary condition in the literatures. In many models, the researchers used a fully sticking condition [7, 9], where there is assumed to be no slipping at the interface. Later, an empirical equation [8] and experimental work [13] were proposed to determine the interfacial velocity. More recently, the shear-stress based frictional boundary conditions [14] were developed to capture the extent of sticking or sliding at the interface and used in the recent simulations [15].

Heat generation. Keeping high temperature is indeed necessary to join metals in solid state during FSW. Thus the heat generation in FSW is very important topic. The heat generation during FSW is a fully coupled thermal-mechanical process, which can be divided into two parts, i.e. the heat due to friction and plastic deformation. In the early CFD simulation of FSW, the heat generation was usually treated as a facial heat fluxes at the tool/workpiece interface [8]. In recent studies, the heat flux due to plastic deformation was been treated as a volumetric heat flux [4, 5]. The simulation that takes the heat flux as a volumetric heat flux reflects more

physical nature of the FSW process and captures the non-uniform distribution of the heat flux, which provides more information to understand the local temperature distribution.

Transient tool motion. The welding tool is an important part in FSW, which rotates at high rate during the welding process. The real FSW tool is usually designed on purpose to be not axis-symmetric in order to effectively drive the material flow. As such, the transient motion and the geometry of the welding tool plays a unique role in fundamental understanding of the in-process material flow. In the early models, the transient the motion of the welding tool is simplified by using steady-state model [16], while in many other work, the geometry feature such as threads on pin are ignored [17]. In the recent CFD simulation, the mesh motion [9, 13, 18] is generally adopted to represent the influent of the transient motion of the welding tool on the material flow.

Prediction of Microstructural Features and Defects in Welds

Both the microstructural feature and the defects in the FS welds are closely linked to the performance of the welds. The CFD simulation is approaching to the point that the microstructural feature and the defects can be directly predicted. Early simulation work focused more on prediction of the state variables during the welding process, such as the temperature, processing force [19, 20]. Predicting the essential in-process variables is the basis for further prediction of the microstructural and defects in the welds, because the features in the weld are history dependent. Prediction of these feature requires to collect the information along the whole flow path. In recent studies, the temporal evolution of the material state during welding is analyzed by interpolation and integration along the flow paths, which is further used to predict the typical feature and defects in the welds [15]. By analyzing the temporal evolution of material state versus time could be obtained, which make it possible to integrate more kinetic model, such as the precipitate evolution, into the CFD to study more concerns in the welding engineering.

Validation of Simulation Data

It is necessary to use experimental data to confirm the validity of the simulation results before further application for analysis. This concept has been recognized widely in the CFD simulation of FSW. Some of the CFD simulations used only the temperature data to validate the simulation results [4, 21]. However, the temperature results and material flow results are weakly related. The material flow need separate validation. Recently, more and more researchers has employed the microstructural

features [8, 10, 15, 22] in the weld to further support the simulation model. In addition, owing to the advanced experimental approaches [23, 24], more information on the material flow during FSW can be obtained. We expect more studies to validate the simulation results.

Conclusions and Outlook

In summary, CFD simulation has been successfully applied in simulating the FSW process, because both the temperature and material flow are important in the fundamental understanding of FSW. Based on the data mining and validation, the CFD simulation of FSW are approaching to the point that the engineering problems could be directly investigated by the CFD simulation to support the engineering design. In this paper, we discuss the concepts and the approaches that have been employed in the recent development and application of the CFD simulation for FSW. The current concepts and approaches in the simulation of FSW could be applied in CFD-based studies on other similar thermal-mechanical processes, which are summarized as blow.

(1) Special considerations on friction, heat generation and transient tool motion is required to capture the fully-coupled thermal-mechanical phenomenon during FSW.
(2) Temporal evolution of the material state variables during welding can be analyzed by interpolation and integration along the flow paths, which can be further used to predict the typical feature and defects in the welds.
(3) Both the predictions on temperature and material flow are need to be validated by proper experimental measurements.

Acknowledgements The research was supported by the National Natural Science Foundation of China (Grant No. 51375259 and Grant No. 51705280) and the National Science and Technology Major Project of the Ministry of Science and Technology of China (No. 2012ZX04012-011).

References

1. Mishra RS, Ma ZY (2005) Friction stir welding and processing. Mater Sci Eng R 50 (1–2): 1–78
2. Shi L, Wu CS, Liu HJ (2015) The effect of the welding parameters and tool size on the thermal process and tool torque in reverse dual-rotation friction stir welding. Int J Mach Tool Manuf 91:1–11
3. Fratini L, Buffa G (2005) CDRX modelling in friction stir welding of aluminium alloys. Int J Mach Tool Manuf 45(10):1188–1194
4. Chen GQ, Shi QY, Li YJ, Sun YJ, Dai QL, Jia JY, Zhu YC, Wu JJ (2013) Computational fluid dynamics studies on heat generation during friction stir welding of aluminum alloy. Comput Mater Sci 79:540–546

5. Su H, Wu CS, Pittner A, Rethmeier M (2014) Thermal energy generation and distribution in friction stir welding of aluminum alloys. Energy 77:720–731
6. Colegrove PA, Shercliff HR (2003) Experimental and numerical analysis of aluminium alloy 7075-T7351 friction stir welds. Sci Technol Weld Joining 8(5):360–368
7. Colegrove PA, Shercliff HR (2005) 3-dimensional CFD modelling of flow round a threaded friction stir welding tool profile. J Mater Proc Technol 169(2):320–327
8. Nandan R, Roy GG, Lienert TJ, Debroy T (2007) Three-dimensional heat and material flow during friction stir welding of mild steel. Acta Mater 55(3):883–895
9. Yu Z, Zhang W, Choo H, Feng Z (2012) Transient heat and material flow modeling of friction stir processing of magnesium alloy using threaded tool. Metal Mater Trans A 43(2):724–737
10. Liu X, Chen G, Ni J, Feng Z (2016) Computational fluid dynamics modeling on steady-state friction stir welding of aluminum alloy 6061 to TRIP steel. J Manuf Sci Eng 139(5):051004
11. Kumar K, Kalyan C, Kailas SV, Srivatsan TS (2009) An investigation of friction during friction stir welding of metallic materials. Mater Manuf Process 24(4):438–445
12. Davim JP (ed) (2012) Tribology in manufacturing technology. Springer, Berlin
13. Su H, Wu CS, Bachmann M, Rethmeier M (2015) Numerical modeling for the effect of pin profiles on thermal and material flow characteristics in friction stir welding. Mater Des 77:114–125
14. Chen G, Feng Z, Zhu Y, Shi Q (2016) An alternative frictional boundary condition for computational fluid dynamics simulation of friction stir welding. J Mater Eng Perform 25 (9):4016–4023
15. Zhu Y, Chen G, Chen Q, Zhang G, Shi Q (2016) Simulation of material plastic flow driven by non-uniform friction force during friction stir welding and related defect prediction. Mater Des 108:400–410
16. Colegrove PA, Shercliff HR (2004) Development of Trivex friction stir welding tool Part 2—three-dimensional flow modelling. Sci Technol Weld Joining 9(4):352–361
17. Nandan R, Roy GG, Lienert TJ, Debroy T (2006) Numerical modelling of 3D plastic flow and heat transfer during friction stir welding of stainless steel. Sci Technol Weld Joining 11 (5):526–537
18. Ji S, Shi Q, Zhang L, Zou A, Gao S, Zan L (2012) Numerical simulation of material flow behavior of friction stir welding influenced by rotational tool geometry. Comput Mater Sci 63:218–226
19. Arora A, Nandan R, Reynolds AP, Debroy T (2009) Torque, power requirement and stir zone geometry in friction stir welding through modeling and experiments. Script Mater 60(1): 13–16
20. Atharifar H, Lin D, Kovacevic R (2009) Numerical and experimental investigations on the loads carried by the tool during friction stir welding. J Mater Eng Perform 18(4):339–350
21. Pan WX, Li DS, Tartakovsky AM, Ahzi S, Khraisheh M, Khaleel M (2013) A new smoothed particle hydrodynamics non-Newtonian model for friction stir welding: process modeling and simulation of microstructure evolution in a magnesium alloy. Int J Plast 48:189–204
22. Chen G, Feng Z, Chen J, Liu L, Li H, Liu Q, Zhang S, Cao X, Zhang G, Shi Q (2017) Analytical approach for describing the collapse of surface asperities under compressive stress during rapid solid state bonding, Script Mater 128:41–44
23. Morisada Y, Imaizumi T, Fujii H (2015) Determination of strain rate in Friction stir welding by three-dimensional visualization of material flow using X-ray radiography. Script Mater 106:57–60
24. Seidel T, Reynolds AP (2001) Visualization of the material flow in AA2195 friction-stir welds using a marker insert technique. Metal Mater Trans A 32(11):2879–2884

Modeling of Argon Gas Behavior in Continuous Casting of Steel

Hyunjin Yang, Surya P. Vanka and Brian G. Thomas

Abstract In continuous casting of steel, argon gas injection is a popular method to reduce nozzle clogging. Multiphase turbulent flow of molten steel with argon gas through complicated-geometry nozzles increases the complexity of the flow dynamics. In this study, these complex multiphase turbulent flow behaviors are simulated in a lab-scale continuous caster using a new hybrid model that involves a Eulerian-Eulerian (EE) model coupled simultaneously with a Discrete Phase Model (DPM). The complex behavior of the argon gas including formation of gas pockets, intermittent shearing off of the gas pockets, volumetric expansion, coalescence and breakup of bubbles, and transport of the bubbles in both the nozzle and mold are all simulated. The model is validated with measurements on a benchmark experiment of liquid-metal argon flow in a laboratory-scale system. This hybrid model is a promising tool to estimate realistic bubble size distributions and multiphase flow in a real caster.

Keywords Bubble size distribution · Coalescence · Breakup · Volumetric expansion · Shearing off

H. Yang (✉) · S. P. Vanka
Department of Mechanical Science and Engineering, University of Illinois at Urbana-Champaign, 1206 W. Green Street, Urbana, IL 61801, USA
e-mail: hyang69@illinois.edu

S. P. Vanka
e-mail: spvanka@illinois.edu

B. G. Thomas
Department of Mechanical Engineering, Colorado School of Mines, Brown Hall W370-B, 1610 Illinois Street, Golden, CO 80401, USA
e-mail: bgthomas@mines.edu

L. Nastac et al. (eds.), *CFD Modeling and Simulation in Materials Processing 2018*, The Minerals, Metals & Materials Series,
https://doi.org/10.1007/978-3-319-72059-3_12

Introduction

In continuous casting of steel, argon gas injection has an important influence on the fluid flow in the mold, including surface velocity, level fluctuations, and the consequent entrainment of mold slag and formation of other defects. The bubble size distribution is very important, controlling not only the flow pattern [1], but also the distribution of bubbles and particles entrapped into the solidifying shell [2]. This size distribution is very difficult to determine, and is an ongoing issue in computational modeling where unjustified assumptions must be made. A previous study [3] showed that the evolving argon bubble size distribution is a consequence of several phenomena: the formation of argon gas pockets in low-velocity regions inside the nozzle, intermittent shearing off of the gas pockets, bubble interactions such as coalescence and breakup, and volumetric expansion of the bubbles according to the surrounding liquid steel pressure. To accurately model the evolution of the bubble size distribution locally and transiently, sophisticated numerical and mathematical models are needed to simulate the complex argon gas behavior are necessary. In this work, a new hybrid model EEDPM is developed to model all of the phenomena mentioned above.

Model Description

Governing Equations of EEDPM

As the name of the model suggests, the governing equations are composed of two parts: an Eulerian-Eulerian (EE) model calculates velocity and volume fraction fields of each phase with a shared pressure field [4] from a continuity and Navier Stokes equations for each phase.

$$\frac{\partial(\alpha_k \rho_k)}{\partial t} + \nabla \cdot (\alpha_k \rho_k \boldsymbol{u}_k) = 0 \tag{1}$$

$$\frac{\partial(\alpha_k \rho_k \boldsymbol{u}_k)}{\partial t} + \nabla \cdot (\alpha_k \rho_k \boldsymbol{u}_k \boldsymbol{u}_k) = -\alpha_k \nabla p + \nabla \cdot \left(\mu_k \alpha_k \left(\nabla \boldsymbol{u}_k + \nabla \boldsymbol{u}_k^T\right)\right) + \alpha_k \rho_k \boldsymbol{g} + \boldsymbol{F_D} \tag{2}$$

A DPM model tracks each bubble as a point-mass, tracking position and velocity of the bubble [5].

$$\rho_g V_p \frac{d\boldsymbol{v_i}}{dt} = V_c(\boldsymbol{F_D} + \boldsymbol{F}_V + \boldsymbol{F}_P + \boldsymbol{F_B}) \tag{3}$$

$$\frac{d\boldsymbol{x_i}}{dt} = \boldsymbol{v_i} \tag{4}$$

These two models are run together as separate models in the same domain, but are coupled in several ways: the DPM momentum terms (RHS of Eq. 3) depend on the flow field from the EE model. Drag, virtual mass, pressure gradient and buoyancy forces are considered [6]. The DPM bubble size also evolves transiently by bubble interactions (coalescence and breakup), and volumetric expansion. At the same time, the instantaneous, spatially varying DPM bubble size distribution is given to the EE model, where it influences the drag force $\boldsymbol{F_D}$ between the gas and liquid phases in the EE model. Here, Tomiyama drag force model is used for the drag [7]. As the EE liquid phase flow field is changed by the drag force based on the DPM bubble size, this model system is two-way coupled. Consequently, this hybrid model can predict the spatially and time-varying bubble size distributions. Mass conservation problems are avoided because no mass is exchanged between the two models. For turbulence modeling, SST k-ω model is used with this EEDPM multiphase flow model. These governing equations are solved with ANSYS-Fluent using extensive user-defined subroutines developed specifically for this work.

Modeling of Shearing off Process

Figure 1 shows a flow chart of the overall algorithm of EEDPM including the shearing off process. To simulate the shearing off process of small bubbles from a large gas pocket, a new mathematical model is developed [8]. To locate the gas pockets, the model uses the gas volume fraction field from the EE model solution. The EE model captures both flow recirculation zones and gas pocket formation. To extract a sharp interface, α^*, from the continuous gas volume fraction field, α, a

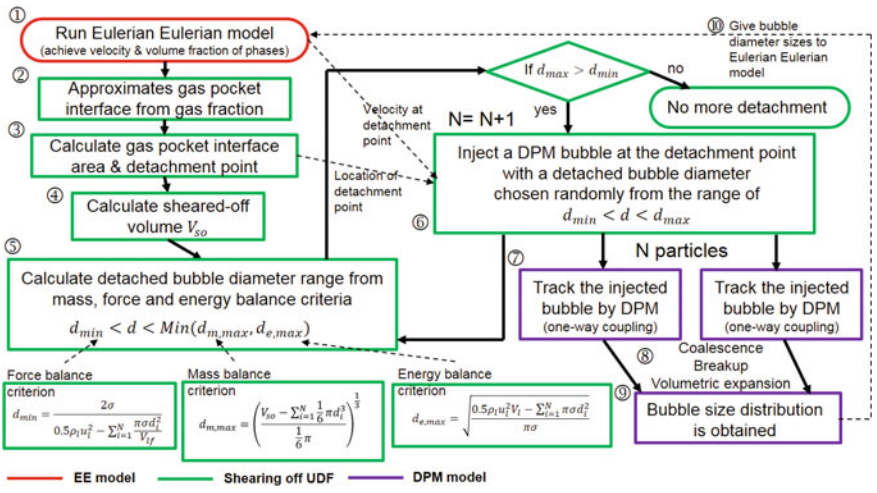

Fig. 1 Flow chart of EEDPM including shearing off process

criterion function is used ($\alpha^* = 1\ if\ \alpha \geq 0.95, otherwise\ \alpha^* = 0$). After approximating the gas pocket interface, the interface area (A_{int}) and detachment point of small bubbles are calculated numerically. The detachment point is assumed to be the lowest point of the gas pocket. The sheared off volume from the gas pocket is calculated by multiplying the interface area by the thickness of the sheared off layer ($V_{so} = A_{int}\delta_g^*$). The sheared off gas layer thickness (δ_g^*) is calculated using boundary layer theory. Once the sheared off volume is calculated, it is redistributed into small DPM bubbles. According to previous works for bubble breakup, the daughter bubble size is a stochastic variable [9]. Thus, the detached bubble size by the shearing off process is assumed to be a random variable (all sizes have equal probability). However, it is still important to specify a range of allowable daughter bubble sizes using mass, force and energy balance criteria. By adjusting the criteria of Luo and Svendsen (1996) [10] and Wang et al. [11], energy and force criteria are derived for the shearing off process (⑤ in Fig. 1). Also, a new mass criterion is added based on mass conservation, so that the total volume of detached bubbles cannot exceed the sheared off volume from the gas pocket. The force criterion generates the lower bound, and the mass and energy criteria generate the upper bound of bubble size range. The daughter bubbles must satisfy all three criteria. Then, the daughter bubble size is decided through a random generator in the range, and a bubble is injected at the detachment point as a Discrete Phase Model (DPM) bubble with that bubble size. The bounds evolve because mass, momentum and energy are consumed as bubbles detach from the gas pocket: the upper bound of bubble size decreases, and the lower bound increases. The shearing off process ends when the upper bound becomes less than the lower bound. The shearing off frequency is found by dividing the gas pocket length by the average liquid velocity. Detached DPM bubbles change their size transiently by coalescence, breakup and volumetric expansion. The locally and time-varying bubble size distribution obtained from DPM bubbles is updated every time step to EE model for the calculation of accurate local drag force.

Modeling of Bubble Interactions

Figure 2 shows a flow chart of the coalescence model. First, collision is easily handled from the calculation of distance between a pair of DPM bubbles. Here, only distances of pairs located in the same computational cell are considered to decrease the computational cost from n^2 to n. If the distance between a pair is smaller than a sum of radius of two bubbles ($r_1 + r_2$), the pair is counted as a collided pair. And then, the coalescence efficiency e is calculated based on the drainage model [12], based on the drainage time ($t_{drainage}$) and the contact time ($t_{contact}$), from previous models [13]. Here, we assume constant e = 0.1. Coalescence is randomly determined with the probability based on the coalescence efficiency after collision. If two bubbles coalesce, a coalesced bubble size and a velocity of the bubble are

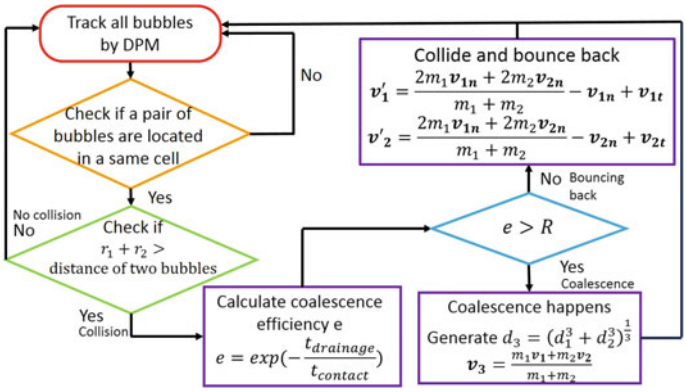

Fig. 2 Flow chart of coalescence model

calculated by mass and momentum conservation. Otherwise, two bubbles bounce apart via an elastic collision. This is a reasonable assumption for small bubbles since the strong surface tension makes them act like hard spheres. Figure 3 describes the algorithm of the breakup model for DPM bubbles. The first criterion of breakup is to check the bubble size: if the size is greater than the maximum stable bubble size d_{crit} [14], the first criterion is satisfied. And then, a range of smaller daughter bubble size is calculated by mass and force balance criteria. If the upper bound is greater than the lower bound, the model counts that the bubble breaks up and a smaller daughter bubble diameter is randomly determined in the range. The other daughter bubble size is automatically determined by the mass conservation.

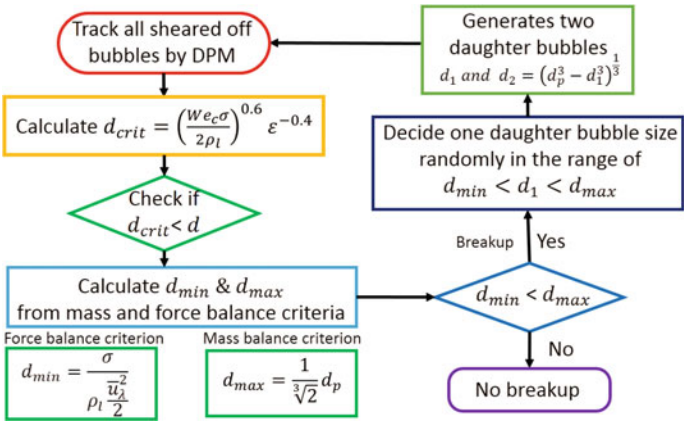

Fig. 3 Flow chart of breakup model

Modeling of Volumetric Expansion

Gas bubbles can expand or shrink according to the surrounding liquid pressure field. To calculate the size change of bubble due to the liquid pressure, a cubic equation with respect to r_{new} (new bubble radius) is derived from the Young-Laplace equation and the ideal gas law [6]:

$$p_{l,new}\left(\frac{d_{new}}{2}\right)^3 + 2\sigma\left(\frac{d_{new}}{2}\right)^2 - p_{g,old}\left(\frac{d_{old}}{2}\right)^3 = 0 \tag{5}$$

By solving this equation for each DPM bubble, volumetric expansion or shrinkage of bubbles by the surrounding liquid pressure is calculated. In this work, the volumetric expansion is counted every 10-time step to decrease the computational cost.

Results and Discussion

An experiment of lab-scale stopper rod system done by Timmel's research group [3] is benchmarked to validate the EEDPM hybrid model. As shown in Fig. 4, this is a slot-shaped geometry: front view geometry is projected into thickness direction by 12 mm. Liquid Galinstan is supplied from the top of funnel shape and flows

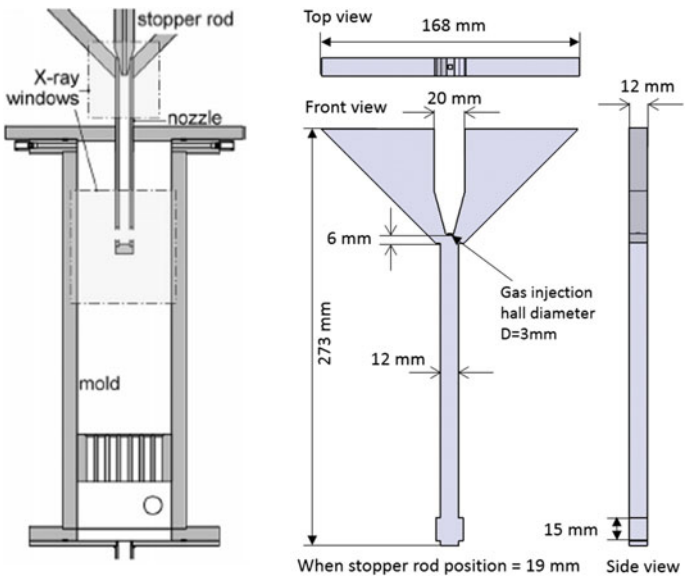

Fig. 4 Geometry of lab-scale stopper rod system

Table 1 Operating condition and material properties [3]

Operating condition	Value	Material property	Value
Operating temperature	293 K	Galinstan density	6440 kg/s
Stopper rod position	19 mm	Galinstan viscosity	0.0024 Pa
Tundish level	70 mm	Galinstan surface tension coefficient	0.718 N/m
Galinstan flow rate	140 cm/s	Argon gas density	1.6228 kg/m^3
Argon gas flow rate	0.24 cm/s	Argon gas viscosity	2.125 $\times$ 10^{-5} Pas
Submergence depth	92 mm		
Wall roughness	Smooth wall (acrylic)		
Mold size	100 $\times$ 15 $\times$ 426 mm^3		

downward by gravity. Argon gas is injected from the tip of stopper rod. Operating conditions and material properties are given in Table 1.

Due to the low melting point of Galinstan, this experiment is conducted at room temperature. Argon gas behavior is measured through X-ray shots from front: projected gas volume fraction field is obtained from the X-ray intensity (brightness $\cong$ volume fraction). Since this geometry is much smaller, thinner, and rectangular than the real scale stopper-rod system, the argon gas behavior may be different than a commercial casting nozzle. However, this experiment is still valuable for validation as: (1) bubbles behavior in liquid metal is measured (with similar high surface tension and buoyancy), (2) experiments of bubbly downflow with sudden expansion are rare.

Figure 5 shows the gas pocket formation at the recirculation zones through accumulation of argon gas from the stopper tip and the detachment of small bubbles from them. The shearing off model injects DPM bubbles as detached small bubbles. The transient solution shows that large bubbles ($d > 6$ mm) are detached intermittently, but break down to smaller bubbles in few time steps due to the development of high turbulence dissipation rate near the gas pockets.

Figure 6 displays the sheared DPM bubbles with flow field information. Due to the very thin mold, jets injecting from the nozzle ports obstruct most of the bubbles from rising to the top once bubbles flow into the lower mold. It is observed that bubbles circulate in the lower roll and experience coalescence and breakup repeatedly. Very large bubbles ($d > 7$ mm) evolve due to serial coalescence and are

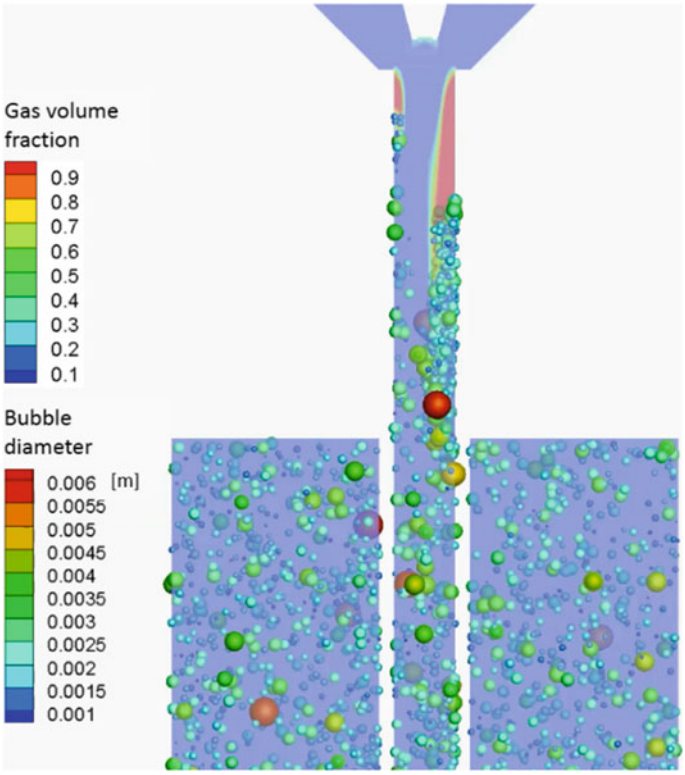

Fig. 5 Sheared off DPM bubbles from gas pockets at t = 22.0925 s

able to overcome the jet obstruction and float to the top sporadically. Figure 7 shows the DPM bubbles with the turbulence dissipation rate field. High ε is observed near the bottom of the port due to the development of swirl and it causes breakup of big bubbles (d > 6 mm) when they pass through the port. Also, two relatively-large bubbles are observed staying at the top of each port due to the coalescence of accumulated DPM bubbles at the recirculation zones.

Figure 8 describes the time-averaged results of number, size and residence time of DPM bubbles in the domain. In the nozzle, roughly 1000 bubbles are found and zone 1 has the largest number of bubbles due to the accumulation of bubbles in the recirculation zones near the inlet of nozzle. Residence time of zone 1 is longer than zone 2 because of the same reason. The average bubble size increases as it goes down except zone 4 due to the residence time effect: big bubbles try to stay longer in the nozzle due to stronger buoyancy. The reason that zone 4 does not follow this

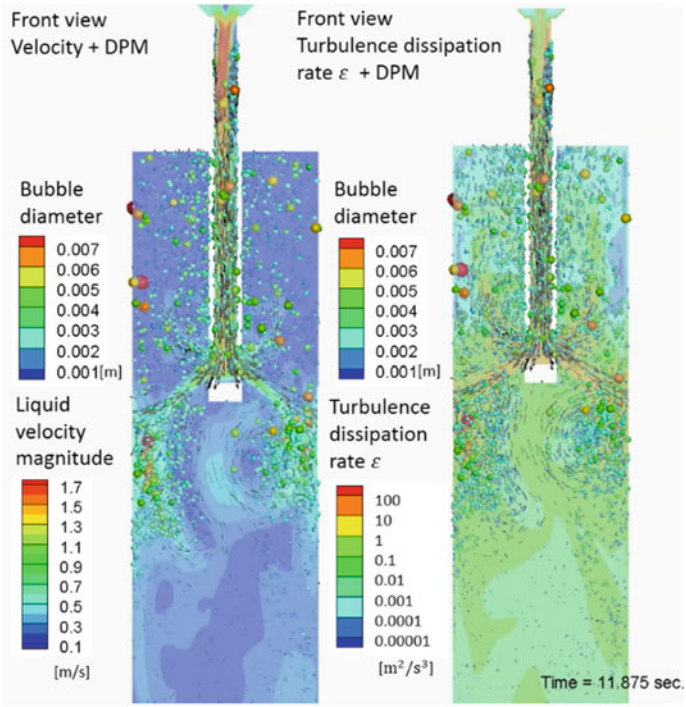

Fig. 6 DPM bubble distribution with velocity (left) and turbulence dissipation rate field (right) at t = 11.875 s

trend is because of the breakup of bubbles by the swirl developed at the bottom of the nozzle. In case of the bubbles in the mold, 4000 bubbles are observed in total, and zone 7 has the largest number of bubbles due to the jet obstruction effect. A decrease of average bubble size between zone 4 (in nozzle) and 7 (in mold) is caused by the swirl effect discussed in Fig. 7. Also, zone 7 has the largest average bubble size in the mold because of the coalescence of bubbles: high number density of bubbles results more collision, and ultimately more chance of coalescence. The residence time of zone 7 and 8 is longer than other zones, due to the jet obstruction effect.

Figure 9 shows the transition of bubble size distribution by time. It shows that the bubble size distribution does not change much by time. Figure 10 compares the bubble size distribution with the experimental measurement [3]. The calculation results show reasonable agreement. The majority of bubbles have d = 1–3 mm because the average turbulence dissipation rate in the nozzle ($\varepsilon = 1-10\,\mathrm{m}^2/\mathrm{s}^3$) allows maximum stable bubble sizes in the range.

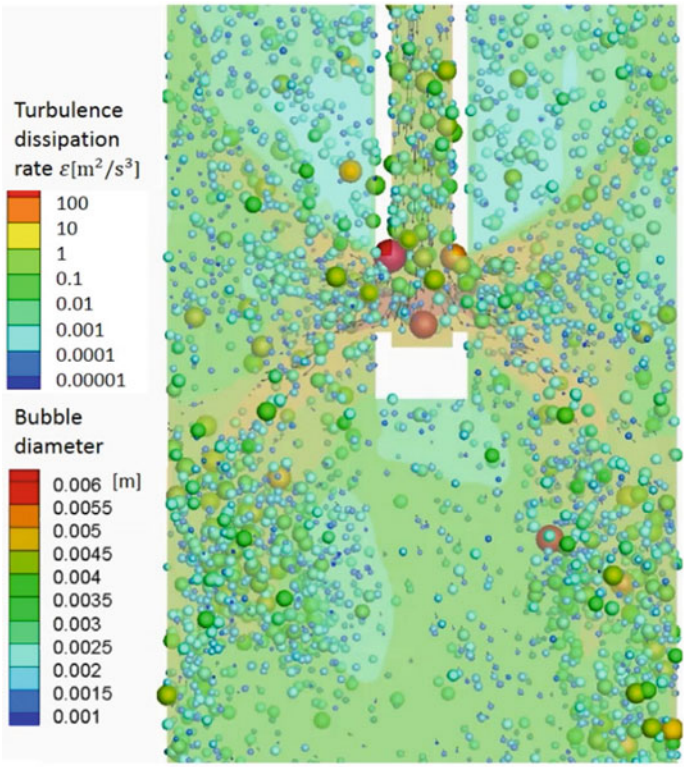

Fig. 7 DPM bubble distribution with turbulence dissipation rate field near the bottom of the nozzle at t = 22.23 s

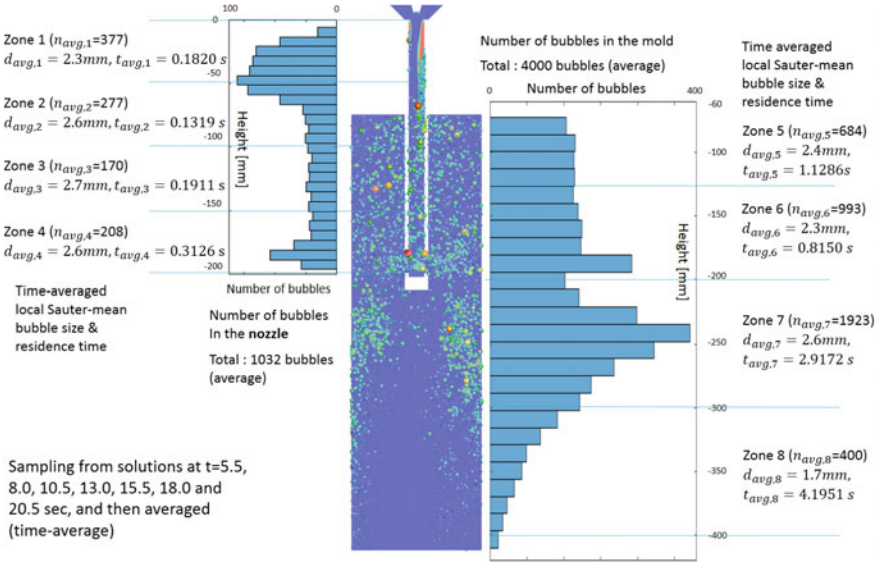

Fig. 8 Number, size and residence time of DPM bubbles in the domain

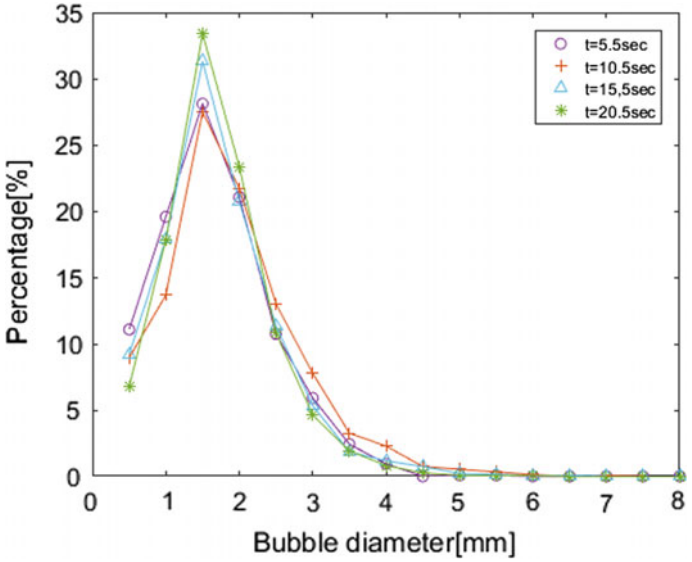

Fig. 9 Transition of bubble size distribution by time

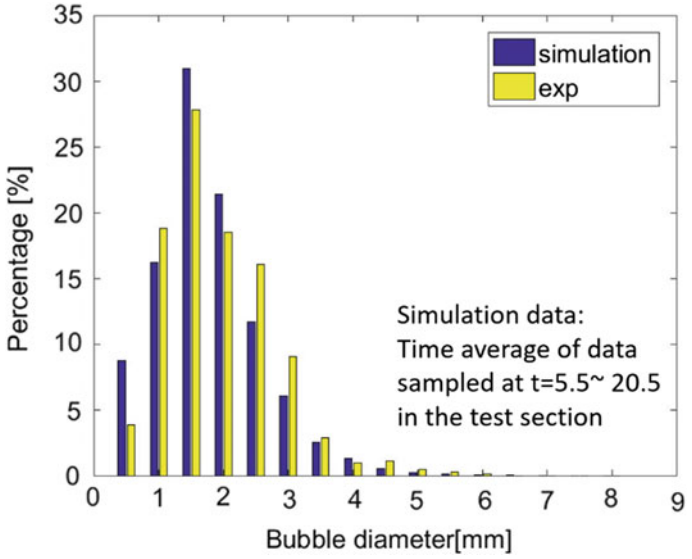

Fig. 10 Comparison of bubble size distribution to the measurement

Conclusions

The lab-scale stopper rod system is simulated through the new hybrid model EEDPM. The complex behavior of argon gas in the process is modeled, including formation of argon gas pockets, intermittent shearing off of the gas pockets, volumetric expansion, coalescence and breakup of bubbles. Those models are validated by comparison with the measured bubble size distribution in the mold. This model is able to simulate realistic phenomena observed in the experiment such as intermittent floatation of big bubbles near the narrow face in the lower mold by the serial coalescence, and breakup of big bubbles at the bottom of the nozzle port by the swirl development. The turbulent dissipation rate strongly affects the bubble size distribution through the maximum stable bubble size in the breakup model. The majority of bubbles have d = $1 \sim 3$ mm corresponding to the average turbulence dissipation rate $\varepsilon = 1 \sim 10 \mathrm{m}^2/s^3$ in the nozzle flow. Due to the balance of all of the phenomena changing the bubble size, the bubble size distribution does not change much by time.

Acknowledgements This work was supported by the National Science Foundation (Grant No. CMMI 15-63553) and the Continuous Casting Consortium, University of Illinois at Urbana-Champaign, USA.

Nomenclature

Symbols

A_{int} Interface area of gas pocket, d: diameter of a bubble, $\boldsymbol{F}$: force, $\boldsymbol{g}$: gravity

m_b Mass of a bubble, N: total number of bubble created by shearing off p: pressure

R Random number between 0 and 1, r: bubble radius, t: time, $\boldsymbol{u}$: velocity field, u: velocity magnitude, $\bar{u}_\lambda$: eddy velocity, V: volume, $\boldsymbol{v_i}$: velocity of ith DPM bubble, $\boldsymbol{v_i'}$: velocity of i-th DPM bubble after collision

We_c Critical Weber number, $\boldsymbol{x_i}$: ith DPM bubble velocity, α: EE volume fraction field

α^* Approximated volume fraction field, μ: viscosity, ρ: density, ε: liquid turbulence dissipation rate

σ Surface tension coefficient, δ_g^*: sheared off gas layer thickness

$\sum_{j=1}^{N}$ Summation of sheared off bubbles created in one shearing off process

Subscripts

k and q	Arbitrary phase (gas or liquid), B: buoyancy, D: drag, g: gas, l: liquid, lf: liquid film
N	Normal, t: tangent, new: new position, old: old position, P: pressure gradient, p: parent bubble
SO	Sheared off, V: virtual mass, 1: smaller bubble in a pair, 2: larger bubble in a pair
3	Created bubble by coalescence

References

1. Liu Z, Qi F, Li B, Jiang M (2014) Multiple size group modeling of polydispersed bubbly flow in the mold: an analysis of turbulence and interfacial force models. Metall Mater Trans B 46:933–952
2. Jin K, Thomas BG, Ruan X (2015) Modeling and measurements of multiphase flow and bubble entrapment in steel continuous casting. Metall Mater Trans B 47:548–565
3. Timmel K, Shevchenko N, Röder M, Anderhuber M, Gardin P, Eckert S, Gerbeth G (2014) Visualization of liquid metal two-phase flows in a physical model of the continuous casting process of steel. Metall Mater Trans B 46:700–710
4. Harlow FH, Amsden AA (1975) Numerical calculation of multiphase fluid flow. J Comput Phys 17:19–52
5. Riley JJ (1974) Diffusion experiments with numerically integrated isotropic turbulence. Phys Fluids 17(2): 292–297
6. Yang H, Vanka SP, Thomas BG (2017) Hybrid eulerian eulerian discrete phase model of turbulent bubbly flow. In: Proceedings of the ASME 2017 international mechanical engineering congress & exposition, ASME. Tampa, Florida
7. Tomiyama A, Kataoka I, Zun I, Sakaguchi T (1998) Drag coefficients of single bubbles under normal and micro gravity conditions. JSME Int J Ser B 41:472–479
8. Yang H, Thomas BG (2017) Multiphase flow and bubble size distribution in continuous casters using a hybrid EEDPM model. STEELSIM 2017, Quingdao, China
9. Hesketh RP, Etchells AW, Russell TWF (1991) Experimental observations of bubble breakage in turbulent flow. Ind Eng Chem Res 30:835–841
10. Luo H, Svendsen HF (1996) Theoretical model for drop and bubble breakup in turbulent dispersions. AIChE J 42:1225–1233
11. Wang T, Wang J, Jin Y (2003) A novel theoretical breakup kernel function for bubbles/droplets in a turbulent flow. Chem Eng Sci 58:4629–4637
12. Prince MJ, Blanch HW (1990) Bubble coalescence and break-up in air-sparged bubble columns. AIChE J 36:1485–1499
13. Liao Y, Lucas D (2009) A literature review of theoretical models for drop and bubble breakup in turbulent dispersions. Chem Eng Sci 64:3389–3406
14. Evans GM, Jameson GJ, Atkinson BW (1992) Prediction of the bubble size generated by a plunging liquid jet bubble column. Chem Eng Sci 47:3265–3272

CFD Modeling of Transport Phenomena and Inclusion Removal in a Gas-Stirred Ladle

Qing Cao and Laurentiu Nastac

Abstract A three-dimensional, transient CFD modeling approach has been developed to predict the multiphase fluid flow, slag-steel interface characteristics and inclusion removal in a gas-stirred ladle with taking the fluctuant top slag layer into account. The comparison with experimental data indicates that the model can accurately predict the slag-steel interface and slag eye characteristics. The discrete phase model was used to trace the individual inclusion movement through particle trajectory. Finally, the contribution of different removal mechanisms on the inclusion removal was investigated. The results show that the slag capture is the prevailing mechanism for inclusion removal. The bubble-inclusion attachment also helps remove a considerable amount of inclusions, while the inclusion removal ratio by wall adhesion is quite low.

Keywords CFD modeling · Ladle metallurgical furnace · Gas stirring
Fluid flow · Slag eye · Inclusion removal

Introduction

A significant amount of nonmetallic inclusions is generated in the metallurgical reactor during the steelmaking process. These inclusions would produce void nucleation, surface defects and initiate fatigue cracks, affecting the weldability, tensile strength and workability of the final steel products [1, 2]. With the increasing demands for the high quality steel year by year, the inclusion removal has become one of the main objectives in the steelmaking industry.

Q. Cao · L. Nastac (✉)
Department of Metallurgical and Materials Engineering, The University of Alabama, 870202, Tuscaloosa, AL 35487, USA
e-mail: qcao3@crimson.ua.edu

L. Nastac
e-mail: lnastac@eng.ua.edu

L. Nastac et al. (eds.), *CFD Modeling and Simulation in Materials Processing 2018*, The Minerals, Metals & Materials Series,
https://doi.org/10.1007/978-3-319-72059-3_13

Computational fluid dynamics (CFD) modeling is considered as the most effective way to predict the fluid flow and thermodynamic phenomenon in the gas-stirred ladles. Over the past decades, many mathematical simulation studies were conducted to describe the inclusion evolution process during ladle treatments [3–5]. Generally, the inclusions in steel are removed mainly by three mechanisms, namely slag capture, wall adhesion, and bubble attachment. Gas stirring is commonly performed to promote the inclusion removal process in industrial ladle operations [6]. In addition, the slag phase characteristic and slag-steel interfacial area are also critical factors for inclusion removal.

The purpose of this study is to develop a numerical model to describe the movement and removal of inclusions under gas stirring by taking into account the effects of slag phase on the fluid flow and the slag-steel interface.

Mathematical Model

Simulations were carried out using the VOF-DPM (Volume of Fluid-Discrete Phase Model) coupled CFD model available in ANSYS's Fluent [7]. The mathematical model for the fluid flow and inclusion removal was based on the following assumptions:

(a) The liquid phases are Newtonian, viscous and non-miscible, and the fluid flow in the ladle is isothermal.
(b) Inclusions are assumed to be spherical and their density is the same as that of the alumina particles.
(c) Initially, the inclusions are supposed to be uniformly distributed in the bulk steel. It is also assumed that there is no interaction among inclusions.
(d) The inclusions are removed mainly by three mechanisms: floating to the slag-steel interface and captured by the slag, adhesion to the ladle wall, and attachment to the bubbles. At the ladle wall, only a part of inclusions with a velocity smaller than the critical velocity are adhered and the critical velocity is determined based on Ref. [8]. The probability of inclusion attachment to a bubble is determined according to Ref. [6].

DPM Model. The DPM method [7] was used to calculate the trajectory of both the gas bubbles and the inclusions by solving the force balance on each particle within a Lagrangian reference frame.

Discrete random walk model was applied to account for the effects of turbulent dispersion on the discrete particles. Two-way turbulence coupling was implemented to facilitate the momentum transfer between the discrete and the continuous phases. This was accomplished by adding a momentum transfer source in the continuous phase momentum equation [9].

Table 1 The ladle dimensions and other parameters employed in the model

Diameter of ladle (up)	3100 mm	Density of inclusions	3900 kg/m^3
Diameter of ladle (down)	2660 mm	Diameter of the two off-centered plugs	0.092 m
Height of ladle	3500 mm	Viscosity of slag	0.03 kg/(m s)
Argon gas flow rate	1 L/s	Viscosity of steel	0.006 kg/(m s)
Thickness of slag	150 mm	Viscosity of argon	2.125×10^{-5} kg/(m s)
Density of liquid steel	7020 kg/m^3	Interfacial tension between steel and gas	1.4 N/m
Density of slag	3500 kg/m^3		

Gas Density and Bubble size. In the computation domain, the density and the diameter of the gas bubbles were calculated at each position according to the local pressure and the temperature, using the ideal gas law.

Multiphase Flow Model. The VOF model was applied for describing the continuous phases and for tracking the interface among the liquid steel, slag, and top air phases [10]. The realizable k-ε turbulence model is chosen to account for the multiphase turbulence flow. A more detailed description for the model can be found in the Ref. [11].

Boundary conditions. The ladle dimensions and other parameters employed in the model are shown in Table 1. The geometry and mesh used to study the removal of inclusions is displayed in Fig. 1. Initially, the slag layer rests on the top of the steel bath, and the inclusions are considered to be uniformly distributed in the bulk steel. The argon gas is injected from the bottom plugs and the injected velocity is calculated according the gas flow rate [11]. The pressure outlet boundary condition is used at the top surface of the ladle, where the gas bubbles are allowed to escape.

Results and Discussion

Figure 2 shows the slag-steel interface and the open eyes predicted by the CFD model. Recently, Krishnapisharody and Irons [12] proposed a mathematical model to estimate the open-eye area in gas-stirred ladles based on the analysis of a large number of experiments, in which the dimensionless open-eye area (Ae*/Ap*) fits a linear relationship with the parameter $(1-\rho^*)^{-\frac{1}{2}}(Q^*)^{\frac{1}{3}}(H/h)^{1/2}$. The terms in this equation are explained in Ref. [12]. A quantitative comparison of the predicted non-dimensional open-eye area ratio in this study against the experimental results collected by Krishnapisharody and Irons [12] is shown in Fig. 3. The model appears to capture the appropriate influences of the ladle operating variables on the eye formation and to be comparable with the experimental data.

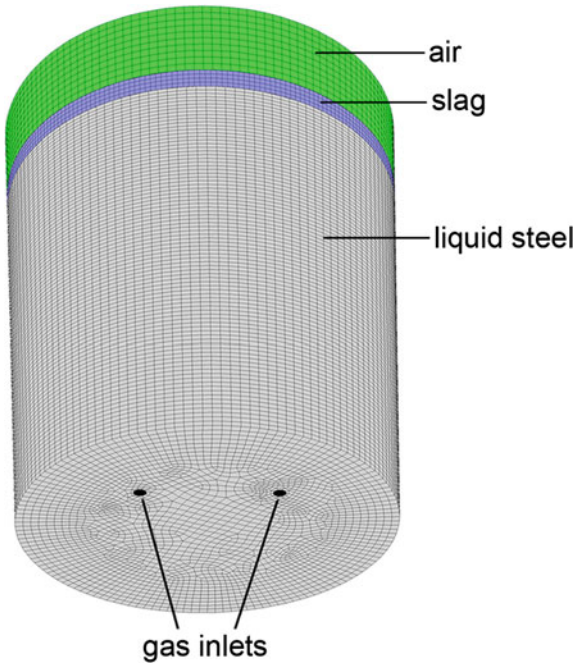

Fig. 1 The geometry and mesh used in the model

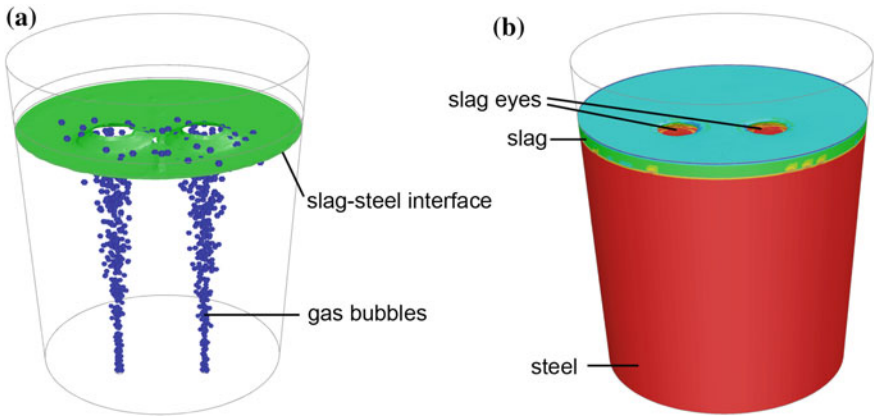

Fig. 2 **a** The slag-steel interface and **b** the open eyes under gas stirring predicted by CFD model

Figure 4 displays the variation of the inclusion distribution and their velocity magnitude with time. The diameter of the inclusions is 1 μm and the gas flow rate is 1 L/s in this case. It can be seen that the inclusion number density in steel decreases over time. The inclusions are sparser in the upper region of the bulk steel under

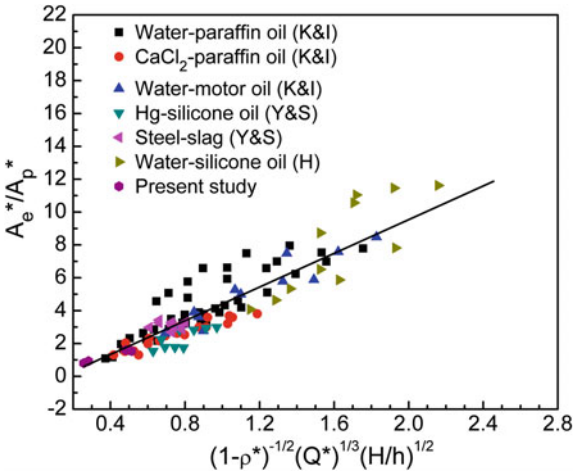

Fig. 3 Comparison of the predicted dimensionless open-eye area (Ae*/Ap*) versus the parameter $(1-\rho^*)^{-\frac{1}{2}}(Q^*)^{\frac{1}{3}}(H/h)^{1/2}$ with the available experimental data (K&I: Krishnapisharody and Irons [13]; Y & S: Yonezawa and Schwerdtfeger [14]; Han et al. [15])

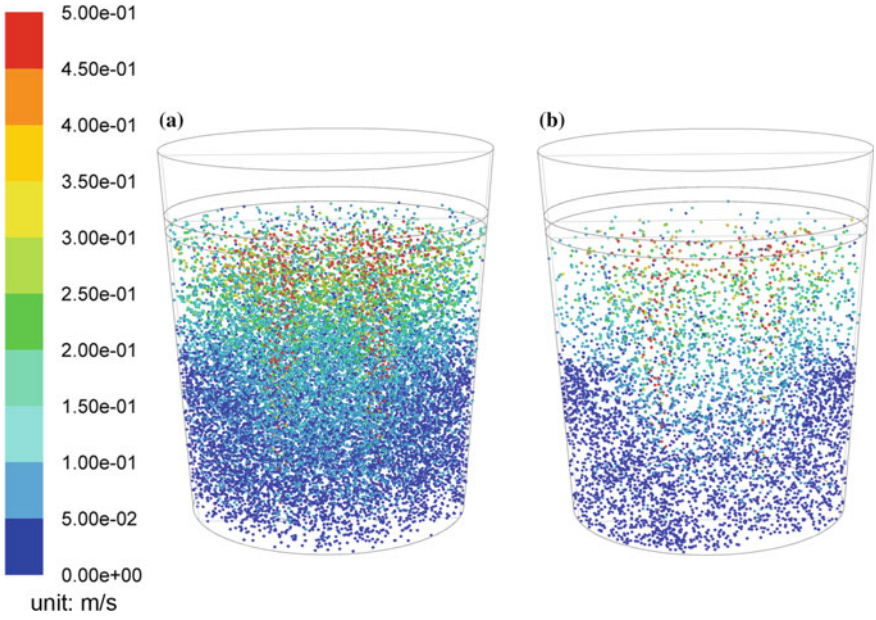

Fig. 4 The inclusion distribution in the steel after **a** 20 s, **b** 150 s (the color scale represents the velocity magnitude of the inclusions)

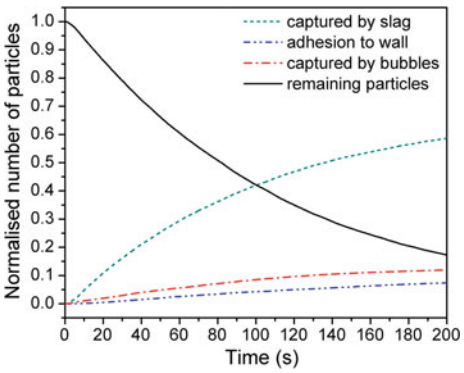

Fig. 5 Predicted evolution of the inclusion removal with time under the gas flow rate of 1 L/s

gas-stirring. The velocity of the inclusions obviously improves near the gas plume region because of the strong upward steel flow and bubble wake flow. The gas bubble flow accelerates the transport of the inclusions to the slag-steel interface where they may be captured by slag. Below the slag-steel interface, the steel flow brings the inclusions toward the ladle wall. Some of the inclusions may impact and adhere to the ladle wall, while some of them would follow the circulation steel flow and move downward toward the bottom.

Figure 5 shows the time evolution of the entrapment ratio of inclusions by different removal mechanisms. It is shown that the slag capture is the prevailing mechanism for inclusion removal; the bubble-inclusion attachment also helps remove a considerable amount of inclusions. Therefore, the effect of gas bubbles on the inclusion removal is non-negligible. While the inclusion removal ratio by wall adhesion is quite low. Venturini [8] has demonstrated that as the particle size increases, the critical velocity for a particle sticking to the wall surface largely decreases. Thus, for the inclusions larger than 1 μm, the probability of wall adhesion would be much lower.

Conclusions

A fully transient 3D CFD modeling approach capable of predicting the multiphase fluid flow, the inclusion transport and removal in the gas-stirred ladle was developed by taking the fluctuant top slag layer into account. The modeling results show that the model can predict reasonably well the slag-steel interface and slag eye characteristics inside the ladle. The transport of inclusions in the ladle is predicted by tracing the individual inclusion movement. The results indicate that the slag capture is the prevailing mechanism for inclusion removal; the bubble-inclusion attachment also aids in the removal of a considerable amount of inclusions; while the inclusion removal ratio by wall adhesion is quite low.

References

1. Lou WT, Zhu MY (2013) Numerical simulations of inclusion behavior in gas-stirred ladles. Metall Mater Trans B 44B:762–782
2. Geng DQ, Lei H, He JC (2010) Numerical simulation for collision and growth of inclusions in ladles stirred with different porous plug configurations. ISIJ Int 50:1597–1605
3. Kang YJ, Yu L, Du SC (2007) Study of inclusion removal mechanism around open eye in ladle treatment. Ironmak. Steelmak 34:253–261
4. Hallberg M, Jonsson PG, Jonsson TLI, Eriksson R (2005) Process model of inclusion separation in a stirred steel ladle. Scand J Metall 34:41–56
5. O'Malley RJ (2017) Inclusion evolution and removal in ladle refining. Paper presented at the AISTech 2017 conference and exposition, Nashville, TN, 8–11 May 2017
6. Zhang L, Aoki J, Thomas BG (2004) Inclusion removal by bubble flotation in continuous casting mold. In: MS&T 2004 conference proceedings, New Orleans, LA, pp 161–177
7. ANSYS FLUENT 17.1: User's guide. ANSYS, Inc.
8. Venturini P (2010) Modelling of particle wall-deposition in two phase gas-solid flows. PhD thesis, Sapienza University of Rome
9. Xu YG, Ersson M, Jönsson PG (2016) A numerical study about the influence of a bubble wake flow on the removal of inclusions. ISIJ Int 56:1982–1988
10. Cao Q, Pitts A, Nastac L (2016) Numerical modelling of fluid flow and desulphurisation kinetics in an argon-stirred ladle furnace. Ironmak. Steelmak. Accessed online 07 Dec 2016
11. Nastac L, Zhang DJ, Cao Q, Pitts A, Williams R (2016) 3D CFD modelling of the LMF system. Paper presented at the 145th TMS annual meeting, Nashville, TN
12. Krishnapisharody K, Irons GA (2008) An extended model for slag eye size in ladle metallurgy. ISIJ Int 48:1807–1809
13. Krishnapisharody K, Irons GA (2006) Modeling of slag eye formation over a metal bath due to gas bubbling. Metall Mater Trans B 37B:763–772
14. Yonezawa K, Schwerdtfeger K (1999) Spout eyes formed by an emerging gas plume at the surface of a slag-covered metal melt. Metall Mater Trans B 30B:411–418
15. Han JW, Heo SH, Kam DH, You BD, Pak JJ, Song HS (2001) Transient fluid flow phenomena in a gas stirred liquid bath with top oil layer-approach by numerical simulation and water model experiments. ISIJ Int 41:1165–1173

An Innovative Modeling Approach for Predicting the Desulfurization Kinetics in an Argon-Stirred Ladle Furnace

Qing Cao and Laurentiu Nastac

Abstract The ladle metallurgical furnace (LMF) is one of the most important secondary steel refining equipment to remove inclusions and produce clean low-sulfur steel. With the increasing demand for high desulfurization efficiency in the LMF process, it is very useful to predict the slag-steel interaction and the desulfurization behavior for providing assistance in the industrial process control. In this study, a modeling analysis tool for predicting the slag-metal reactions and desulfurization kinetics in gas-stirred ladles has been developed. The model consists of two uncoupled components: (i) a computation fluid dynamics (CFD) model for predicting fluid flow and slag-steel interface characteristics, and (ii) a multicomponent reaction kinetics model for predicting desulfurization. The slag eye behavior, slag-steel interface area, and mass transfer rates in the LMF were simulated by the CFD model. The desulfurization kinetics were predicted using the CFD simulation results together with the thermodynamic calculations. This approach is validated in terms of the evolution of the sulfur content based on industrial data. As the model can considerably decrease the computational time and cost for the analysis of the sulfur evolution during the LMF processing, it would be a very useful tool for the steel industry for quick and accurate predictions of the sulfur evolution in the ladle refining process.

Keywords Ladle furnace · Uncoupled modeling approach · Slag-metal reactions Mass transfer rates · Desulfurization

Q. Cao · L. Nastac (✉)
Department of Metallurgical and Materials Engineering, The University of Alabama, Box 870202, Tuscaloosa, AL 35487, USA
e-mail: lnastac@eng.ua.edu

Q. Cao
e-mail: qcao3@crimson.ua.edu

L. Nastac et al. (eds.), *CFD Modeling and Simulation in Materials Processing 2018*, The Minerals, Metals & Materials Series,
https://doi.org/10.1007/978-3-319-72059-3_14

Introduction

Steel alloys with ultralow sulfur contents are widely used in the manufacturing pipes for transporting oil and construction of offshore platforms, which require high impact strength and resistance to lamellar crack formation [1]. With the higher requirement of steel quality, there is an increasing demand for low-sulfur steel (below 0.005% and even below 0.001%) [2]. Ladle metallurgical furnace (LMF) is one of the most important secondary steel refining units in which various phenomena such as deoxidation, desulfurization, inclusion removal, and homogenization of alloy composition take place.

The gas-stirring is of enormous importance during LMF operations in steelmaking [3, 4]. The bubbly plume flow is produced by blowing inert gas through the ladle bottom plug, which yields steel flow circulation in the ladle, homogenize the temperature and composition of the melt, enhance the mass transfer of the species and promote slag-metal reactions [5, 6]. The rising bubbly plume can also create a raised area or "spout" at the bath surface, exposing an open area of liquid metal to the atmosphere, known as the "slag eye" [7]. The rising gas bubbles also stir the slag layer, and create the slag-steel mixing region, which significantly increases the contact area between slag and molten steel.

The interfacial thermodynamic equilibrium and the kinetic mass transfer coefficients are important factors for desulfurization prediction model. Since the temperature of the melt in LMF is extremely high, it is almost impossible to measure the actual interfacial area and assess turbulent flows in gas-stirred ladles during plant operations. Thus, it is desired to develop a mathematical model to predict the slag-steel interaction and desulfurization behavior to assist the industrial process control.

In this study, we employed a computational fluid dynamics (CFD) model to predict the turbulence flow, slag-steel interfacial area and species mass transfer in gas-stirred ladle furnace. Then the slag-steel interfacial area and mass transfer rates obtained by CFD model would be used to compute interfacial thermodynamic equilibrium for predicting desulfurization reactions.

Model Description

The following model assumptions are made in the simulation.

- The chemistry and temperature of slag and metal phases are assumed homogeneously distributed.
- All the chemical reactions occur very fast. Thermodynamic equilibrium is assumed at slag/steel interface.
- Interactions between ladle refractory and slag/metal phases is neglected.

CFD Model

A three-dimensional, transient CFD modeling approach capable of predicting the multiphase fluid flow characteristics and steel-slag interfacial area is developed. The multiphase volume of fluid (VOF) model is applied for tracking the interfaces among argon gas, steel, slag and air phases.

The continuity equation of the qth phase is described in the following form [8, 9]:

$$\frac{1}{\rho_q}\left[\frac{\partial}{\partial t}\left(\alpha_q \rho_q\right) + \nabla \cdot \left(\alpha_q \rho_q \overrightarrow{v_q}\right)\right] = 0 \tag{1}$$

where the volume fraction α_q is constrained by $\sum_{q=1}^{n} \alpha_q = 1$.

The momentum equation expressed as Eq. (2) is dependent on the volume fractions of all phases through the properties ρ and μ.

$$\frac{\partial}{\partial t}(\rho\vec{v}) + \nabla \cdot (\rho\vec{v}\vec{v}) = -\nabla p + \nabla \cdot \left[\mu\left(\nabla\vec{v} + \nabla\vec{v}^T\right)\right] + \rho\vec{g} \tag{2}$$

where the ρ is the density of mixture, $\vec{v}$ is the underlying velocity field, p is the local pressure, and μ is the effective viscosity.

Realizable k-ε turbulence model was chosen to account for multiphase turbulence flow in the current model [10]. The standard wall functions were used as near-wall treatments for wall-bounded turbulent flows. The mass transfer coefficient in steel, k_m, can be calculated through the Kolmogorov theory of isotropic turbulence as follows:

$$k_m = cD_m^{0.5}\left(\frac{\varepsilon_l}{\nu}\right)^{0.25} \tag{3}$$

where c is a constant and is 0.4 for this work. Dm is the diffusion coefficients of the species in liquid steel as described by Lou and Zhu [11]. ε_l is turbulent energy dissipation rate and ν is kinematic viscosity.

The overall mass transfer coefficient of element i is calculated as

$$m_{eff,i} = \frac{k_{m,i}k_{s,i}L_i\rho_s}{k_{s,i}L_i\rho_s + \rho_m k_{m,i}} \tag{4}$$

where $k_{m,i}$, $k_{s,i}$ are the mass transfer coefficient of species i in liquid steel and slag, respectively.

$$k_{s,i} = 0.1k_{m,i} \tag{5}$$

Desulfurization Kinetics Modeling Approach

The desulfurization process occurs by transferring sulfur dissolved in bulk steel to slag/steel interface where it will react with oxygen from the slag and be removed.

$$\left(O^{2-}\right) + [S] = [O] + \left(S^{2-}\right) \tag{6}$$

Because of the high temperature of the molten melt, thermodynamic equilibrium will occur very quickly at the slag/steel interface. Thus the limiting factors of reaction kinetics in argon-stirred ladles are not chemical reaction rate but the mass transfer rates of species in the melt to slag/steel interface.

By combining the rate-limiting effects of mass transfers in both slag and steel phases, the removal rate of sulfur in steel can be expressed by an overall mass transfer coefficient:

$$RR_S = m_{eff,S}\left(\frac{A}{V}\right)\left\{[wt.\%S] - \frac{(wt.\%S)}{L_S}\right\} \tag{7}$$

where A and V are the interface area of slag/metal phases and the steel volume at the interfacial region, respectively, $m_{eff,S}$ characterizes the overall mass transfer coefficient of sulfur. L_S is the equilibrium distribution ratio of sulfur between slag and steel phases. $[wt.\%S]$ and (wt%S) is mass fraction of sulfur in liquid steel and slag, respectively. The mass transfer coefficients and slag/steel interface area are obtained by CFD model.

The desulfurization evolution in the LMF is calculated by using the Microsoft Excel. The theory for computing thermodynamics properties such as sulfide capacity, optical basicity, sulfur distribution ratio, activity of species in steel and slag are illustrated in detail in Refs. [12] and [13].

Results and Discussion

Kinetic Results by CFD Model

Figure 1a shows the predicted open slag eyes. The predicted size of slag eyes is in reasonable agreement with the experimental observations (see Fig. 1b). Figure 2 displays the velocity vector of the fluid flow inside the ladle. The flow buoyancy from the injected gas causes high upward-directed steel velocities in the ladle. The upwelling steel pushes slag towards ladle wall, forming slag eyes. Outside the open eyes, the steel flows along the slag/steel interface. When the steel flow reaches the ladle wall, it is directed downward toward the bottom, causing circulation loops in

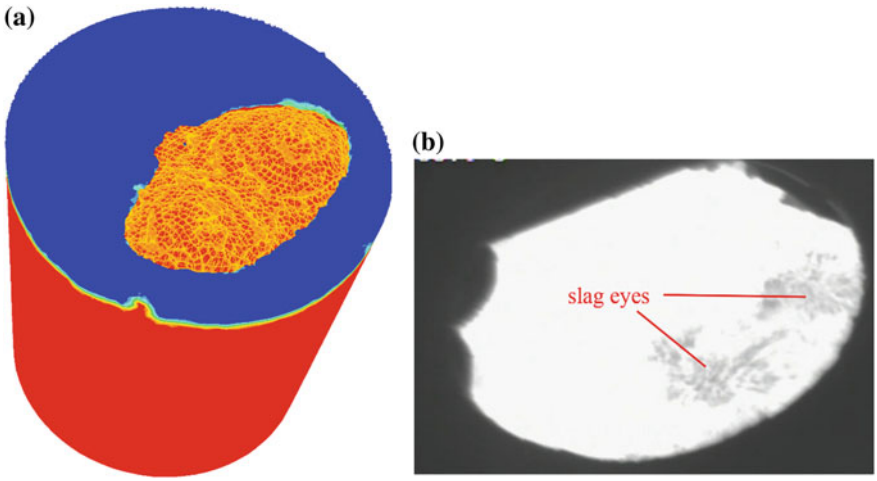

Fig. 1 Open slag eye in the ladle: **a** simulated result, **b** experimental observation

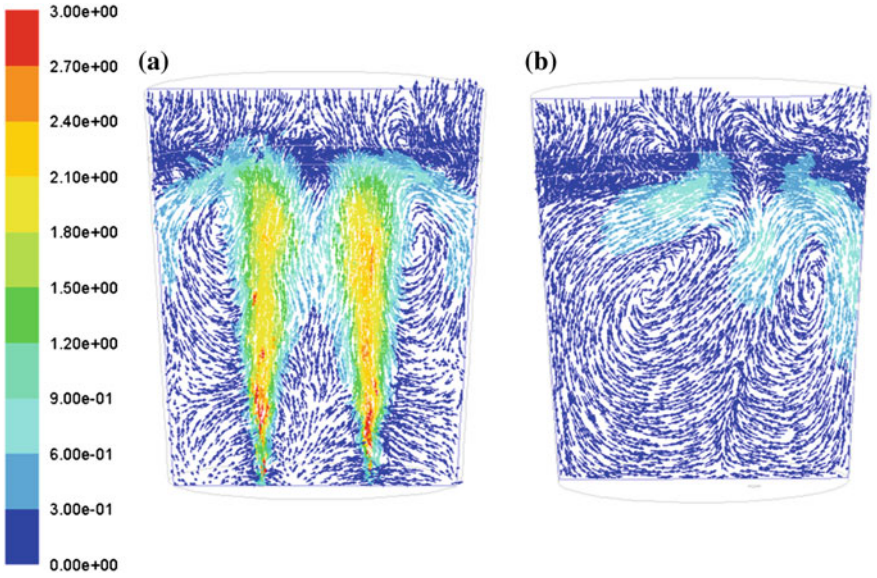

Fig. 2 The velocity vectors of: **a** the two-plug section plane and **b** the symmetry plane of the ladle perpendicular to the two-plug section plane (legend units: m/s)

the ladle. Figure 3 illustrates the velocity vector of slag eye and the slag-steel interface predicted by CFD model, which reflects the fluid flow behavior inside and outside spout eye. The velocity vectors at the slag-steel interface are not horizontal. Slag-steel interface shows non-flat and wavelike shape.

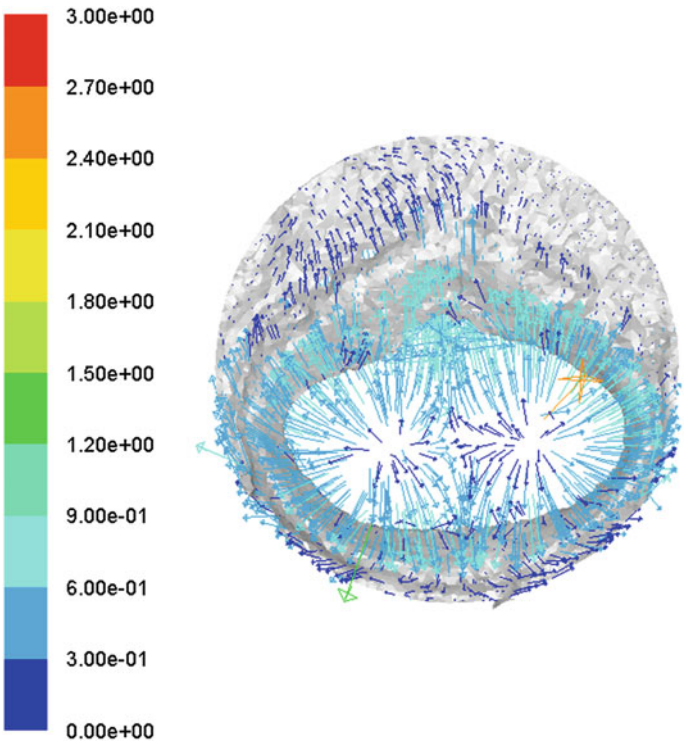

Fig. 3 The velocity vector in the slag eye and at the slag-steel interface predicted by the CFD model (legend units: m/s)

Desulfurization Predictions

Desulfurization predictions were conducted by a postprocessing spreadsheet-based model using thermodynamic equations as well as the mass transfer coefficients and the slag/steel interface area obtained from the CFD simulation. Validation of the desulfurization results were carried out for a LMF case. The dimensions and operating conditions of the experimental LMF process are presented in a previous study [12].

Figure 4 compares the predicted average sulfur content in steel with the measured data as a function of time as well as the simulation results obtained by the CFD-desulfurization coupled model described in Ref. [12]. As it can be seen from Fig. 4, the trend of the sulfur content variation based on the post-processing calculations matches reasonably well the variation in the measured data. There are some differences between the current predicted results and the simulation data obtained by the CFD-desulfurization coupled model. The reason is that the CFD-desulfurization coupled model captures the compositional variations in the slag-steel mixing region. However, the CFD-desulfurization coupled model would require significantly higher

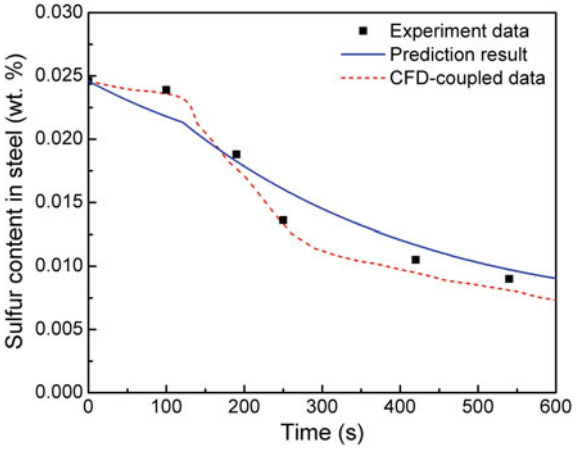

Fig. 4 Predicted and measured mass fraction of sulfur in molten steel with time

computational time and computational power. Therefore, the current desulfurization predictive approach is quite useful and inexpensive to quickly predict the sulfur content evolution during the LMF process.

Concluding Remarks

A three-dimensional, transient CFD modeling approach capable of predicting the multiphase fluid flow characteristics and the steel-slag interfacial area has been developed and validated against experimental data. The multiphase VOF model was applied for tracking the steel/slag interface. The fluid flow characteristics, slag-steel interfacial area and mass transfer rates in the ladle furnace were predicted by the CFD model. Desulfurization predictions were conducted by combining thermodynamic calculations as well as the mass transfer coefficients and the slag/steel interface area computed by the CFD model.

Because the desulfurization predictions were fully uncoupled from the CFD simulation, the computational time for the prediction of sulfur evolution was decreased by more than 100 times. Thus, this proposed approach would be quite useful, fast, and relatively inexpensive, yet accurate enough, for the steel industry to estimate the sulfur evolution during the LMF process.

References

1. Solecki M (2015) Mass transfer: advancement in process modelling. InTech. ISBN 9789535121923
2. Lehmann J, Nadif M (2011) Interactions between metal and slag melts: steel desulfurization. Rev Miner Geochem 73(1):493–511

3. Mazumdar D, Guthrie RIL (1995) The physical and mathematical modelling of gas stirred ladle systems. ISIJ Int 35(1):1–20
4. Krishnapisharody K, Irons GA (2015) A model for slag eyes in steel refining ladles covered with thick slag. Metall Mater Trans B 46(1):191–198
5. Ilegbusi OJ, Szekely J (1990) The modeling of gas-bubble driven circulations systems. ISIJ Int 30(9):731–739
6. Liu YH, Zhu H, Pan LP (2014) Numerical investigations on the slag eye in steel ladles. Adv Mech Eng 6:834103
7. Sahajwalla V, Castillejos AH, Brimacombe JK (1990) The spout of air jets upwardly injected into a water bath. Metall Mater Trans B 21(1):71–80
8. Li L, Liu Z, Cao M (2015) Large eddy simulation of bubbly flow and slag layer behavior in ladle with discrete phase model (DPM)–volume of fluid (VOF) coupled model. JOM 67 (7):1459–1467
9. Liu HP, Qi ZY, Xu MG (2011) Numerical simulation of fluid flow and interfacial behavior in three-phase argon-stirred ladles with one plug and dual plugs. Steel Res Int 82(4):440–458
10. Nastac L, Zhang D, Cao Q et al (2016) 3D CFD modeling of the LMF system. Paper presented at the 145th TMS Annual Meeting, Nashville, TN
11. Lou WT, Zhu MY (2015) Numerical simulation of slag-metal reactions and desulfurization efficiency in gas-stirred ladles with different thermodynamics and kinetics. ISIJ Int 55: 961–969
12. Cao Q, Pitts A, Nastac L (2016) Numerical modelling of fluid flow and desulphurisation kinetics in an argon-stirred ladle furnace. Ironmak. Steelmak 43:1–8
13. Cao Q, Pitts A, Nastac L (2017) CFD modeling of slag-metal reactions and sulfur refining evolution in an argon gas-stirred ladle furnace. Paper presented at the 146th TMS annual meeting, San Diego, California

Simulation of Non-metallic Inclusion Deposition and Clogging of Nozzle

Hadi Barati, Menghuai Wu, Tobias Holzmann, Abdellah Kharicha and Andreas Ludwig

Abstract Motion of non-metallic inclusions (NMIs) in molten steel and deposition of them on nozzle wall leading to clogging are simulated using a two-way coupling model. In this model different steps of clogging have been considered including transport of NMIs by turbulent melt flow towards the nozzle wall, adhesion of the NMI on the wall, and formation and growth of clogging material by the NMI deposition. The model is used to simulate clogging in a pilot scale device. The results show that the model reproduces these clogging steps well until complete blockage of the flow path in the nozzle. It is found that clog growth step plays critical role for prediction of the clogging process and understanding melt flow and NMI behaviors during the process. Without implementation of this step, unrealistic melt flow rate is obtained leading to incorrect particle deposition rate. In addition, if the clog growth is ignored, distribution of deposition material becomes more uniform with overestimated amount of total deposition mass.

Keywords Clogging · Non-metallic inclusion · Deposition · Nozzle
Steel casting

H. Barati · M. Wu · T. Holzmann (✉) · A. Kharicha · A. Ludwig
Chair for Modeling and Simulation of Metallurgical Processes, Department of Metallurgy, Montanuniversitaet Leoben, Franz-Josef Street 18, 8700 Leoben, Austria
e-mail: tobias.holzmann@unileoben.ac.at

H. Barati
e-mail: hadi.barati@unileoben.ac.at

M. Wu
e-mail: menghuai.wu@unileoben.ac.at

H. Barati
K1-MET, Franz-Josef Street 18, 8700 Leoben, Austria

L. Nastac et al. (eds.), *CFD Modeling and Simulation in Materials Processing 2018*, The Minerals, Metals & Materials Series,
https://doi.org/10.1007/978-3-319-72059-3_15

Introduction

Blockage of submerged entry nozzle (SEN) is a long-term problem in steel continuous casting. It can result in operation disruptions and different casting defects [1–3]. Among several mechanisms suggested for clogging, deposition of non-metallic inclusions (NMIs) as de-oxidation and re-oxidation products, e.g. Al_2O_3, on the SEN wall is considered as the primary reason [4], because similar morphologies and chemical compositions of NMIs were observed in the melt, clog material, and as-cast product [5].

Clogging generally occurs through four steps, as depicted in Fig. 1: (1) transport of particles to the wall, (2) interactions of the fluid and the particles with the wall, (3) formation and growth of the clog, and (4) probable fragmentation or resuspension of the clog.

High temperature, opaque nature of steel melt, and difficulties of precise control of steel casting make experimental investigation of the process very hard. Therefore, numerical modeling provides a helpful tool to study the clogging process. Diverse modeling efforts have been made for the clogging of SEN by emphasizing one or more critical steps of Fig. 1. Bai and Thomas [6] studied the effect of the clog on the flow through a slide-gate nozzle and Zhang et al. [1] investigated influence of blocking half of one out-port of the SEN. They manually changed the geometry of SEN to mimic the as build clog. To model clogging the Eulerian-Lagrangian approach is a common method which provides detailed information about particle and its trajectory. It was used to find correlations between SEN designs and clogging tendency [7], to study the influence of the velocity gradient of the melt flow and the turbulent kinetic energy on the particle deposition [8], and to investigate effects of SEN diameter on clogging [9]. Eulerian-Eulerian is also used to simulate the inclusion deposition rate in a SEN [10, 11].

Most of the modeling efforts about SEN clogging focused only on the fluid flow and particle transport, i.e. step 1 of Fig. 1, and other steps were ignored. Moreover,

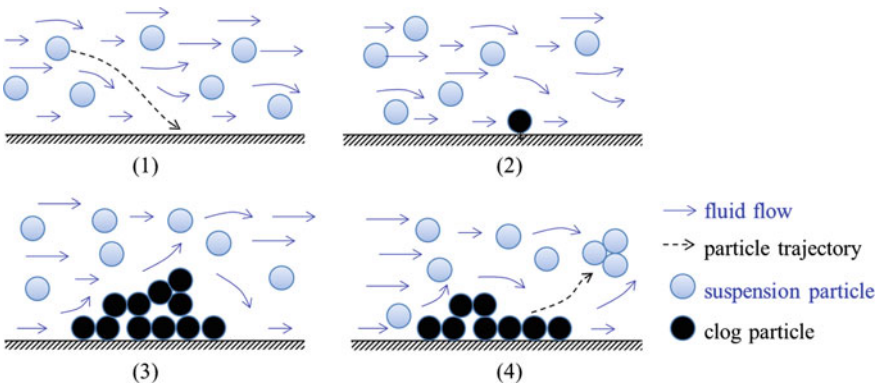

Fig. 1 Schematic of clogging phenomenon (four steps)

in previous simulations clogging was assumed as a steady process and SEN wall stays clean during the process. To the knowledge of authors, none of them has calculated mutual interactions of the clog growth with the melt flow. In the current paper a transient model has been proposed to simulate nozzle clogging in pilot scale by considering the further clogging step (steps 1–3). The current version of the model neglects fragmentation of the clog (step 4).

Model in Brief

In the present paper an Eulerian-Lagrangian model as developed by the authors [12] is used. The flow of the melt as the primary continuous medium is described by the conservation equations of mass and momentum. To model the turbulence, shear-stress transport (SST) k-ω model is adopted. The solid non-metallic inclusions are assumed as spherical particles and a force balance of buoyancy, drag, lift, virtual mass, and pressure gradient controls motion of them. The equations for the turbulent flow and forces acting on particle are listed in Tables 1 and 2, respectively.

Due to the different structure of flow in bulk and near the wall, a stochastic model [13], which is developed for particle motion in wall-bounded flow, is used for wall boundary cells.

Table 1 Governing equations for the fluid flow

Conservation equations		Symbol definition
Mass	$\nabla \cdot (\rho \vec{u}) = 0$	ρ: density of fluid (kg/m^3) μ: viscosity of fluid (kg m^{-1} s^{-1}) t: time (s) $\vec{u}$: velocity of fluid (m/s) k: turbulence kinetic energy (m^2 s^{-2}) ω: specific dissipation rate of turbulence kinetic energy (s^{-1}) Γ_k, Γ_ω: diffusivity for k and ω (kg m^{-1} s^{-1}, kg m^{-2}) $\tilde{G}_k$, G_ω: generation of turbulence kinetic energy for k and ω (kg m^{-1} s^{-3}, kg m^{-2} s^{-2}) Y_k, Y_ω: dissipation of k and ω (kg m^{-1} s^{-3}, kg m^{-2} s^{-2}) D_ω: cross-diffusion term of ω (kg m^{-2} s^{-2}) S_k, S_ω, $\vec{S}_u$: source term due to porous medium of clog (kg m^{-1} s^{-3}, kg m^{-2} s^{-2}, kg m^{-2} s^{-2})
Momentum	$\rho \frac{\partial \vec{u}}{\partial t} + \nabla \cdot (\rho \vec{u}\vec{u}) = -\nabla p + \nabla(\mu \nabla \cdot \vec{u}) + \vec{S}_u$	
Turbulence kinetic energy	$\rho \frac{\partial k}{\partial t} + \nabla \cdot (\rho k \vec{u}) = \nabla \cdot (\Gamma_k \nabla \cdot k) + \tilde{G}_k - Y_k + S_k$	
Specific dissipation rate	$\rho \frac{\partial \omega}{\partial t} + \nabla \cdot (\rho \omega \vec{u}) = \nabla \cdot (\Gamma_\omega \nabla \cdot k) + G_\omega - Y_\omega + D_\omega + S_\omega$	

Table 2 Equations for particle transport and forces acting on a particle in bulk flow

Equation		Symbols definition
Particle transport	$m_p \frac{d\vec{u}_p}{dt} = \vec{F}_B + \vec{F}_D + \vec{F}_L + \vec{F}_{VM} + \vec{F}_{press}$	$\vec{u}_p$: velocity of particle (m/s) m_p: mass of particle (kg) $\vec{g}$: gravity (m s^{-2}) ρ_p: density of particle (kg m^{-3}) d_p: diameter of particle (m) C_D: drag coefficient (–) Re_p: particle Reynolds number (–) U_s: difference between instantaneous streamwise velocities for fluid and particle (m s^{-1}) G: local velocity gradients (s^{-1}) J: correction factor of the lift force (–)
Buoyancy force	$\vec{F}_B = \frac{(\rho_p - \rho)\pi d_p^3}{6}\vec{g}$	
Drag force	$\vec{F}_D = \frac{1}{8}\pi d_p^2 \rho C_D \lvert\vec{u} - \vec{u}_p\rvert(\vec{u} - \vec{u}_p)$ $C_D = \begin{cases} \frac{24}{Re_p}, & \text{if } Re_p \le 0.1 \\ \frac{24}{Re_p}\left(1 + 0.15Re_p^{0.687}\right), & \text{if } 0.1 \le Re_p \le 10^3 \\ 0.44, & \text{if } Re_p > 10^3 \end{cases}$ $Re_p = \frac{\lvert\vec{u} - \vec{u}_p\rvert d_p \rho}{\mu}$	
Lift force	$\vec{F}_L = -\frac{9}{4\pi}\mu d_p^2 U_s \mathrm{sgn}(G)\left(\frac{\rho}{\mu}\lvert G\rvert\right)^{\frac{1}{2}} J$	
Virtual mass force	$\vec{F}_{VM} = \frac{\rho\pi d_p^3}{12}\frac{d}{dt}(\vec{u} - \vec{u}_p)$	
Pressure gradient force	$\vec{F}_{press} = \frac{\rho\pi d_p^3}{6}\frac{D\vec{u}}{Dt}$	

When a NMI meets the SEN wall, made of refractory or ceramic, the capillary force, also termed adhesion force, is the dominant force. Several studies concluded that once the capillary force is imposed, the particle stays in contact with the wall [14–16]. The model has considered a tricking probability of particles as they approaching wall. This sticking probability must be determined experimentally or using other models. In this paper, it is assumed to be 100%. To couple particle deposition with the fluid flow pattern, two stages are considered for clogging. In early stage, particle deposition leads to change in wall roughness, as shown in Fig. 2a, b. This stage lasts until the roughness height is larger than half of boundary cell thickness. Thereafter, in later stage, the computational cell is converted to a porous medium, marked in gray in Fig. 2c. Further deposition results in fully occupation of the cell by particles, as indicated by line pattern in Fig. 2d. Neighbor cells then are exposed to particle deposition. Hence, the clog material grows as a porous medium. Regarding to the permeability of the clog, Darcy source terms are applied for the clog region to take into account the effects of clog growth on the fluid flow. More details about the model can be found in [12].

Clogging in a pilot scale device which has been used to investigate the nozzle clogging [1, 17, 18] has been simulated. This device is made from a laboratory induction furnace and a circular nozzle with 5 mm diameter as situated at the bottom of the furnace. Molten steel flows through the nozzle until clogging in the nozzle stops the flow. Figure 3 shows mesh and boundary conditions. Regarding the physics controlling the process, multiphase fluid flow (melt and air) is modeled

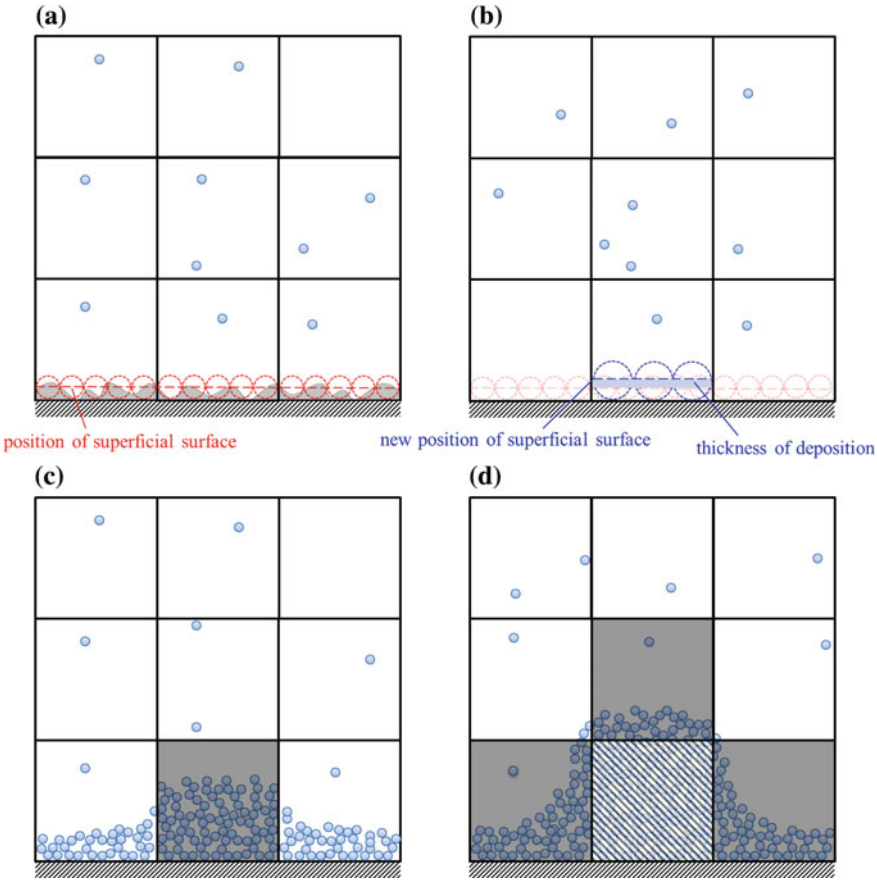

Fig. 2 Schematic illustration of clogging evolution in the model: **a** initial wall roughness considered as uniform sand-grain roughness, **b** enhanced wall roughness due to the particle deposition, **c** formation of porous clog, and **d** clog growth

using volume of fluid (VOF) method. On the top surface, pressure-inlet boundary condition is set for air, and for the nozzle outlet, pressure-outlet is imposed. Due to the gravity, the furnace becomes empty gradually. However, due to the clogging, the nozzle could be blocked before run out of the whole melt. Non-slip boundary condition is applied on all walls. To save computation costs and avoid unimportant calculation of particle tracking in the furnace, particles are injected on the connection plane between bottom of the furnace and top of the nozzle. A full 3D domain is simulated and the equations are numerically solved using commercial CFD code ANSYS-FLUENT with extended user defined functions (UDFs) for considering the growth of clog.

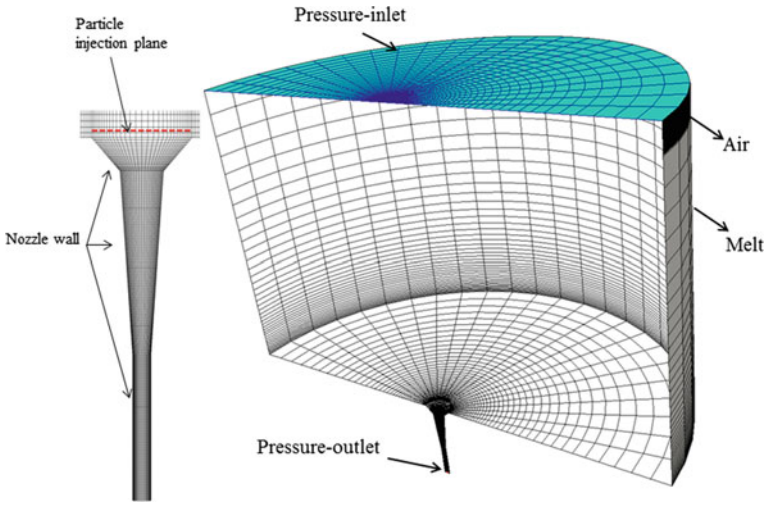

Fig. 3 Computational domain and boundary conditions. The initial interface between air and melt is plotted on the furnace wall

Results and Discussion

Clogging process and the clog growth are plotted in Fig. 4 by snapshots of the clog from different views. It shows that after 50 s a smooth layer of deposited material covers the nozzle wall. Continuous deposition of particles leads to formation of some bulges in narrowest section of the nozzle and a part of the middle section. Growth of the clog bulges finally blocks the flow passage as shown at 250 s.

In Fig. 5a velocity magnitude during the process is plotted on a vertical symmetry plane. The clog front is marked by solid lines and here the velocity magnitude in the clog material decreases because of its porous character. At 250 s the melt still flows due the small hole left in the clog, as shown in Fig. 4, however the value of the melt velocity is negligible. Figure 5b depicts a zoomed view of the flow field and the clog at 150 s. It shows how the presence of the clog changes the flow pattern. Some eddies can be found below bulges which may result in trapping of particles and finally attaching them to the clog. Therefore, it reveals that two-way coupling between flow field and particle deposition is critical to understand the clogging process.

To show the importance of clog growth in simulation of clogging, particle deposition results are compared with a case without effects of clog growth on the melt flow, i.e. particles are deleted from calculation once reach the nozzle wall and nozzle wall stays with constant roughness during the process. In Fig. 6 total deposition mass along height of the nozzle is shown for different times. The comparison of two graphs indicates that in both cases at first, deposition is almost uniform and then after 100 s becomes wavy. In the case (a) deposition mass decreases dramatically at $y = 0.040$ m when $t = 200$ s, while it happens at $y = 0.054$ m fore case (b).

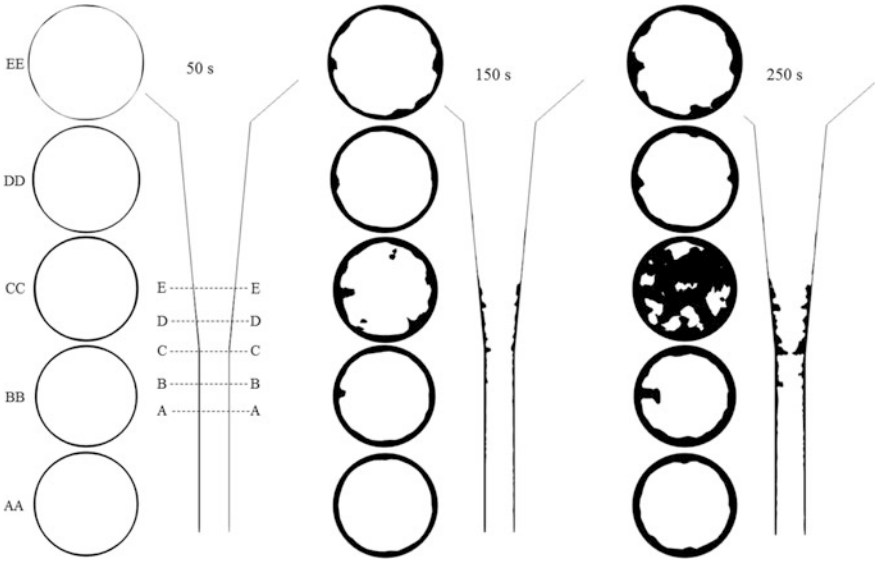

Fig. 4 Evolution of the clogging in the nozzle. Horizontal cross sections in different heights and the vertical sections are shown at different times

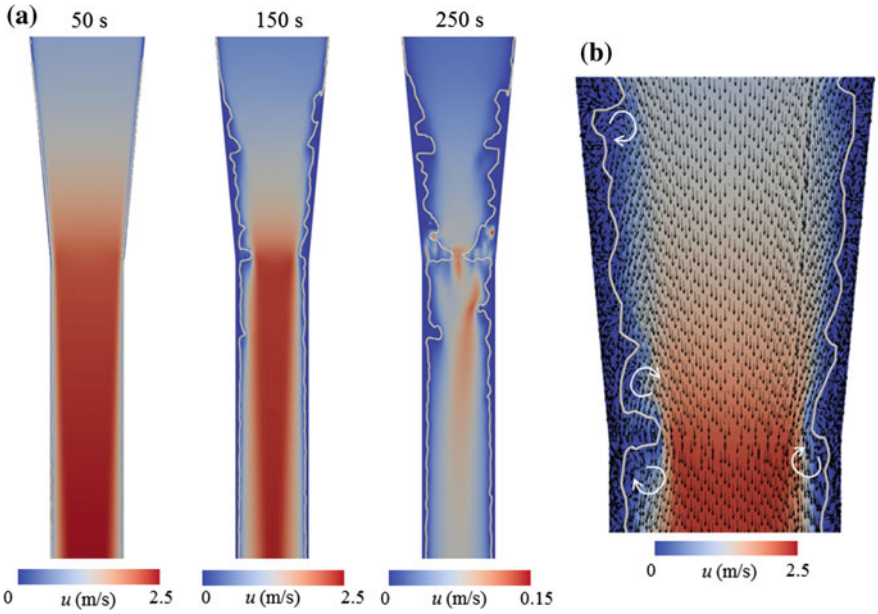

Fig. 5 Changes in melt velocity magnitude during clogging process (**a**) and zoomed view of flow arrows at 150 s (**b**). The clog front is marked by solid lines

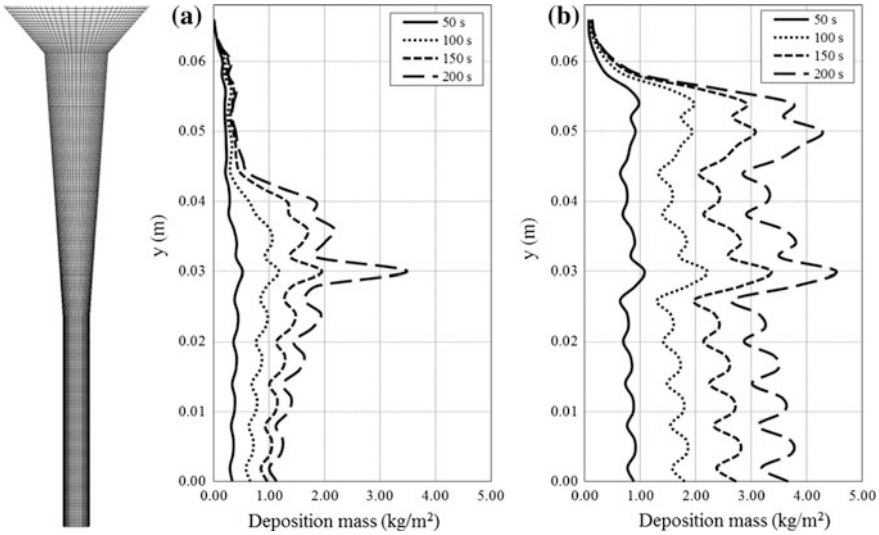

Fig. 6 Comparison of deposition mass along nozzle height during time with (**a**) and without (**b**) considering the clog growth

Moreover, the maximum deposition occurs at y = 0.03 m in case (a), whereas in case (b), maximum deposition happens at y = 0.03 and 0.05 m. The difference between deposition mass at maximum peak(s) and other positions in Fig. 6a is much larger than that in Fig. 6b. However without clog growth, case (a), initial deposition areas can be found, they may change after a while due to the change of the flow pattern, as found in case (b). The deposition mass values generally in Fig. 6b are larger than those in Fig. 6a. It is because of different melt flow rates in two cases, as shown in Fig. 7. In case (a), the melt flow rate decreases during the process because

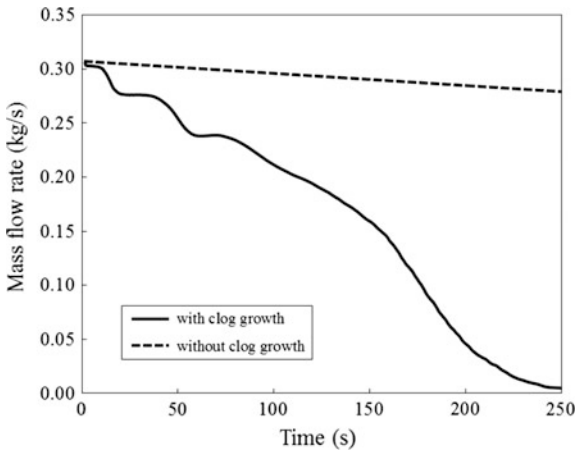

Fig. 7 Mass flow rate of the melt during the process with and without considering the clog growth

of narrowing of the flow passage in addition to hydrostatic pressure loss. While, in case (b), the only reason is the hydrostatic pressure loss. Therefore, simulation without considering clog growth leads to unrealistic results and would show incorrect time and region of nozzle blockage.

Conclusions

A two-way coupling model is used to simulate clogging in pilot scale. The model covers most of clogging steps, i.e. transport of particles by turbulent flow, deposition of particle on the wall, and growth of the clog due to the particle deposition. Interactions between particle deposition and fluid flow are taken into account in two stages: enhancement of wall roughness in early stage of particle deposition and development of clog as a porous medium in later stage. The simulation results declare that the model can reproduce clogging steps well particularly clog growth step. This step is critical to understand the clogging as a transient process. In the present pilot scale neglecting the clog growth leads to unrealistic high melt flow rate and hence incorrect particle deposition rate for whole process. Moreover, when the clog growth is ignored, distribution of deposition material on the nozzle is modeled much more uniform than that when the clog growth is considered in the simulation.

Acknowledgements The research leading to these results has received funding from the European Union's Research Fund for Coal and Steel (RFCS) research program under grant agreement No. RFSR-CT-2014-00009. The authors also gratefully acknowledge the funding support of K1-MET, metallurgical competence center. The research program of the K1-MET competence center is supported by COMET (Competence Center for Excellent Technologies), the Austrian program for competence centers. COMET is funded by the Federal Ministry for Transport, Innovation and Technology, the Federal Ministry for Science, Research and Economy, the provinces of Upper Austria, Tyrol and Styria as well as the Styrian Business Promotion Agency (SFG).

References

1. Zhang L, Wang Y, Zuo X (2008) Flow transport and inclusion motion in steel continuous-casting mold under submerged entry nozzle clogging condition. Metall Mater Trans B 39(4):534–550
2. Vermeulen Y, Coletti B, Blanpain B, Wollants P, Vleugels J (2002) Material evaluation to prevent nozzle clogging during continuous casting of Al killed steels. ISIJ Int 42(11): 1234–1240
3. Kojola N, Ekerot S, Jönsson P (2011) Pilot plant study of clogging rates in low carbon and stainless steel grades. Ironmak. Steelmak 38(2):81–89
4. Thomas BG, Bai H (2001) Tundish nozzle clogging-application of computational models. In: Proceedings of the 18th process technology division conference, Warrendale, Pennsylvania, 25–28 Mar 2001

5. Singh SN (1974) Mechanism of alumina buildup in tundish nozzles during continuous casting of aluminum-killed steels. Metall Trans 5(10):2165–2178
6. Bai H, Thomas BG (2001) Turbulent flow of liquid steel and argon bubbles in slide-gate tundish nozzles: part I. Model development and validation. Metall Mater Trans B 32(2): 253–267
7. Sambasivam R (2013) Clogging resistant submerged entry nozzle design through mathematical modelling. Ironmak Steelmak 33(6):439–453
8. Mohammadi-Ghaleni M, Zaeem MA, Smith JD, O'Malley R (2016) Comparison of CFD simulations with experimental measurements of nozzle clogging in continuous casting of steels. Metall Mater Trans B 47(6):3384–3393
9. Long M, Zuo X, Zhang L, Chen D (2010) Kinetic modeling on nozzle clogging during steel billet continuous casting. ISIJ Int 50(5):712–720
10. Ni P, Jonsson LTI, Ersson M, Jönsson PG (2014) The use of an enhanced Eulerian deposition model to investigate nozzle clogging during continuous casting of steel. Metall Mater Trans B 45(6):2414–2424
11. Ni P, Jonsson LTI, Ersson M, Jönsson PG (2014) On the deposition of particles in liquid metals onto vertical ceramic walls. Int J Multiph Flow 62:152–160
12. Barati H, Wu M, Kharicha A, Ludwig A (2017) A transient model for nozzle clogging—part I: model description. Powder Technol. (Manuscript under review)
13. Guingo M, Minier JP (2008) A stochastic model of coherent structures for particle deposition in turbulent flows. Phys Fluids 20(5):053303
14. Heuzeroth F, Fritzsche J, Werzner E, Mendes MA, Ray S, Trimis D, Peuker UA (2015) Viscous force—an important parameter for the modeling of deep bed filtration in liquid media. Powder Technol 283:190–198
15. Sasai K, Mizukami Y (2001) Mechanism of alumina adhesion to continuous caster nozzle with reoxidation of molten steel. ISIJ Int 41(11):1331–1339
16. Uemura KI, Takahashi M, Koyama S, Nitta M (1992) Filtration mechanism of non-metallic inclusions in steel by ceramic loop filter. ISIJ Int 32(1):150–156
17. Janis D, Karasev A, Inoue R, Jönsson PG (2015) A study of cluster characteristics in liquid stainless steel and in a clogged nozzle. Steel Res Int 86(11):1271–1278
18. Roos E, Karasev A, Jönsson PG (2015) Effect of Si and Ce contents on the nozzle clogging in a REM alloyed stainless steel. Steel Res Int 86(11):1279–1288

Research on the Flow Properties and Erosion Characteristics in Combined Blown Converter at Steelmaking Temperature

Shaoyan Hu, Rong Zhu, Runzao Liu and Kai Dong

Abstract The coupling stirring effect driven by top blown supersonic jets and bottom blown jets plays a crucial role in converter bath movement. Based on numerical simulation, jet-bath interactions inside a 110-ton commercial converter at room temperature and at steelmaking temperature were compared. Penetration depth and flow velocity in molten bath are larger at steelmaking temperature because the velocity attenuation of supersonic jet is suppressed. The mathematical model was then used to investigate the effect of radial angle between oxygen lance nozzles and bottom blowing tuyeres on molten bath flow properties, which revealed the fluid flow mechanism in combined blown converter. Based on the molten bath flow field, mathematical model describing the erosion behavior of converter lining was established and erosion characteristics in combined blown converter was researched. The results showed that radial angle between oxygen lance nozzles and bottom blowing tuyeres has an important influence on converter bath velocity field distribution and lining erosion.

Keywords Ambient temperature · Combined blown converter · Jet characteristics Flow properties · Erosion

Introduction

Converter steelmaking is the main method of steelmaking in the world. Molten bath is driven by top blown supersonic oxygen jets and bottom blown nitrogen/argon jets, which determines the movement state and mixing effect in steelmaking con-

S. Hu (✉) · R. Zhu · R. Liu · K. Dong
School of Metallurgical and Ecological Engineering, University of Science and Technology Beijing, Beijing 100083, China
e-mail: hushaoyanvip@126.com

S. Hu · R. Zhu · R. Liu · K. Dong
Beijing Key Laboratory of Research Center of Special Melting and Preparation of High-End Metal Materials, University of Science and Technology Beijing, Beijing 100083, China

L. Nastac et al. (eds.), *CFD Modeling and Simulation in Materials Processing 2018*, The Minerals, Metals & Materials Series,
https://doi.org/10.1007/978-3-319-72059-3_16

verter. Therefore, a lot of researches have been done to study the characteristics of multiple supersonic oxygen jets and its impacting capability onto converter bath. However, many researches [1–4] only analyzed the jet characteristics at room temperature, because of the limitations of experiment method. Sumi [5] studied characteristics of single-jet under different ambient temperature by experiments. Alam [6] found that the potential flow core length of single-strand oxygen jet at steelmaking temperatures (1800 K) is 2.5 times as long as that at room temperature, using a modified k-ε turbulence model. Zhao [7] also found that ambient temperature has a significant influence on the single-strand jet by numerical simulations and experiments. But the top blown oxygen lance used in converter usually has multi nozzles, generating multiple supersonic jets interfering each other. Few works has been done to reveal the influence of ambient temperature on the multiple supersonic jets. More importantly, the difference of jet characteristics inevitably leads to difference of jet impacting capability. Jet-bath interactions at room temperature and at steelmaking temperature has never been compared, because most of converter multi-phase simulations assumed that ambient temperature is room temperature. Penetration depth and flow velocity in molten bath based on inaccurate ambient temperature is not accurate enough. Based on numerical simulation, effect of ambient temperature on multiple oxygen jets characteristics was studied, at the same time jet-bath interactions at room temperature and at steelmaking temperature were compared by multi-phase simulation.

Based on that, effect of radial angle between oxygen lance nozzles and bottom blown tuyeres on molten bath flow properties was studied in detail to reveal the fluid flow mechanism in combined blown converter. Many researchers [8–10] on combined converter focused on the influence of lance height, oxygen flow rate, bottom blowing intensity, et al., but ignored the influence of relative position between multi nozzles and multi tuyeres. The relative position depends on the installation process of oxygen lance tip, because the position of bottom blowing tuyeres are fixed. Besides the analysis on the molten bath flow field, the erosion behavior of converter lining was also discussed in this paper.

Mathematical Model

Geometry Model and Computation Procedure

A commercial 110-ton converter with a four-nozzle oxygen lance and four bottom blowing tuyeres was considered to study the fluid flow properties in converter steelmaking process. Figure 1 shows the diagrammatic sketch of converter as well as details of oxygen lance and tuyeres. Three geometric models with different radial angle between multi nozzles and multi tuyeres were established in this work, named as Arrangement-A, Arrangement–B and Arrangement-C respectively, shown in Fig. 2. Mesh refinement was done to capture the sharply oscillation of fluid flow, as presented

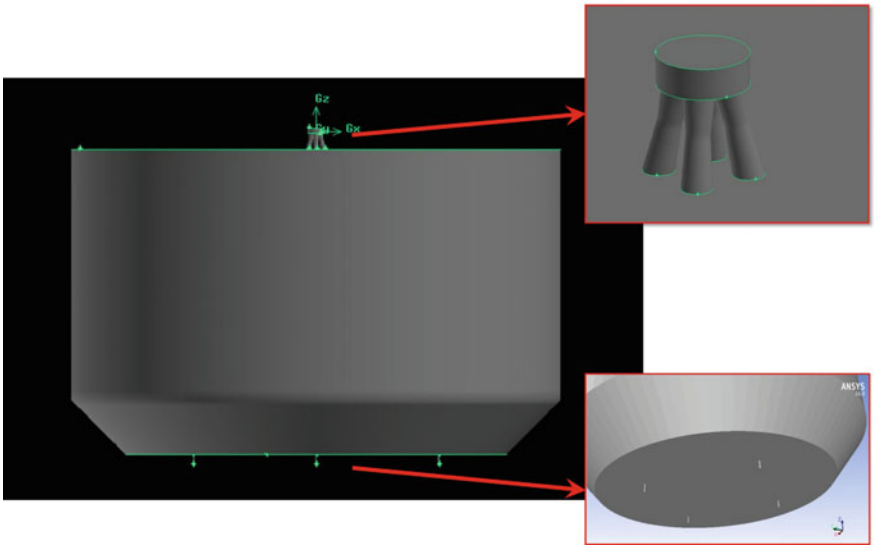

Fig. 1 Diagrammatic sketch of converter, and details of oxygen lance, tuyeres

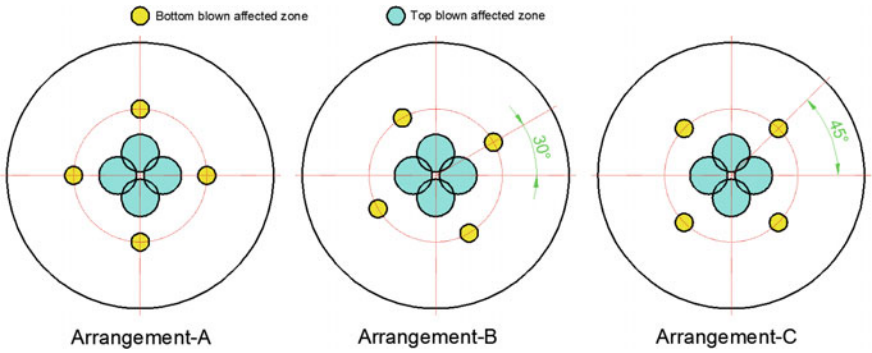

Fig. 2 Illustrations of radial angle between multi nozzles and multi tuyeres

in Fig. 3. Every geometry model consisted of more than 670,000 cells. Table 1 lists the key geometric and operational parameters of the converter used in this work.

Effect of ambient temperature on multiple jets and jet-bath interactions was researched based on the geometry model of Arrangement-A. For the free jets simulation, the effect of ambient temperature was studied in detail, which changes from 300 to 1723 K gradually, as shown in Table 2. Because the cell number was large and the computational model was complex, only jet-bath interactions at room temperature (300 K) and steelmaking temperature (1723 K) were studied and

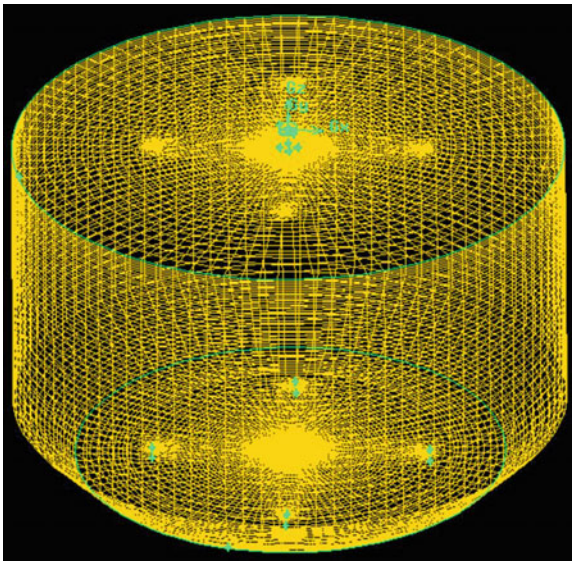

Fig. 3 Detailed grid arrangement of converter model

Table 1 Key geometric and operational parameters of the converter

Items	Value
Converter capacity (ton)	110
Molten bath height (m)	1.3
Lance height (m)	1.5
Furnace diameter (m)	4.5
Bottom blown flow rate (Nm^3/h)	660
Number of tuyeres	4
Installation radius of tuyeres	0.5R
Top blown oxygen flow rate (Nm^3/h)	23,000
Number of nozzles	4
Nozzle throat diameter (mm)	38.7
Nozzle outlet diameter (mm)	50.2
Nozzle inclination angle (°)	12

compared by multi-phase simulations. Then fluid flow properties of three geometry models at steelmaking temperature were researched by multi-phase simulations.

During converter steelmaking process, slag exists as foaming slag and its state is unstable. Therefore, molten slag was ignored, only oxygen and molten steel were considered in multi-phase simulation works. The thermophysical properties of the oxygen and molten steel are shown in Table 3.

Table 2 Ambient temperature of free jets simulation

No.	1	2	3	4	5	6
Ambient temperature (K)	300	600	900	1200	1500	1723

Table 3 Thermophysical properties of the oxygen and molten steel

	Molten steel	Oxygen
Viscosity (kg/m s)	0.0065	1.919e−5
Density (kg/m^3)	7200	Ideal gas
Thermal conductivity (W/m K)	15	0.0246
Heat capacity (J/kg K)	670	919.31
Temperature (K)	1723	300

Turbulence and VOF Model

The standard $k-\varepsilon$ model with compressibility correction was implemented for modeling the supersonic oxygen jet and turbulent flow, which was a semi-empirical model based on model transport equations for the turbulence kinetic energy (k) and its dissipation rate (ε) [11, 12].

Turbulence kinetic energy equation (k equation):

$$\frac{\partial(\rho k)}{\partial t}+\frac{\partial(\rho k u_i)}{\partial t_i}=\frac{\partial}{\partial x_j}\left[\left(\mu+\frac{\mu_t}{\sigma_k}\right)\frac{\partial k}{\partial x_i}\right]+G_k+G_b-\rho_\varepsilon-Y_M+S_k \quad (1)$$

Turbulence dissipation equation (ε equation):

$$\frac{\partial(\rho\varepsilon)}{\partial t}+\frac{\partial(\rho\varepsilon u_i)}{\partial x_i}=\frac{\partial}{\partial x_j}\left[\left(\mu+\frac{\mu_t}{\sigma_\varepsilon}\right)\frac{\partial\varepsilon}{\partial x_i}\right]+C_{1\varepsilon}\frac{\varepsilon}{k}(G_k+C_{3\varepsilon}G_b)+C_{2\varepsilon}\rho\frac{\varepsilon^2}{k}+\mathrm{S}_\varepsilon \quad (2)$$

For the situation of gas injection operations considered in the present study, the well known volume of fluid method (VOF) was applied to describe the sharp gas-liquid interface between oxygen, slag and molten metal. For the VOF model, two or more fluids or phases were not interpenetrating. Each phase in the model has its own volume fraction α. The sum of the volume fraction of each phase in an arbitrary calculation area is 1. The variables and parameters in control volume were calculated by the volume average method using the volume fraction α.

In VOF method, the different fluids are modelled as single continuum obeying the same set of governing equations, with the different fluids identified locally by a volume fraction field as discussed above.

Energy Model

The energy equation is also shared among the phases, as shown in Eq. [3]

$$\frac{\partial}{\partial t}(\rho E) + \nabla \cdot [u(\rho E + P)] = \nabla \cdot \left(k_{eff} \nabla T\right) + S_h \tag{3}$$

The VOF model treats energy E and temperature T as mass-averaged variables.

$$\mathrm{E} = \sum_{i=1}^{n} \alpha_i \rho_i E_i \Big/ \sum_{i=1}^{n} \alpha_i \rho_i \tag{4}$$

Assumptions

(1) The chemical reactions in the converter steelmaking process was ignored.
(2) The molten slag in the converter was ignored.
(3) The gas phase was regarded as ideal gas, while the liquids as incompressible Newtonian fluid.

Results and Discussion

Effect of Ambient Temperature on Jet Characteristics

The final computational flow field distributions of the multiple jets are shown in Fig. 4. Although the multiple jets flow from the same gas source in the oxygen lance, ambient temperature has significant effect on jets velocity attenuation and radial expansion. With the increase of the ambient temperature, velocity attenuation of the multiple jets is inhibited and radial expansion of the jets is aggravated. The multiple jets keep entraining atmospheric gas into the jets while flowing, inducing velocity attenuation and jets expansion. Comparing with low-temperature environment, the atmospheric gas density is lower in high-temperature environment, which means less energy loss of mass transfer. High-temperature and low-density atmospheric gas is easier to be sucked into multiple jets.

For converter steelmaking process, jet-bath interactions mainly occurs nearby the molten bath level. Hence, multiple jets characteristics in the radial direction at the cross-section of lance height are more worthy of attention, which is 1.5 m from the lance tip in this research.

Figure 5 shows the velocity distribution in the radial direction at the cross-section mentioned above. There is a peak velocity in each center of the individual jet, and the peak velocity increases significantly with the increase of

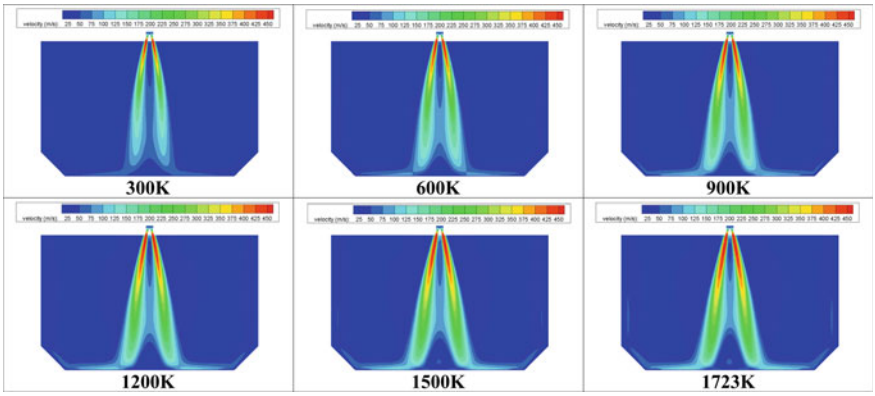

Fig. 4 Flow field distributions of the free multiple jets

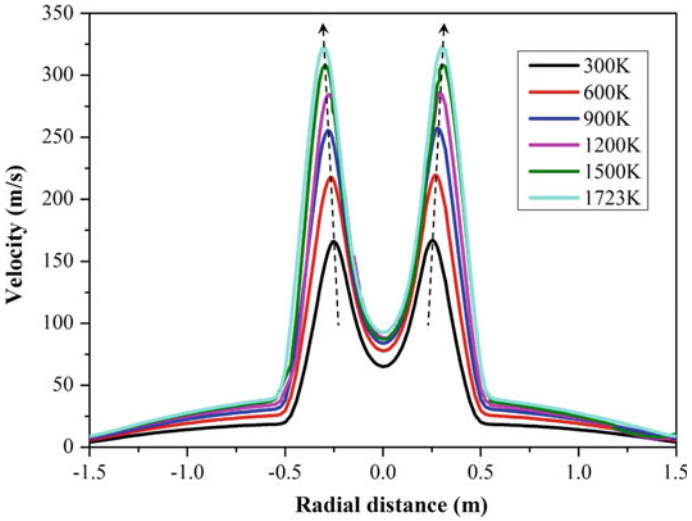

Fig. 5 Radial velocity distribution at the cross-section of 1.5 m from lance tip

ambient temperature. For instance, the peak velocity at ambient temperature of 300 K is only 166 m/s, and the velocity reaches 322 m/s at steelmaking temperature of 1723 K. It should be noted that the increasing rate of peak velocity gets slow down as the ambient temperature increases. In addition, center of individual jet gets away from lance axis gradually with the increase of ambient temperature, indicating that coalescence between multiple jets is suppressed in higher ambient temperature.

Actually, dynamic pressure rather than velocity is the most crucial parameter for evaluating the impact power of oxygen jets. The dynamic pressure increases from 19,229 to 24,848 Pa when the ambient temperature is raised from 300 to 1723 K, as shown in Fig. 6. The effect of ambient temperature on dynamic pressure is not as

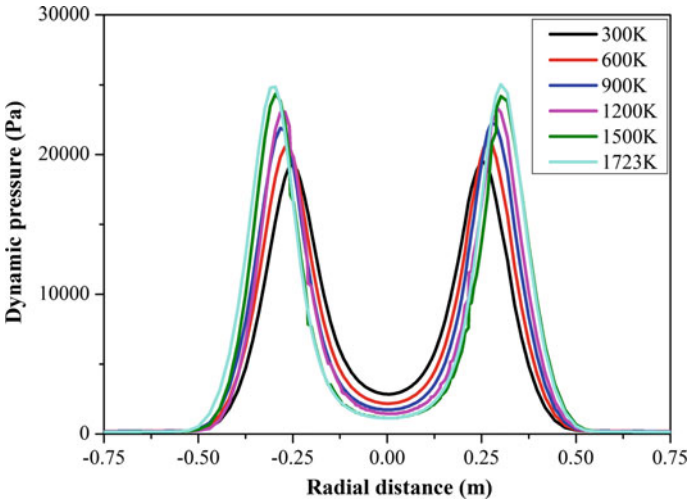

Fig. 6 Radial dynamic pressure distribution at the cross-section of 1.5 m from lance tip

significant as that on velocity, because the dynamic pressure is also closely related to the jet density. Along with the ambient temperature increasing, the jet itself will be heated and warmed up, inducing the jet density decrease and limiting the increase of jet dynamic pressure. Anyway, the multiple jets has stronger impact power at high-temperature environment, and its impact effect will be discussed in the next section.

Effect of Ambient Temperature on Jet-Bath Interactions

Multiple jets impacts on the molten bath level, forming a penetration cavity, meanwhile bottom blowing bubbles floating through the bath, the coupling force of which drives the molten steel movement. Because of the jet shear force and gas-liquid surface tension, a large amount of metallurgic droplets are produced nearby the penetration cavity, just as shown in Fig. 7. In order to compare the penetration depth of multiple jets at room temperature and at steelmaking temperature, jet-bath interface profiles are plotted in Fig. 8. The penetration depth of multiple jets increases from 0.11035 to 0.14807 m when the ambient temperature is raised from 300 to 1723 K. The penetration depth is increased by 34.18%, which means that the influence of ambient temperature can not be ignored in converter flow field research.

Figure 9 shows the velocity distribution contours at the cross-section of 0.3 m below the molten bath level. The velocity distribution pattern is similar in general whether the ambient temperature is room temperature or steelmaking temperature. In addition to the region near bottom flow and penetration cavity, high velocity

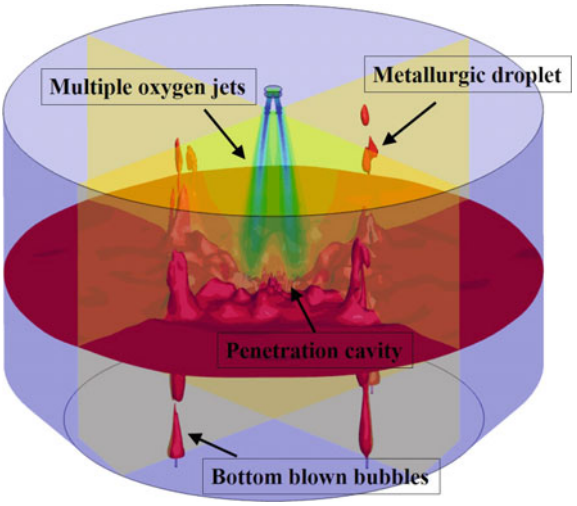

Fig. 7 Flow phenomenon illustration in combined blown converter

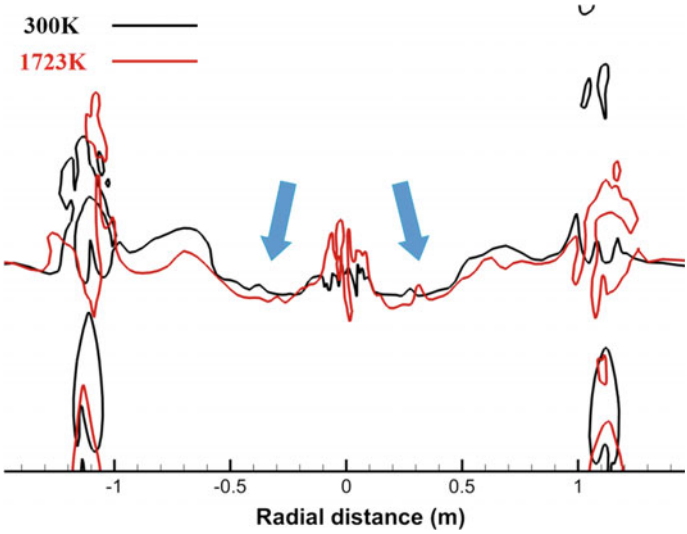

Fig. 8 Jet-bath interface profiles at room temperature and steelmaking temperature

zone is also distributed at the included region between two oxygen lance nozzles (while also between two bottom blowing tuyeres), as region A shows. And outer region of the extension line of bath center and tuyere is dead zone, as region B shows. The influence of ambient temperature can be expressed as that area of high velocity zone and value of average flow velocity in molten bath are both larger at steelmaking temperature.

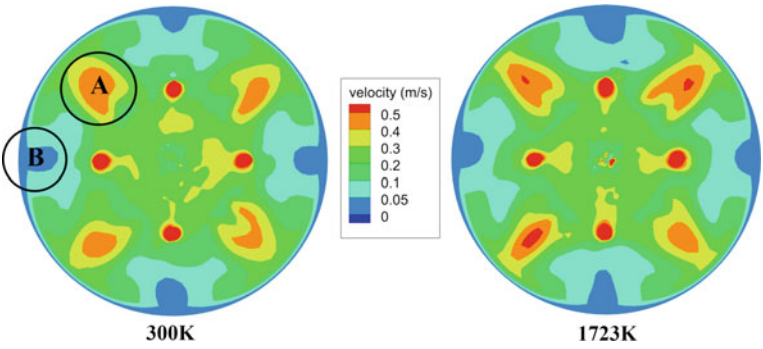

Fig. 9 Velocity distribution contours at room temperature and steelmaking temperature

Effect of Radial Angle Between Multi Nozzles and Multi Tuyeres on Flow Properties

Figure 10 shows the velocity distribution contours of three geometric models at the cross-section of 0.3 m below the molten bath level. Unlike the influence of ambient temperature, arrangement has distinct influence on the velocity distribution pattern. As presented in Fig. 10, for Arrangement-A and Arrangement-B, there exists high velocity zone in the direction of angular bisector of two oxygen nozzles, not the direction of angular bisector of two bottom blowing tuyeres. The radial angle between multi tuyeres and multi nozzles of Arrangement-B is 30°, where the tuyeres are near the angular bisector of nozzles, and the area of high velocity zone of Arrangement-B is smaller than that of Arrangement-A. For Arrangement-C, bottom tuyeres happen to be arranged on the angular bisector, and the high velocity zone vanishes in that region. It seems that the high velocity zone is formed mainly

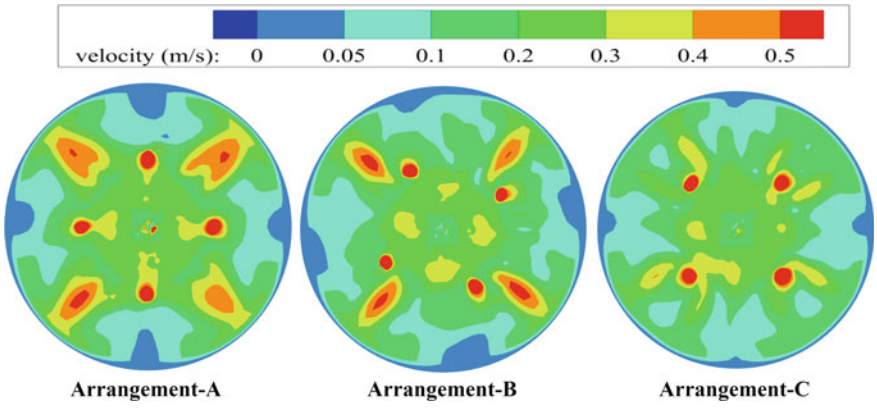

Fig. 10 Velocity distribution contours of three geometric models

by flow of top blown oxygen jets. Moreover, the bottom blown flow blocks the fluid movement in that region. The area-weighted average flow velocity of molten bath with Arrangement-A, Arrangement-B and Arrangement-C is 0.2137, 0.1990 and 0.1980 m/s, respectively. By comparison, the stirring effect of Arrangement-A is the best.

In order to verify the reason for above discussed phenomenon and reveal the fluid flow mechanism in combined blown converter, velocity vectors are shown in Fig. 11. Different arrowheads represent different flow directions, and different colors represent different velocity values. As can be seen from Fig. 11, in the central region of the whole bath, molten steel flows converging to the center due to the formation of penetration cavity. Molten steel with different radial velocities interferes and collides with each other at the bath center, which leads to the kinetic energy loss and no high velocity zone formation at the bath center. In the included region between two oxygen nozzles, molten steel flows outwards and towards the furnace wall until be bounced to other direction, forming the high velocity zone in the direction of angular bisector of two oxygen nozzles. Once the bottom blowing tuyeres is arranged at the included region, like Arrangement-B and Arrangement C, floating molten steel driven by bottom bubbles will hinder the molten steel flowing outwards. Molten steel flowing outwards can only get round the floating molten steel after fluid collision and kinetic energy loss. Although the high velocity zone in the direction of angular bisector of two oxygen nozzles is reduced in size, even disappeared, but the dead zone shrinks slightly. Overall, Arrangement-A is the best choice of above mentioned three arrangements, because of largest area of high velocity zone and highest value of flow velocity.

Wall shear stress is a crucial index to quantitative study the erosion rate of converter lining. Figure 12 shows the wall shear stress distribution contours of three arrangements. For the bottom-wall, erosion rate of tuyeres margins is highest, followed by the annular region near tuyeres. For the side-wall, erosion rate is closed related to the velocity magnitude near wall. It seems that the area of high wall shear

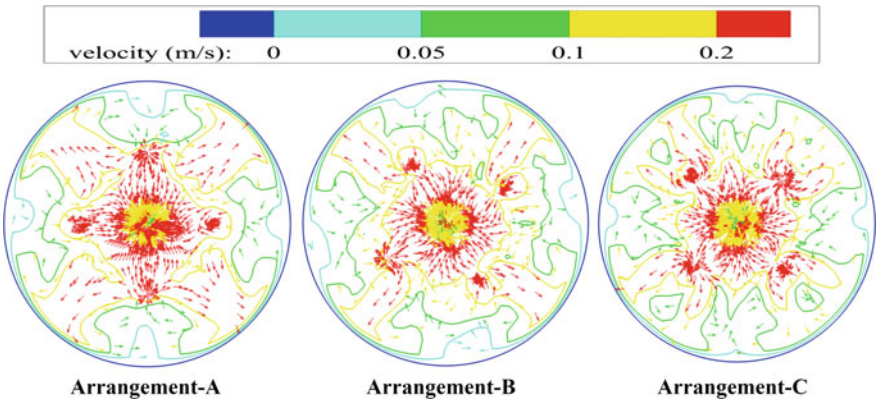

Fig. 11 Velocity vectors of three geometric models

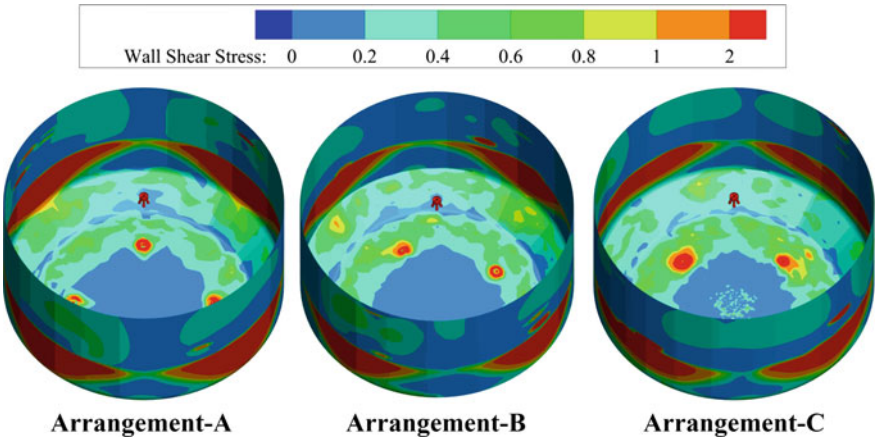

Fig. 12 Wall shear stress distribution contours of three arrangements

stress zone is larger under the case of Arrangement-C, because the dead zone near wall shrinks slightly, which can be seen from Fig. 10.

Conclusions

Effect of ambient temperature on multiple jets characteristics and jet-bath interactions have been studied and compared in detail using computational simulation, proving that ambient temperature can not be ignored in converter flow field research. Then effect of radial angle between multi nozzles and multi tuyeres on flow properties at steelmaking temperature has been analyzed. The following conclusions have been reached from the current study:

(1) With the increase of the ambient temperature, velocity attenuation of the multiple jets is inhibited and radial expansion of the jets is aggravated.
(2) Penetration depth of multiple jets increases from 0.11035 to 0.14807 m when the ambient temperature is raised from 300 to 1723 K, resulting in larger flow velocity in molten bath at steelmaking temperature.
(3) In combined blown converter, high velocity zone is distributed in the included region between two oxygen nozzles, formed mainly by flow of top blown oxygen jets, rather than the bottom blown flow. Based on the analysis of velocity vector, floating molten steel driven by bottom bubbles will hinder the molten steel flowing outwards, leading to fluid collision and kinetic energy loss.

Radial angle between multi nozzles and multi tuyeres should be paid more attention in converter operating and research.

Acknowledgements This work was financially supported by the National Natural Science Foundation of China (Grant No. 51574021 and No. 51474024).

References

1. Corrsin S, Uberoi MS (1949) Further experiments on the flow and heat transfer in a heated turbulent air jet. Technical report archive & image library
2. Kataoka K, Takam T (1977) Experimental study of eddy diffusion model for heated turbulent free jets. AIChE 23(6):889–896
3. Sforza PM, Stasi W (1979) Heated three-dimensional turbulent jets. Heat Transf 101(2): 53–359
4. Lau JC, Morris PJ, Fisher MJ (2006) Measurements in subsonic and supersonic free jets using a laser velocimeter. Fluid Mechs 93(1):1–27
5. Sumi I, Kishimoto Y, Kikuchi Y et al (2006) Effect of high-temperature field on supersonic oxygen jet behavior. ISIJ Int 46(9):1312–1317
6. Alam M, Naser J, Brooks G (2010) Computational fluid dynamics simulation of supersonic oxygen jet behavior at steelmaking temperature. Metall Mat Trans B 41(3):636–645
7. Zhao F, Zhang YL, Zhu R et al (2014) Numerical simulation of environmental temperature effect on supersonic oxygen jet behavior. J Univ Sci Technol Beijing 24(5):669–673
8. Dong K, Zhu R, Gao W et al (2014) Simulation of three-phase flow and lance height effect on the cavity shape. Int J Min Metall Mat 21(6):523–530
9. Fabritius TMJ, Luomala MJ, Virtanen EO et al (2007) Effect of bottom nozzle arrangement on splashing and spitting in combined blowing converter. ISIJ Int 42(8):861–867
10. Ma E, Wen C (1991) Effects of multi-jet characteristics of an oxygen converter lance on steelmaking process. Chin J Process Eng
11. Liu FH, Zhu R, Wang QG, Bai RG (2015) Simulation and application of top lance with various tilt angles in dephosphorization ladle furnace. ISIJ Int 55(8):1633–1641
12. Launder BE, Spalding DB (1972) Lectures in mathematical model of turbulence. Academic Press, London

Part V
Processing: III

Effect of Carbide Configuration on the Current Distribution in Submerged Arc Furnaces for Silicon Production—A Modelling Approach

Y. A. Tesfahunegn, T. Magnusson, M. Tangstad and G. Saevarsdottir

Abstract Current distribution is critical for good operation of Submerged Arc Furnaces for silicon production. Control systems do not offer this information as it is not directly measureable, but metallurgists operate furnaces based on experienced interpretation of available data. A number of recent dig-outs of industrial furnaces has expanded available information on location dependent charge properties, thus enabling numerical models with reasonably realistic domain configurations. This has the potential to enhance understanding of critical process parameters allowing more accurate furnace control. This work presents computations of electric current distributions inside an industrial submerged arc furnace for silicon production. A 3D model has been developed in ANSYS Fluent using electric potential solver. Electrode, arc, crater, crater wall, and side arc that connects electrode and crater wall are considered for each phase. In this paper the current distributions in electrode, arc and crater wall for different configurations and thickness of the crater walls are presented. The side-arcs are modelled as either a single concentrated arc, or a smeared out arc, in order to capture extreme cases. The main result is that side arc configuration is more important for the fraction of the current passing through the crater wall than the carbide thickness. The current fraction bypassing the main arc through the charge is highly influenced by the ease of contact between electrode and conducting charge material. Qualitatively, the results are in a good agreement with previously published results from literature.

Y. A. Tesfahunegn (✉) · G. Saevarsdottir
School of Science and Engineering, Reykjavik University, Menntavegur 1, 101, Reykjavik, Iceland
e-mail: yonatant@ru.is

G. Saevarsdottir
e-mail: gudrunsa@ru.is

T. Magnusson
United Silicon, Stakksbraut 9, 230, Reykjanesbæ, Iceland
e-mail: tm@silicon.is

M. Tangstad
Department of Materials Science and Engineering, NTNU, 7491 Trondheim, Norway
e-mail: merete.tangstad@ntnu.no

L. Nastac et al. (eds.), *CFD Modeling and Simulation in Materials Processing 2018*, The Minerals, Metals & Materials Series,
https://doi.org/10.1007/978-3-319-72059-3_17

Keywords Current distribution · Current paths · Submerged arc furnace

Introduction

In the silicon production process, quartz and carbon materials are fed into a Submerged Arc Furnace. The raw material mix fills up the furnace and forms a charge. Three electrodes sticking into the charge from above. The energy for the reactions in the furnace is provided by electric heating from the current passed to the furnace through the electrodes, but each carries one of three phases of 50 Hz AC current, cancelling out at a star-point in the furnace.

The overall reaction for producing silicon is:

$$SiO_2 + 2C = Si + 2CO(g) \tag{1}$$

This reaction however happens through a series of sub-reactions, changing the properties of the charge along the way as intermediary reaction products are formed. The current passes from the electrodes through and the raw-material charge and an electric arc burning at the tip of the electrode. The arc, which consists of thermal plasma at 20,000 K, is necessary for the energy consuming silicon producing reaction (4) while the SiC forming reaction and SiO(g) condensation, reactions (2) and (3) happen at a lower temperature further up in the furnace, see Schei et al. [1]:

$$SiO(g) + 2C = SiC + CO(g) \tag{2}$$

$$2SiO(g) = Si + SiO_2 \tag{3}$$

$$SiO_2 + SiC = SiO(g) + CO(g) + Si(l) \tag{4}$$

It is extremely important for the silicon recovery in this process that there is a balance between the high temperature reactions (4) and the low temperature reactions (2) and (3). Therefor it is necessary that sufficient heat is released in the arc, while a certain part should be released in the raw-material charge.

This is however not well known for silicon furnaces, and cannot be directly measured. Sævarsdottir [2] calculated that the arc could be maximum 10–15 cm, based on the electrical parameters. Although much has been speculated on this, and papers published as well [3], results from an accurate model where the current distribution can be calculated have not been published to date.

The geometry of the zones in a Si furnace is dependent on the operation history, and hence it can be a number of different geometries, sizes and composition of the various parts of the furnace. Report from recent excavations of industrial furnaces published by Tranell et al. [4] describe the various zones in a FeSi furnace. The results are summarized in Fig. 1. Myrhaug [5] reported some of the similar features

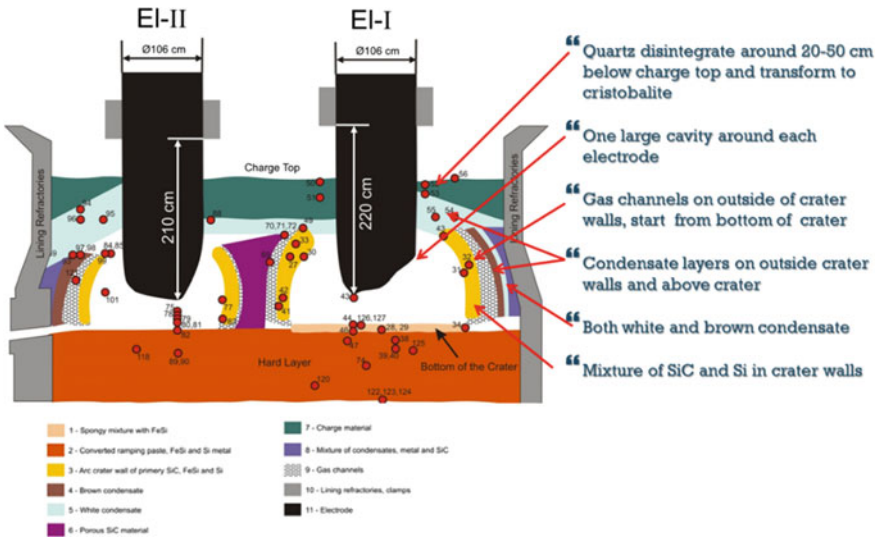

Fig. 1 Reaction zones at a 17.5 MW industrial FeSi furnace reproduced from Tranell et al. [4]

from a pilot scale excavation operating around 150 kW. Tangstad et al. [6] published results from excavation of industrial furnaces in 2013, where the interior of the furnace is divided into zones depending on the materials and their degree of conversion. Mapping the material distribution gives a basis for quantifying the location dependent physical properties of the charge materials, among others the electrical conductivity.

A master's thesis by Krokstad [7] published in 2014 describes measurements of the electrical conductivity of silicon carbide and Vangskåsen [8] in 2012 looked in detail at the metal producing mechanisms. Molnas [9] and Nell [10] have also published data on digout samples and material analysis that are relevant. These are some of the basic components necessary to set up a reasonably realistic modeling domain with correct physical properties in order to model the current distribution within a furnace and therefore there is now a unique opportunity to create a model which enables understanding of the current distribution in the furnace. These results can be used in the development of furnace control strategies that can enable improved silicon recovery and current efficiency.

A number of researchers have published results on current distribution of Submerged Arc Furnaces using Computational Fluid Dynamics (CFD) and Finite Element Method (FEM). Diahnaut [11] presented computations of electric field in SAF using CFD. The author showed the effect of contact resistance by studying the contact between two coke particles before dealing with a full-scale furnace. The furnace is partitioned in layers to consider different materials and no assumption has been made on the current path. Bezuidenhout et al. [12] applied CFD on a three-phase electric smelting furnace to investigate the electrical aspects, thermal

and flow behavior. They showed relationships between electrode positions, current distribution and slag electrical resistivity. Darmana et al. [13] developed a modeling concept applicable for SAFs using CFD that considers various physical phenomena such as thermodynamics, electricity, hydrodynamics, heat radiation and chemical reactions. Wang et al. [14] investigated the thermal behavior inside three different electric furnaces for MgO production.

This paper presents computations of electric current distributions inside an industrial submerged arc furnace for silicon production. A 3D model has been developed in ANSYS Fluent [15] using electric potential solver. Electrode, central arc, crater, crater wall, and side arc that connects electrode and crater wall are considered for each phase. The current distributions in electrode, arc and crater wall for different configurations and thickness of the crater walls are presented. The side-arcs are modelled as either a single concentrated arc, or a smeared out arc, in order to represent extreme cases. The results are compared with previously published results from literature [3].

Computational Model

In this section, we describe the mathematical modeling, the furnace geometry, material properties, mesh generation and boundary conditions.

Mathematical Modeling

In this paper we will focus only on the electrical aspects of SAF. The 3D electrical model is developed in ANSYS Fluent [15] using electric potential solver. This will neither capture the time-dependent effects nor the induced magnetic field and the resulting magnetic forces in the system, but for the considerations in this paper a quasi-static approach using the potential solver is deemed sufficient. The electric potential equation is therefore given by:

$$\nabla \cdot (\sigma \nabla \varphi) = 0 \tag{5}$$

where φ and σ are the scalar potential and electrical conductivity, respectively. Equation (5) is solved using the finite volume method implemented in commercial CFD software ANSYS Fluent version 17 [15] based on the User Defined Scalar (UDS) solver. Once it is solved, the electric field ($\boldsymbol{E}$) and hence the electric current density ($\boldsymbol{J}$) using Ohm's law can be determined as shown in Eqs. (6) and (7), respectively.

$$\boldsymbol{E} = -\nabla\varphi \tag{6}$$

$$\boldsymbol{J} = \sigma\boldsymbol{E} \tag{7}$$

Furnace Geometry and Material Properties

The computational domain is based on the actual design of a 32 MW industrial furnace. A simplified schematic drawing of the furnace is shown in Fig. 2. Due to the proprietary right, the dimensions of the furnace are not indicated in the figure. Hence the furnace is partitioned into different zones based on the material properties. Included in the modelling are the furnace lining, three electrodes, charge, molten material, three arcs below electrodes, side arcs, three craters with crater walls made of carbides. For brevity a section of the furnace and one electrode are depicted in Fig. 2. For each phase, two arcs are included. The main-arc, burning below the electrode, with arc length of 10 cm and diameter of 5 cm [3], and a shorter arc connecting the carbide layer to the side of the electrode, in this paper the word "side arc" is used for the configuration with an arc/arcs connecting electrode and the carbide crater wall The curvature of the three crater walls is assumed to be a section of a circle with a diameter of 100 cm [16]. In this study five values of crater wall carbide thickness carbide values are simulated i.e. 10, 25, 35, 45 and 55 cm. The furnace geometry has been created using ICEM-CFD [17] mesh generator software. Each of the zones are assumed to have constant electrical conductivity. The conductivity of each zone are taken from various literature sources and summarized in Table 1.

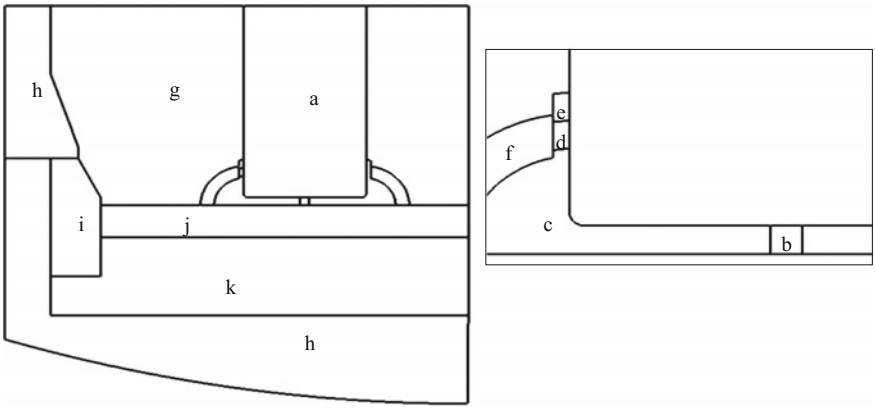

Fig. 2 Schematic of the industrial silicon SAF with different zones (a) electrode, (b) arc, (c) crater, (d) side arc, (e) gap, (f) carbide, (g) charge, (h) alumina brick, (i) carbon block and carbide, (j) molten material, and (k) carbon block

Table 1 Electrical conductivity of different zones

Zones	Electrical conductivity (S/m)
Electrode [7]	225,000
Arc [16]	7000
Crater	1e−14
Carbide [7]	400
Charge	0.15
Molten material [18]	1,388,900
Carbon block	225,000
Alumina brick	1e−14

Mesh Generation and Boundary Conditions

Mesh generation is a crucial part of any computational method. It has a significant influence on the runtime and memory use of simulation, as well as the accuracy and stability of the solution. The material volumes described in Section "Furnace Geometry and Material Properties" were meshed using ICEM-CFD [17]. The mesh is generated using unstructured grid because of the complexity of the furnace geometry. After performing preliminary grid convergence study, the minimum and maximum element sizes are set 2 and 30 cm, respectively. In order to reduce the cell count the fine unstructured mesh is converted to polyhedral mesh in ANSYS Fluent reducing cell count to almost a third, enabling faster convergence and saving computational expense.

The model boundary conditions were specified to resemble the actual furnace as closely as possible. The outer furnace walls are set as nonconductive wall. The top surface of the electrodes defined as conductive walls by applying the respective phase currents as current density, a total current of 99,000 A was applied at the top of electrode 1, and a corresponding current density giving −49,500 A on phase 2 and 3. The interface walls between different zones implemented as coupled boundary conditions.

Numerical Cases

In this section, we study the effect of carbide thickness on current distribution through different parts of the furnace. Five different carbide thickness values were used, i.e. 10, 25, 35, 45 and 55 cm at a fixed gap value of 5 cm. The 10 cm carbide thickness was used only in one simulation case where all the phases set to 10 cm. Hence, each phase has four levels of thickness values and combinations of these levels gave 64 simulation cases plus the symmetric case for the 10 cm. The cases are identified by the carbide thickness applied on the phases. For example, 25–35–45 refers to 25, 35 and 45 cm carbide thickness applied on phase 1, 2 and 3, respectively. Since phase 2 and 3 have the same applied current, for instance case

25–35–45 and 25–45–35 have the same effect. Therefore, the total number of simulation cases reduced to 13 cases.

For all cases the simulations were performed by a second order upwind scheme based on an implicit formulation. Asymptotic convergence to a steady state solution is obtained for each case. The iterative convergence of each solution is examined by monitoring the overall residual, which is the sum (over all the cells in the computational domain) of the L^2 norm of all the governing equations solved in each cell. The solution convergence criterion for all models is the one that occurs first of the following: a reduction of the residuals by twelve orders of magnitude, or a maximum number of iterations of 3000. The simulation time per a case on average is around 3 h.

For each simulation, at several sections of the furnace on different parts, lumped current values were calculated from the current density using ANSYS Fluent's surface integrator. By integrating the current density component along the furnace height direction multiplied with the normal vector for the area associated with it, we get the current passing through the area. Table 2 shows the simulation cases along with associated results. These cases can be categorized into five possible scenarios that can exist during the furnace operation. We assume the following scenarios:

(a) All phases have the same value and change simultaneously.
(b) One phase is varying and the other phases are fixed with different carbide thickness.
(c) One phase is varying and the other phases are fixed with the same carbide thickness.
(d) One phase is fixed the other phases are varying simultaneously with different carbide thickness.
(e) One phase is fixed the other phases are varying simultaneously with the same carbide thickness.

Each simulation case listed in Table 2 has been simulated twice based on two side arc-modelling approaches. The first approach is a single concentrated side-arc on each phase connecting the crater wall carbide to the side of the electrodes. The length of the side arcs is 5 cm with a radius of 5 cm and their conductivity is the same as the main arc. In the second approach, which is modelled to mimic the case of multiple side-arcs, the arc is evenly distributed on the circumference of the electrodes and the carbides. The main idea is that the arc-resistance of the distributed and concentrated arcs are assumed to be equal. From this relationship, it is possible to determine the conductivity of the distributed side arc as shown in Eq. 8:

$$\sigma_{dis} = \sigma_{con} \frac{r_a}{4r_e} \tag{8}$$

where σ_{dis}, σ_{con}, r_a and r_e conductivity of distributed side arc, conductivity of concentrated side arc, radius of arc, and radius of electrode, respectively. With this approach the effect of concentrating the current within the carbide and electrode, in

Table 2 Normalized main-arc current fractions for each of the 13 cases

No.	Case	Concentrated side arc			Distributed side arc		
		Phase 1	Phase 2	Phase 3	Phase 1	Phase 2	Phase 3
1	10-10-10	0.924	0.922	0.924	0.628	0.627	0.626
2	25-25-25	0.881	0.881	0.881	0.429	0.429	0.428
3	35-35-35	0.866	0.873	0.873	0.358	0.362	0.362
4	45-45-45	0.869	0.867	0.871	0.318	0.317	0.318
5	55-55-55	0.866	0.867	0.869	0.285	0.284	0.285
6	25-35-25	0.877	0.869	0.877	0.426	0.360	0.425
7	35-35-25	0.871	0.869	0.880	0.361	0.361	0.427
8	45-35-25	0.868	0.874	0.883	0.317	0.363	0.430
9	55-35-25	0.862	0.869	0.881	0.283	0.361	0.428
10	35-25-25	0.869	0.880	0.881	0.360	0.426	0.425
11	45-25-25	0.867	0.883	0.883	0.318	0.428	0.430
12	45-25-45	0.869	0.882	0.869	0.317	0.429	0.317
13	45-35-45	0.868	0.874	0.867	0.317	0.362	0.317

the close vicinity of the side-arc can be compared to a more spread connection between electrode and the crater wall. For discussions, scenario (a) is considered. Using scenario (a) we study the two side arc modelling approaches as a function of carbide thickness. Figure 3 shows the total current through electrode and the central main arc at different height of the furnace on the electrodes and arcs for both side arc-modelling approaches. The vertical axis is a normalized current, which is the fraction of the phase current in the electrode and arc. The horizontal axis is dimensionless furnace height, which is the ratio between a given height and the total height of the furnace. In this paper, we define the total height of the furnace from the bottom of the furnace to the top of the electrodes. In all plots we can see that the current on each electrode is almost constant from the top of furnace (1) to 0.59 normalized height, below 0.57 height, where the side arcs are attached the

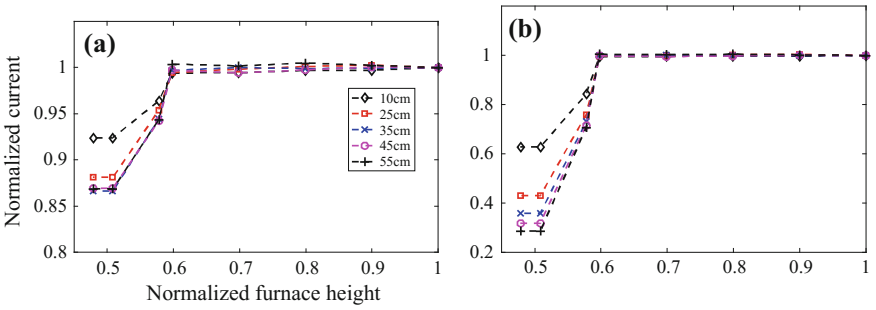

Fig. 3 Normalized current passing through electrode and main arc as a function of normalized distance form furnace bottom for **a** a single concentrated arc, and **b** distributed side-arc

current fraction decreases as part of it bypasses the main-arc into the crater wall depending the value of the carbide thickness.

Figure 3a shows results for the concentrated side arc and Fig. 3b for distributed side arc at different carbide thickness values. The actual main-arc current at around 0.5 on the horizontal axis decreases non-linearly as the carbide thickness increases. In the case of single concentrated side-arc the maximum and minimum main-arc current obtained are about 92 and 86% of total current, respectively. In the distributed arc the corresponding values are 62 and 28%, for 10 and 55 cm thick carbide respectively, the supplementing current passing through the carbide. As the total side-arc resistance is identical for these cases, this difference between single arc and distributed arc is due to the way the current is distributed in the carbide. In the case of a single concentrated side-arc, the current must pass through a small area of carbide which is attached to the arc. This proves to be the limiting factor due to the voltage drop associated. In the distributed side arc case, the current is evenly distributed throughout the carbide as it can be seen in Fig. 4. The real case is probably somewhere between these two extremes, there are probably a number of side-arcs connecting the electrode and crater wall, but it is clear that the resistance in the carbide at the arc attachment is the limiting factor on how much current passes through the charge.

From Table 2 based on the distributed side arc case we can see that up to 2/3 of the current is bypassing the main arc through the carbide. Limited amount of research has been published on this, but this is in reasonable agreement with the work of Saevarsdottir and Bakken [3]. Their work describes measurements of current and voltage on an industrial submerged arc furnace producing FeSi75 to determine the current in the arc and the charge. Their result showed that under normal operation of the furnace, approximately half of the current bypasses the arc through the charge. They also deduced that it is likely more than one arc present in the phase considered.

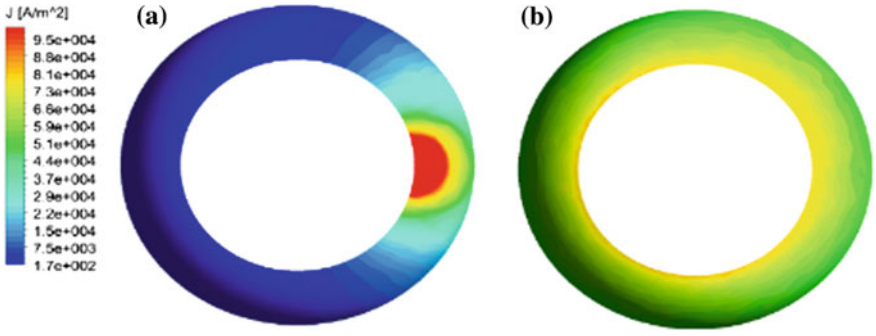

Fig. 4 Current density in the carbide crater wall for **a** single concentrated side arc modelling and **b** distributed side arc modelling

Conclusions

This paper presents computations of electric current distributions inside an industrial submerged arc furnace for silicon production. A 3D model has been developed in ANSYS Fluent using electric potential solver. Electrodes, arcs, crater, crater wall, and side-arcs that connect electrode and crater wall are considered for each phase. In this paper, the current distributions between main-arc and crater wall or charge are presented for different values of crater wall carbide thickness. Five levels of carbide thickness have been considered for each phase. Based on the combination of the levels, 13 simulation cases were generated. Each of these carbide configuration cases was simulated twice, assuming either a single concentrated side-arc or a distributed side arc to resemble the extreme case of multiple side-arcs. It was observed that the voltage drop due to constrained carbide area the current passes through in the case of single side-arc is the limiting factor for the charge current bypassing the arc, rather than thickness of crater wall carbide. A thicker carbide will draw more current which bypasses the main-arc through the carbide containing charge, but all the current will pass through the limited arc attachment area.

Acknowledgements The Icelandic Technology development fund is greatly acknowledged for their funding of this work.

References

1. Schei A, Tuset JK, Tveit H (1998) Production of high silicon alloys. Tapir Forlag, Trondheim
2. Sævarsdottir GA, Bakken JA, Sevastyanenko VG, Liping G (2011) High power ac arcs in metallurgical furnaces. High Temp Mat Process 15(3)
3. Saevarsdottir GA, Bakken JA (2010) Current distribution in submerged arc furnaces for silicon metal/ferrosilicon production, In: proceedings INFACON12
4. Tranell G, Andersson M, Ringdalen E, Ostrovski O, Stenmo JJ (2010) Reaction zones in a FeSi75 furnace—results from an industrial excavation. INFACON XII, pp 709–715
5. Myrhaug EH (2003) Non-fossil reduction materials in the silicon process-properties and behavior. Ph.D. thesis, NTNU
6. Tangstad M, Ksiazek M, Andersen JE (2014) Zones and materials in the Si furnace. In: proceedings of the silicon for the chemical and solar industry XII, Trondheim, Norway, 24–27 June 2014
7. Krokstad M (2014) Electrical resistivity of industrial SiC crusts, MSc-thesis NTNU
8. Vangskåsen J (2012) Metal-producing mechanisms in the carbothermic silicon process. M.Sc. thesis, NTNU
9. Mølnås H (2010) Investigation of SiO condensate formation in the silicon process, Project report in TMT 4500, NTNU, Norway
10. Nell J, Joubert C (2013) Phase chemistry of digout samples from a ferrosilicon furnace, Infacon proceedings Kazakhstan
11. Dhainaut M (2004) Simulation of the electric field in a submerged arc furnace. INFACON X, pp 605–613
12. Bezuidenhout JJ, Eksteen JJ, Bardshaw SM (2009) Computational fluid dynamic modelling of an electric furnace used in the smelting of PGM containing concentrates. Min Eng 22:995–1006. https://doi.org/10.1016/j.mineng.2009.03.009

13. Darmana D, Olsen JE, Tang K, Ringldalen E (2012) Modelling concept for submerged arc furnaces. Paper presented at the ninth international conference on CFD in the minerals and process industries CSIRO, Melbourne, Australia, 10–12 Dec 2012
14. Wang Z, Fu Y, Wang N, Feng L (2014) 3D numerical simulation of electrical arc furnaces for the MgO production. J Mat Process Tecnol 214:2284–2291. http://dx.doi.org/10.1016/j.jmatprotec.2014.04.033
15. FLUENT, ver. 17.0 (2017) ANSYS Inc., Southpointe, 275 Technology Drive, Canonsburg, PA 15317
16. Sævarsdottir GA (2002) High current ac arcs in silicon and ferrosilicon furnaces. Ph.D. thesis, NTNU
17. ICEM-CFD, ver. 17.0 (2017) ANSYS Inc., Southpointe, 275 Technology Drive, Canonsburg, PA 15317
18. Sasaki H, Ikari A, Terashima K, Kimura S (1995) Temperature dependence of the electrical resistivity of molten silicon. Jpn J Appl Phys. https://doi.org/10.1143/JJAP.34.3426

Investigation of Combustion and Heat Transfer in an Industrial Reheating Furnace Using CFD

Yuchao Chen, Xiang Liu, Armin K. Silaen, Kurt Johnson and Chenn Q. Zhou

Abstract The reheating furnace is used to reheat steel slabs to a target rolling temperature in the steelmaking process. The flue gas temperature distribution inside the reheating furnace is one of the main determining factors of the furnace performance. In this study, a three-dimensional steady-state computational fluid dynamics (CFD) model was developed to investigate the flow field in an industrial reheating furnace. The commercial software ANSYS Fluent® was employed to solve the transport equations to calculate gas flow, combustion and heat transfer. The simulation was carried out based on real operating conditions and data collected from industrial manufacturers. Validation of the CFD model was conducted by comparing the temperature prediction by the model with the real thermocouple measurements. The simulation results indicate that the combustion gas flow characteristics inside the reheating furnace have a significant effect on the temperature distribution. The effect of fuel/oxidant input flow rate on the temperature distribution was also investigated.

Keywords Walking-beam reheating furnace · CFD · Combustion

Introduction

In a reheating furnace, fuel is fed into a chamber through burners installed on the walls. Combustion generates high-temperature gas flow which serves to heat up the slabs, primarily through radiation, until a target temperature is reached. Reheating furnaces can be classified into batch type furnaces and continuous type furnaces. Continuous furnaces can be further divided into pusher and walking beam type

Y. Chen · X. Liu · A. K. Silaen · C. Q. Zhou (✉)
Center for Innovation Through Visualization and Simulation (CIVS),
Purdue University Northwest, 2200 169th Street, Hammond, IN 46323, USA
e-mail: czhou@pnw.edu

K. Johnson
ArcelorMittal Global Research and Development, 3001 E Columbus Dr,
East Chicago, IN 46312, USA

L. Nastac et al. (eds.), *CFD Modeling and Simulation in Materials Processing 2018*, The Minerals, Metals & Materials Series,
https://doi.org/10.1007/978-3-319-72059-3_18

reheating furnaces based on the movement of the steel stock inside the furnace. In this study, a walking beam type reheating furnace was analyzed, taking into account the moving system below the slabs. The slabs are supported by water-cooled skids that serve to advance them through the furnace. Heat is transferred from the slab bottom surface to the cooling water inside the moving structures through the skids [1].

During the past several decades, the steelmaking industry has worked to reduce energy consumption and the environmental impacts of the reheating furnace process through analysis of design and operating conditions [2]. In order to accomplish this, it is necessary to have a full understanding of the physical and chemical phenomena inside the reheating furnace. Industrial and research experience has shown that uneven temperature distributions inside the furnace caused by certain operating conditions or designs may lead to negative impacts on slab quality as well as on fuel consumption and pollutant emission. However, it is difficult to predict the impact of any given set of conditions accurately and economically through the use of traditional methods due to the complex three-dimensional structure of the furnace [3, 4]. To remedy this issue, computational modeling of fluid flow and heat transfer inside the walking beam type reheating furnace has become a popular method of analysis.

In this study, a three-dimensional steady-state computational fluid dynamics (CFD) model was developed in order to investigate the flow field in an industrial scale reheating furnace. The commercial software ANSYS Fluent® was employed to solve the transport equations related to gas flow, combustion, and heat transfer. A baseline case was firstly simulated based on real operating conditions, and further validation of this case was conducted by comparing simulation results with thermocouple measurements from industrial sites in order to confirm the accuracy of the CFD model. Additionally, parametric studies, which focused on the bottom intermediate zone, were then carried out to investigate the effect of fuel/oxidant input flow rate on the uniformity of gas temperature distribution in the bottom intermediate zone of the walking-beam-type reheating furnace.

Numerical Models

Since the emphasis of this study was to determine the flow distribution during a certain time period when flow conditions are essentially continuous, this study assumed that a steady-state case can represent the conditions of typical furnace operation. In this study, turbulent flow including combustion accompanied with heat and mass transfer was considered. The realizable k-e turbulence model was employed to predict flow turbulence. The eddy dissipation species transport model was conducted to determine species distribution during the working process. The Discrete Ordinates (DO) radiation model coupled with the Weighted-Sum-of-Gray-Gases Model (WSGGM) was used to calculate the heat transfer inside the furnace mainly through radiation. All general transport equations used in this study are listed below.

The Species Conservation Equation

$$\nabla \cdot (\rho \vec{v} Y_i) = -\nabla \cdot \overrightarrow{j_i} + R_i \tag{1}$$

where R_i is the net rate of production of species i by chemical reactions, which is calculated through the eddy dissipation concept model [5]. $\overrightarrow{j_i}$ is the diffusion flux term of species i, which arises due to gradients of concentration and temperature, under which the diffusion flux is given as follows:

$$\overrightarrow{j_i} = -\left(\rho D_{i,m} + \frac{\mu_t}{Sc_t}\right)\nabla Y_i - D_{T,i}\frac{\nabla T}{T} \tag{2}$$

where $D_{i,m}$ is the diffusivity for species i in the gas mixture, 2.88E−5 m^2/s. μ_t is turbulent viscosity, $D_{T,i}$ is the thermal diffusion coefficient, which is calculated from thermal conductivity divided by density and specific heat capacity at a constant pressure. Sc_t is the turbulent Schmidt number, which is 0.7.

Combustion Model (Eddy Dissipation Concept)

The detailed Arrhenius chemical reaction kinetics of natural gas combustion can be incorporated in turbulent flames through the eddy-dissipation concept (EDC) model [5]. The EDC model relies on the Kolmogorov cascade of energy dissipation on all length scales in turbulence flow. The source term in the conservation equation for the mean species i is modeled as:

$$R_i = \frac{\rho(\xi^*)^2}{\tau^*\left[1-(\xi^*)^3\right]}(Y_i^* - Y_i) \tag{3}$$

where Y_i^* is the mass fraction of species i within the fine structures after reacting over the time τ^*. Y_i is the Favre-averaged mass fraction of species i obtained from

$$Y_i = (\xi^*)^3 Y_i^* + (1-(\xi^*)^3)Y_i^0 \tag{4}$$

where Y_i^0 represents the mass fraction of species i in the fluid surrounding the fine structures, and ξ^*, the mass fraction occupied by the fine structure regions, can be expressed as

$$\xi^* = C_\xi\left(\frac{\nu\varepsilon}{k^2}\right)^{1/4} \tag{5}$$

where C_ξ is a volume fraction constant and the value is 2.1377. The reactions are assumed to occur in the fine structures over a residence time scale τ^*, which is defined as

$$\tau^* = C_\tau \left(\frac{\nu}{\varepsilon}\right)^{1/2} \tag{6}$$

The Discrete Ordinates (DO) Radiation Model

$$\nabla \cdot (I(\vec{r},\vec{s})\vec{s}) + (a+\delta_S)I(\vec{r},\vec{s}) = an^2\frac{\delta T^4}{\pi} + \frac{\delta_S}{4\pi}\int_0^{4\pi} I(\vec{r},\vec{s}\,')\phi(\vec{s}\cdot\vec{s}\,')d\Omega' \tag{7}$$

where $\overrightarrow{\mathrm{r}}$ is position vector, $\overrightarrow{\mathrm{s}}$ is the direction vector, and $\overrightarrow{\mathrm{s}}'$ is the scattering direction vector. a is the absorption coefficient. n is the refractive index. σ_s is the scattering coefficient. σ is the Stefan-Boltzmann constant (5.669×10^{-8} W/m^2 T^4). I is radiation intensity, which depends on position $\overrightarrow{\mathrm{r}}$ and direction $\overrightarrow{\mathrm{s}}$. T is the local temperature. Φ is the phase function. Ω' is the solid angle.

The Weighted-Sum-of-Gray-Gases Model (WSGGM)

The weighted-sum-of-gray-gases model (WSGGM) is a reasonable compromise between the oversimplified gray gas model and a complete model which takes into account particular absorption bands. The emissivity over the distance S can be presented as:

$$\varepsilon = \sum_{i=0}^{I} a_{\varepsilon,i}(T)(1 - \mathrm{e}^{-K_i PS}) \tag{8}$$

where $a_{\varepsilon,i}$ is the emissivity weighting factor for the ith fictitious gray gas, the bracketed quantity is the ith fictitious gray gas emissivity, K_i is the absorption coefficient of the ith gray gas, P is the sum of the partial pressures of all absorbing gases, and S is the path length.

The absorption coefficient for i = 0 is assigned a value of zero to account for windows in the spectrum between spectral regions of high absorptions ($\sum_{i=0}^{I} a_{\varepsilon,i} < 1$) and the weighting factor for i = 0 is evaluated as:

$$a_{\varepsilon,0} = 1 - \sum_{i=0}^{I} a_{\varepsilon,i} \tag{9}$$

The temperature dependence of the emissivity weighting factor can be approximated by the function:

$$a_{\varepsilon,i} = \sum_{j=0}^{J} b_{\varepsilon,i,j} T^{j-1} \tag{10}$$

where $b_{\varepsilon,i,j}$ is the emissivity gas temperature polynomial coefficients. If $K_i PS \ll 1$, Eq. 10 can be simplified to:

$$a_{\varepsilon,i} = \sum_{j=0}^{J} b_{\varepsilon,i,j} T^{j-1} \tag{11}$$

Simulation Conditions

Simulation Domain and Mesh

The basic structure of the walking-beam-type reheating furnace, based on the drawings provided by ArcelorMittal, is given in Fig. 1b including four temperature zones: preheating zone, heating zone, intermediate zone and soaking zone according to the heating characteristics.

Ten different types of burners are installed within the different temperature zones according to the working requirements, as illustrated in Fig. 2. The burners are named correspond to the zone name and burner locations. From front to rear, these burners are grouped as top/bottom preheating burners, top/bottom heating 1 burners, top/bottom heating 2 burners, top/bottom intermediate burners and top/bottom soaking burners. For the top and bottom soaking zone, the burners are classified into two sets according to their direction.

The geometry shown in Fig. 2 is further divided into computational grids where a set of transport equations can be applied to each cell and solved. As can be seen

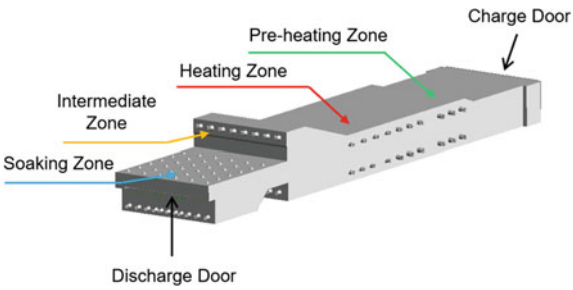

Fig. 1 Geometry of four temperature zones in reheating furnace

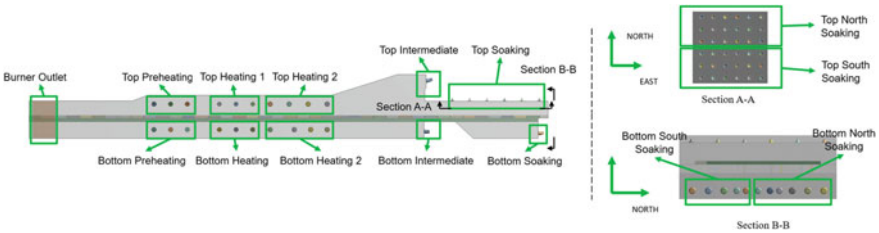

Fig. 2 The burner installation locations

Fig. 3 A hybrid mesh with 9.5 million elements used for the furnace

from Fig. 3, a hybrid mesh including the structured and unstructured grids with 9.5 million elements was generated for numerical calculation.

Boundary Conditions

Natural gas which contains approximately 96% methane was charged as fuel in this study. A two-step reaction mechanism was employed in order to obtain more accurate representation of species concentrations in the simulation results. The reaction mechanism and kinetics are from literature [6].

This study is based on the assumption that the injected fuel and air flow are both uniform. Therefore, the average mass flow rate measured from industrial sites is considered for corresponding fuel and air inlets. The boundary conditions used in this study are listed in Table 1.

Based on the operating data provided by ArcelorMittal, the slab charging temperature is 174.2 °F, and the slab discharge temperature is 2278.26 °F. The temperatures of the other 37 slabs inside the furnace are assumed to be linearly increasing from the charge temperature to the discharge temperature. The furnace wall is treated as an adiabatic wall with an emissivity of 0.75 [2]. The charge and discharge doors are assumed to be closed, and boundary conditions on the doors are identical to the furnace walls.

Table 1 Boundary conditions

	Top Preheating	Bottom Preheating	Top Heating 1	Bottom Heating 1	Top Heating 2	Bottom Heating 2
Combustion air temp.(°F)	692.6	692.6	692.6	692.6	692.6	692.6
Combustion Air (kg/s)	0.794979	0.899528	6.721339	8.093713	11.20947	11.1297
Fuel Temp. (°F)	80	80	80	80	80	80
Fuel (kg/s)	0.001222	0.001018	0.330461	0.441022	0.56441	0.6033
	Top Intermediate	Bottom Intermediate	Top North Soaking	Top South Soaking	Bottom North Soaking	Bottom South Soaking
Combustion air temp. (°F)	692.6	692.6	692.6	692.6	692.6	692.6
Combustion Air (kg/s)	4.748828	5.966415	1.104892	1.192129	1.292604	2.083849
Fuel temp. (°F)	80	80	80	80	80	80
Fuel (kg/s)	0.265102	0.322316	0.055586	0.055586	0.063323	0.109543

Model Validation

Simulation results of the baseline case were firstly validated by comparing results with the thermocouple readings from industrial sites. According to the real thermocouple position, measured points in the same locations marked in the domain to get the simulated temperature. The detailed positions of the measured points are shown in Fig. 4.

A comparison between simulation results and thermocouple readings is given in Table 2. As seen from the table, the difference between the two data sets is within 15%. The maximum deviation happens near the outlet, which is acceptable, as the outlet conditions are not the focus of this study.

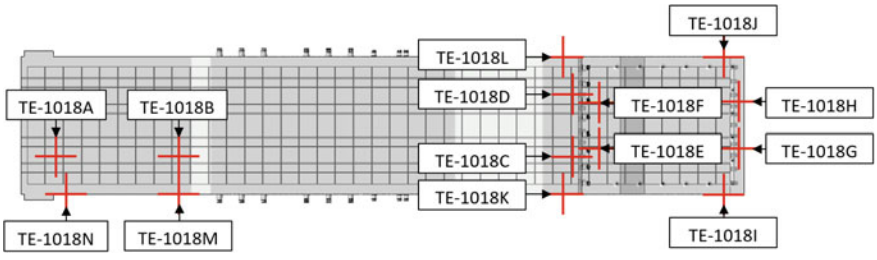

Fig. 4 The position of the measured points in simulation domain

Table 2 Comparison between simulation results and thermocouple readings

No.	TE-1018A	TE-1018B	TE-1018C	TE-1018D	TE-1018E	TE-1018F	TE-1018G	TE-1018H
Reading (°C)	823	908	1314	1311	1274	1264	1267	1268
CFD (°C)	849	1039	1202	1196	1183	1195	1353	1350
Difference (%)	3.2	14.4	8.6	8.8	7.2	5.5	6.8	6.4

Results and Discussion

Furnace Gas Temperature

Top view of temperature contours given in Fig. 5 shows the overall gas temperature distribution in the baseline case. In the front of the furnace, in the early stage of heating, the average gas temperature is largely impacted by the low temperature from charge door and outlet, which is restricted around 1600 °F.

However, once slabs are brought into the heating zone, slab temperature will rapidly increase due to high gas temperatures generated from heating burners located at both sides of the furnace wall. Because of the heating zone, the average gas temperature is elevated to around 2500 °F. The intermediate zone and the soaking zone are identified as the areas for stabilizing the slab temperture to the target rolling temperature. Therefore, the average gas temperature in those zones remains around 2400 °F.

Parameter Study in Bottom Intermediate Zone

It is well known that uneven temperature distributions inside the furnace may lead to negative impacts on slab quality, fuel consumption, and pollutant emission. In this parameter study, the effect of fuel/oxidant input flow rate on the temperature distribution was investigated. In order to balance the computational time and simulation accuracy, only the bottom intermediate zone, where typical operating conditions will be used, was included for the further study. The simulation domain shown in Fig. 6 is used to generate the mesh, which contains roughly 3.8 million elements.

Based on the baseline case, operating conditions in the bottom intermediate zone are listed in Table 3 for three studied groups with 50% fuel, 25% fuel, and 10% fuel respectively. In each group, the air mass flow rate of the latter case is 1.09 times that of the previous case, and the air/fuel ratio in a group varies from 16.6 to 23.3. The temperature distribution contour on a cross-section of burner #6 is illustrated in Fig. 7. Group 1 has the highest average overall gas temperature up to 2600 °F, while this temperature has been significantly decreased in both group 2 and 3 due to the lower fuel input. The area of high-temperature zone created by combustion in group 1 is much larger than those of group 2 and 3, where the hot gas can almost reach the center of the domain.

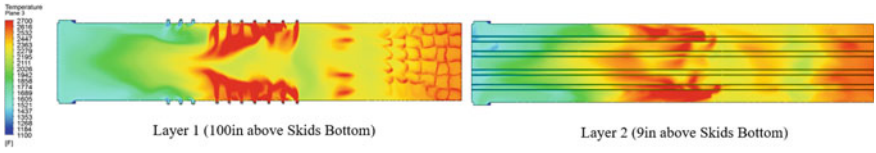

Fig. 5 Top view of temperature contours on different cross-sections above skids bottom

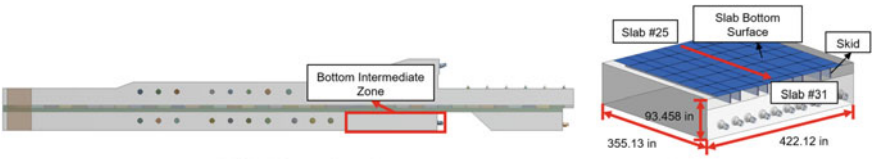

(a) Whole Furnace Domain (b) Domain for Bottom Intermediate Zone

Fig. 6 Simulation domain and mesh for parameter study

Table 3 The detailed fuel/oxidant input flow in three studied groups

No.			Case 1	Case 2	Case 3	Case 4	Case 5
Group 1 50% fuel	Fuel	Mass flow rate (kg/s)	0.225	0.225	0.225	0.225	0.225
		Temperature (°F)	80	80	80	80	80
	Air	Mass flow rate (kg/s)	3.758	4.133	4.509	4.885	5.261
		Temperature (°F)	662	662	662	662	662
No.			Case 6	Case 7	Case 8	Case 9	Case 10
Group 2 25% fuel	Fuel	Mass flow rate (kg/s)	0.113	0.113	0.113	0.113	0.113
		Temperature (°F)	80	80	80	80	80
	Air	Mass flow rate (kg/s)	1.879	2.067	2.255	2.442	2.63
		Temperature (°F)	662	662	662	662	662
No.			Case 11	Case 12	Case 13	Case 14	Case 15
Group 3 10% fuel	Fuel	Mass flow rate (kg/s)	0.045	0.045	0.045	0.045	0.045
		Temperature (°F)	80	80	80	80	80
	Air	Mass flow rate (kg/s)	0.752	0.827	0.902	0.977	1.052
		Temperature (°F)	662	662	662	662	662

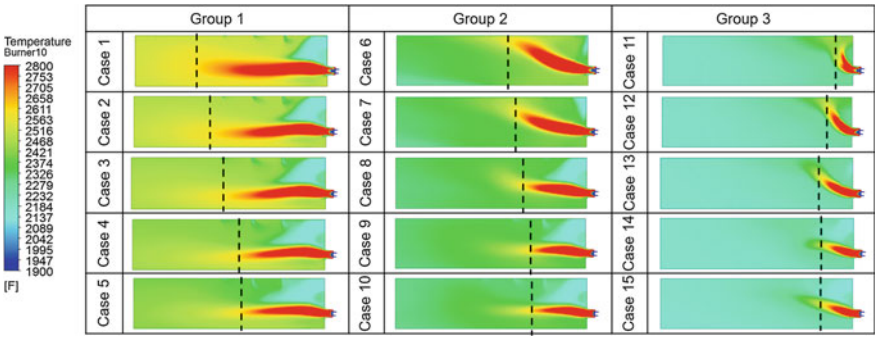

Fig. 7 Temperature distribution contour on a cross-section of burner #6

Streamlines colored by temperature for case 2 in group 1, case 7 in group 2, and case 12 in group 3 are given in Fig. 8. It is clear that the low mass flow rate for both air and gas input leads to low momentum for the fluid, which allows the hot gas to rise and touch the slab bottom surface. This situation may result in uneven heat

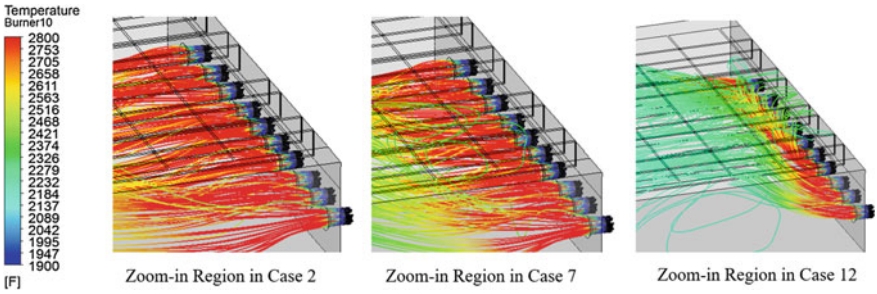

Fig. 8 Streamlines colored by temperature for case 2, 7, 12

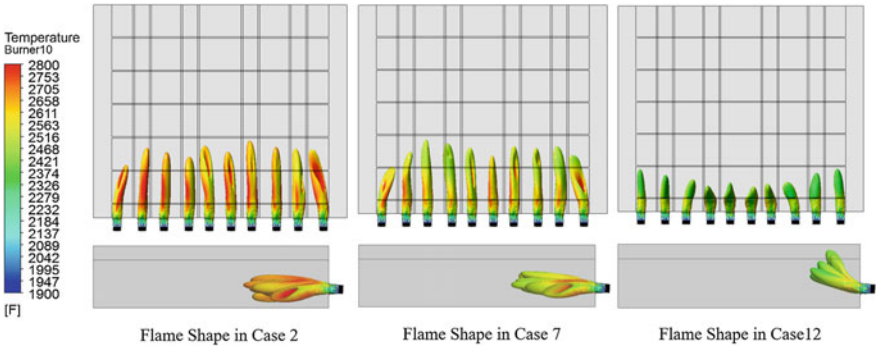

Fig. 9 Flame shape described by CO distribution using 500 ppm mass fraction for case 2, 7, 12

distribution and poor slab quality in the temperature stabilization stage, and these operating conditions should be avoided if possible.

Corresponding CO distributions for case 2, 7, 12 are shown in Fig. 9. The flame shape is described by CO distribution using 500 ppm mass fraction. It can be seen from the figure that, reducing the percentage of both air and gas input will significantly reduce the average flame temperature from 2700 to 2250 °F. However, due to the similar air/fuel ratio, case 2, 7 and 12 have almost the same flame length but different lift-angles because of the different momentum for the input fluid. The flame shape in case 2 is straightforward, while case 7 has a small rising-angle. The rising angle in case 12 is larger still.

Conclusions

A comprehensive three-dimensional CFD model based on actual operation boundary conditions was developed to simulate the steady-state flow inside the walking-beam-type reheating furnace. The CFD model provides detailed flow and

temperature profiles for investigation of complicated combustion and heat transfer processes. Validation of the model has been conducted by comparing numerical results with measured data provided by ArcelorMittal. The current model is capable of predicting the temperature distribution and also the flame shape inside the furnace. A parameter study focusing on the bottom intermediate zone was conducted to investigate the combustion and heat transfer processes underneath the slab. The influence of input air/fuel ratio to the flame size and shape has been illustrated, potentially providing information that can be used to reduce the possibility of uneven heat distribution and corresponding poor slab quality.

Acknowledgements The authors would like to thank ArcelorMittal for their great support in the course of the project. The Center for Innovation through Visualization and Simulation (CIVS) at Purdue University Northwest is also gratefully acknowledged for providing all the resources required for this work.

References

1. Hsieh CT, Huang MJ, Lee ST, Wang C (2008) Numerical modeling of a walking-beam-type slab reheating furnace. Numer Heat Transfer, Part A 53:966–981
2. Kim MY (2007) A heat transfer model for the analysis of transient heating of the slab in a direct-fired walking beam type reheating furnace. Int J Heat Mass Transfer 50:3740–3748
3. Han SH, Chang D, Kim CY (2010) A numerical analysis of slab heating characteristics in a walking beam type reheating furnace. Int J Heat Mass Transfer 53:3855–3861
4. Tang G, Wu B, Bai D, Wang Y, Bodnar R, Zhou CQ (2017) Modeling of the slab heating process in a walking beam reheating furnace for process optimization. Int J Heat Mass Transfer 113:1142–1151
5. Graca M, Duarte A, Coelho PJ, Costa M (2013) Numerical simulation of a reversed flow small-scale combustor. Fuel Process Technol 107:126–137
6. Tang G, Wu B, Bai D, Wang Y, Rick B, Zhou CQ (2017) Numerical simulation of a walking beam type steel slab reheating furnace. Iron Steel Technol, pp 78–88

Finite Element Modelling of Electrokinetic Deposition of Zinc on Mild Steel with ZnO-*Citrus sinensis* as Nano-Additive

Oluseyi O. Ajayi, Olasubomi F. Omowa, Oluwabunmi P. Abioye, Olugbenga A. Omotosho, Esther T. Akinlabi, Stephen A. Akinlabi, Abiodun A. Abioye, Felicia T. Owoeye and Sunday A. Afolalu

Abstract The electrokinetic deposition of zinc on mild steel substrate under the influence of ZnO-*Citrus sinensis* nano-additive was investigated numerically using a Finite Element (FE) solver. The conductivity of the Acid chloride plus ZnO-*Citrus sinensis* nano-additive electrolyte and the properties of Zinc and mild steel electrodes were used as the input codes for the model. The model was designed on a 3-dimensional scale. The boundary conditions were set and the model was meshed using the finer mesh capability in the FE solver. The model was processed and readings of the modelled zinc deposited mild steel were taken, validated and analysed so as to get the optimum parameters from the deposition process. Based on the results, the deposition mass and thickness increased with deposition time with ZnO-*Citrus sinensis* nano-additive, it is thus recommended that relatively high deposition time should be used in order to achieve optimum deposition.

Keywords Nano-additive · Nanotechnology · Corrosion protection Electrodeposition · Mild steel · Finite element · CFD

O. O. Ajayi (✉) · O. F. Omowa · O. P. Abioye · O. A. Omotosho · A. A. Abioye
S. A. Afolalu
Department of Mechanical Engineering, Covenant University, Canaan Land, Ota, Ogun State, Nigeria
e-mail: oluseyi.ajayi@covenanatuniversity.edu.ng

E. T. Akinlabi
Department of Mechanical Engineering Science, University of Johannesburg, Johannesburg, South Africa

S. A. Akinlabi
Department of Mechanical and Industrial Engineering Technology, University of Johannesburg, Johannesburg, South Africa

F. T. Owoeye
Department of Chemistry, Covenant University, Canaan Land, Ota, Ogun State, Nigeria

L. Nastac et al. (eds.), *CFD Modeling and Simulation in Materials Processing 2018*, The Minerals, Metals & Materials Series,
https://doi.org/10.1007/978-3-319-72059-3_19

Introduction

Electrodeposition is a process of coating a thin layer of a metal on top of another metal so as to modify its surface properties. It helps in accomplishing the desired properties in a material. Such properties include the electrical and corrosion resistance, wear resistance, heat tolerance enhancement and decoration purposes [1, 2]. One of the ways to improve mild steel's value includes electrodeposition [3–5]. Electrokinetic deposition process is lately a process of interest to researchers because of its ability to enhance properties of different substrate materials such as mild steel at an affordable cost. Moreover, the phenomenon of electrodeposition comes by as a result of several experimentations which can be time consuming, repetitive, cost intensive and cumbersome, when there is the need to find optimum conditions. However, with the advent of computational fluid dynamics and finite element modelling/analysis, the process of simulating electrokinetic deposition becomes a cost-effective way to understand, optimize and control the electrodeposition processes.

Mild steel is an outstanding structural material. It is very affordable for engineering applications, can be easily formed and is mechanically strong. However, it rusts at low temperatures, and oxidises rapidly at high temperature [6]. Hence, there is a great need to improve the value of mild steel so that its intrinsic properties can be leveraged on and thus make the alloy more valuable in essential applications such as in our day to day lives and in industries which include the automotive, construction, electronics, electrical appliances, recreational and materials handling.

Relatively half of the world's consumption of zinc is used for the purpose of coating zinc on steel while electrodeposition of steel sheets consumes about 25–30% of the zinc produced [7, 8]. Zinc is appropriate to be utilised as a sacrificial cathode protector of steel from corrosion because its electronegativity of −0.6 V/standard hydrogen electrode (SHE) is over iron (Fe/Fe^{2+} 0.44 V/SHE) [9]. The exceptional resistive nature of zinc to corrosion is due to its ability to form adherent corrosion product films. Also, its corrosion rate is significantly lower than that of ferrous material (10–100 times depending on the environment). Additionally, zinc plating is fit to come in contact with edibles because zinc is nontoxic.

Acid chloride zinc plating is one of the most popular plating methods employed in developed countries. The first plating baths employed were acidic and zinc sulfate based. A great increase in the use of acid-zinc based bath has been noticed recently, as a result of environmental impact of cyanide-based bath which is toxic and expensive [10, 11].

The use of additives in aqueous electroplating solutions is really important because of its significant effects on the growth and structure of the deposits. Its benefits include enhancing mechanical and physical properties; brightening of the deposit, grain size reduction, stress and pitting reduction; increase in the current density range and stimulating levelling. However, the additives, which may be organic or metallic, ionic or non-ionic, are absorbed on the plated surface. For all

types of coating, the surface condition of the substrate is critical in terms of coating performance and durability [12].

A typical simulation produces the current distribution in the electrodeposition cell and at the electrodes' surface. The chosen FE solver is able to model cells when the thickness deposited is negligible compared to the inter-electrode gap and in event the growth and dissolution of the electrodes have to be considered using dynamic boundaries. Artificially modelling electrodeposition using for instance a Finite Element (FE) solver can help in the investigation of the influence of different parameters such as the time and additive concentration in the electrokinetic deposition process. This is the focus of this study. It additionally showed the ability to artificially model and analyse electrokinetic deposition of zinc on mild steel under the influence of organic zinc oxide-*Citrus sinensis* nanoadditive. It aimed to contribute to the very limited studies in this direction and employed a 3-D modelling procedure rather 2-D.

Materials and Methods

The modelling and simulation were carried out using a commercially available FE solver. The procedure follows three stages of pre-processing, processing and analysis, and post-processing.

Pre-processing

The FE model wizard was launched and a space dimension of 3-D was chosen. The electrodeposition module was used for the simulation. The geometry of the electrokinetic deposition setup was captured in the model. The model is as shown in Fig. 1.

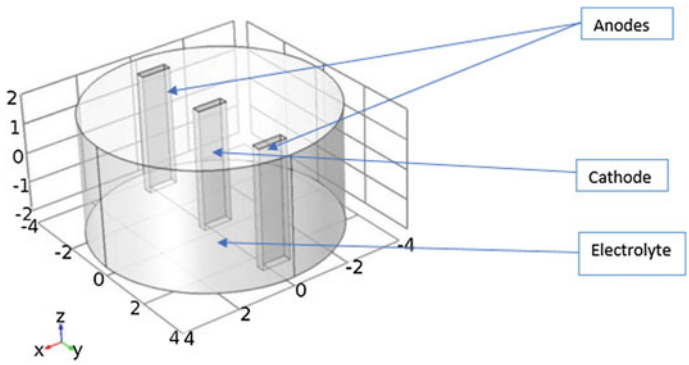

Fig. 1 The electrokinetic deposition setup model

Table 1 The geometry statistics of the model

Description	Value
Space dimension	3
Number of domains	1
Number of boundaries	18
Number of edges	48
Number of vertices	32

The electrokinetic deposition setup model consisted of the cathode, anodes and the container holding the electrolyte. The explicit selection node was created which allows for the boundary creation. The boundaries of the anodes and cathode were respectively defined, with boundaries 5–7, 11–13, 16, 18 for cathode and boundaries 8–10, 17 for the anode. The geometry statistics are defined as shown in Table 1.

Also, the combination of properties for the surface and the reaction stoichiometry which will determine how the magnitude and direction of the growth velocity of the deposited layer relate to the electrode reaction currents were defined. The external depositing electrode (i.e. the anode), surface properties and electrode reaction nodes were also defined (definitions are shown in Table 2).

Table 2 Parameters for the deposition model

Parameters	Value
Electrolyte conductivity (acid chloride + 1 Mol ZnO-*Citrus sinensis* nano-additive)	0.1964 S/m
Electrolyte conductivity (acid chloride only)	0.2013 S/m
Current	0.8 A
Cathode current density (mild steel)	0.020 A/m^2
Density of anode (Zinc)	7.13 g/mL
Density of cathode (Steel)	7.85 g/mL
Assumption	Model is isotropic
Equilibrium potential	0.7618 V
Temperature derivative of equilibrium potential	0 [V/K]
Kinetics expression type	Linearized butler—Volmer
Exchange current density	2.6e5 [A/m^2]
Molar mass of zinc	0.06538 kg/mol
Molar mass of steel	0.05584 kg/mol
Anodic transfer coefficient	0.5
Cathodic transfer coefficient	0.5
Active specific surface area	1e6 [1/m]
Limiting current density	Off
Number of participating electrons	2
Stoichiometric coefficient	1

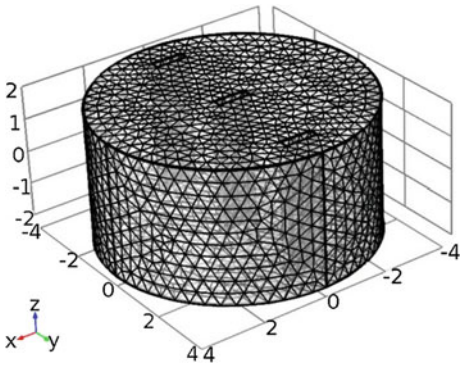

Fig. 2 Meshed electrokinetic deposition model

The cathode was defined to be mild steel, Anodes were made of pure zinc and the electrolyte initially used was acid chloride which was later changed to acid chloride + 1 Mol Zinc Oxide-*Citrus sinensis* nano-additive. The properties of the Cathode, Anode and electrolytes were thus captured as the input codes for the model as the model parameters (as shown in Table 2). Some of the parameters used for the model were measured while others were as obtained in the literature.

Meshing was done on the model using a physics-controlled mesh with finer mesh element size employed. The meshed model is shown in Fig. 2.

The simulation was set as time dependent and fixed geometry. The processing time was configured in seconds and in a range (0, 30, 1500).

Processing and Analysis

The simulation was computed by varying the deposition time with and without the ZnO-*Citrus sinensis* nano-additive. The FE solver then solved the problem at every node during the simulated deposition process.

The analysis was done by the FE solver as explained below.

The overpotential, μ_i, for an electrode reaction of index i, can be defined according to the following equation:

$$\mu_i = \beta_{m,0} - \beta_1 - X_{eq,i} \tag{1}$$

where $\beta_{m,0}$ denotes the electric potential of the metal, β_1 denotes the potential in the electrolyte, and $X_{eq,i}$ denotes the difference between the metal and electrolyte potentials at the electrode surface measured at equilibrium using a common reference potential. The electric potential of the metal at the anode is equal to the cell voltage. The potential of the electrolyte floats and adapts to satisfy the balance of current, so that an equal amount of current that leaves at the cathode also enters at the anode. This then determines the overpotential at the anode and the cathode.

The model used the electrodeposition and secondary interface to solve for the electrolyte potential, β_l (V), according to:

$$\begin{aligned} n_l &= -\alpha_l \Delta \beta_l \\ \Delta \cdot n_l &= 0 \end{aligned} \tag{2}$$

where n_l(A/m^2) is the electrolyte current density vector and α_l (S/m) is the electrolyte conductivity, which is assumed to be a constant. Using the default Insulation condition for all boundaries excluding the anode and cathode surfaces:

$$p \cdot n_l = 0 \tag{3}$$

as p is the normal vector, pointing out of the domain. The main electrode reaction on both the anode and the cathode surfaces is the zinc deposition/dissolution reaction given as:

$$\mathrm{Zn}^{2+} + 2\mathrm{e}^- \leftrightarrow \mathrm{Zn}(s) \tag{4}$$

Using the Butler-Volmer expression to model this reaction, this will set the local current density to:

$$n_{loc,\mathrm{Zn}} = n_{0,\mathrm{Zn}} \left(\exp\left(\frac{\varepsilon_a F \mu_{Zn}}{RT} \right) - \exp\left(\frac{\varepsilon_c F \mu_{Zn}}{RT} \right) \right) \tag{5}$$

The rate of deposition at the cathode boundary surfaces and the rate of dissolution at the anode boundary surface, with a velocity in the normal direction, v (m/s), can be calculated according to:

$$V = \frac{n_{loc,\mathrm{Zn}}}{pF} \frac{M}{\rho} \tag{6}$$

where M is the mean molar mass (65 g/mol) and ρ is the density (7130 kg/m^3) of the Zinc atoms and p is number of participating electrons. It should be noted that the local current density is positive at the anode and negative at the cathode surfaces. On the anode the electrolyte current density is set to the local current density of the zinc deposition reaction:

$$p \cdot n_l = n_{loc,\mathrm{Zn}} \tag{7}$$

On the cathode, a second electrode reaction was added to model the parasitic hydrogen evolution reaction:

$$2\mathrm{H}^+ + 2\mathrm{e}^- \leftrightarrow \mathrm{H}_2 \tag{8}$$

A cathodic Tafel equation was used to model the kinetics of the hydrogen reaction on the cathode, this will thus set the local current density to:

$$n_{loc,\mathrm{H}} = -n_{o,\mathrm{H}} 10^{-\mu/A} \tag{9}$$

The hydrogen reaction will not affect the rate of deposition of zinc, but it will affect the total current density at the cathode surface:

$$p \cdot n_l = n_{loc,\mathrm{Zn}} + n_{loc,\mathrm{H}} \tag{10}$$

Thus, simulating the deposition with time dependent and fixed geometry,

$$n_1 \cdot p = n_{total} \tag{11}$$

$$n_{total} = \sum_i n_{loc \cdot i} + n_{dl} \tag{12}$$

$$\frac{\partial C_{m,n}}{\partial t} + \Delta_t \cdot \left(-D_n \Delta_t c_{m,n}\right) = R_{m,n} \tag{13}$$

$$N_{m,n} = -D_n \Delta_t c_{m,n} \tag{14}$$

$$\emptyset_n = \frac{c_{m,n} \alpha_n}{\neg_s} \tag{15}$$

$$\frac{\partial c_{dep,n}}{\partial t} = R_{dep \cdot n} \tag{16}$$

$$p \cdot \frac{\partial x}{\partial t} = \sum_n \frac{R_{dep,n} M_n}{\rho_n} \tag{17}$$

$$\Delta \cdot n_l = Q_i \tag{18}$$

$$n_1 = -\alpha_1 \Delta \beta_1 \tag{19}$$

Also with:

$$\Delta \cdot n_m = Q_m \tag{20}$$

$$n_m = -\alpha_m \Delta \beta_m \tag{21}$$

where,

β_1 = phil and β_m = phis; phil is the electrolyte potential and phis is the electric potential.

Post-processing

The solution data set was added, the surface plot was created to get the thickness and mass change of the electrodes and the second surface plot for current efficiency was created. Likewise, the thickness and mass changes were captured when the electrolyte conductivity is updated with the addition of 1 Mol ZnO-*Citrus sinensis* nano-additive data.

Results and Discussion

Electrolyte Potential

Figure 3 shows the potential of the electrolyte during deposition. Based on the simulation, the electrolyte has the lowest value of potential around the cathode and highest value of potential around the anodes.

Anode Electrode Change

The anode's thickness and mass reduced significantly as shown in the simulation in Fig. 4. Also, Fig. 5a, b shows that the anode electrodes thickness and mass consistently decreased with time. The anode reduced by about 2.1×10^{-6} m in thickness and 0.0145 kg/m^3 after depositing for 1500 s.

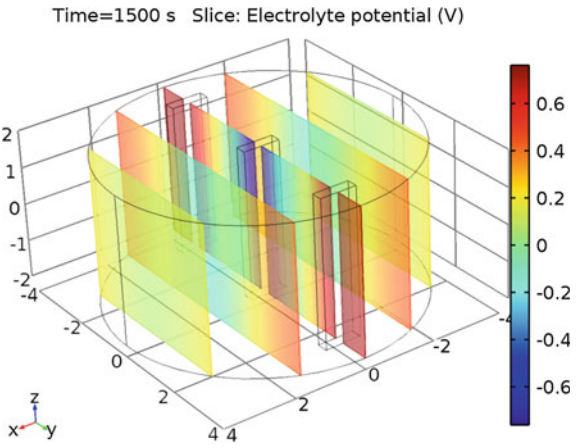

Fig. 3 Potential of the electrolyte during deposition

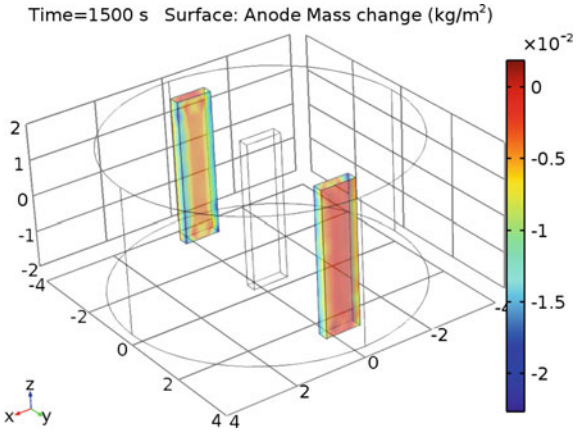

Fig. 4 Surface: anode mass change (kg/m^2) at the end of deposition

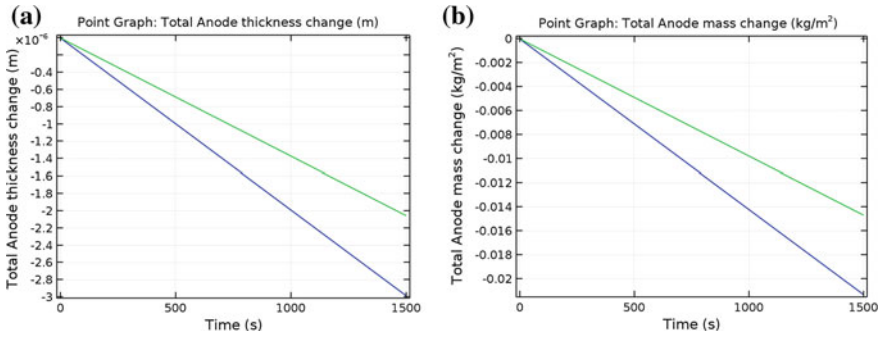

Fig. 5 Point graph, **a** Total anode thickness change (m), **b** Total anode mass change (kg/m^2)

Cathode Electrode Change

At the end of the deposition, significant increase in mass was observed in the cathode, this confirms that the deposition process led to a mass increase in the cathode as shown in Fig. 6. Also, Fig. 7a, b shows that the cathode electrode thickness and mass consistently increased with time. The cathode increased by about 2.2×10^{-6} m in thickness and 0.017 kg/m^3 in mass after depositing for 1500 s.

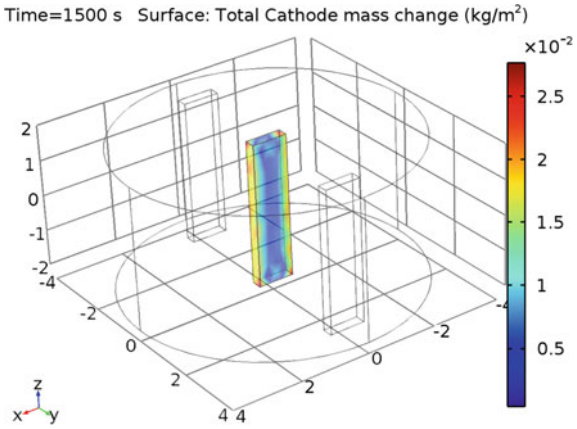

Fig. 6 Surface: Total Cathode mass change (kg/m^2) at the end of deposition

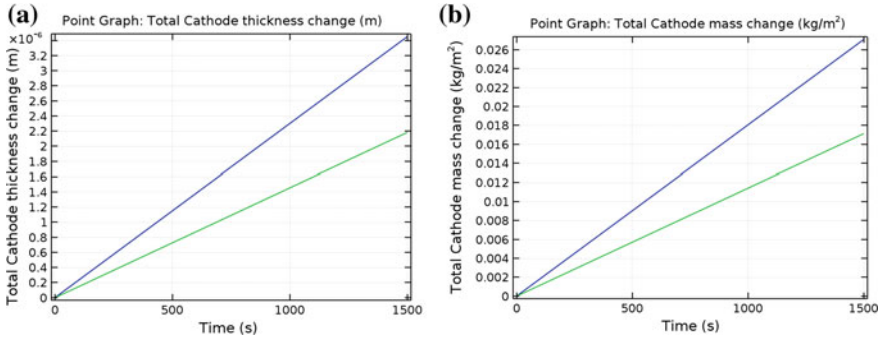

Fig. 7 Point graph, **a** Total cathode thickness change (m), **b** Total cathode mass change (kg/m^2)

Comparison of the Results of Cathode Change from the FE Solver with Experimentation

Figure 8 shows the result of the cathode mass change, the same mass change trend was observed both in the simulated result (shown in Fig. 7b) and experimental result. The experimental result shows the actual mass change from the deposition while the simulated result shows the expected result in an ideal situation (thus the reason for the slight deviation seen between 600 and 900 s in the experimental result's graph). This mass change trend in the experimental result validates the accuracy of the simulation.

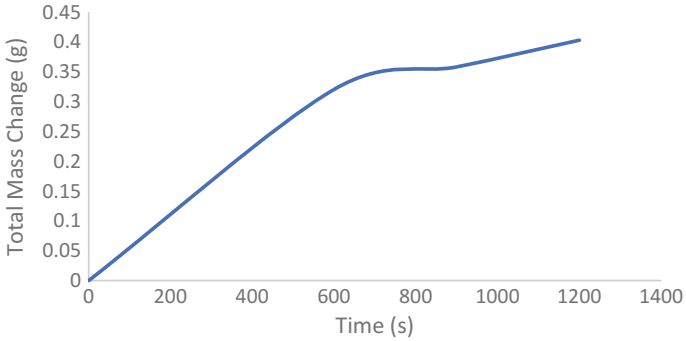

Fig. 8 Experimental result of the cathode mass change

*Effect of ZnO-*Citrus sinensis *Nano-Additive on the Electrokinetic Deposition*

To get the effect of ZnO-*Citrus sinensis* nano-additive on the electrokinetic deposition, the data of the electroconductivity in the model was updated with the data for 1 Mol of ZnO-*Citrus sinensis* nano-additive (as stated in Table 2). Figure 9 shows the result showing the impact of the 1 Mol ZnO-*Citrus sinensis* nano-additive on the cathode thickness and mass changes.

Without the additive, the cathode increased by about 2.2×10^{-6} m in thickness and 0.017 kg/m^3 in mass after depositing for 1500 s; while with 1 Mol ZnO-*Citrus sinensis* nano-additive, the cathode increased by about 2.18×10^{-6} m in thickness and approximately 0.017 kg/m^3 after depositing for 1500 s. Based on the results from the simulation, the impact of 1 Mol of the nanoadditive used is insignificant in electrokinetic deposition of zinc on mild steel in acid chloride environment. Similar results were also gotten at the anodes when comparing with and without the 1 Mol ZnO-*Citrus sinensis* nano-additive (i.e. The anode reduced by about 2.1×10^{-6} m in thickness and 0.0145 kg/m^3 after depositing for 1500 s).

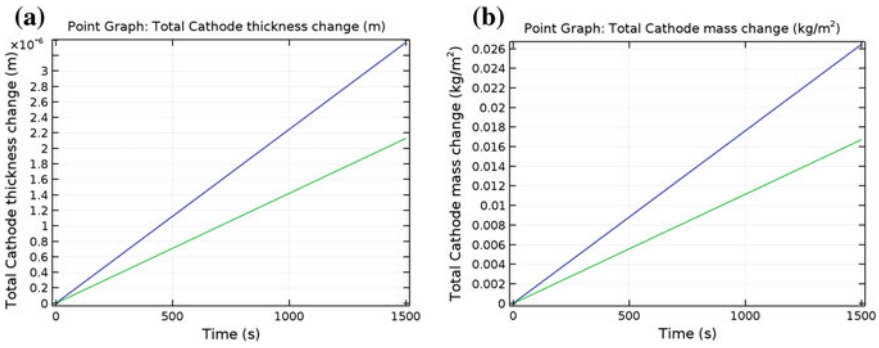

Fig. 9 Point graph, **a** Total cathode thickness change (m), **b** total cathode mass change (kg/m^2)

Although physical examination of the zinc deposited mild steel shows a smoother surface finish when ZnO-*Citrus sinensis* as nano-additive was included in the electrolyte solution, the simulation and experiment showed an insignificant impact of the nano-additive on mass and thickness changes in the deposition.

Conclusion

The electrokinetic deposition of zinc on mild steel with ZnO-*Citrus sinensis* as nano-additive was artificially studied using a commercially available FE solver. With and without the ZnO-*Citrus sinensis* nano-additive, the Cathode's thickness and mass increased while the Anode's thickness and mass reduced with the deposition time. The amount of mass and thickness increment in the Cathode is similar to the total amount of mass and thickness reduction in the anodes. Thus, high deposition time is required for optimum deposition. This study showed that electrokinetic deposition aid consistent mass exchange between the cathode and anode, thus it is an efficient and effective deposition method. Also, there was no significant impact of the ZnO-*Citrus sinensis* nano-additive on the mass and thickness changes in the anodes and cathode from the simulation and experiment despite a smoother surface achieved with ZnO-*Citrus sinensis* nano-additive when examined physically.

It also shows that the process can effectively be investigated artificially without recourse to experimentation.

References

1. Bruce KG (2012) Electro chemical deposition: principles, methods and applications
2. Schlesinger M, Paunovic M (eds) (2000) Modern electroplating, 4th ed. Wiley, New York
3. Loto CA, Olefjord I (1992) Corr Prev Control J 39:142–149
4. Loto CA, Olefjord I (1990) Corr Prev Control J 37(5):158–163
5. Loto CA., Olefjord I, Mattson H (1992) Corros Prev Control J 39:82–88
6. Ashby MF, Jones DRH (2002) Engineering materials 1. An introduction to their properties and applications. Second Edition. Department of Engineering, University of Cambridge, UK. ISBN 0 7506 3081 7, pp 211–232
7. Asamura T (1998) Proceedings of the 4th international conference on zinc and zinc alloy coated steel sheet. Galvatech '98, Chiba, Japan. The iron and steel institute of Japan, pp 14–21
8. Goodwin FE (1998) Proceedings of the 4th international conference on xinc and zinc alloy coated steel sheet. Galvatech '98, Chiba, Japan. The iron and steel institute of Japan, pp 31–39
9. Winand R (2010) Electrodeposition of zinc and zinc alloys. Wiley, USA. pp 285–307
10. Loto CA (2012) Influence of *Ananas comosus* juice extract as additive on the electrodeposition of zinc on mild steel in acid chloride solution. Int J Electrochem Sci 7:10748–10762

11. Loto CA, Olofinjana A, Popoola API (2012) Effect of *Saccharum officinarum* juice extract additive on the electrodeposition of zinc on mild steel in acid chloride solution. Int J Electrochem Sci 7:9795–9811
12. Park DY, Myung NV, Schwartz M, Nobe K (2002) Electrochim Acta 47:2893–2900

Implementing CFD Modelling to Address Defect Formation in Core Injection Moulding

Stefano Cademartori, Nicholas Humphreys, Jean-Christophe Gebelin and Jeffery Brooks

Abstract Ceramic cores are used in casting processes to create complex internal shapes within the final component. The work presented here uses Computational Fluid Dynamics (CFD) analysis to predict the filling and solidification behaviour of ceramic core material during the Ceramic Injection Moulding (CIM) process in the large, complex geometries now typical of modern cores. The aim of the study is to develop a predictive capability to identify key defects in the core that might otherwise only be observed after a number of expensive manufacturing processes. Manufacturing trials using short shots have been carried out in order to validate the transient flow patterns of the paste; this has highlighted the occurrence of jetting, weld lines and flow defects that are highly dependent on the injection parameters and runner designs employed. Analysis of the modelled solidification, shear rates, stagnation points and phase migration has driven die and process optimisation in a production environment.

Keywords CIM · Injection moulding · CFD · Process · Simulation Ceramic · Defect · StarCCM+

Introduction

High working temperatures increase the efficiency of gas-turbines engines, therefore modern components are designed for extreme operating conditions, even beyond the melting temperature of the alloy. Flowing cooling air within and across the surfaces of the components, or film cooling, is one of the technologies used to cool down the turbine blades and vanes [1]. The geometry of the channels is usually complex to increase turbulence and surface area for heat exchange. To achieve such

S. Cademartori (✉) · J. Brooks
University of Birmingham, Edgbaston, Birmingham, B15 2TT, United Kingdom
e-mail: stefano.cademartori@gmail.com

N. Humphreys · J.-C. Gebelin
Doncasters Group, Innovation House, Droitwich, WR9 9RB, United Kingdom

L. Nastac et al. (eds.), *CFD Modeling and Simulation in Materials Processing 2018*, The Minerals, Metals & Materials Series,
https://doi.org/10.1007/978-3-319-72059-3_20

degree of complexity, metal is cast around ceramic cores housed inside investment moulds. The cores are then removed via chemical etching [2].

The shape complexity, the high production volume and the surface quality required in the production of cores, make injection moulding the most frequently used forming technique for this purpose. However, the selection of the process parameters, often found empirically, makes the process challenging to set up and not suitable for small production runs. The core material is formed of ceramic powders, mixed with a suitable wax binder system, which promotes an even distribution of the powder while injected into a mould. The binder also allows compaction of the powder to form a so-called 'green body', which is heated in a furnace for de-binding, and then sintering [2].

If the selection of injection parameters or paste formulation is poor, it can lead to the formation of defects, that may only be detectable after costly thermal treatments (the most time consuming and energy expensive steps of the process) [2, 3]. Moreover, to inject sound cores, the dies used in CIM require high wear resistance, fluid cooling channels, gas vents and an ejection system to extract the solid core. Despite the consequential high up-front cost of tooling, the dies are not commonly designed accounting for the behaviour of the fluid material during injection.

The implementation of a mathematical model able to predict defect formation in the production of complex CIM parts opens the possibility for engineers to design dies specifically for the injected material, shifting from a tool-maker die design to a process oriented die design. Furthermore, the understanding of the injection conditions enables the optimisation of machine parameters in order to reduce production problems with existing moulds.

This work reports some of the insight on defect formation achieved through modelling of a number of core geometries, injection profiles and material systems. Due to the strictly confidential origin of the work neither material data nor detailed pictures will be given.

Materials and Methods

The core materials injected into the die are highly loaded ceramic wax systems. These ceramic pastes must be able to achieve a complex shape, fine surface detail, maintain a homogenous chemical composition, and behave like a fluid during injection while guaranteeing sufficient wet strength for extraction. The selection of materials in the ceramic core is further limited to those that can be dissolved out using an etchant after casting of the metal blade. Two categories of material are commonly employed: silica and alumina based ceramics [2, 4, 5]. In this work two separate ceramic-wax pastes were considered; one having a higher viscosity, typically injected at higher pressures, the other having a lower viscosity, more suitable for lower pressures and larger cores.

The paste was thermally characterised using several methods: Differential Scanning Calorimetry (DSC) for liquidus and solidus temperatures—Thermal

Gravimetric Analysis (TGA) to assess wax content—laser flash for the thermal diffusivity, and material density using the Archimedes' method.

The flow behaviour of the pastes was characterised using rotational and capillary rheometry, at low and high shear rates respectively. A range of rotational and capillary experiments were carried out from injection temperature to just above the solidification temperature. Yield stress was measured by twin plate rotational rheology, using a stress linear ramp at the injection temperature [6]. All the viscosity readings were fitted using the Herschel-Bulkley model [7] for Bingham plastics limited by a maximum and a minimum viscosity value:

$$\mu(\dot{\gamma}) = \begin{cases} \alpha_T \, \mu_0, & \dot{\gamma} < \frac{\tau_0}{\mu_0} \\ \alpha_T \, \dfrac{\tau_0 + k\left[\alpha_T\left(\dot{\gamma} - \frac{\tau_0}{\mu_0}\right)\right]}{\alpha_T \, \dot{\gamma}}, & \dot{\gamma} \geq \frac{\tau_0}{\mu_0} \end{cases}$$

where μ [Pa s] is the viscosity, $\dot{\gamma}$ [s^{-1}] is the shear rate, α_T the temperature shift factor, τ_0 [Pa] is the yield stress, k the consistency factor and μ_0 [Pa s] the yielding viscosity [8].

The dependence to the temperature is of the Arrhenius' type as follow:

$$\log(\alpha_T) = \frac{E_a}{R}\left(\frac{1}{T} - \frac{1}{T_0}\right)$$

where E_a [J/mol] is the activation energy, $R\left[\frac{\mathrm{J}}{\mathrm{mol\,K}}\right]$ the universal gas constant and T_0 [K] the reference temperature [8].

The computational fluid dynamic (CFD) software environment used was StarCCM+. A fully coupled fluid flow and heat transfer model was created, with physical domains for the dies, fluid volumes, cooling channels, and any additional volumes such as stabilising quartz pins. Regions were meshed using polyhedral elements with multiple prism layers at the walls to capture the heat transfer and high fluid shear rates. A continuous fluid volume was modelled as a Eulerian multiphase problem, with the ceramic paste acting as a liquid phase, and a compressible ideal gas as a secondary phase. Transient simulations were carried out using an implicit unsteady solver, with timestep limited to obtain a target mean value of the Courant-Friedrichs-Lewy number (CFL) of 0.5. The high fidelity of mesh resolution, and small timestep (typically 1e−4), as well as highly viscous fluid meant turbulence was modelled directly, with no additional models required [9]. Gas in the dies was vented at pressure outlets, stopping as soon as obstructed by paste.

The injection parameters used in production were modelled using the defined ramping time and pressure limits. The injection stage comprised of the filling, then the compaction of the material at high pressure; afterwards the injection pressure is removed and the core left to solidify. The cooling and solidification of the core was driven by the large thermal mass of the steel die, with additional cooling channels, which were fully modelled.

Results and Discussion

Simulations of injection and solidification of different die geometries were carried out along with production data analysis. Moreover, two different pastes have been employed depending on the core. Results have been divided by the three highly interacting factors influencing the occurrence of defects after sintering: filling pattern, shear rate, and temperature distribution. The first is highly dependent on the die geometry and the rheology of the paste. The process variable driving the second is the injection speed, while the nozzle temperature and the cooling of the die are responsible for the temperature distribution of the paste.

Filling Pattern

An initial assessment of the material models, boundary conditions and process description was carried out through comparison of simulated injections and real short shots (Fig. 1). The simulations are in excellent agreement with experiments, and are easy to measure using the features on the core, giving confidence in the process description. The material description has also been validated by simulating rheological experiments directly—to be discussed in a later paper.

Short shots are useful to visualise the transient filling pattern, but thanks to modelling it was possible to gather more specific information on the paste such as its residence time and distribution after injection. Figure 2 highlights the injection

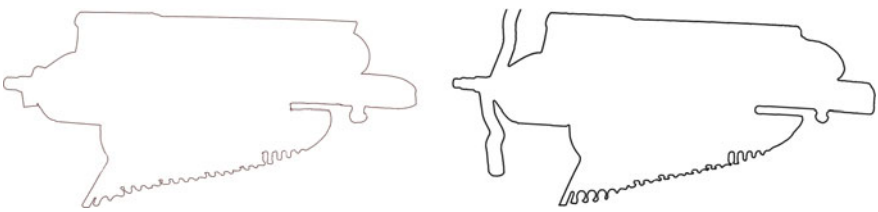

Fig. 1 Outline comparison of a short shot (left) and the simulation (right) at identical injected volume

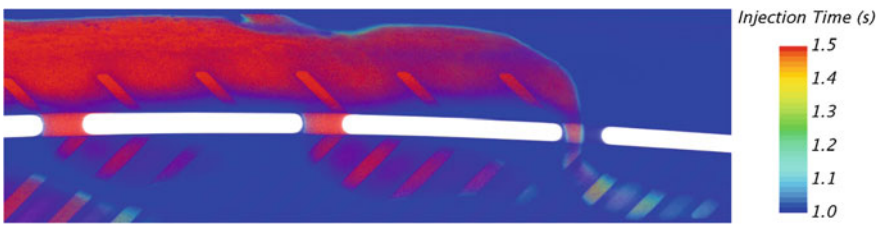

Fig. 2 Turbine blade core detail showing injection time of paste into the mould. Scale highlights the flow of new material into stagnant one

time, showing how streams of newly injected paste interact with the rest of the material. The study of the filling enables prediction of the position of weld lines, to visualise the residence time of the injected paste into the die and highlights crucial information such as stagnant location and feeder efficiency.

The ability of the paste to weld together when two fronts meet is essential in the production of complex shapes. If the temperature of the paste and/or local pressure are not high enough, a weld line will appear, producing a surface defect and an optimal crack initiator [10, 11]. Weld lines are usually identified post injection, with the part scrapped before firing, however, cracks may also be seen post-firing at the meeting point of paste fronts that appeared to have welded together well. The example reported in Fig. 3 demonstrates an area where two fronts meet along an extruded section of the core. Cracks in the fired core, in the location of the simulated meeting fronts are shown. It is common that feeders are under-dimensioned or in a suboptimal location to achieve the required pressure to continuously feed part of the die without stopping, furthermore, long sections with small cross sections are subjected to a higher thermal exchange that the rest of the die, increasing the paste viscosity and therefore the pressure required to weld together. With the merging fronts having a low surface temperature, it seems fair to attribute longitudinal cracks found in this location to such phenomena. As the defect is only detectable post-firing, it is arguable that the two fronts adhered to some degree, but leaving the ceramic particles strongly orientated, so that the stress produced by later shrinkage was released by crack formation.

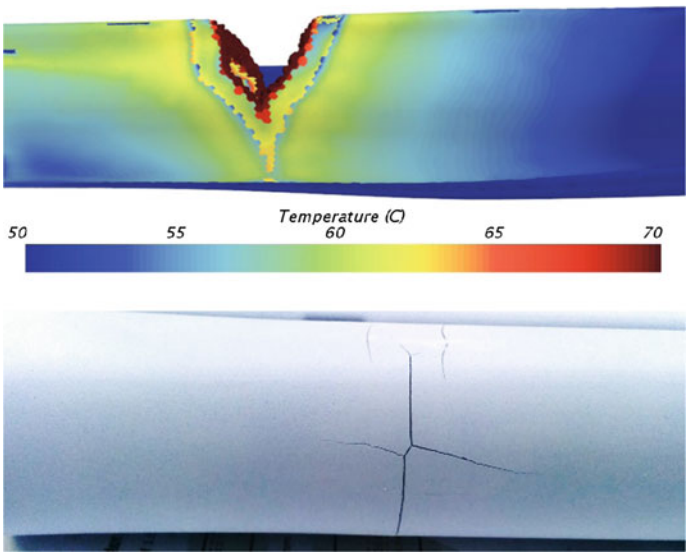

Fig. 3 Top—Simulation showing the last filled volume of a core. Bottom—a post-firing core showing a crack along the weld line

Shear Rates

Temperature, viscosity and instantaneous injection flow rate, in combination with localised die cross-section in the complex geometries typical of technical ceramics determine the velocity and shear rate of the paste. Loaded materials are subjected to phase migration and orientation in areas exhibiting high shear rates [12, 13]. Occurrence of such conditions have been tested by microstructural analysis in different sections and additionally by thermogravimetric investigations on green bodies.

By developing a simple yet useful criterion, recording the maximum shear rate applied to the paste as it moves through the core, the simulation was able to predict the location of cracks recorded after firing of the part. In particular cracks were located where the shear rate was high compared to the surrounding area, suggesting that the geometry variation responsible for the higher local speed has produced a weaker structure (Fig. 4). It is likely that only the liquid phase accommodates the strain by forming particle-free regions away from die walls, where the local speed is higher, whereas particles packed aligned along the walls [14].

Clearly, all of the injected material in the final core will have passed through the inlet, and as such, any poor flow condition here will detrimentally affect the properties of the part. A design modification at the inlet is shown in Fig. 5. The use of conical section from the nozzle to the bulk of the core was optimised through simulation to reduce the maximum shear rate achieved by more than 60%. Furthermore, often such modification can be applied to existing dies. Conical

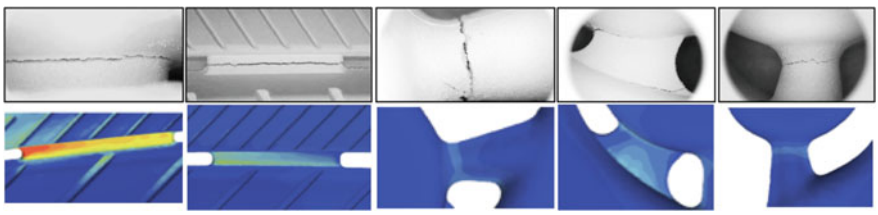

Fig. 4 Localised high values of maximum shear rates and reported post-firing cracks

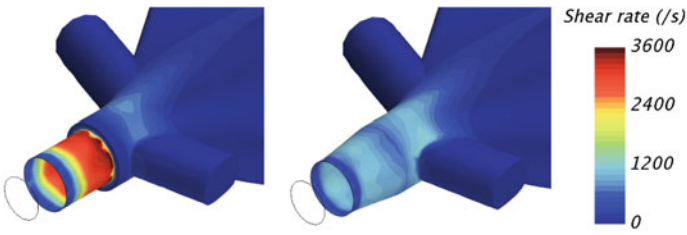

Fig. 5 Shear rate at the inlet using a square section (top) and conical (bottom)

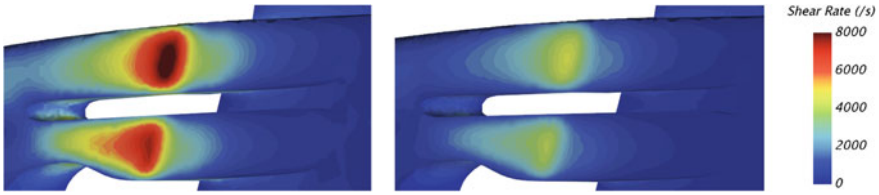

Fig. 6 By changing the flow rate profile of the injection the shear rates achieved in the trailing edge were halved

sections have been reported in a number of investigations [15] to limit the amount of phase migration.

Typical of all blades, high shear rates are found in the trailing edge, as the thinnest section of a core and usually last to fill. In extreme cases, the trailing edge is so thin that the paste velocity increases enough to prevent efficient venting. X-ray radiography has showed the presence of trapped air at the location where stagnant paste in the trailing edge meet with a flux of high velocity new paste. With the ability to simulate the filling, it is possible to modify the injection parameters to reduce the piston or screw speed as the filling front reaches the trailing edge. In this way, the thermal and shear distribution in the bulk of the core is unchanged, with only the last phase of the filling varying. Figure 6 demonstrates a shear rate 50% lower in the most critical section of a core, where most of the defects are located.

Solidification

The thermal conductivity and melting temperature of the pastes simulated were measured. Although CIM solidification has been previously modelled [16, 17] this work also simulated the shape of the water cooling channels within the die, in order to achieve a more representative description of the heat distribution of the tool. It was therefore possible to reproduce the solidification after injection. Other than the formation of weld lines, one of the most severe problems driven by a non-optimal solidification control is the inlet freezing: if the inlet has high thermal losses, it will freeze off prematurely, preventing new injection material to compensate for the solidification shrinkage in the bulk of the core. The resulting ineffective compaction phase leads to internal voids, delamination between the solid skin and the bulk and also weakness on this boundary, due to orientation as reported by other investigations [16, 18, 19]. Figure 7 shows a simulation of a solidifying core, and the isolated liquid phase in the centre of the aerofoil after the inlet has frozen, compared to a picture of the fired core with visible internal lamination.

The primary cause of scrap in our analysis of complex core production is post-firing cracking of the trailing edge, where simulated heat loss predicted the material solidifying along two divergent fronts, pulling the fragile sections apart. In

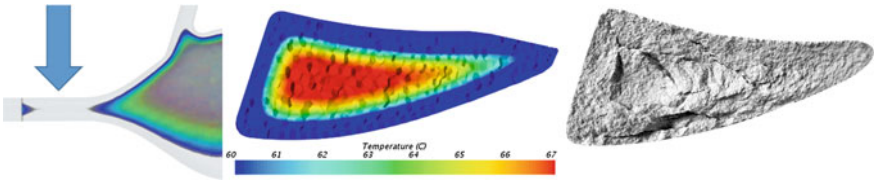

Fig. 7 Left—Molten paste during the compaction phase of the injection, at the point at which the inlet has frozen. Right—a broken core after firing: showing a crack following the perimeter of the part

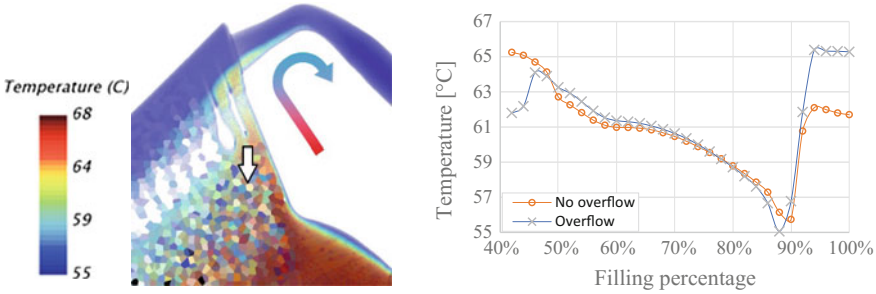

Fig. 8 An additional overflow added to flush through warm paste into critical regions (path of coloured arrow). Graph shows higher temperature achieved with overflow in probe position (white arrow) (Figure censored over critical geometry)

this context, our model was able to provide an insight into the combined flow and solidification results. In particular the die has been modified to have an empty volume next to the trailing edge; this region is partially filled, but remains stagnant during the initial stage of the filling, while the paste flows preferentially into the thickest sections. The empty volume subsequently allows additional, hotter material to flush through the cold, stagnant paste in the last phase of filling, into a non-critical location for the component in Fig. 8. This modification, allowing on average a 5 °C increase in temperature above liquidus has driven an outstanding improvement in production.

Conclusions

In this work filling and solidification of different ceramic cores have been modelled. In particular, results have showed that:

- Cracks form where there are high shear rate gradients
- Weld lines can be eliminated by the use of well-designed feeders and packing stage optimisation

- Injection velocity can be optimised depending on the section being filled
- Die design can be modified to limit phase migration
- Stagnant paste related defects can be overcome by adding sacrificial volumes.

Future work will include the following:

- Building of an experimental system to investigate the severity of weld lines in ceramic pastes at different forming conditions
- Statistical analysis of the production to verify the effect of the die changes made
- Test shots using the proposed injection flow profiles
- Use of an instrumented die to validate further filling and solidification.

In conclusion, by combining accurate description of the process and material behaviour, with an understanding of typical defects formation mechanics this work can be used at the mould design phase to reduce problems often only detectable at the end of the production and reduce design iteration of the die.

Acknowledgements The author gratefully acknowledges financial support from the Centre for Doctoral Training in Innovative Metal Processing (IMPaCT) funded by the UK Engineering and Physical Sciences Research Council (EPSRC), grant reference EP/L016206/1 and Doncasters Group.

A special thanks to Thomas Wright and the Doncasters Technical Centre and to the staff members of the University of Birmingham, in particular Richard Turner, Stuart Blackburn, John Wedderburn and Frank Biddleston.

References

1. Pradyumna R, Baig MAH (2012) Ceramic cores for turbine blades: a tooling perspective. Int J Mech Indus Eng 2(4):1–7
2. Wereszczak AA, Breder K, Ferber MK, Kirkland TP, Payzant EA, Rawn CJ, Krug E, Larocco CL, Pietras RA, Karakus M (2002) Dimensional changes and creep of silica core ceramics used in investment casting of superalloys. J Mat Sci 37(19):4235–4245. doi:https://doi.org/10.1023/A:1020060508311
3. Knight J, William A (2000) Structure property relationships of silica based performed cores for investment casting. Ph.D. thesis, University of Birmingham
4. Wu H, Li D, Tang Y, Sun B, Xu D (2009) Rapid fabrication of alumina-based ceramic cores for gas turbine blades by stereolithography and gelcasting. J Mat Process Technol 209(18–19):5886–5891. doi:https://doi.org/10.1016/j.jmatprotec.2009.07.002
5. Gromada M, Swieca A, Kostecki M, Olszyna A, Cygan R (2015) Ceramic cores for turbine blades via injection moulding. J Mat Process Technol 220:107–112
6. Cheng DCH (1986) Yield stress: a time-dependent property and how to measure it. Rheologica Acta 25(5):542–554. doi:https://doi.org/10.1007/BF01774406
7. Herschel WH, Bulkley R (1926) Measurement of consistency as applied to rubber-benzene solutions. Am Soc Test Proc 26:621
8. STARCCM+ Users Manual. http://www.cd-adapco.com/products/star-ccm/documentation. Accessed 31 Aug 2017
9. Humphreys NJ, McBride D, Shevchenko DM, Croft TN, Withey P, Green NR, Cross M (2013) Modelling and validation: Casting of Al and TiAl alloys in gravity and centrifugal casting processes. Appl Math Model 37(14):7633–7643. doi:https://doi.org/10.1016/j.apm.2013.03.030

10. Hwang J, Choi S, Hong S, Kim N (2013) Determination of the flow stress and thermal properties of ceramic powder feedstock in ceramic injection molding. J Mech Sci Technolo 27(6):1815–1824. doi:https://doi.org/10.1007/s12206-013-0432-0
11. Edirisinghe MJ, Evans JRG (1986) Review: fabrication of engineering ceramics by injection moulding. II. Techniques. Int J High Technol Ceram 2(4):249–278
12. Patel MJ, Wedderburn J, Blackburn S, Wilson DI (2009) Maldistribution of fluids in extrudates. J Eur Ceram Soc 29(5):937–941. doi:https://doi.org/10.1016/j.jeurceramsoc.2008.07.037
13. Barnes EC, Wilson DI, Johns ML (2006) Velocity profiling inside a ram extruder using magnetic resonance (MR) techniques. Chem Eng Sci 61(5):1357–1367
14. Mueller S, Llewellin SW, Mader HM (2009) The rheology of suspensions of solid particles. Kolloid-Zeitschrift 39(4):291–300. https://doi.org/10.1098/rspa.2009.0445
15. Mascia S, Patel MJ, Rough SL, Martin PJ, Wilson DI (2006) Liquid phase migration in the extrusion and squeezing of microcrystalline cellulose pastes. European J Pharm Sci 29(1):22–34
16. Zhang T, Blackburn S, Bridgwater J (1997) Orientation of binders and particles during ceramic injection moulding. J Eur Ceram Soc 2219(96):101–108. doi:https://doi.org/10.1016/S0955-2219(96)00070-2
17. Bilovol VV (2003) Mould filling simulations during powder injection moulding. Delft University of Technology, Netherlands
18. Krug S, Evans JRG, Ter Maat JHH (2002) Differential sintering in ceramic injection moulding: particle orientation effects. J Eur Ceram Soc 22(2):173–181. doi:https://doi.org/10.1016/S0955-2219(01)00259-X
19. Mannschatz A, Muller A, Moritz T, Müller A, Moritz T (2011) Influence of powder morphology on properties of ceramic injection moulding feedstocks. J Eur Ceram Soc 31(14):2551–2558. doi:https://doi.org/10.1016/j.jeurceramsoc.2011.01.013

Numerical Simulation of Turbulence Flow and Solidification in a Bloom Continuous Casting Mould with Electromagnetic Stirring

Shaoxiang Li, Peng Lan and Jiaquan Zhang

Abstract Based on the Maxwell's equations and a revised low-Reynolds number k-e turbulence model, a coupled three-dimensional numerical model has been developed to describe the electromagnetic field, fluid flow and solidification in a bloom continuous casting mould with electromagnetic stirring (M-EMS). The stirring electric current effects on the turbulent flow, temperature distribution and shell growth are investigated numerically. According to the simulation result, the electromagnetic force has a circumferential distribution on the strand transverse section, and a swirling flow field along the axial direction is observed in the mould region with the application of M-EMS, which changes the flow pattern of melt in the mould significantly and promotes the superheat dissipation of the molten steel. Moreover, overlarge current intensity will generate an inhomogeneous solidified shell at the exit of the mould due to the tangential velocity of the swirling flow and the installed position of the M-EMS.

Keywords Continuous casting · Electromagnetic stirring · Electromagnetic field Fluid flow · Solidification

Introduction

The mould electromagnetic stirring has been widely used in the process of bloom continuous casting, and its metallurgical effectiveness for improving the quality of cast products is mainly obtained by controlling the flow pattern of melt in the given

S. Li · P. Lan · J. Zhang (✉)
School of Metallurgical and Ecological Engineering, University of Science and Technology, Beijing 100083, People's Republic of China
e-mail: jqzhang@metall.ustb.edu.cn

L. Nastac et al. (eds.), *CFD Modeling and Simulation in Materials Processing 2018*, The Minerals, Metals & Materials Series,
https://doi.org/10.1007/978-3-319-72059-3_21

region of the mould. The optimized flow velocity will enhance the columnar-to-equiaxed transition during solidification and reduce the surface and subsurface defects [1, 2]. Since the complexity of transport phenomena in continuous casting process, it is difficult for plant measurements and physical experiments to investigate the melt flow and solidification with M-EMS. Therefore, numerical simulation method is very necessary for the research of electromagnetic stirring. Previous researchers have devoted significant efforts to develop the mathematical models for numerical studying of the characteristics in the continuous casting process with M-EMS [3–10]. However, the superheat dissipation effect of the M-EMS and the solidifying shell growth under M-EMS have rarely been reported.

In this research, a 250 × 280 mm bloom mould with electromagnetic stirring is studied by the numerical simulation method. A coupled model has been developed to analyse the characteristic of the three-dimensional electromagnetic field, turbulent flow, heat transfer and solidification in the bloom strand with M-EMS. The influences of stirring current intensity on the superheat dissipation and shell growth are studied in detail.

Mathematical Model

The schematic diagram of the bloom continuous casting with M-EMS discussed in this paper is shown in Fig. 1a, and the location of the M-EMS is given in Fig. 1b. The model of M-EMS mainly includes molten steel, stirring coil, copper mould, iron core and air (not shown). The origin of the coordinates is at the center of the mould meniscus, and the casting direction is along the positive direction of Z axis. The mid-plane of the stirrer is located at Z = 0.45 m. Below the mould exit, the length of the water spray zone is 0.35 m and the air-mist cooling zone is 1.005 m. And the straight through SEN is used in this study.

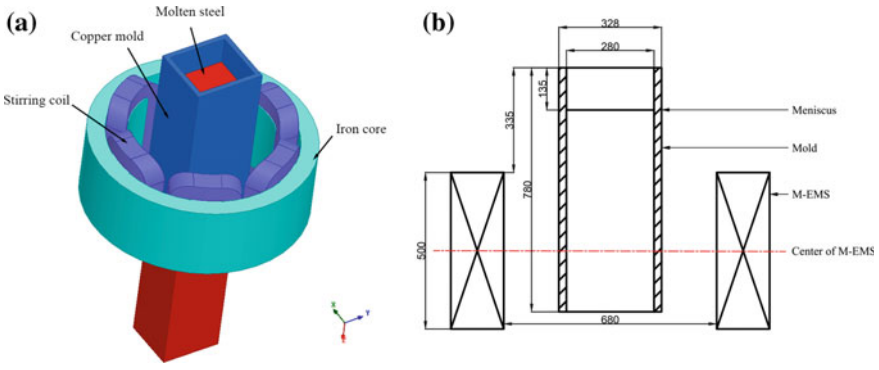

Fig. 1 Schematic diagram (**a**) and location (**b**) of the M-EMS

Assumptions

The following assumptions are made to simplify the mathematical model and make it more efficient:

1. Because of the low magnetic Reynolds number (about 0.01) in continuous casting with M-EMS, the effect of the melt flow on the electromagnetic field was ignored.
2. The electromagnetic phenomena were assumed to be a magneto quasi-static problem, and the displacement current in Maxwell's equations was ignored.
3. The molten steel was assumed to be incompressible Newtonian fluid. The viscosity, the specific heat, and the thermal conductivity were assumed to be constant.
4. The mushy zone was treated as a porous medium, where the flow obeys Darcy's law.
5. The influence of mould oscillation and mould taper on the fluid flow was not considered.

Governing Equations

1. Electromagnetic field
   At the low frequency of M-EMS, the Maxwell's equations can be found elsewhere [11].
   The time-averaged Lorentz force can be calculated by:

$$F_E = \tfrac{1}{2} Re(j \times B) \tag{1}$$

   where B is the magnetic induction intensity and j is the induced current density in the melt.

2. Fluid flow

   Continuity equation:

$$\frac{\partial u_i}{\partial x_i} = 0 \tag{2}$$

   The momentum equation is:

$$\rho \frac{\partial \mu_i \mu_j}{\partial x_j} = \frac{\partial}{\partial x_j}\left[\mu_{eff}\left(\frac{\partial \mu_i}{\partial x_j} + \frac{\partial \mu_j}{\partial x_i}\right)\right] - \frac{\partial P}{\partial x_i} + \rho g_i + F_E + S_P \tag{3}$$

where ρ is the density of molten steel, P is the pressure, g is the acceleration of gravity. μ_{eff} is the effective viscosity coefficient, which is calculated by:

$$\mu_{eff} = \mu + \mu_t \tag{4}$$

μ_t represents the turbulent viscosity determined by the low Reynolds number $k - \varepsilon$ turbulent model [12], while μ is the viscosity of molten steel. F_E represents the electromagnetic force, as the source term in the momentum equation. The last term S_P accounts for the phase interaction force within the mushy zone, and described by the Darcy's law:

$$S_P = \frac{(1-f_L)^2}{\left(f_L^3 + 0.001\right)} A_{mush}\left(u_i - u_{S,i}\right) \tag{5}$$

A_{mush} is the mushy zone constant, depending on the morphology of the solidifying interface. The value of A_{mush} must be large enough to make the velocity of the solid phase equal to the casting speed and is usually between 1×10^5–1×10^8 [13]. In present research, is used 5×10^8 for A_{mush}. f_L is the liquid fraction and is given by the lever rule in the mushy zone as follows:

$$f_L = 1 - f_S = \begin{cases} 0 & T \le T_S \\ \frac{T-T_S}{T_L-T_S} & T_S < T < T_L \\ 1 & T \ge T_L \end{cases} \tag{6}$$

where T_L and T_s are the liquidus and solidus temperature, respectively.

3. Solidification and Heat-Transfer

To obtain a precise prediction of the temperature field and macroscopic solidification behavior in the continuous casting process, the enthalpy equation is employed. The energy equation is:

$$\rho\mu_i \frac{\partial H}{\partial x_i} = \frac{\partial}{\partial x_i}\left[\left(k_l + \frac{\mu_t}{Pr_t}\right)\frac{\partial H}{\partial x_i}\right] \tag{7}$$

where k_l is the thermal conductivity, Pr_t is the turbulent Prandtl number and set at 0.9.

Boundary Conditions

Electromagnetic Field

1. Three phase alternating current is connected to the coils of M-EMS, and the phase difference is 120°.
2. The magnetic flux is assumed to be parallel to the boundary at the side of the air cylinder, and it is assumed to satisfy a Neumann boundary condition on the top and bottom surfaces.

3. An insulating layer is used between the iron core and the coil, as well as between the strand and the mould to represent the mould powder layer, so the current is enclosed within the coil and the induced current is enclosed within the molten steel.

Flow-Solidification

1. Inlet: the inlet velocity is computed according to the mass conservation between the inlet and outlet based on the casting speed, and the inlet temperature is set as the sum of the liquidus temperature and the superheat. The values of turbulent kinetic energy and turbulent dissipation rate at the inlet are calculated by the semiempirical equations.
2. Outlet: the fully developed flow condition is adopted.
3. Free surface: considering the heat insulation of mould flux, the adiabatic condition is applied to the free surface with zero-shear force.
4. Strand surface: The stationary wall condition is employed. The heat flux boundary condition is applied on the mould zone according to Savage and Pritchard:

$$q_s = 2{,}680{,}000 - b\sqrt{L/V_c} \tag{8}$$

and a convective boundary condition is imposed on the secondary cooling zone and the integrated heat transfer coefficient is calculated by:

$$\text{Water spray region: } h = 0.42w^{0.351} \tag{9}$$

$$\text{Air-mist spray region: } h = 116 + 10.44w^{0.851} \tag{10}$$

Numerical Solution Procedure

The numerical simulation is divided into two steps: Firstly, the electromagnetic field is calculated via the finite element code Ansys Maxwell by solving Maxwell's equations, and then the time-averaged electromagnetic forces are extracted. Secondly, the phenomena of the fluid flow, heat transfer and solidification in the continuous casting process is simulated by the control-volume-based Fluent software, and the data of electromagnetic forces are imported into the momentum equation as source term by user defined functions of the Fluent. The 1.45 m long strand from the meniscus is simulated for electromagnetic field calculations in order to save computation consumption, and 2.0 m for the flow field and solidification so that the fluid flow will get a full development. The main dimensions and material physical properties used in the current study are listed in Table 1.

Table 1 Main dimensions and material properties for the numerical simulation

Parameter	Value	Parameter	Value
Mould cross section/mm^2	250 × 280	Density/kg m^{-3}	7020
Mould length/mm	780	Viscosity/ kg m^{-1} s^{-1}	0.0055
Mould working length/mm	645	Specific heat/ J kg^{-1} K^{-1}	680
Mould thickness/mm	24	Thermal conductivity/ W m^{-1} K^{-1}	29
SEN external diameter/mm	90	Liquidus temperature/K	1766
SEN inner diameter/mm	40	Solidus temperature/K	1718
SEN submerged depth/mm	100	Latent heat of molten steel/ J kg^{-1}	270,000
Magnetic permeability of vacuum/H m^{-1}	1.257 × 10^{-6}	Superheat/K	30
Relative permeability of the steel, copper mould, stirring coil and air	1	EMS current intensity/A	200, 350, 500
Iron core relative permeability	1000	EMS current frequency/Hz	3
Electrical conductivity of molten steel/S m^{-1}	7.14 × 10^5	Casting speed/ m min^{-1}	1.05
Copper mould conductivity (423 K) [11]/ S m^{-1}	3.18 × 10^7	Grade of steel	45 Steel

Results and Discussion

Electromagnetic Field

Figure 2 shows contour plots of the magnetic flux density on the strand surface with 350 A. The magnetic flux density increases firstly and then decreases gradually along the casting direction, the tendency matches well with the results measured by Trindade [11]. Figure 3 gives the center magnetic flux density along the casting direction (a) and in the stirrer center (b) under different currents, the values are in agreement with the measured data under 350 A. It can be seen that the magnetic flux density increases distinctly with the increasing current intensity. However, the maximum magnetic flux density does not appear at the center plane of the stirrer but nearby the exit of the mould. It can be accounted for the electromagnetic shielding effect of the copper mould, which affects the electromagnetic field distribution. Besides, the center magnetic flux density has a favourable linear relation with the running current, where every 150 A increase in current, the magnetic flux density will increase 22.9 mT.

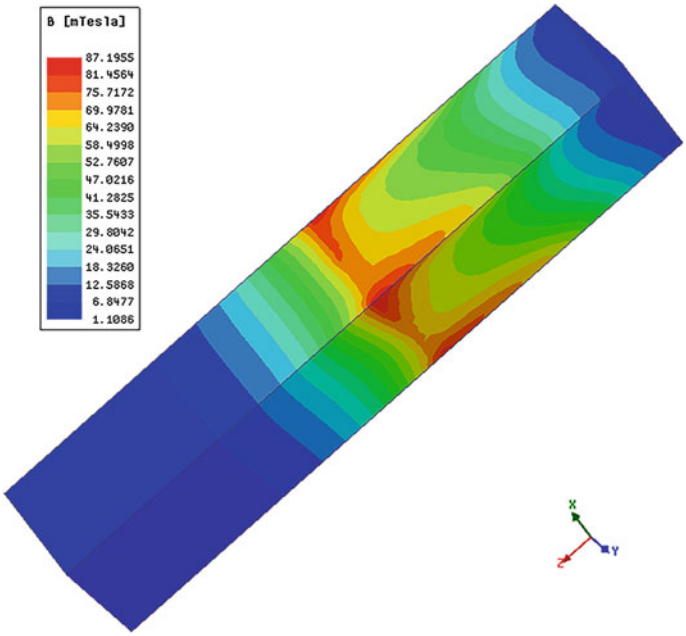

Fig. 2 Distribution of magnetic flux density on the strand surface with 350 A

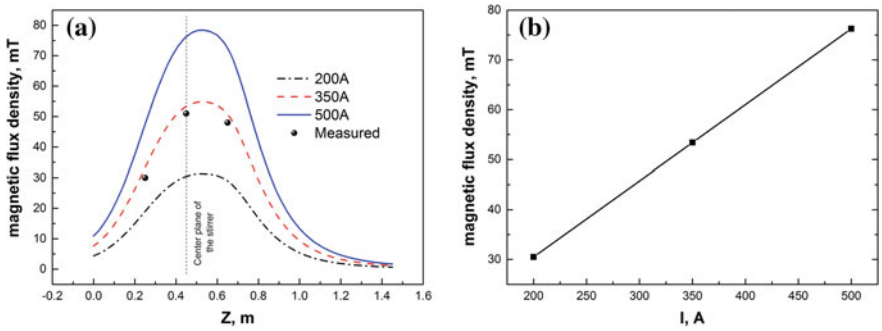

Fig. 3 Comparison of the magnetic flux density (**a**) along central axis of the strand, and (**b**) in the stirrer center under the cases of different currents

Figure 4 shows the vector of the time averaged electromagnetic force density on the plane Z = 0.45 m with 350 A. The electromagnetic force density has a circumferential distribution on the transverse plane to the bloom strand, being greatest at the corners of the bloom and decreasing towards the center. Figure 5 shows the distribution of tangential electromagnetic force along Y direction at center plane of stirrer. The tangential electromagnetic force increases obviously with the increasing

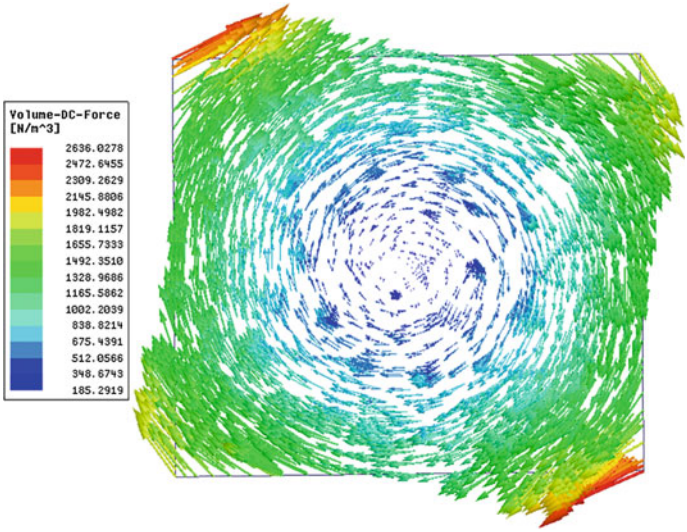

Fig. 4 Distribution of electromagnetic force density on the plane Z = 0.45 m with 350 A

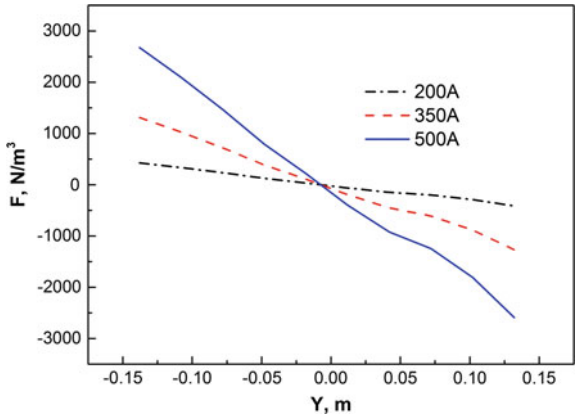

Fig. 5 Variation of tangential electromagnetic force along Y direction at center plane of stirrer

current intensity, The maximum tangential electromagnetic force increases form 428 N/m^3 at 200 A to 2675 N/m^3 at 500 A.

Flow Field and Solidification

Figure 6 displays the velocity contour and streamline on the central symmetry plane of strand wide face (X = 0) under (a) without electromagnetic stirring and (b) the

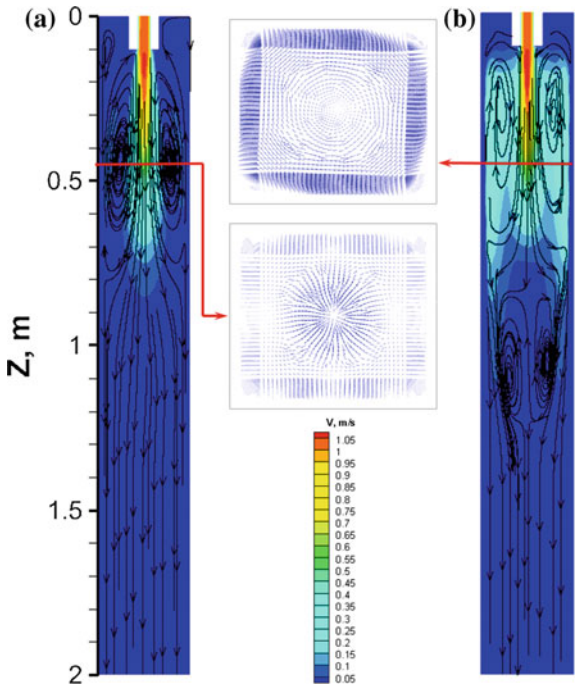

Fig. 6 Velocity contour and streamline on the plane X = 0 m, **a** without EMS **b** I = 350 A

stirring current intensity is 350 A. Without M-EMS, the impinging jet from the straight through SEN flows down into the depths of liquid core and then returns upward along the solidification front, finally forms a pair of large recirculation zones owing to the continuum of the fluid. Meanwhile, a pair of smaller vortices appears near the meniscus. After applying the M-EMS, the molten steel flow pattern changes significantly. In addition to a clockwise recirculation zone formed at the upper part, another pair of recirculation zone forms in the lower region, which flows anticlockwise. Besides, with the effect of the rotary electromagnetic force, a horizontal clockwise swirling flow is formed at the cross section of the strand, which is in agreement with the direction of electromagnetic force. The tangential velocity can break the dendrites from the solidification front effectively and promote nucleation, consequently enhance the transition from a columnar to an equiaxed crystal structure. Figure 7 shows the streamline of the molten steel in the mould under various current intensity. It can be seen that, with the increase of the current intensity, the swirl flow of the molten steel in the mould becomes stronger because of the larger electromagnetic force.

Figure 8 shows the distribution of the tangential velocity at cross section through the center plane of stirrer (Z = 0.45 m). It can be seen that the tangential velocity is zero without EMS. When EMS is applied, the tangential velocity rises with the increasing current intensity. The maximum tangential velocity is 0.117, 0.279 and

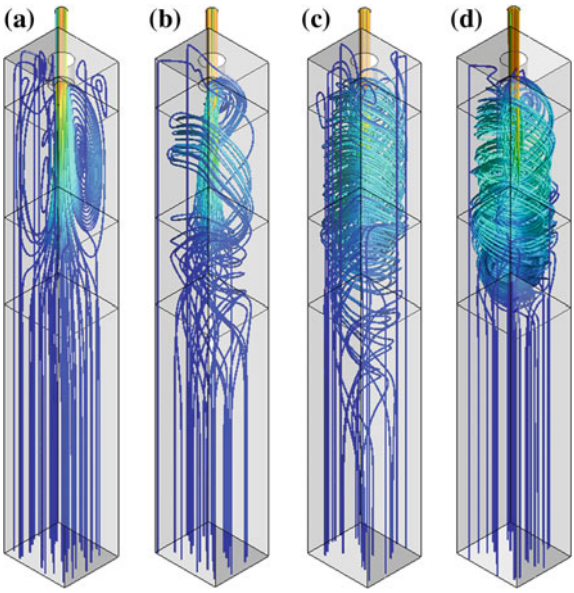

Fig. 7 Streamline of the molten steel for **a** I = 0 A, **b** I = 200 A, **c** I = 350 A and **d** I = 500 A

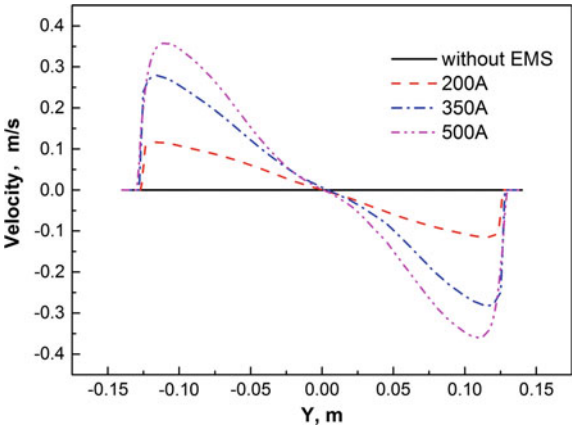

Fig. 8 Tangential velocity profile along Y direction at center plane of stirrer

0.358 m/s under the current intensity of 200, 350 and 500 A, respectively. Meanwhile, the magnitude of tangential velocity increases from the edge firstly, which reaches the maximum near the solidification front region, and then gradually decreases when it is closer to the center of the bloom.

Figure 9 shows the temperature distribution at the centerline of the strand along casting direction. Because of the rotary electromagnetic force and the lower recirculation zone, the adoption of M-EMS can reduce the impingement depth of

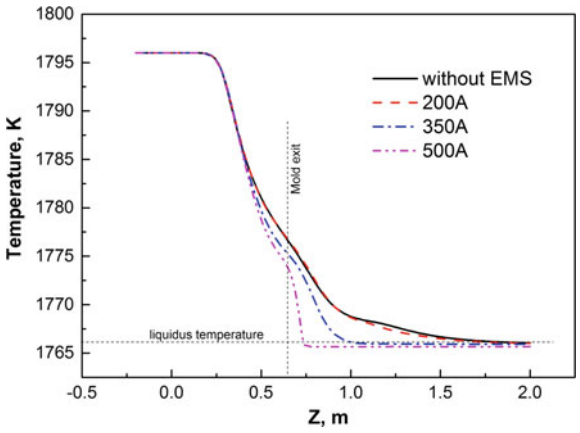

Fig. 9 Temperature variations at strand center along the casting direction

the bulk flow from the SEN, which will be beneficial for melt superheat dissipation and the floatation removal of inclusions. It can be seen that when the running current is 200 A, the temperature distribution at the centerline is approximate to the case of without EMS, which means I = 200 A can't generate sufficient stirring intensity to achieve the better superheat dissipation effect under the present operating condition. However, when I = 350, 500 A, the temperature at the centerline drops clearly below Z = 0.4 m. The remained superheat of molten steel at the mould exit are 10.8, 10.7, 9.3 and 7.9 K, respectively.

Figure 10 shows the growth of shell thickness on its broad surface along with the casting direction, where the liquid fraction of 0.3 is defined as a solidification front. It can be seen that when I = 200 A the shell thickness profile is almost the same as that without M-EMS. When the stirring current increases to 350 or 500 A, the shell of strand begin to growth slowly near the stirrer installed position, which means the M-EMS will inhibit the shell growth as the current intensity increases. This phenomenon can attribute to the superheat dissipation effect of the M-EMS. Moreover, it is seen that the shell thicknesses at the mould exit (Z = 0.645 m) are 13.7, 13.5, 13.0 and 11.3 mm under the four different cases of without M-EMS, I = 200, 350 and 500 A, respectively.

Figure 11 illustrates the liquid fraction on the cross plane at the mould exit. It should be noticed that when the current intensity is 500 A, the tangential velocity on the transverse section of the mould exit is still very high, which is about 0.3 m/s at maximum. Besides, the stirrer locates at the lower part of the mould, which expands the action range of the stirrer. This condition generates an inhomogeneous solidifying shell, which deflect along with the swirling flow direction. That means that it is not the bigger the better situation for the stirring current intensity, and 350 A is a more reasonable case for the present continuous casting process.

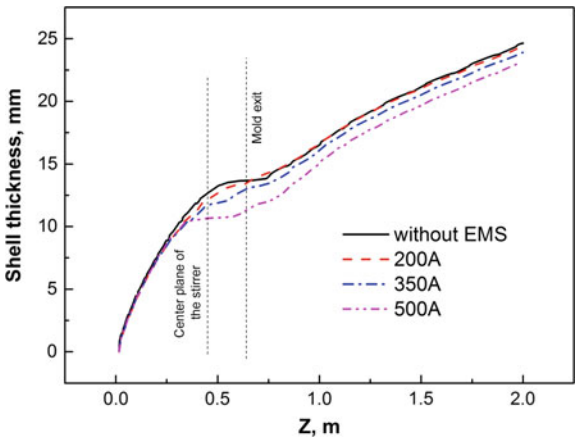

Fig. 10 Variation of the shell thickness along the casting direction

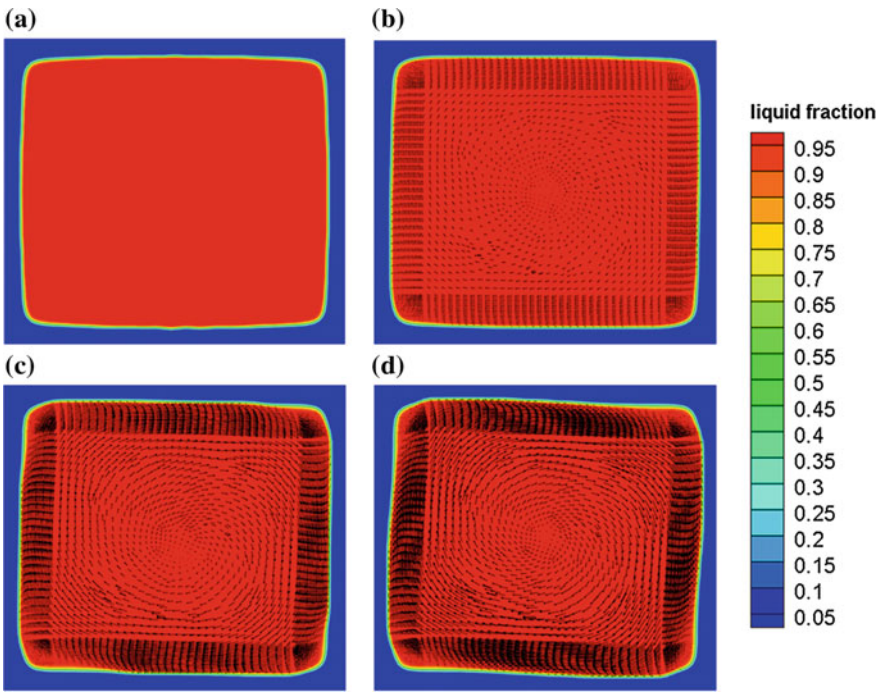

Fig. 11 Liquid fraction contour on the cross plane at the mould exit (Z = 0.645 m) for **a** I = 0 A, **b** I = 200 A, **c** I = 350 A and **d** I = 500 A

Conclusion

1. M-EMS generates a circumferential distribution electromagnetic force on the transverse plane to the bloom strand, with maxima at the corner and decline to the center. Moreover, the distribution of the magnetic flux density and electromagnetic force increase remarkably with the rise of the current intensity.
2. M-EMS changes the flow pattern of melt in the mould distinctly with additional pair of longitudinal anticlockwise flow recirculation in the lower region. The lower recirculation zone reduces the impingement depth of the bulk flow from the SEN, which will be beneficial for melt superheat dissipation and the removal of inclusions.
3. The thickness of the shell decreases with the incremental current intensity, which can be attributed to the increasing superheat dissipation effect of the M-EMS.
4. When the stirrer locates at the lower part of the mould, overlarge current intensity will lead to higher tangential velocity, which will generate an inhomogeneous solidifying shell. And M-EMS with current 350 A is a more reasonable case for the present continuous casting process.

References

1. Kunstreich S (2003) Electromagnetic stirring for continuous casting. Revue de Métallurgie 100(4):395–408
2. Kunstreich S (2003) Electromagnetic stirring for continuous casting-Part 2. Revue de Métallurgie 100(11):1043–1061
3. Natarajan TT, El-Kaddah N (2004) Finite element analysis of electromagnetic and fluid flow phenomena in rotary electromagnetic stirring of steel. Appl Math Model 28(1):47–61
4. Trindade LB, Nadalon JEA, Vilela ACF et al (2007) Numerical modeling of inclusion removal in electromagnetic stirred steel billets. Steel Res Intl 78(9):708–713
5. Liu H, Xu M, Qiu S et al (2012) Numerical simulation of fluid flow in a round bloom mould with in-mould rotary electromagnetic stirring. Metall Mater Trans B 43(6):1657–1675
6. Cho MJ, Park EB, Kim SW (2010) Shield for improving wavy meniscus in the billet continuous casting mould with electromagnetic stirring. ISIJ Intl 50(8):1180–1184
7. Haiqi Y, Miaoyong Z (2010) Three-dimensional magnetohydrodynamic calculation for coupling multiphase flow in round billet continuous casting mould with electromagnetic stirring. IEEE Trans Magn 46(1):82–86
8. Sun H, Zhang J (2014) Study on the macrosegregation behavior for the bloom continuous casting: model development and validation. Metall Mater Trans B 45(3):1133–1149
9. Ren BZ, Chen DF, Wang HD et al (2015) Numerical simulation of fluid flow and solidification in bloom continuous casting mould with electromagnetic stirring. Ironmak Steelmak 42(6):401–408
10. Maurya A, Jha PK (2017) Influence of electromagnetic stirrer position on fluid flow and solidification in continuous casting mould. Appl Math Model
11. Trindade LB, Vilela ACF, Vilhena MTMB et al (2002) Numerical model of electromagnetic stirring for continuous casting billets. IEEE Trans Magn 38(6):3658–3660

12. Jones WP, Launder BE (1973) The calculation of low-Reynolds-number phenomena with a two-equation model of turbulence. Intl J Heat Mass Transf 16(6):1119–1130
13. Aboutalebi MR, Hasan M, Guthrie RIL (1995) Coupled turbulent flow, heat, and solute transport in continuous casting processes. Metall Mater Trans B 26(4):731–744

Author Index

L. Nastac et al. (eds.), *CFD Modeling and Simulation in Materials Processing 2018*, The Minerals, Metals & Materials Series,
https://doi.org/10.1007/978-3-319-72059-3

Subject Index

L. Nastac et al. (eds.), *CFD Modeling and Simulation in Materials Processing 2018*, The Minerals, Metals & Materials Series,
https://doi.org/10.1007/978-3-319-72059-3